Entanglement Generation in Non-Markovian Waveguide Quantum Electrodynamics

vorgelegt von
M. Sc.
Kisa Henriette Barkemeyer

an der Fakultät II - Mathematik und Naturwissenschaften
der Technischen Universität Berlin
zur Erlangung des akademischen Grades

Doktor der Naturwissenschaften
—Dr. rer. nat.—

genehmigte Dissertation

Promotionsausschuss:

Vorsitzender: Prof. Dr. Janik Wolters
Gutachter: Prof. Dr. Andreas Knorr
Gutachter: Prof. Dr. Scott Parkins

Tag der wissenschaftlichen Aussprache: 06. April 2022

Berlin 2022

[N]ature isn't classical, dammit, and if you want to make a simulation of nature, you'd better make it quantum mechanical, and by golly it's a wonderful problem, because it doesn't look so easy.

— **Richard Feynman**

Abstract

Large-scale quantum networks in which quantum information is transferred between flying and stationary qubits play a central role in quantum information processing and communication. A promising platform for their implementation is waveguide quantum electrodynamics (WQED). In such setups, non-negligible delay times offer the possibility to control the system dynamics. From a theorist's point of view, however, they present a difficulty since they require a description beyond the Markov approximation. In this thesis, we explore characteristic features of WQED systems with feedback focussing on the generation of entanglement in different realms.

The first part of the thesis is concerned with multiphoton pulses in WQED systems with feedback, the inclusion of which is essential to account for the transmission of quantum information. For the simulation of the dynamics, we employ two different methods complementing each other. The first is based on the matrix product state (MPS) framework and allows for the inclusion of multiple photons due to the efficient handling of the entanglement in the system. In the fundamental setup of a two-level emitter coupled to a semi-infinite waveguide, a bound state exists in the continuum of propagating modes. Our simulations show that in the highly non-Markovian regime of long delay times, the excitation of the bound state by multiphoton pulses via stimulated emission can be significantly more efficient than its excitation via the spontaneous decay of an initially excited emitter. The second method is a Heisenberg-operator approach, where the arising hierarchy of multi-time correlations is unraveled by introducing a Hilbert space unity. The method allows for the straightforward inclusion of arbitrary pulse shapes and makes the microscopic dynamics accessible so that additional dissipation channels can be included. This way, we are able to examine the complex interplay of the pulse shape and the feedback delay time, as well as the influence of a phenomenological pure dephasing rendering the bound state unattainable. Proceeding toward more complex multi-emitter networks, we study the entanglement of two macroscopically separated emitters coupled to an infinite waveguide with MPS. Investigating different excitation schemes, we find that, by addressing the bound state in the system, it is possible to generate stable and controllable long-range entanglement.

The second part of the thesis deals with photon pairs entangled in different degrees of freedom and possibilities to control their entanglement. The energy-time entanglement of a pair of photons emitted from a ladder-type three-level system can be detected in a Franson-type interferometer via an interference in the second-order coherence function. The visibility of this interference depends crucially on the decay rates of the emitter. Simulating the time evolution within the MPS framework, we show that the implementation of an additional feedback channel allows controlling the decay process. As a consequence, the visibility can be increased for a wide range of parameters. Furthermore, the polarization entanglement of a pair of photons emitted from a biexciton cascade in a semiconductor quantum dot exhibiting an excitonic spin precession is investigated. We model the precession as a coherent process and, after the verification of the model using experimental data, find that it affects the entanglement in the same way as a finite fine-structure splitting. Thus, the precession is detrimental in a time-integrated measurement setup, while, for a time-resolved measurement, a high degree of entanglement is attainable nevertheless.

Kurzfassung

Quantennetzwerke, in denen Quanteninformation zwischen fliegenden und stationären Qubits übertragen wird, spielen eine zentrale Rolle in der Quanteninformationsverarbeitung sowie der Quantenkommunikation. Für ihre Realisierung stellt die Wellenleiter-Quantenelektrodynamik (WQED) eine vielversprechende Plattform dar. Im Falle nicht vernachlässigbarer Laufzeiten bietet die kohärente zeitverzögerte Feedbackkontrolle die Möglichkeit, die Systemdynamik zu steuern. Allerdings führen die Verzögerungszeiten zu einer Komplikation der theoretischen Beschreibung, da sie die Markov-Näherung invalidieren. In dieser Arbeit werden charakteristische Eigenschaften von WQED-Systemen mit Feedback untersucht, wobei der Fokus auf der Erzeugung von Verschränkung liegt.

Im ersten Teil der Arbeit werden Multiphotonenpulse in WQED-Systemen mit Feedback untersucht, die es ermöglichen, die Übertragung von Quanteninformation selbstkonsistent zu beschreiben. Für die Simulation der Dynamik werden zwei verschiedene Methoden verwendet und ein Zwei-Niveau-System vor einem Spiegel betrachtet, für das ein gebundener Zustand im Kontinuum der propagierenden Moden existiert. Die erste Methode basiert auf der Zeitevolution mit Matrix-Produkt-Zuständen (MPS). Durch den effizienten Umgang mit der Verschränkung im System ermöglicht sie es, eine Vielzahl von Photonen zu betrachten. Die MPS-Simulationen zeigen, dass die Anregung des gebundenen Zustandes mittels stimulierter Emission durch Multiphotonenpulse im Bereich langer Laufzeiten wesentlich effizienter sein kann als seine Anregung über den spontanen Zerfall eines initial angeregten Emitters. Bei der zweiten Methode handelt es sich um einen Heisenberg-Operator-Ansatz, wobei die auftretende Hierarchie von Mehr-Zeiten-Korrelationen durch die Einführung eines Einselements aufgelöst wird. Sie ermöglicht die direkte Simulation beliebiger Pulsformen und macht die mikroskopische Dynamik zugänglich, sodass zusätzliche Dissipationskanäle einbezogen werden können. Somit kann das komplexe Zusammenspiel von Pulsform und Feedback-Verzögerungszeit sowie der Einfluss einer phänomenologischen reinen Dephasierung, welche den gebundenen Zustand unzugänglich macht, untersucht werden. Auf dem Weg hin zu komplexen Multi-Emitter-Netzwerken werden zudem zwei Emitter, die an einen Wellenleiter koppeln, betrachtet. Dabei zeigt die Simulation verschiedener Anregungsszenarien mittels MPS, dass es möglich ist, verbunden mit der Anregung des gebundenen Zustandes im System eine stabile Verschränkung zwischen den Emittern zu erzeugen.

Der zweite Teil der Arbeit befasst sich mit Möglichkeiten, die Verschränkung von Photonenpaaren in verschiedenen Freiheitsgraden zu kontrollieren. Die Energie-Zeit-Verschränkung eines Photonenpaares ist über die Zwei-Photonen-Interferenz in einem Franson-Interferometer detektierbar. Die Simulation des Systems mittels MPS offenbart, dass der Emissionsprozess durch einen zusätzlichen Feedbackkanal beeinflusst und so die Visibilität der Interferenz erhöht werden kann. Darüber hinaus wird die Polarisationsverschränkung eines Photonenpaares untersucht, das von einer Biexziton-Kaskade in einem Halbleiterquantenpunkt emittiert wird, der eine exzitonische Spinpräzession aufweist. Die Modellierung dieser Spinpräzession als kohärenter Prozess führt zu einer guten Übereinstimmung mit experimentellen Daten. Innerhalb dieses Modells wird die Verschränkung auf die gleiche Weise beeinflusst wie durch eine Feinstrukturaufspaltung, die bei einem zeitintegrierten Messaufbau problematisch ist, während bei einer zeitaufgelösten Messung trotzdem ein hoher Grad an Polarisationsverschränkung erreicht werden kann.

Publications

- **K. Barkemeyer**, A. Knorr, and A. Carmele, "Heisenberg treatment of multiphoton pulses in non-Markovian waveguide-QED", arXiv:2111.02816 (2021).

- **K. Barkemeyer**, M. Hohn, S. Reitzenstein, and A. Carmele, "Boosting energy-time entanglement using coherent time-delayed feedback", Phys. Rev. A **103**, 062423 (2021).

- **K. Barkemeyer**, A. Knorr, and A. Carmele, "Strongly correlated system-reservoir dynamics with quantized pulses: Controlling the atom-photon bound state ", Phys. Rev. A **103**, 033704 (2021).

- S. Bounouar, G. Rein, **K. Barkemeyer**, J. Schleibner, P. Schnauber, M. Gschrey, J.-H. Schulze, A. Strittmatter, S. Rodt, A. Knorr, A. Carmele, and S. Reitzenstein, "Entanglement robustness to excitonic spin precession in a quantum dot", Phys. Rev. B **102**, 045304 (2020).

- **K. Barkemeyer**, R. Finsterhölzl, A. Knorr, and A. Carmele, "Revisiting Quantum Feedback Control: Disentangling the Feedback-induced Phase from the Corresponding Amplitude", Adv. Quantum Technol. **3**, 1900078 (2020).

Contents

List of abbreviations

3LS	three-level system
CHSH	Clauser, Horne, Shimony, and Holt
CQED	cavity quantum electrodynamics
EPR	Einstein, Podolsky, and Rosen
LHVT	local hidden-variable theory
LOCC	local operations and classical communication
MPO	matrix product operator
MPS	matrix product state
OC	orthogonality center
PPT	positive partial transpose
SVD	singular value decomposition
TLS	two-level system
WQED	waveguide quantum electrodynamics

1 Introduction

1.1 Motivation

The exploitation of characteristic quantum mechanical features for information processing has led to a technological paradigm shift. With the current advances in quantum technology, the solution of problems that are hard to solve classically comes within reach. Among them are the factorization of large numbers [1] and the search in unsorted databases [2] with potential applications for the realization as well as the breaking of cryptography protocols [3, 4]. The simulation of quantum systems [5] and the realization of a quantum internet [6, 7] are further auspicious fields of application. The smallest unit of quantum information, the qubit, a quantum mechanical two-level system (TLS), is based on fundamentally different principles than the classical bit. While the classical bit yields a deterministic measurement outcome, for the qubit, measurement outcomes are probabilistic. This is the case because the qubit can be in a superposition state, which gives rise to interference effects and inherent parallelism. At the heart of many quantum technological applications lies, furthermore, the concept of entanglement, which describes nonlocal correlations that are unattainable classically. Already in 1935, Schrödinger acknowledged entanglement as "*the* characteristic trait of quantum mechanics, the one that enforces its entire departure from classical lines of thought" [8]. Since then, entanglement has undergone an impressive development from a theoretical concept [9–11] to an essential resource in quantum information processing [12–19].

For the implementation of quantum information processing applications, waveguide quantum electrodynamics (WQED) provides a promising platform [20–22]. In WQED, the light field is confined to a one-dimensional geometry, which allows for strong interactions between quantum emitters and photonic waveguide modes, while, in free space, the leakage to external modes typically dominates. A strong light-matter interaction, however, is a prerequisite for the observability of quantum optical phenomena. As a consequence, WQED setups are natural building blocks for quantum networks [6, 23] and suitable candidates for the realization of single-photon transistors [24, 25]. For their theoretical description, it is convenient to treat WQED systems within the framework of open quantum systems, where a distinction is made between the system of interest and its environment so that different approximation methods can be applied to the individual components [26]. This approach enables a numerical treatment despite the exponential growth of the corresponding Hilbert space with the number of elements in the system. In this way, it allows accounting for decoherence and dissipation. To handle open quantum systems, commonly, master equations are employed, of which the best-known form is the Lindblad master equation [27, 28]. It relies on the Markov approximation, which assumes a unidirectional flow of information from the system of interest into the environment and, thereby, neglects any retardation effects. However, recent technological developments allow for the preparation, the manip-

ulation, and the measurement of quantum systems on ever shorter time scales. Therefore, the time-scale separation implied by the Markov approximation becomes questionable and non-Markovian methods that go beyond this assumption gain in importance [29, 30].

The ability to control quantum systems is an essential prerequisite for the realization of quantum information processing protocols. One way to achieve this is by means of feedback, which has been applied to both classical [31–33] and quantum systems [34–38]. In the quantum regime, feedback control can be either measurement-based or coherent depending on how information is extracted. In measurement-based feedback control schemes, quantum coherence gets lost due to the involved measurement process [39–41]. Coherent feedback control, in contrast, uses another quantum system or the system to be controlled itself as the control unit and preserves coherence by construction [42]. Consequently, the latter approach is eligible for the control of inherently quantum mechanical properties such as entanglement [43–46]. In addition to that, time-delayed feedback has been proposed as a way of creating entangled photonic cluster states enabling universal photonic quantum computation [47]. If feedback delay times are non-negligible, the Markov approximation is inapplicable so that non-Markovian methods have to be employed. In contrast to the non-Markovianity imposed by structured reservoirs [48–51], the time delays cannot be treated appropriately using perturbative methods. Among the possible approaches for the simulation of the time-delayed feedback are cascaded quantum systems [52], the evaluation of the quantum stochastic Schrödinger equation within the matrix product state (MPS) framework [53], and quantum trajectory simulations [54, 55].

In this thesis, we theoretically study WQED systems with time-delayed feedback concentrating, in particular, on the generation of entanglement in different realms. First, we look at WQED setups with feedback, where strongly entangled emitter-reservoir states emerge due to the non-Markovianity of the dynamics. Incorporating quantum pulses in the model allows for the self-consistent description of the transmission of quantum information. Furthermore, interesting phenomena, such as the population of a bound state in the continuum via multiphoton scattering and the emergence of stable long-range entanglement between the emitters, can be investigated. For the numerical simulation, we employ different methods. On the one hand, we calculate the time evolution of the system state using MPS. On the other hand, we propose an alternative approach based on the calculation of the dynamics within a Heisenberg representation. Here, the focus of the investigation determines which method is preferable. Moreover, we study photon pairs entangled in different degrees of freedom and explore possibilities to control the degree of their entanglement. Applying coherent time-delayed feedback to a two-photon source allows manipulating the emission process. Therefore, this method is, in principle, suitable for controlling the energy-time entanglement of the photons, which is detectable using the Franson interferometer. Furthermore, we consider the polarization entanglement of a pair of photons emitted from a biexciton cascade in a semiconductor quantum dot. In this context, we focus on the effect of an excitonic spin precession as well as the impact of the detector resolution on the entanglement of the photons and compare the calculations with experimental data.

1.2 Structure of the thesis

The thesis consists of three main parts. In part I, we introduce the basic concepts underlying the work presented in this thesis. In Chap. 2, a summary of the quantum mechanical framework is given to establish common ground and clarify the notation. Thereby, we focus on the different pictures of quantum mechanics, the concept of the density matrix, and the quantization of the light field. An introduction with respect to the field of WQED is given in Chap. 3, where we discuss experimental platforms as well as their theoretical description. In this context, we formalize the light-matter interaction and touch upon the theory of open quantum systems. The theoretical background of entanglement is presented in Chap. 4. First, we outline the concept of entanglement and, subsequently, consider different possibilities to characterize and quantify it.

Part II of the thesis is concerned with the study of WQED systems with feedback inducing entanglement in the emitter-reservoir state. In Chap. 5, a two-level emitter with self-feedback is studied, where multiphoton pulses can lead to population trapping due to the excitation of a bound state in the continuum. We start the chapter with an introduction of the MPS formalism and the corresponding time evolution method. Since we are interested in the role of multiphoton pulses, we discuss how it is possible to model them in the MPS framework. Subsequently, we examine the resulting feedback dynamics focussing, in particular, on the dependence of the bound-state excitation probability on the number of photons in the pulse. An alternative approach for the study of WQED systems with feedback using Heisenberg equations is proposed in Chap. 6. After introducing and benchmarking the method for the TLS with self-feedback, we use it to consider arbitrary pulse shapes so that the impact of the pulse shape on the excitation efficiency of the atom-photon bound state can be examined. Furthermore, it allows including additional dissipation channels such as the phenomenological pure dephasing we include for demonstration purposes. To proceed toward more complex multi-emitter networks, in Chap. 7, we study the onset of collective effects for two macroscopically separated two-level emitters. Simulating the dynamics in this WQED setup using MPS, we explore the potential of different excitation schemes for the generation of stable long-range entanglement between the emitters.

The subject of part III of the thesis is the control of photon entanglement in different degrees of freedom. The energy-time entanglement of a pair of photons can be detected using the Franson interferometer, which we study in Chap. 8. First, we consider the conventional Franson interferometer without feedback, where the visibility of the two-photon interference depends on the decay rates of the three-level emitter we assume as the two-photon source. The subsequent addition of coherent time-delayed feedback opens up the possibility to control the emission dynamics and has the potential to enhance the energy-time entanglement of the photons. In Chap. 9, we concentrate on the polarization entanglement of a pair of photons emitted from a biexciton cascade, for which an excitonic spin precession can be detected. We model the system treating the spin precession as a coherent process, where the comparison of the results with experimental data allows verifying the model. After that, we use the model to estimate the degree of entanglement for arbitrary precession strengths and temporal resolution of the corresponding detector.

Finally, in Chap. 10, the thesis concludes with a summary of the results and an outlook on possible future research directions.

Part I

Theoretical background

2 Quantum mechanical framework

The success story of quantum mechanics has been closely intertwined with the study of the interaction of light and matter from its very beginning. In the early 20th century, Planck was able to explain the spectrum of the black-body radiation by quantizing the energy in discrete packages via the introduction of the quantum of action [56]. Subsequently, Einstein succeeded in describing the photoelectric effect by postulating that the electromagnetic field itself consists of individual light quanta, which later led to the concept of the photon [57]. It was, however, not until Dirac formally combined the wave-like and the particle-like properties of light that it became possible to treat light and matter on an equal footing via the association of each mode of the light field with a quantized harmonic oscillator [58]. This treatment reveals properties that cannot be found when assuming a classical light field. In particular, the discovery of vacuum fluctuations has had far-reaching consequences.

While the quantum theory was spectacularly successful in explaining experimental observations from a mathematical point of view, it also raised fundamental questions about our understanding of the world. In classical mechanics, a system follows, at least in principle, a deterministic evolution. Everything we can say about a quantum mechanical system, in contrast, according to the Copenhagen interpretation, is of probabilistic nature. The disparity between the predictions of quantum mechanics and the intuitively valid assumptions of locality and reality becomes most apparent in the discussion of the Einstein-Podolsky-Rosen paradox and the concept of entanglement, see Chap. 4.

This chapter aims to review some quantum mechanical basics. This allows clarifying the notation and lays the foundation for the subsequent work. Since the methods we employ in this thesis are based on different pictures, the possible pictures of quantum mechanics and their connections are discussed in Sec. 2.1. Furthermore, in Sec. 2.2, we introduce the density matrix, which is an important concept in the context of open quantum systems and allows for the description of the state of a system the preparation of which is not fully known. Finally, we outline the quantization of the electromagnetic field in Sec. 2.3 as a preparation for the fully quantized description of the interaction of light and matter as covered in Chap. 3.

2.1 Quantum mechanics in different pictures

Quantum mechanics provides a mathematical framework for the modeling of physical systems. At its heart lies the description of the state of a system as a unit vector $|\psi\rangle$, $\langle\psi|\psi\rangle = 1$, in an associated Hilbert space $\mathcal{H}$. Classically, an individual system has a defined state and follows a deterministic time evolution. Quantum mechanics, in contrast, allows for the description of a system in a linear combination of the basis states $\{|\psi_i\rangle\}$,

that is, in a superposition state

$$|\psi\rangle = \sum_i c_i \, |\psi_i\rangle \, . \tag{2.1}$$

Here, the coefficients c_i can be interpreted as the probability amplitudes that give the probabilities $|c_i|^2$ to find the system in the state $|\psi_i\rangle$ when measuring in the respective basis. For a physical system composed of multiple subsystems, the associated state space is the tensor product of the subspaces, $\mathcal{H} = \mathcal{H}^1 \otimes \mathcal{H}^2 \otimes \cdots \otimes \mathcal{H}^n$. If the subsystem i is prepared in the state $|\psi_i\rangle \in \mathcal{H}^i$, the state of the composite system is given as $|\psi\rangle = |\psi_1\rangle \otimes |\psi_2\rangle \otimes \cdots \otimes |\psi_n\rangle$. For notational simplicity, however, we often refrain from explicitly expressing the state as a tensor product.

Measurements allow extracting information about a system. They correspond to the evaluation of an observable represented by a Hermitian operator $\hat{O}$ with a spectral decomposition

$$\hat{O} = \sum_i O_i \, |\phi_i\rangle \, \langle\phi_i| \, . \tag{2.2}$$

The eigenvalues O_i are the possible outcomes of the measurement, occurring with probabilities $p_i = |\langle\phi_i|\psi\rangle|^2$. When an experimentalist performs a measurement, the state of the system is projected onto the eigenvector $|\phi_i\rangle$ associated with the measured value O_i. This is often referred to as the "collapse of the wavefunction". Thus, only at the moment of the measurement, the system is forced to assume a definite state. Therefore, in quantum mechanics, the measurement process itself is of central importance. In general, we cannot predict the outcome of an individual measurement. It is, however, possible to calculate expectation values. For a system in the state $|\psi\rangle$, the expectation value of the operator $\hat{O}$ is given as

$$\langle\hat{O}\rangle = \langle\psi| \, \hat{O} \, |\psi\rangle \, . \tag{2.3}$$

Since measurements influence the state of the system, the order in which multiple measurements are performed is decisive. This is reflected in the fact that two operators $\hat{O}_1$ and $\hat{O}_2$ do not necessarily commute but satisfy the commutation relation

$$\left[\hat{O}_1, \hat{O}_2\right] = \hat{O}_1\hat{O}_2 - \hat{O}_2\hat{O}_1. \tag{2.4}$$

To model an experiment theoretically, we need to know how the system evolves with time. The time evolution of a closed quantum system is reversible and can, therefore, be described as a unitary transformation. For a system the total energy of which is represented by the Hamiltonian H, the state $|\psi\rangle$ obeys

$$|\psi\,(t)\rangle = U\,(t, t_0)\,|\psi\,(t_0)\rangle\,, \quad U\,(t, t_0) = \mathcal{T}\exp\left[-\frac{i}{\hbar}\int_{t_0}^{t} dt'\,H(t')\right], \tag{2.5}$$

where $U\,(t, t_0)$ is the time evolution operator from time t_0 to time t. The explicit form of the time evolution operator arises from the integration of the Schrödinger equation

$$\frac{\mathrm{d}}{\mathrm{d}t}\,|\psi(t)\rangle = -\frac{i}{\hbar}H\,|\psi(t)\rangle\,. \tag{2.6}$$

In general, for the time evolution operator $U(t, t_0)$, Eq. (2.5), the time ordering operator $\mathcal{T}$ has to be accounted for since the Hamiltonian of the system does not necessarily commute with itself at different times.

When calculating the time evolution via the Schrödinger equation, the state of the system is assumed to change with time while the operators are constant. This is referred to as the Schrödinger picture of quantum mechanics. While this approach is common, other pictures of quantum mechanics are possible. Within the Heisenberg picture, the state of the system is assumed to be time-independent, whereas the operators evolve in time according to the Heisenberg equation of motion

$$\frac{\mathrm{d}}{\mathrm{d}t}\hat{O}_{\mathrm{HB}}(t) = \frac{i}{\hbar}\left[H, \hat{O}_{\mathrm{HB}}(t)\right] + \left(\frac{\partial}{\partial t}\hat{O}_{\mathrm{S}}\right)_{\mathrm{HB}}. \tag{2.7}$$

The last term on the right-hand side of Eq. (2.7) is usually omitted, which is justified if there is no explicit time dependence of the operator $\hat{O}_{\mathrm{S}}$, which could arise, for example, from a time-dependent external field. The transformation between the Schrödinger (S) and the Heisenberg picture (HB) is possible via the time evolution operator U, as introduced in Eq. (2.5), according to

$$|\psi(t)\rangle_{\mathrm{S}} = U\left(t, t_0\right)|\psi\rangle_{\mathrm{HB}}\,, \quad U^{\dagger}\left(t, t_0\right)\hat{O}_{\mathrm{S}}\, U\left(t, t_0\right) = \hat{O}_{\mathrm{HB}}(t). \tag{2.8}$$

This implies that the formulations coincide at the starting time of the dynamics, $t = t_0$.

Another picture of quantum mechanics is the interaction picture, where both the states and the operators carry part of the time dependence. This picture is particularly useful for the separation of the free evolution of a system from its evolution due to interactions, that is, if the Hamiltonian can be written as

$$H = H_0 + H_1, \tag{2.9}$$

where H_0 describes the free evolution while H_1 refers to an interaction. We can choose the interaction picture, for example, in such a way that states and operators evolve according to

$$\frac{\mathrm{d}}{\mathrm{d}t}|\psi(t)\rangle_{\mathrm{I}} = -\frac{i}{\hbar}H_{\mathrm{I}}(t)\,|\psi(t)\rangle_{\mathrm{I}}\,, \quad \frac{\mathrm{d}}{\mathrm{d}t}\hat{O}_{\mathrm{I}}(t) = \frac{i}{\hbar}\left[H_0, \hat{O}_{\mathrm{I}}(t)\right] + \left(\frac{\partial}{\partial t}\hat{O}_{\mathrm{S}}\right)_{\mathrm{I}}, \tag{2.10}$$

respectively, where, under the assumption of a time-independent H_0,

$$H_{\mathrm{I}}(t) = U_{\mathrm{I}}^{\dagger}(t, t_0)H_1U_{\mathrm{I}}(t, t_0), \quad U_{\mathrm{I}}(t, t_0) = \exp\left[-\frac{i}{\hbar}H_0(t - t_0)\right]. \tag{2.11}$$

The transformation between the Schrödinger (S) and the interaction picture (I) is possible via

$$|\psi(t)\rangle_{\mathrm{I}} = U_{\mathrm{I}}^{\dagger}(t, t_0)\,|\psi(t)\rangle_{\mathrm{S}} = U_{\mathrm{I}}^{\dagger}(t, t_0)U\left(t, t_0\right)|\psi\left(t_0\right)\rangle_{\mathrm{S}}\,, \; \hat{O}_{\mathrm{I}}(t) = U_{\mathrm{I}}^{\dagger}(t, t_0)\hat{O}_{\mathrm{S}}U_{\mathrm{I}}(t, t_0). \tag{2.12}$$

The experimentally accessible and, thus, physically relevant quantities such as eigenvalues and expectation values are independent of the specific picture, and it depends on the problem at hand which picture is most convenient.

2.2 Density matrix

So far we assumed our system to be in a pure state $|\psi\rangle$ represented by a specific vector in the associated Hilbert space. However, there are many scenarios in which we do not fully

know the preparation of the system. One reason for this is that a realistic physical system can never be fully isolated but always interacts with its environment to some extent. Under these circumstances, often the best we have is a statistical ensemble of states the system might be prepared in. A generalization of pure to such mixed states is possible by means of the density matrix ρ,

$$\rho = \sum_m p_m \left|\psi_m\right\rangle \left\langle\psi_m\right| , \tag{2.13}$$

where p_m denotes the probability that the system is prepared in the state $|\psi_m\rangle$. The time evolution of the density matrix can be determined by extending the Schrödinger equation to the case of mixed states, where we obtain the Von-Neumann equation

$$\frac{\mathrm{d}}{\mathrm{d}t}\rho = -\frac{i}{\hbar}\left[H, \rho\right] . \tag{2.14}$$

The calculation of expectation values can be generalized to the notion of mixed states via the trace,

$$\langle \hat{O} \rangle = \mathrm{tr}\left(\rho \hat{O}\right) . \tag{2.15}$$

If we consider a mixed state of a composite system, $\rho_{\mathrm{AB}} \in \mathcal{H}_{\mathrm{A}} \otimes \mathcal{H}_{\mathrm{B}}$, but we are only interested in the state of subsystem A, we can calculate the reduced density matrix by taking the partial trace with respect to subsystem B with basis states $\{|\psi_{\mathrm{B},i}\rangle\}$,

$$\rho_{\mathrm{A}} = \mathrm{tr}_{\mathrm{B}}\left(\rho_{\mathrm{AB}}\right) = \sum_i \left\langle\psi_{\mathrm{B},i}\right| \rho_{\mathrm{AB}} \left|\psi_{\mathrm{B},i}\right\rangle \in \mathcal{H}_{\mathrm{A}}. \tag{2.16}$$

The expectation value of an operator $\hat{O}_{\mathrm{A}}$ acting only on $\mathcal{H}_{\mathrm{A}}$, so that in the composite system it can be expressed as $\hat{O}_{\mathrm{A}} \otimes \mathbb{1}_{\mathrm{B}}$, where $\mathbb{1}_{\mathrm{B}}$ denotes the identity in the Hilbert space $\mathcal{H}_{\mathrm{B}}$, can be calculated with this reduced density matrix according to

$$\langle \hat{O}_{\mathrm{A}} \rangle = \mathrm{tr}_{\mathrm{A}}\left(\rho_{\mathrm{A}} \hat{O}_{\mathrm{A}}\right) . \tag{2.17}$$

It is important to note that the pure coherent superposition state introduced in Eq. (2.1) can give rise to interference of the probability amplitudes. The density matrix in Eq. (2.13), in contrast, describes an incoherent statistical mixture of the states $\{|\psi_m\rangle\}$ and, thus, does not lead to interference between these states. The density matrix is particularly useful for the treatment of open quantum systems as discussed in Chap. 3. Furthermore, mixed states play an important role in the context of entanglement, see Chap. 4.

2.3 Quantized light field

The fully quantized interaction of light and matter is a central topic of this thesis. Due to its importance for this work, here, we outline the approach for the quantization of the free electromagnetic field where we identify the field with a set of quantized harmonic oscillators. More details on the derivation can be found, for example, in Refs. [59, 60].

The starting point for the quantization of the electromagnetic field in vacuum is the Lagrangian density

$$\mathcal{L} = \frac{\epsilon_0}{2}\mathbf{E}^2 - \frac{1}{2\mu_0}\mathbf{B}^2, \tag{2.18}$$

with the electric field $\mathbf{E}$ and the magnetic field $\mathbf{B}$ as well as the permittivity ϵ_0 and the permeability μ_0 of free space, $\epsilon_0\mu_0 = c^{-2}$, where c is the speed of light in vacuum. The Lagrangian density $\mathcal{L}$ postulated in Eq. (2.18) is justified since, when evaluating Lagrange's equations, Maxwell's equations can be recovered, which read

$$\nabla \cdot \mathbf{E} = 0, \quad \nabla \times \mathbf{E} = -\frac{\partial \mathbf{B}}{\partial t}, \quad \nabla \cdot \mathbf{B} = 0, \quad \nabla \times \mathbf{B} = \frac{1}{c^2}\frac{\partial \mathbf{E}}{\partial t}. \tag{2.19}$$

The electric and the magnetic field can be calculated from the vector potential $\mathbf{A}$ in the Coulomb gauge, where $\nabla \cdot \mathbf{A} = 0$, according to

$$\mathbf{E} = -\frac{\partial}{\partial t}\mathbf{A}, \quad \mathbf{B} = \nabla \times \mathbf{A}. \tag{2.20}$$

The state of the electromagnetic field is, thus, determined by the components of the vector potential, A_i, $i \in \{\mathrm{x}, \mathrm{y}, \mathrm{z}\}$, with the associated conjugate momenta

$$\Pi_i = \frac{\partial \mathcal{L}}{\partial \dot{A}_i} = -\epsilon_0 E_i. \tag{2.21}$$

Performing the Legendre transformation of the Lagrangian density to switch from the representation in terms of the coordinates A_i and the velocities $\dot{A}_i$ to one in terms of the coordinates A_i and the conjugate momenta Π_i according to

$$\mathcal{H} = \sum_i \Pi_i \dot{A}_i - \mathcal{L}, \tag{2.22}$$

we obtain the Hamiltonian of the electromagnetic field

$$H = \int d^3r\, \mathcal{H} = \int d^3r \left[\frac{\epsilon_0}{2}\mathbf{E}^2 + \frac{1}{2\mu_0}\mathbf{B}^2\right]. \tag{2.23}$$

From Maxwell's equations, Eq. (2.19), for the vector potential in Coulomb gauge, the wave equation

$$\Box \mathbf{A} = 0 \tag{2.24}$$

can be derived. Therefore, it is reasonable to expand the vector potential in terms of the plane wave mode functions $\mathbf{u}_{(\lambda,\mathbf{k})}(\mathbf{r})$, which, under the assumption of a field restricted to a cubic volume in space, a cavity of volume $V = L^3$, take the form

$$\mathbf{u}_{(\lambda,\mathbf{k})}(\mathbf{r}) = \frac{1}{\sqrt{V}}\hat{\mathbf{e}}^{(\lambda)} e^{i\mathbf{k}\cdot\mathbf{r}}. \tag{2.25}$$

Here, $\hat{\mathbf{e}}^{(\lambda)}$ is the unit polarization vector, $\lambda \in \{1, 2\}$, and $\mathbf{k}$ the wave vector, the components of which, for periodic boundary conditions, take on the values

$$k_x = \frac{2\pi n_x}{L}, \quad k_y = \frac{2\pi n_y}{L}, \quad k_z = \frac{2\pi n_z}{L}, \quad n_x, n_y, n_z \in \mathbb{Z}. \tag{2.26}$$

In the following, for the sake of readability, we combine the polarization λ as well as the wave vector $\mathbf{k}$ into a multi-index k, $(\lambda, \mathbf{k}) \to k$. Since the mode functions are required to satisfy the transversality condition, $\nabla \cdot \mathbf{u}_k(\mathbf{r}) = 0$, the polarization vector $\hat{\mathbf{e}}^{(\lambda)}$ and the wave vector $\mathbf{k}$ have to be perpendicular [61]. Note that the case where one of the components of the wave vector $\mathbf{k}$ vanishes represents a special case for which there is only a single polarization direction [62].

The vector potential can now be expressed as

$$\mathbf{A}(\mathbf{r},t) = \sum_k \left[c_k \mathbf{u}_k(\mathbf{r}) e^{-i\omega_k t} + c_k^* \mathbf{u}_k^*(\mathbf{r}) e^{i\omega_k t}\right] \tag{2.27}$$

with $\omega_k = c\,|\mathbf{k}|$, where the complex conjugate contribution in the expansion ensures that $\mathbf{A}$ is real. Introducing the dimensionless amplitudes $a_k^{(*)}$ to normalize the coefficients $c_k^{(*)}$, we rewrite the vector potential as

$$\mathbf{A}(\mathbf{r},t) = \sum_k \left(\frac{\hbar}{2\omega_k \epsilon_0}\right)^{1/2} \left[a_k \mathbf{u}_k(\mathbf{r}) e^{-i\omega_k t} + a_k^* \mathbf{u}_k^*(\mathbf{r}) e^{i\omega_k t}\right]. \tag{2.28}$$

Plugging in the plane wave mode functions from Eq. (2.25), for the electric field, accordingly, the expression

$$\mathbf{E}(\mathbf{r},t) = i \sum_k \left(\frac{\hbar\omega_k}{2\epsilon_0 V}\right)^{1/2} \hat{\mathbf{e}}^{(\lambda)} \left[a_k e^{-i\omega_k t + i\mathbf{k}\cdot\mathbf{r}} - a_k^* e^{i\omega_k t - i\mathbf{k}\cdot\mathbf{r}}\right] \tag{2.29}$$

can be found as well as a corresponding expression for the magnetic field $\mathbf{B}$. To now describe the field in terms of the second quantization, the complex amplitudes $a_k^{(*)}$ are replaced by operators $r_k^{(\dagger)}$ satisfying the bosonic commutation relations

$$\left[r_k, r_{k'}^\dagger\right] = \delta_{kk'}, \quad [r_k, r_{k'}] = \left[r_k^\dagger, r_{k'}^\dagger\right] = 0. \tag{2.30}$$

These operators describe the annihilation (creation) of a photon in the associated mode k and, this way, allow modeling the electromagnetic field as a collection of quantized harmonic oscillators according to

$$\mathbf{E}(\mathbf{r},t) = i \sum_k \left(\frac{\hbar\omega_k}{2\epsilon_0 V}\right)^{1/2} \hat{\mathbf{e}}^{(\lambda)} \left[r_k e^{-i\omega_k t + i\mathbf{k}\cdot\mathbf{r}} - r_k^\dagger e^{i\omega_k t - i\mathbf{k}\cdot\mathbf{r}}\right]. \tag{2.31}$$

To obtain the second quantized Hamiltonian of the free electromagnetic field, we plug the quantized electric field and the corresponding expression for $\mathbf{B}$ into the classical Hamiltonian of the electromagnetic field, Eq. (2.23), which yields

$$H = \sum_k \hbar\omega_k \left(r_k^\dagger r_k + \frac{1}{2}\right). \tag{2.32}$$

Here, $r_k^\dagger r_k$ is the occupation number operator of the k-th photon mode, that is, the mode defined by $(\lambda, \mathbf{k})$, with energy $\hbar\omega_k$. The term $\hbar\omega_k/2$ describes the respective vacuum fluctuations, which arise since the operators r_k and $r_k^\dagger$ do not commute, Eq. (2.30). The vacuum fluctuations are, thus, an inherently quantum mechanical phenomenon. The eigenvalue of the occupation number operator $r_k^\dagger r_k$ is the occupation number n_k, $n_k \in \mathbb{N}$, with the corresponding eigenstate $|n_k\rangle$. The states $\{|n_k\rangle\}$ are the Fock states, which form a basis of the Hilbert space. The Fock state describing n_k excitations in the k-th mode can be created from the vacuum state of the k-th mode according to

$$|n_k\rangle = \frac{\left(r_k^\dagger\right)^{n_k}}{\sqrt{n_k!}} |0\rangle. \tag{2.33}$$

3 Waveguide quantum electrodynamics

The study of the quantized interaction of light and matter has resulted in fundamental discoveries such as spontaneous emission [58], the Lamb shift [63], and Dicke superradiance [64]. Furthermore, it enabled a thorough understanding of the laser, which has become an integral part of our everyday life [65]. At the few-photon level, a strong light-matter interaction, that is, an interaction strong in relation to any dissipation and decoherence processes, is essential for the observability of predicted quantum optical effects. In free space, however, the coupling is typically inefficient due to a small atomic dipole moment and a large extension of the unconfined light field. As a consequence, enhancing the light-matter interaction is a central goal, for the achievement of which two main approaches have been developed.

The first approach is an enhancement of the light-matter interaction via the confinement of the light field to a cavity supporting a discrete set of modes [66–69]. Technological advances have enabled the fabrication of small-scale cavities with high quality factors. This opens up the possibility to increase the light-matter interaction significantly by letting the light pass emitters placed inside the cavity multiple times. Already in the weak-coupling regime, where the losses from the system exceed the light-matter coupling strength, the modification of the environment in cavity quantum electrodynamics (CQED) setups can result in effects such as increased or inhibited emission rates as proposed by Purcell [70] and cavity-induced energy shifts following Casimir and Polder [71]. In the strong-coupling regime, the interaction of a two-level emitter with a single cavity mode allows for a description via the Jaynes-Cummings model, which predicts Rabi oscillations due to the oscillatory exchange of energy between the emitter and the cavity mode [72, 73].

While remarkable progress has been made, CQED setups may be difficult to scale up. As an alternative approach, the field of WQED has emerged [21, 74]. In these setups, emitters are coupled to the continuum of propagating modes in a quasi-one-dimensional waveguide. Due to the confinement of the light field, strong light-matter interactions are achievable in a single pass. WQED setups are natural building blocks for quantum networks, in which photons transport quantum information between emitters [6, 20]. Input and output channels, which allow for the preparation and the measurement of the light field, respectively, can be implemented straightforwardly. Furthermore, fundamentally new phenomena such as chiral interactions [75] and the formation of atom-photon bound states, which mediate long-range interactions between emitters, emerge [76].

This chapter serves as an introduction to the field of WQED. We begin with an overview of experimental platforms in Sec. 3.1, discussing quantum emitters in the form of natural and artificial atoms as well as waveguide implementations. Subsequently, in Sec. 3.2, we derive the fully quantized interaction of quantum emitters and the light field, while in Sec. 3.3, the theory of open quantum systems is introduced, which forms the basis for an efficient numerical simulation of the system dynamics.

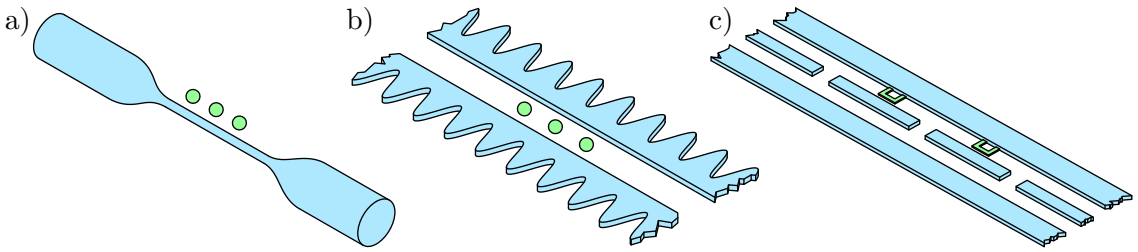

Figure 3.1: Schematic representation of platforms for the experimental realization of WQED. (a) Atoms coupled to an optical nanofiber, based on Ref. [81]. (b) Atoms coupled to an alligator photonic crystal waveguide, based on Ref. [82]. (c) Superconducting circuit, based on Ref. [83].

3.1 Experimental platforms

WQED is concerned with the interaction of quantum emitters with photons propagating in a quasi-one-dimensional waveguide. The emitters can be realized either as natural atoms (such as neutral atoms or ions) or as artificial atoms (such as spins in solids or superconducting circuits). In this section, we review some state-of-the-art platforms for the implementation of WQED. Their suitability for quantum computational tasks can be assessed using DiVincenzo's criteria [77]. A WQED-specific estimate can be obtained by considering the number of atoms that can be coupled to the waveguide, N, as well as the coupling efficiency $\beta = \Gamma_{1D}/\Gamma_{tot}$, that is, the ratio of the radiative decay rate of an individual emitter into the waveguide modes, Γ_{1D}, and its total decay rate, $\Gamma_{tot} = \Gamma_{1D} + \Gamma_{loss}$, where Γ_{loss} describes the decay into external modes [78].

Probably the most obvious realization of a qubit is a natural atom. Out of the typically complex level structure, a single transition in the optical or microwave regime can be isolated to create an effective two-level system. Due to their weak interaction with the environment, the coherence times of natural atoms are long so that the qubit states are protected from the destructive impact of the noisy environment for a long time. A further advantage is that atomic level structures as well as ways to control and measure atomic states have been studied extensively in the past so that a lot of knowledge has been accumulated. Neutral atoms can be cooled down and arranged in optical lattices created by laser beams allowing for their manipulation and measurement [79], whereas ions can be laser-cooled and trapped by electric or magnetic fields [80].

For the realization of a WQED setup, atoms can be trapped close to an optical nanofiber as has been shown with laser-cooled cesium [81, 84] as well as rubidium atoms [85] and is schematically illustrated in Fig. 3.1 a. Optical nanofibers are optical fibers that are tapered to a diameter below the optical wavelength. This results in the possibility of significant evanescent fields on the outside of the fiber surface, which allows for a strong interaction of the waveguide modes with emitters close to the fiber. To arrange the atoms, in practice, two types of lasers are used, a laser red-detuned from resonance to attract the atoms and a blue-detuned laser to keep the atoms away from the surface of the nanofiber [86, 87]. In experiments, optical nanofibers have been coupled to a high number of atoms, $N \sim 1000$. The coupling efficiency, however, is typically low, $\beta \sim 0.01$.

A possibility to increase the coupling efficiency when working with natural atoms is by coupling them to a photonic crystal waveguide. Photonic crystals are nanostructures exhibiting a periodicity in their refractive index, which results in the appearance of a band gap for the propagating photons. In analogy to an electronic band gap, a photonic band gap defines an energy range of inhibited optical modes. To create a low-loss waveguide, a line defect is introduced into the crystal, through which the light propagates. In this structure, the light field is confined by Bragg reflection resulting from the photonic band structure together with total internal reflection. Near the band edge, the strong dispersion in the waveguide results in a reduced group velocity. By aligning the band edge to an atomic transition, thus, an enhanced emission into the waveguide via a slow-light effect is enabled [88, 89]. It has been shown that when coupling trapped cesium atoms to an alligator photonic crystal waveguide, as illustrated in Fig. 3.1 b, a coupling efficiency of $\beta = 0.5$ can be obtained. This comes, however, at the cost of a reduced number of atoms coupling to the waveguide, $N \sim 3$ [82, 90].

While for natural atoms, their efficient trapping is a major challenge, this obstacle is eliminated for artificial atoms realized as solid-state emitters as they are fixed in their host material. This category includes semiconductor quantum dots, which are nanostructures with a diameter of a few nanometers. Their electrons are confined in all three dimensions, which results in a discrete atom-like level structure. A variety of fabrication techniques such as molecular beam epitaxy or lithography allows engineering the energy levels. Furthermore, the incorporation into the solid-state material opens up the possibility to control the quantum dots either electronically or optically. A drawback, however, is the emergence of several decoherence mechanisms. For example, the interaction with the lattice vibrations of the surrounding material results in a reduction of the coherence time in comparison to isolated cold atoms [91, 92]. Since solid-state emitters are directly incorporated into the photonic structure, their coupling efficiency is typically very high: A coupling efficiency of $\beta = 0.99$ has been observed for a quantum dot coupled to a photonic crystal waveguide [93]. In addition to semiconductor quantum dots, another type of artificial atom based on spins in solids is given by point defects such as nitrogen-vacancy color centers in diamond [94].

A different approach to the realization of artificial atoms is superconducting circuits operating in the microwave regime. As with spin-based qubits, their properties such as their energy levels can be tuned, which is an advantage over natural atoms. The key element for the creation of a qubit is the Josephson junction introducing a nonlinear element into the circuit. This way, the energy spectrum is rendered anharmonic, which allows isolating a single transition to create an effective TLS. There are three fundamental types of superconducting qubits, the charge, the flux, and the phase qubit, encoding quantum information in different ways. Controlling and measuring these qubits is possible using currents, voltages, magnetic fields, or microwave photons [95]. A particularly important type of superconducting charge qubit is the so-called transmon qubit. This type of qubit has been used for the famous $N = 53$ qubit chip that Google researchers claimed to have achieved quantum supremacy [96] (or quantum advantage, following the criticism of the original term [97]). For WQED setups with superconducting circuits, the waveguide is typically realized as a microwave transmission line, to which $N \sim 10$ superconducting qubits can be coupled either inductively or capacitively [98]. Such setups, as schematically shown in Fig. 3.1 c, which are closely related to circuit QED, allow for an on-chip integration and can achieve high coupling efficiencies [83, 99, 100]. For example, the coupling efficiency for

a transmon qubit coupled to a transmission line via a capacitor has been shown to exceed $\beta = 0.995$ [101].

3.2 Light-matter interaction

The interaction of light and matter forms the basis of the phenomena considered in this thesis. Here, we derive the Hamiltonian describing the coupling between quantum emitters and the quantized electromagnetic field. There are situations in which a semiclassical treatment of the light-matter interaction is sufficient, where the emitters are treated quantum mechanically while the light field is considered to be a classical system. However, only the fully quantized treatment of the light-matter interaction allows accounting rigorously for effects such as spontaneous emission as well as including quantum pulses. We start with the light-matter interaction in free space, where we make use of the quantized light field derived in Sec. 2.3 and, subsequently, discuss some waveguide-specific properties.

3.2.1 Free space

The total energy of an emitter interacting with the light field can be described by the minimal coupling Hamiltonian in the dipole approximation [102]

$$H = H_\mathrm{A} + H_\mathrm{F} - e\mathbf{r}\cdot\mathbf{E}, \tag{3.1}$$

so that the energy of the composite system is given as the sum of the energies of the individual components plus an interaction contribution. By applying the dipole approximation, we assume that the wavelength of the light is much larger than the extent of the emitter as is typically justified so that the light field can be assumed to be uniform over the entire emitter. The emitter characterized by the energy eigenvalues E_i and the eigenstates $\{|i\rangle\}$ with the corresponding transition operators $\sigma_{ij} = |i\rangle\langle j|$ is described by the Hamiltonian

$$H_\mathrm{A} = \sum_i E_i \sigma_{ii}. \tag{3.2}$$

As derived in Sec. 2.3, the quantization of the free electromagnetic field results in the Hamiltonian of the light field

$$H_\mathrm{F} = \sum_k \hbar\omega_k \left(r_k^\dagger r_k + \frac{1}{2}\right). \tag{3.3}$$

Here, k is the multi-index denoting the polarization λ as well as the components of the wave vector $\mathbf{k}$, $(\lambda, \mathbf{k}) \to k$. In the following, the zero-point energy is omitted. For the quantization of the light-matter interaction, we rewrite

$$e\mathbf{r} = \sum_{i,j} \mu_{ij}\sigma_{ij} \tag{3.4}$$

with the electric-dipole transition matrix element $\mu_{ij} = e\langle i|\,\mathbf{r}\,|j\rangle$. Subsequently, we plug the quantized version of the electric field, Eq. (2.29), evaluated at the position of the

emitter into Eq. (3.1). This finally results in the expression

$$H = \sum_i E_i \sigma_{ii} + \sum_k \hbar\omega_k r_k^\dagger r_k + \sum_{i,j} \sum_k \hbar\sigma_{ij} \left(g_k^{ij} r_k + g_k^{ij*} r_k^\dagger \right) \tag{3.5}$$

with the coupling constant

$$g_k^{ij} = -\frac{i}{\hbar} \sqrt{\frac{\hbar\omega_k}{2\epsilon_0 V}} \mu_{ij} \cdot \hat{e}^{(\lambda)}. \tag{3.6}$$

Let us now consider the special case of a two-level emitter with ground state $|\mathrm{g}\rangle \equiv |0\rangle$, the energy of which we set to zero, $E_\mathrm{g} = 0$, and excited state $|\mathrm{e}\rangle \equiv |1\rangle$ with energy $E_\mathrm{e} = \hbar\omega_0$. In this case, under the assumption of a real coupling constant, $g_k^{\mathrm{ge}} = g_k^{\mathrm{eg}} = g_k$, the Hamiltonian takes the form

$$H = \hbar\omega_0 \sigma_+ \sigma_- + \sum_k \hbar\omega_k r_k^\dagger r_k + \sum_k \hbar g_k \left(\sigma_+ + \sigma_- \right) \left(r_k + r_k^\dagger \right) \tag{3.7}$$

with $\sigma_- \equiv |\mathrm{g}\rangle \langle \mathrm{e}|$, $\sigma_+ \equiv |\mathrm{e}\rangle \langle \mathrm{g}| = \sigma_-^\dagger$. We proceed by transforming the Hamiltonian into the rotating frame defined by its non-interacting part, that is, by performing a transformation into the interaction picture as introduced in Sec. 2.1. To that end, we define the unitary operator

$$U = \exp\left[-\frac{i}{\hbar} H_0 t \right], \quad H_0 = \hbar\omega_0 \sigma_+ \sigma_- + \sum_k \hbar\omega_k r_k^\dagger r_k, \tag{3.8}$$

and calculate the interaction picture Hamiltonian

$$\begin{aligned} H_\mathrm{I} &= U^\dagger \left(H - H_0 \right) U = \\ &\sum_k \hbar g_k \left(\sigma_+ r_k e^{i(\omega_0 - \omega_k)t} + \sigma_+ r_k^\dagger e^{i(\omega_0 + \omega_k)t} + \sigma_- r_k e^{-i(\omega_0 + \omega_k)t} + \sigma_- r_k^\dagger e^{-i(\omega_0 - \omega_k)t} \right). \end{aligned} \tag{3.9}$$

Under the assumption of a light field, the dominant frequency of which is approximately resonant with the transition frequency of the emitter, $\omega_{k_0} \approx \omega_0$, the terms rotating rapidly at frequency $\omega_0 + \omega_k$ can be neglected. They are assumed to average to zero while the terms varying slowly with $\omega_0 - \omega_k$ are kept. This is the rotating wave approximation and translates to discarding the terms in the Hamiltonian that describe energy nonconserving processes. This way, the number of excitations in the system is conserved. The application of the rotating wave approximation is, however, only valid for a coupling that is weak in comparison to the transition frequency of the emitter, $|g_k| \ll \omega_0$. After the back transformation, we arrive at the Hamiltonian

$$H = \hbar\omega_0 \sigma_+ \sigma_- + \sum_k \hbar\omega_k r_k^\dagger r_k + \sum_k \hbar g_k \left(\sigma_+ r_k + \sigma_- r_k^\dagger \right) \tag{3.10}$$

describing the interaction of a two-level emitter with the quantized light field in the dipole and the rotating wave approximation.

3.2.2 Waveguide

Thus far, we considered the electromagnetic field in free space, where the field can propagate in arbitrary directions. In a quasi-one-dimensional waveguide, in contrast, there is a

single direction of propagation. As a consequence, we are dealing with a scalar instead of a three-dimensional wavevector, $\mathbf{k} \to k$. Without loss of generality, we can, for example, assume the light to propagate in the z-direction while being polarized in the x-direction. The quantization of the electromagnetic field in such a structure works analogously to the quantization in free space presented in Sec. 2.3. As we saw in Sec. 3.1, a variety of platforms can be used for the implementation of WQED, and a rigorous treatment of the light-matter interaction is possible using a Green's function approach for the specific geometry and material [103, 104]. For the interaction of a two-level emitter with the electromagnetic field inside a waveguide, in the dipole and the rotating wave approximation, a Hamiltonian of the same form as in Eq. (3.10) can be derived where, for our purposes, it suffices to consider a general coupling strength g_k.

A waveguide that we assume to expand infinitely supports a continuum of modes, where the mode spacing goes to zero, $\Delta k = 2\pi/L \to 0$. Therefore, it is justified to replace the sum over the photon modes in the light-matter interaction Hamiltonian, Eq. (3.10), by an integral, $\sum_k \to \frac{L}{2\pi} \int dk$. Absorbing the prefactors into the operators r_k and $r_k^\dagger$ as well as into the coupling strength g_k, we can express the Hamiltonian as

$$H = \hbar\omega_0 \sigma_+ \sigma_- + \int dk\, \hbar\omega_k r_k^\dagger r_k + \int dk\, \hbar g_k \left(\sigma_+ r_k + \sigma_- r_k^\dagger\right). \tag{3.11}$$

Furthermore, commonly, the Hamiltonian is given in frequency space, where a change of variables under the assumption of a linear dispersion relation $\omega = c\,|k|$, $\int_{-\infty}^{\infty} dk \to \frac{2}{c}\int_0^\infty d\omega$, results in

$$H = \hbar\omega_0 \sigma_+ \sigma_- + \int d\omega\, \hbar\omega r_\omega^\dagger r_\omega + \int d\omega\, \hbar g(\omega) \left(\sigma_+ r_\omega + \sigma_- r_\omega^\dagger\right). \tag{3.12}$$

Here, the bosonic operator $r_\omega^{(\dagger)}$ describes the annihilation (creation) of a photon with frequency ω and the coupling of the emitter to the photon mode with frequency ω is quantified by the coupling strength $g(\omega)$.

3.3 Theory of open quantum systems

A central effort in the experimental realization of quantum technologies such as quantum computers is to isolate the system of interest from its environment so as to reduce the leakage to environmental modes. Such an unwanted interaction with the environment introduces decoherence as well as dissipation. If the loss of coherence is too strong, the genuine quantum effects relying on interference, which are essential for quantum information processing tasks, cannot be exploited anymore. However, a system can never be fully isolated from the environment. Already at the fundamental level, the interaction with the environment is inevitable since any quantum information processing protocol includes a measurement of the system state. To that end, the system has to be brought into contact with a measurement device, which has a generally non-negligible influence on the system. The description of the system dynamics via the unitary time evolution of a pure state, as introduced in Sec. 2.1, is therefore typically insufficient. Yet, including all environmental modes explicitly and treating them on an equal footing with the system modes is, in general, infeasible. The theory of open quantum systems provides a framework to deal with this problem by separating the Hilbert space $\mathcal{H}$ into the Hilbert space of the system of interest, $\mathcal{H}_S$, and the Hilbert space of its environment, $\mathcal{H}_E$, so that $\mathcal{H} = \mathcal{H}_S \otimes \mathcal{H}_E$ [26].

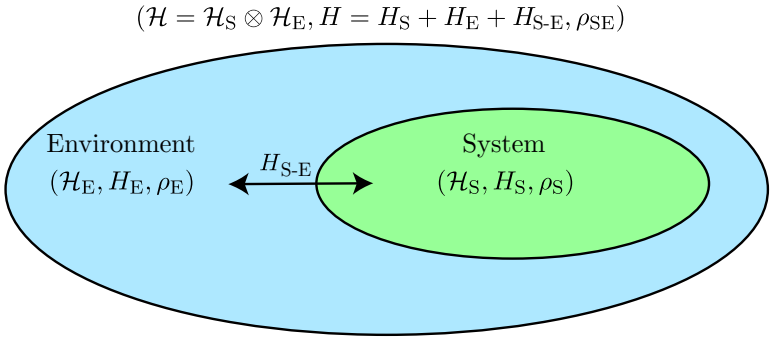

Figure 3.2: Schematic representation of the open quantum systems approach. The total system with the Hilbert space $\mathcal{H}$, the Hamiltonian H, and the state ρ_SE is separated into the system of interest (S) and its environment (E). The system is characterized by the Hilbert space $\mathcal{H}_\mathrm{S}$, the Hamiltonian H_S, and the state ρ_S. The environment is described by the Hilbert space $\mathcal{H}_\mathrm{E}$, the Hamiltonian H_E, and the state ρ_E. The system and the environment interact with each other as included via the interaction Hamiltonian $H_\mathrm{S\text{-}E}$.

This is illustrated in Fig. 3.2. Assuming the total system $S + E$ to be isolated from the larger environment, its total state evolves unitarily in time governed by the Hamiltonian

$$H = H_\mathrm{S} + H_\mathrm{E} + H_\mathrm{S\text{-}E}. \tag{3.13}$$

Here, H_S and H_E are the free Hamiltonians of the system and the environment, respectively, while $H_\mathrm{S\text{-}E}$ describes their interaction. An environment with a continuous mode structure is called a reservoir. If such a reservoir is, furthermore, in a thermal equilibrium, it is referred to as a bath. In analogy to classical thermodynamics, it is often not necessary to completely determine the microscopic behavior of the total system. The open system treament allows applying analytical methods and approximation schemes to the system and the environment separately, thus, making an efficient calculation of the relevant dynamics possible. Commonly, a reduced description in the system space is employed. The reduced system state ρ_S can be obtained from the state of the total system ρ_SE by tracing out the environmental degrees of freedom, as discussed in Sec. 2.2,

$$\rho_\mathrm{S} = \mathrm{tr}_\mathrm{E}\left(\rho_\mathrm{SE}\right). \tag{3.14}$$

The interaction with the environment can impose irreversible dynamics on the reduced system state so that the time evolution of the system state is rendered non-unitary and even an initially pure system state, in general, becomes mixed.

In this thesis, we are mostly concerned with the interaction of few-level emitters with the electromagnetic field in a waveguide. As discussed in Secs. 2.3 and 3.2, the waveguide modes can be identified with harmonic oscillators and form a continuum. The total system, thus, has an infinite number of degrees of freedom making an exact solution generally inaccessible. We can, however, treat the emitters as an open system interacting with a photonic reservoir.

3.3.1 Markov approximation and non-Markovianity

It is the standard approach to describe the dynamics of an open quantum system within the Markov approximation, which assumes a unidirectional flow of information from the system to the environment. This assumption is justified if the correlation functions of the environment decay fast in relation to the processes of interest so that memory effects can be essentially neglected. Using the Markov approximation to derive a master equation for the reduced system state, the well-known Lindblad master equation can be obtained as discussed in more detail in Sec. 3.3.2. However, neglecting the backflow of information from the environment into the system and with it all memory effects is a strong assumption that fails in the presence of strong system-environment couplings, structured reservoirs, or time delays. In this case, non-Markovian approaches that allow for the efficient calculation of the dynamics under the inclusion of memory effects have to be employed.

Throughout this thesis, the notion of non-Markovianity is used in terms of methods that do not rely on the Markov approximation as well as systems the essential features of which cannot be fully captured employing a Markovian approach. Formally, the non-Markovianity of a process can be quantified via different measures, a detailed discussion of which can be found in Refs. [29, 105]. The RHP (Rivas, Huelga, and Plenio) measure quantifies the violation of the divisibility criterion [105, 106], which states that a family of trace-preserving maps $\{\mathcal{E}_{(t_2,t_1)}, t_2 \geq t_1 \geq 0\}$ is divisible and, thus, describes a Markovian evolution, if for all t_2, t_1, $\mathcal{E}_{(t_2,t_1)}$ is a completely positive map satisfying

$$\mathcal{E}(t_3, t_1) = \mathcal{E}(t_3, t_2)\mathcal{E}(t_2, t_1), \quad t_3 \geq t_2 \geq t_1. \tag{3.15}$$

As an alternative possibility to measure the non-Markovianity of a process, the BLP (Breuer, Laine, and Piilo) measure quantifies the backflow of information from the environment into the system in terms of the distinguishability of pairs of evolving quantum states [107].

Approaches for modeling the dynamics of open quantum systems that are not based on the Markov approximation include non-Markovian master equations for the reduced density matrix of the system [108, 109] and path integral methods, which rely on the quantum analogue of the principle of least action and allow going beyond the weak-coupling approximation non-perturbatively [110, 111]. Furthermore, stochastic Schrödinger equations can be employed, where the environment is treated as a noise source for the system state [49, 112–114]. The evaluation of the quantum stochastic Schrödinger equation within the MPS framework is one of the methods employed in this thesis, see Chap. 5. Alternatively, it is possible to describe the open quantum system within a Heisenberg representation, where the input-output formalism, originally derived under the Markov approximation [115], can be generalized to the non-Markovian case [116, 117]. A related Heisenberg approach is proposed in Chap. 6.

3.3.2 Lindblad master equation

One of the most important approaches for treating the dynamics of open quantum systems is the use of master equations. Master equations allow for the calculation of the dynamics of the reduced density matrix of the system without the need to consider the dynamics

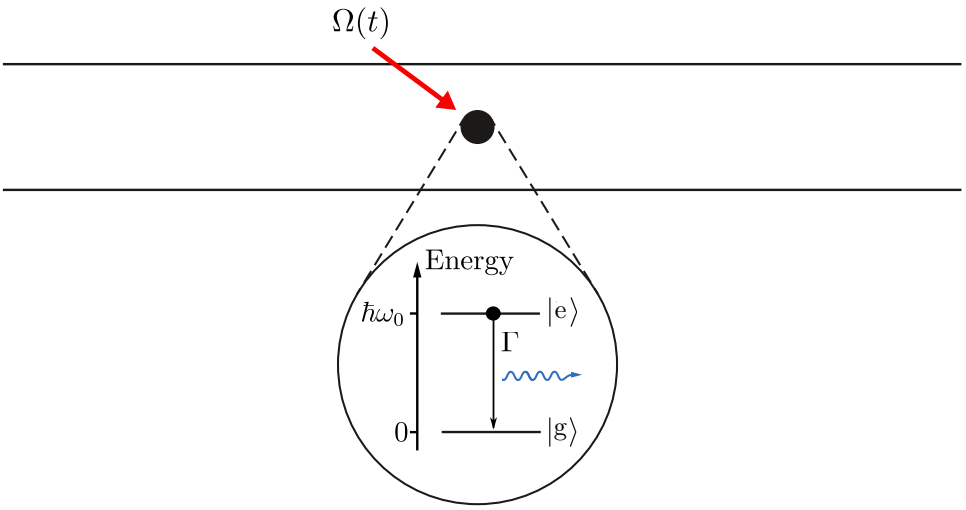

Figure 3.3: TLS coupled to an infinite waveguide. The emitter with energy difference $\hbar\omega_0$ between ground state $|\mathrm{g}\rangle$ and excited state $|\mathrm{e}\rangle$ decays with rate Γ and can be driven via an external laser with Rabi frequency $\Omega(t)$.

of the total system explicitly. Starting from the Von-Neumann equation for the density matrix of the total system, see Sec. 2.2, the Lindblad master equation

$$\frac{\mathrm{d}}{\mathrm{d}t}\rho_\mathrm{S} = -\frac{i}{\hbar}\left[H_\mathrm{S}, \rho_\mathrm{S}\right] + \sum_l \left(2A_l\rho_\mathrm{S}A_l^\dagger - \rho_\mathrm{S}A_l^\dagger A_l - A_l^\dagger A_l\rho_\mathrm{S}\right) \tag{3.16}$$

can be derived for the density matrix ρ_S of the relevant subsystem [27, 28]. Here, the first term on the right-hand side of Eq. (3.16) generates the unitary time evolution. The second term describes effective jumps of the system due to the interaction with the environment, where the system operators A_l are the so-called Lindblad operators. This effective interaction with the reservoir results in irreversible dynamics rendering the time evolution non-unitary. The Lindblad equation is valid under the Born-Markov approximation, which consists essentially of two parts: A weak system-reservoir interaction is assumed so that correlations between system and environment develop slowly and we can approximate $\rho(t) \approx \rho_\mathrm{S}(t) \otimes \rho_B(0)$ (Born approximation). Furthermore, the correlation times of the environment are assumed to be short in comparison to the time scales of the system evolution (Markov approximation). The Lindblad equation corresponds to a completely positive and trace-preserving dynamical map so that the evolution to a valid density matrix is ensured.

For example, for a TLS coupled to the vacuum field inside an infinite waveguide, the relevant Lindblad operator is the transition operator of the emitter $\left(A_l \to \sqrt{\Gamma}\sigma_-\right)$, see Sec. 3.2, and the Lindblad master equation takes the form

$$\frac{\mathrm{d}}{\mathrm{d}t}\rho_\mathrm{S} = -\frac{i}{\hbar}\left[H_\mathrm{S}, \rho_\mathrm{S}\right] + \Gamma\left(2\sigma_-\rho_\mathrm{S}\sigma_+ - \rho_\mathrm{S}\sigma_+\sigma_- - \sigma_+\sigma_-\rho_\mathrm{S}\right). \tag{3.17}$$

The corresponding setup is shown in Fig. 3.3. For an initially excited emitter, the master equation describes the exponential decay of the emitter exitation due to the interaction with the reservoir, where the coupling strength determines the decay rate Γ. Furthermore, it is possible to include an external, classically treated laser field with Rabi frequency $\Omega(t)$ via the system Hamiltonian H_S.

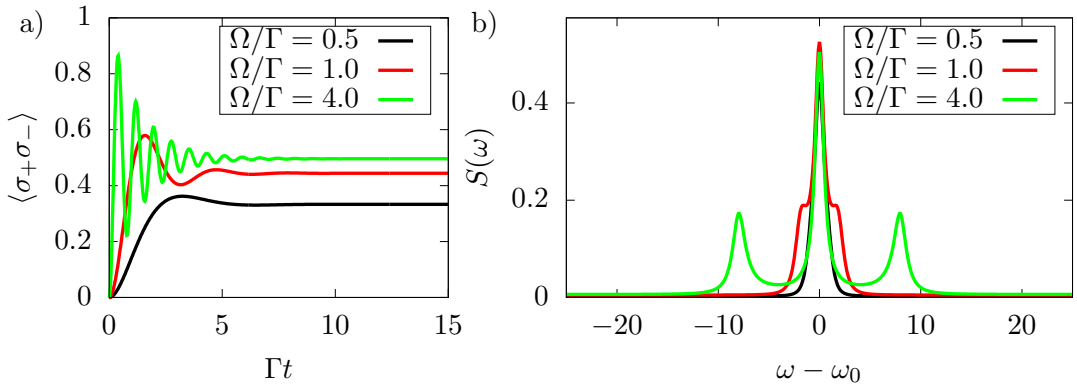

Figure 3.4: TLS with decay rate Γ excited by a continuous-wave laser field with Rabi frequency Ω. (a) Emitter dynamics for different Rabi frequencies Ω. (b) Corresponding power spectra of the TLS emission.

If the TLS is driven by a resonant continuous-wave laser field with Rabi frequency Ω, the phenomenon of resonance fluorescence can be observed [118]. The effects this implies are illustrated in Fig. 3.4. As presented in Fig. 3.4 a, the emitter undergoes Rabi oscillations before reaching a non-zero steady-state population. The particular steady-state value and the transient time depend on the Rabi frequency in comparison to the decay rate of the emitter, Ω/Γ. At most, a steady-state population of $\lim_{t\to\infty}\langle\sigma_+\sigma_-\rangle = 0.5$ is attainable. This is due to the fact that stimulated emission gains in importance in relation to absorption as the population increases so that no stable population inversion can be achieved. A characteristic feature of resonance fluorescence is, furthermore, the emergence of sidebands in the spectrum of the light emitted from the TLS with increasing drive strength, the so-called Mollow triplet, as shown in Fig. 3.4 b. Following the Wiener-Khinchin theorem [119], the power spectrum $S(\omega)$ for a stationary field can be obtained as the Fourier transform of the first-order coherence function $g^{(1)}(\tau)$ according to

$$S(\omega) = \frac{1}{2\pi}\int_{-\infty}^{\infty} d\tau\, g^{(1)}(\tau)e^{i\omega\tau}. \tag{3.18}$$

Because of the stationarity of the field, $g^{(1)}(\tau)$ only depends on the time difference τ and is given as

$$g^{(1)}(\tau) = \frac{\langle E^{(-)}(t)E^{(+)}(t+\tau)\rangle}{\langle E^{(-)}(t)E^{(+)}(t)\rangle}, \tag{3.19}$$

where $E^{(-)}$ and $E^{(+)}$ are the negative and positive frequency part of the quantized electric field, respectively, see Sec. 2.3. In the considered Markovian system of a TLS coupled to an infinite waveguide, the first-order coherence function can be calculated analytically applying the quantum regression theorem [102]. Note, however, that the results presented in Fig. 3.4 are numerical results obtained using the MPS framework as introduced in detail in Chap. 5.

4 Entanglement

Entanglement, as a property of composite quantum systems, describes nonclassical correlations between subsystems and marks the boundary between the classical and the quantum realm. It has preoccupied scientists in different contexts for nearly a century. Initially, entanglement was merely a theoretical concept and the subject of a philosophical debate about the foundations of quantum mechanics. However, with technological progress, entanglement has found its way into the laboratories. It is now considered a fundamental resource for quantum computation [12, 120], enables secure quantum communication, for example via quantum key distribution [121,122], and allows for measurements more precise than achievable classically [16, 123–125].

In 1935, Einstein, Podolsky, and Rosen (EPR) raised concerns about the completeness of quantum mechanics since its predictions turned out to be incompatible with the seemingly natural assumptions of locality and reality [9]. In particular, the fact that the state of one subsystem can be determined by measuring another, possibly distant subsystem seemingly violates the general theory of relativity because of the faster-than-light transmission of information. This "spooky action at a distance" was later termed "Verschränkung" (entanglement) by Schrödinger [8]. EPR hypothesized that the completeness of quantum mechanics could be restored by introducing hidden variables into the theory that determine the outcomes of the measurements in advance. However, since, in 1964, Bell formulated his famous inequality that allows to test quantum mechanics against local hidden-variable theories (LHVT) [10], experimental evidence strongly suggests the correctness of quantum mechanics.

Entanglement can, in principle, be found in any composite quantum system. While EPR focussed on the position and the momentum of a pair of particles, following the reformulation of the EPR paradox by Bohm and Aharonov [126], Bell assumed a pair of spin one-half particles in a singlet state. In optical experiments, typically, polarization-entangled photon pairs are used. This type of entanglement forms the basis of the work presented in Chap. 9. Furthermore, photons can also be entangled in other degrees of freedom such as their orbital angular momenta [127] or with respect to their energies and times of emission [128]. This energy-time entanglement is the subject of study in Chap. 8. Beyond that, other physical systems have also been used for the experimental demonstration of entanglement, among them neutrinos [129], electron spins [130], as well as macroscopic systems such as diamonds [131] and hybrid mechanical-spin oscillators [132].

The purpose of this chapter is to provide an overview of the topic of entanglement and discuss possible ways to detect it. To that end, in Sec. 4.1, we begin by formally introducing the notion of entanglement and, subsequently, in Sec. 4.2, we present different possibilities for its characterization and quantification.

4.1 Concept

To formalize the concept of entanglement, let us consider a bipartite quantum system with the associated Hilbert space $\mathcal{H}_{\mathrm{AB}} = \mathcal{H}_{\mathrm{A}} \otimes \mathcal{H}_{\mathrm{B}}$ spanned by the orthonormal product basis $\{|i\rangle_{\mathrm{A}} \otimes |j\rangle_{\mathrm{B}}\}$. Due to the superposition principle, a general pure state of the system can be written as

$$|\psi\rangle = \sum_{i,j} \psi_{i,j} \, |i\rangle_{\mathrm{A}} \otimes |j\rangle_{\mathrm{B}} \, . \tag{4.1}$$

Product states of the form $|\psi\rangle = |\phi\rangle_{\mathrm{A}} \otimes |\chi\rangle_{\mathrm{B}}$ only constitute a fraction of all possible states. If the system is in such a product state, it is possible to assign single state vectors to the individual subsystems and the composite system is said to be separable. If this is not the case, the composite system is said to be entangled [18].

A prominent example for states that cannot be written as product states are the maximally entangled Bell states or EPR pairs

$$|\phi^{\pm}\rangle = \frac{1}{\sqrt{2}} \left(|00\rangle \pm |11\rangle \right) , \quad |\psi^{\pm}\rangle = \frac{1}{\sqrt{2}} \left(|01\rangle \pm |10\rangle \right) , \tag{4.2}$$

which form a basis of the two-qubit system with Hilbert space $\mathcal{H} = \mathbb{C}^2 \otimes \mathbb{C}^2$. For a two-qubit system in such a state, we have perfect knowledge about the composite system but are completely ignorant with respect to the states of the individual qubits in so far as the composite system is in a pure state, whereas the reduced density matrix of each subsystem describes a mixed state. The fact that the Bell states are maximally entangled signifies that no other state in the considered Hilbert space can exhibit a higher degree of entanglement where an overview on how entanglement can be quantified is given below in Sec. 4.2.

To illustrate the implications of such Bell states we imagine two spatially separated parties (typically called Alice and Bob) each holding one qubit from a source of EPR pairs. Suppose, for example, that the source reliably prepares the state $|\phi^{+}\rangle = \left(|00\rangle + |11\rangle \right) / \sqrt{2}$. If Alice now performs a measurement on her qubit in the $\{|0\rangle , |1\rangle\}$ basis, it is equally likely for her to measure her qubit either in the state $|0\rangle$ or in the state $|1\rangle$. What is remarkable are the consequences of Alice's measurement for Bob: Before the measurement, it was also equally likely for Bob to find his qubit in the state $|0\rangle$ and in the state $|1\rangle$ when measuring in the respective basis. Due to the measurement performed by Alice, however, the wave-function collapses. If Alice measures the state $|0\rangle$, the composite system collapses to the state $|00\rangle$ and Bob necessarily finds his qubit in the state $|0\rangle$. If, in contrast, Alice measures the state $|1\rangle$, afterwards, the total system is in the state $|11\rangle$ and, as a consequence, Bob's qubit can only be found in the state $|1\rangle$. It was this correlation, incompatible with the local realist view of causality, which led EPR to conclude that the quantum mechanical formalism must be incomplete and that there must be hidden variables allowing to restore the determinism of the theory.

Generalizing the definition from the case of pure states, the mixed state ρ_{AB} of the composite system defined on $\mathcal{H}_{\mathrm{AB}} = \mathcal{H}_{\mathrm{A}} \otimes \mathcal{H}_{\mathrm{B}}$ is separable if it can be expressed as

$$\rho_{\mathrm{AB}} = \sum_{i} p_i \rho_{\mathrm{A}}^{i} \otimes \rho_{\mathrm{B}}^{i}, \tag{4.3}$$

where p_i is a probability distribution and $\rho_{\mathrm{A}}^{i} \in \mathcal{H}_{\mathrm{A}}$, $\rho_{\mathrm{B}}^{i} \in \mathcal{H}_{\mathrm{B}}$. That is, the state is separable if it can be expressed as a mixture of separable pure states. Otherwise, it is entangled.

In addition to the bipartite entanglement discussed so far, a system consisting of more than two subsystems can exhibit multipartite entanglement. Detecting and quantifying multipartite entanglement is a rich and active area of research (see for example Refs. [18, 133–137]), which, however, goes beyond the scope of this thesis.

4.2 Quantifying entanglement

After several years of qualitative debates about the concept of entanglement, Bell's inequality provided a first opportunity to test the predictions of quantum mechanics experimentally, thus, adding a quantitative layer to the discussion. Since then, there has been an increasing interest in finding ways to characterize and quantify entanglement, especially with the growing importance of entanglement as a resource in quantum information science.

Thus far, we discussed either separable product states exhibiting no entanglement or maximally entangled Bell states. In general, particularly for mixed states, it is, however, highly non-trivial to decide "how entangled" a state is. To answer this question, various schemes for the classification of entanglement have been proposed. A possibility to detect the presence of entanglement is given by entanglement witnesses. One example is the violation of a Bell-type inequality, which is only possible if the state of a system exhibits nonclassical correlations [138]. Furthermore, we can formally define functions quantifying the amount of entanglement contained in a quantum state, which determine the usefulness of quantum states for specific nonclassical tasks. Such functions, mapping from density matrices to positive real numbers, have to satisfy certain axioms [139, 140]: (1) The functions do not increase under local operations and classical communication (LOCC) [1]. (2) The functions vanish on separable states.

In this section, we concentrate on the entanglement witnesses and measures that are important for the topics covered in this thesis, while the selection is not intended to be exhaustive. Further information can be found, for example, in Refs. [18, 136].

4.2.1 Bell's inequality

In his famous paper "On the Einstein Podolsky Rosen paradox", Bell assumed a singlet spin state of the form $|\psi\rangle = (|\uparrow_1,\downarrow_2\rangle - |\downarrow_1,\uparrow_2\rangle)/\sqrt{2}$ and theoretically showed that the state can produce outcomes in a correlation measurement that violate the upper bound imposed by LHVT [10]. This way, Bell showed that a decisive experiment between LHVT and quantum mechanics can, in principle, be constructed. Bell-type inequalities have been proposed in a variety of forms in the ensuing decades. Particularly common is the Clauser, Horne, Shimony, and Holt (CHSH) inequality [11]. As a generalization of Bell's theorem from perfectly correlated to experimentally accessible states, it enabled actual experimental

[1] LOCC are an important class of operations in quantum information theory. They allow only local operations to be performed on individual subsystems and can only be coordinated via classical communication. This way, it is possible to differentiate between classical and quantum correlations: Classical correlations are the correlations generated by LOCC, while LOCC cannot produce quantum correlations.

tests of the predictions of quantum mechanics against those of LHVT: Assume that we have a correlated pair of particles, which are measured at two spatially separated detectors. The first detector has the possible settings a and a', the second detector can be either set to b or b'. The possible outcomes for all measurements are either $+1$ $(+)$ or -1 $(-)$. Then, under the assumption of local realism, the inequality

$$\left|S(a,a',b,b')\right| = \left|E(a,b) - E(a,b') + E(a',b) + E(a',b')\right| \leq 2 \tag{4.4}$$

holds. Here, $E(a,b)$ is the correlation coefficient for the measurement setting (a,b),

$$E(a,b) = P_{++}(a,b) + P_{--}(a,b) - P_{+-}(a,b) - P_{-+}(a,b), \tag{4.5}$$

where $P_{ij}(a,b)$ describes the probability to measure i at the first detector with setting a and j at the second detector with setting b with $i,j \in \{+,-\}$. Quantum theory, in contrast, allows for a higher upper bound [141],

$$|S_{\mathrm{QM}}| \leq 2\sqrt{2}. \tag{4.6}$$

This upper limit is reached for maximally entangled states. However, also states that are nonclassically correlated but not maximally entangled can lead to a violation of the CHSH inequality since there is a margin not admitting an explanation by LHVT.

A typical experiment to show a violation of the CHSH inequality is an optical experiment where correlations between pairs of photons are analyzed using photon detectors with variable polarizer orientations [142, 143]. The correlations manifest as an interference in the coincidence rate R when varying the angles of the polarizers. The visibility of the interference fringes is defined as

$$V = \frac{R_{\max} - R_{\min}}{R_{\max} + R_{\min}}. \tag{4.7}$$

The connection to the quantity S in the CHSH inequality is given via $S = 2\sqrt{2}V$, where a maximally entangled state corresponds to perfect visibility, $V = 1$. As a consequence, a violation of the CHSH inequality can be found for a visibility $V > 1/\sqrt{2}$. The violation of a Bell-type inequality indicates nonclassical correlations and, thus, can be viewed as an entanglement witness [138]. Furthermore, the amount of violation can be used to define an entanglement measure [136].

A number of experiments has been performed that showed an agreement with the quantum mechanical predictions [144–146]. However, the experimental setup for such a Bell test must be carefully designed to rule out possible loopholes. Such loopholes would in principle allow for LHVT despite the apparent violation of a Bell-type inequality. One issue is that if the detector settings are maintained for a long enough period of time, information about the setting at one detector could travel to the other detector and affect the measurement without violating the locality principle. This is what is know as the "locality loophole" and was regarded by Bell as a fundamental problem, which could, however, be prevented by changing the settings of the measurement devices randomly during the flight of the entangled particles [10, 147]. Another problem is the "detection loophole". It originates from the fact that realistic detectors make it impossible to register all generated pairs. Especially in optical experiments, in the past, efficiencies of the photon detectors were typically low. Initially, experiments could show a violation of a Bell-type inequality only together with a fair sampling hypothesis assuming that the detected subset of particles

is representative of all particles [145]. However, technological progress made new and highly efficient photon detectors available allowing for the omission of this hypothesis in later experiments [148, 149]. After several experiments closing either the locality or the detection loophole, in 2015, three groups managed to close both loopholes simultaneously for the first time [130, 150, 151]. These results significantly strengthen the confidence in the correctness of the quantum mechanical predictions although the possibility of further loopholes prohibits ruling out LHVT altogether.

Another point that is important for this thesis is the postselection loophole in the Franson setup, which we discuss in Chap. 8. In the original Franson setup, even in the case of perfect detection efficiency, 50% of the events are discarded, which allows for the construction of a local hidden-variable model [152]. Only a modified setup and an adapted Bell-type inequality make it possible to show an incompatibility of the observed correlations in energy and time with LHVT [143, 153, 154].

4.2.2 Entanglement and entropy

There is a deep connection between the concepts of entanglement and entropy. Entropy, the key concept of information theory, measures the uncertainty associated with the state of a physical system. In classical information theory, the information we gain on average from the value a random variable X with the probability distribution $p_1, p_2, \ldots, p_n$ takes on is quantified in terms of the Shannon entropy

$$H(X) = -\sum_i p_i \log p_i. \tag{4.8}$$

This way, it is a measure of the uncertainty associated with a classical probability distribution. Its counterpart in the quantum realm is the Von-Neumann entropy [155]. Here, a density matrix ρ with eigenvalues $\lambda_1, \lambda_2, \ldots, \lambda_n$ takes the place of the probability distribution. The Von-Neumann entropy, which we also touch upon in the context of the Schmidt decomposition in Sec. 5.1.2, is defined as

$$S(\rho) = -\mathrm{tr}\rho \log \rho = -\sum_i \lambda_i \log \lambda_i. \tag{4.9}$$

Entanglement as a property of composite quantum systems can be found when analyzing the relation between the information the state of a composite quantum system gives us about the total system and the information it provides about the individual subsystems. For classical systems, it holds that the Shannon entropy of two random variables X and Y is always larger than that of the individual random variables, $H(X,Y) \geq H(X)$, $H(X,Y) \geq H(Y)$. Thus, our knowledge about the total system cannot be larger than the knowledge about the subsystems. In the quantum case, in contrast, there are states violating the corresponding expressions for the Von-Neumann entropy,

$$S\left(\rho_{\mathrm{AB}}\right) - S\left(\rho_{\mathrm{A}}\right) \geq 0, \quad S\left(\rho_{\mathrm{AB}}\right) - S\left(\rho_{\mathrm{B}}\right) \geq 0, \tag{4.10}$$

where $\rho_{\mathrm{AB}} \in \mathcal{H}_{\mathrm{AB}} = \mathcal{H}_{\mathrm{A}} \otimes \mathcal{H}_{\mathrm{B}}$, $\rho_{\mathrm{A}} \in \mathcal{H}_{\mathrm{A}}$, and $\rho_{\mathrm{B}} \in \mathcal{H}_{\mathrm{B}}$. These equations can be used as a criterion of separability since the entropy of a subsystem can only be higher than the entropy of the total system if the state is entangled [156]. If no entanglement is present, the equations are satisfied since for separable states the global disorder is higher than the

local disorder [157, 158]. Based on this concept, the relative entropy of entanglement has emerged as a measure of entanglement [139, 159],

$$E_R = \inf_{\sigma \in \mathrm{SEP}} S(\rho||\sigma), \quad S(\rho||\sigma) = \mathrm{tr}\left[\rho\left(\log\rho - \log\sigma\right)\right]. \tag{4.11}$$

Here, $S(\rho||\sigma)$ is the quantum relative entropy measuring the distinguishability of states ρ and σ, where σ for the relative entropy of entanglement belongs to the set of separable states (SEP).

4.2.3 Concurrence and negativity

Two common approaches to quantify entanglement, which are relevant since in many practical cases their evaluation is convenient, are the concurrence and the negativity. In the case of pure two-qubit states, both are equivalent, by our definition, up to a factor of two as for the concurrence $C \in [0, 1]$, while for the negativity $N \in [0, 0.5]$.

The concurrence of the state ρ is specifically defined for two qubits as

$$C(\rho) = \max\{0, \lambda_1 - \lambda_2 - \lambda_3 - \lambda_4\}, \quad \lambda_1 \geq \lambda_2 \geq \lambda_3 \geq \lambda_4, \tag{4.12}$$

where $\{\lambda_i\}$ are the square roots of the eigenvalues of the matrix $\rho\left(\sigma_y \otimes \sigma_y\right)\rho^*\left(\sigma_y \otimes \sigma_y\right)$ with Pauli matrix σ_y [160, 161]. Although the concurrence itself is not an entanglement measure in the strict sense, it is of interest due to its monotonic relation to the entanglement of formation, which is an actual entanglement measure but rather complicated to evaluate [136]. The concurrence is particularly simple in the case of a pure state of the form $|\psi\rangle = a_{00}|00\rangle + a_{01}|01\rangle + a_{10}|10\rangle + a_{11}|11\rangle$, where it takes on the value $C(|\psi\rangle) = 2\,|a_{00}a_{11} - a_{01}a_{10}|$.

The negativity as an alternative way to quantify entanglement is based on the Peres-Horodecki or positive partial transpose (PPT) criterion of separability [162]. The partial transposition is the transposition of a matrix with respect to one subsystem. Specifically, the partial transpose of a matrix ρ defined on a bipartite system $\mathcal{H}_{\mathrm{AB}} = \mathcal{H}_{\mathrm{A}} \otimes \mathcal{H}_{\mathrm{B}}$ with respect to subsystem B is denoted by $\rho^{T_{\mathrm{B}}}$ and defined via

$$\rho = \sum_{i,j,k,l} \rho_{ij,kl}\,|i\rangle\langle j| \otimes |k\rangle\langle l|, \quad \rho^{T_{\mathrm{B}}} = \sum_{i,j,k,l} \rho_{ij,kl}\,|i\rangle\langle j| \otimes |l\rangle\langle k|. \tag{4.13}$$

The partial transposition can be understood in terms of the partial time reversal in one of the subsystems. Making use of this concept, the PPT criterion states that the state ρ is separable if its partial transpose (with respect to either subsystem) has only non-negative eigenvalues. This signifies that if the two subsystems are not entangled then performing a transposition on one of the subsystems should still result in a valid density matrix. The negativity $N(\rho)$, which is defined as

$$N(\rho) = \frac{1}{2}\left[\mathrm{tr}\left(\sqrt{\left(\rho^{T_{\mathrm{B}}}\right)^\dagger \rho^{T_{\mathrm{B}}}}\right) - 1\right], \tag{4.14}$$

provides a way to quantify the violation of this criterion [163].

Part II

Memory-induced entanglement in WQED with quantum pulses

5 Exciting the atom-photon bound state with multiphoton pulses

Photons are promising candidates for the transport of quantum information between the stationary nodes in a large-scale quantum network realized, for example, as a WQED setup [20, 66, 164–167]. In this context, a semiclassical treatment of the light-matter interaction is, in general, insufficient and a description of the emitter excitation through the waveguide field via quantum pulses is of fundamental importance [168, 169]. Furthermore, if the separations between the nodes are non-negligible compared to the wavelength of the light, the time-delayed back action of the electromagnetic field on the nodes cannot be disregarded and non-Markovian effects emerge. As a consequence, Markovian approaches such as the Lindblad master equation introduced in Sec. 3.3.2 fail to describe the dynamics.

A paradigmatic non-Markovian WQED setup is a TLS in front of a mirror realized via a semi-infinite waveguide [170,171], which has been implemented in a number of experiments [172–177]. A finite emitter-mirror separation results in time-delayed self-feedback, which can potentially be used to govern the system dynamics via coherent feedback control [42]. A remarkable feature in this setup is the existence of an atom-photon bound state with an energy inside the continuum of propagating modes [178]. Since it allows for the trapping of single photons, this phenomenon is of particular interest for the realization of effective quantum memories [179]. There are two possibilities to populate the bound state: Either via the incomplete decay of an excited emitter in vacuum or via multiphoton scattering, where the effectiveness of these schemes depends crucially on the feedback delay time. The behavior is especially complex in the case of multiphoton scattering, where the excitation probability depends non-monotonously on the delay time as well as on the pulse properties, that is, the pulse shape and the contained number of photons [180].

In this chapter, we study the feedback dynamics for a TLS in front of a mirror and, in particular, the excitation of the atom-photon bound state via multiphoton pulses. The chapter is based on our work published in Ref. [181]. For the simulation of the non-Markovian system dynamics, we use the MPS framework, which makes the light field directly accessible and allows including pulses beyond the usual few-photon limit due to the efficient handling of the entanglement in the system. We start with an introduction of the time evolution method based on MPS in Sec. 5.1. In Sec. 5.2, we discuss how quantum pulses can be included in the MPS framework. Subsequently, in Sec. 5.3, we look at the resulting dynamics, where it is possible to find the emitter in the excited state in the long-time limit due to the excitation of the atom-photon bound state. Finally, in Sec. 5.4, we study the excitation of the bound state via multiphoton pulses containing up to four photons and investigate the interplay of the emitter-mirror separation and the photon number.

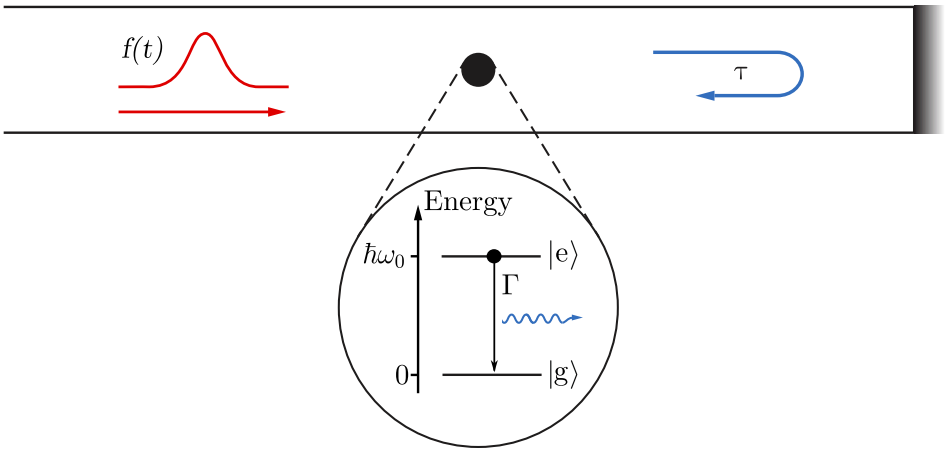

Figure 5.1: TLS coupled to a semi-infinite waveguide. The emitter with energy difference $\hbar\omega_0$ between ground state $|\mathrm{g}\rangle$ and excited state $|\mathrm{e}\rangle$ decays with rate Γ. The closed end of the waveguide functions as a mirror and provides feedback at the delay time τ. An excitation of the TLS via a quantum pulse of shape $f(t)$ is possible.

5.1 Matrix product state framework

The non-Markovian time evolution method based on MPS as introduced by Pichler and Zoller in Ref. [53] is of central importance for this thesis. Here, we present the approach for a TLS coupled to a semi-infinite waveguide. The closed end of the waveguide functions as a mirror and provides feedback for the emitter at the delay time $\tau = 2d/c$ with d being the emitter-mirror separation and c the speed of light in the waveguide. The setup is illustrated in Fig. 5.1. The modeling of the quantum pulse of shape $f(t)$, which describes the excitation of the emitter through the waveguide, is discussed below in Sec. 5.2. MPS form a particular type of tensor network and have been developed in the condensed matter context [182–186]. Originally, they were used to study one-dimensional many-body systems such as spin chains with spatial correlations at a given time. We, in contrast, focus on a single emitter interacting with photons in time bins instead, where the approach enables a time-local description as well as justified truncations of the Hilbert space.

5.1.1 Stroboscopic time evolution in a time-bin basis

We start with the Hamiltonian describing the TLS interacting with the electromagnetic field as derived in Sec. 3.2. The Hamiltonian is transformed into the interaction picture defined by the freely evolving contributions from the emitter and the light field, see Sec. 2.1, which yields

$$H_\mathrm{I} = \int d\omega\, \hbar \left[g(\omega) r_\omega^\dagger \sigma_- e^{i(\omega-\omega_0)t} + \mathrm{H.c.} \right]. \tag{5.1}$$

The bosonic operator $r_\omega^{(\dagger)}$ models the annihilation (creation) of a photon with frequency ω, while the operators $\sigma_- = |\mathrm{g}\rangle\langle\mathrm{e}|$ and $\sigma_+ = |\mathrm{e}\rangle\langle\mathrm{g}| = \sigma_-^\dagger$ are the transition operators of the TLS with ground state $|\mathrm{g}\rangle$ and excited state $|\mathrm{e}\rangle$ separated by the energy $\hbar\omega_0$. The coupling between the TLS and the photonic reservoir is described by $g(\omega)$, which is, in general,

frequency dependent. In the case of a semi-infinite waveguide, the boundary condition of a vanishing electric field at the position of the mirror has to be satisfied. This is encoded via the coupling strength

$$g(\omega) = g_{\mathrm{L}}(\omega)e^{i\omega\tau/2} - g_{\mathrm{R}}(\omega)e^{-i\omega\tau/2}, \tag{5.2}$$

where $g_{\mathrm{L}}(\omega)$ and $g_{\mathrm{R}}(\omega)$ describe the coupling to the left- and right-propagating light field, respectively, and the mirror is assumed to be perfectly reflecting. If we assume the coupling to be constant over the relevant bandwidth due to a flat spectral density of the reservoir modes around resonance and identical for both directions, $g_{\mathrm{L}}(\omega) = g_{\mathrm{R}}(\omega) \equiv g_0/(2i)$, $g(\omega)$ takes on the form [170, 171, 178, 187]

$$g(\omega) = g_0 \sin(\omega\tau/2). \tag{5.3}$$

Note that, this way, the time-delayed feedback mechanism introduces a backflow of information from the environment into the system resulting in non-Markovianity as opposed to non-Markovianity due to structured reservoirs reflected in a coupling that is itself frequency-dependent.

We transform the Hamiltonian from Eq. (5.1) into the time domain by introducing the quantum noise operator

$$r_t^\dagger = \frac{1}{\sqrt{2\pi}} \int d\omega\, r_\omega^\dagger e^{i(\omega-\omega_0)t}. \tag{5.4}$$

While the operator $r_\omega^\dagger$ describes the creation of a photon of frequency ω, as its Fourier transform, the operator $r_t^\dagger$ describes the creation of a photon at time t and satisfies the bosonic commutation relation $\left[r_t, r_{t'}^\dagger\right] = \delta(t-t')$.

This way, after performing a time-independent phase shift $\varphi \to \varphi - \omega\tau/2$ via the unitary transformation

$$H' = U^\dagger H_{\mathrm{I}} U, \quad U = \exp\left(i \int d\omega\, r_\omega^\dagger r_\omega \omega\tau/2\right), \tag{5.5}$$

the Hamiltonian takes on the form

$$H' = -i\hbar\sqrt{\Gamma}\left(r_t^\dagger \sigma_- - r_{t-\tau}^\dagger \sigma_- e^{-i\omega_0\tau} - \mathrm{H.c.}\right) \tag{5.6}$$

with $\Gamma \equiv \pi g_0^2/2$. Here, the first term on the right-hand side accounts for the immediate interaction of the emitter with the light field. The second term arises due to the interaction of the emitter with the feedback signal, that is, the excitation that returns to the emitter from the mirror after the round-trip time τ. This feedback contribution gives the system a memory so that Markovian approaches such as the Lindblad master equation introduced in Sec. 3.3.2 fail to capture the essential features of the dynamics.

To prepare the treatment of the non-Markovian dynamics within the MPS framework, we discretize time into steps Δt that are small in comparison to all emitter time scales. Subsequently, the continuous system evolution can be approximated using the stroboscopic time evolution operator U_k, which describes the discrete time evolution from time t_k to t_{k+1}, $t_k = k\Delta t$, $k \in \mathbb{N}$. As introduced in Sec. 2.1, the time evolution operator can be obtained from solving the Schödinger equation and satisfies

$$|\psi(t_{k+1})\rangle = U_k |\psi(t_k)\rangle, \quad U_k = \mathcal{T} \exp\left[-\frac{i}{\hbar}\int_{t_k}^{t_{k+1}} dt'\, H'(t')\right]. \tag{5.7}$$

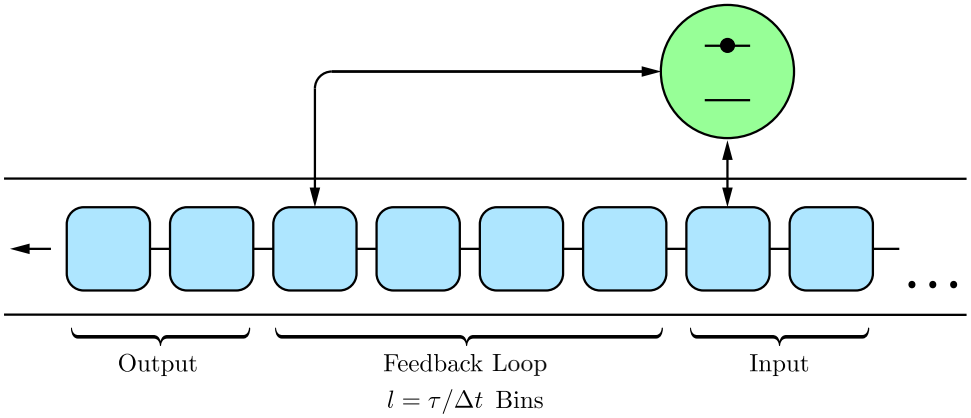

Figure 5.2: Schematic representation of the discretization of the reservoir dynamics via the introduction of a time-bin basis. The reservoir can be envisioned as a conveyor belt of time bins (blue) interacting with the emitter (green) successively. Feedback is accounted for by an additional loop encompassing $l = \tau/\Delta t$ time bins (here $l = 4$). Thus, the emitter interacts with the reservoir at two points in time.

For the considered setup, if we assume that the feedback delay time is a multiple of the step size, $\tau = l\Delta t$, $l \in \mathbb{N}$, U_k can be expressed as

$$U_k = \exp\left[-\sqrt{\Gamma}\left(\Delta R_k^\dagger \sigma_- - \Delta R_{k-l}^\dagger \sigma_- e^{-i\omega_0\tau} - \text{H.c.}\right)\right]. \tag{5.8}$$

Here, we introduced the noise increment

$$\Delta R_k^\dagger = \int_{t_k}^{t_{k+1}} dt\, r_t^\dagger, \tag{5.9}$$

which describes the creation of a photon during the k-th time step and satisfies $\left[\Delta R_k, \Delta R_{k'}^\dagger\right] = \Delta t \delta_{kk'}$, that is, it satisfies bosonic commutation relations up a normalization factor. Note that in comparison to the general time evolution operator, Eq. (5.7), the time ordering operator $\mathcal{T}$ has been omitted in Eq. (5.8). This is justified if the time step is sufficiently small so that H' commutes with itself during one time step.

With the noise increments, a discrete time-bin basis of the Hilbert space can be constructed. The Fock state denoting i_k photons in the k-th time bin can be obtained from the vacuum state via

$$|i_k\rangle_k = \frac{\left[\Delta R_k^\dagger\right]^{i_k}}{\sqrt{i_k!\,(\Delta t)^{i_k}}} |0\rangle_k . \tag{5.10}$$

Thus, the reservoir dynamics are discretized into a "conveyor belt" of time bins, which is shifted by one bin at every time step so that the emitter interacts with the time bins successively as illustrated in Fig. 5.2. The feedback mechanism is translated into an additional loop at the end of which the time bins interact with the emitter for a second time before entering the output channel.

In this time-bin basis, the general state of the emitter and the photonic reservoir can be written as

$$|\psi(t_k)\rangle = \sum_{i_1,\ldots,i_{k-1},i_S,i_k,\ldots,i_N} \psi_{i_1,\ldots,i_{k-1},i_S,i_k,\ldots,i_N} |i_1,\ldots,i_{k-1},i_S,i_k,\ldots,i_N\rangle . \tag{5.11}$$

The index $i_\mathrm{S} \in \{\mathrm{g}, \mathrm{e}\}$ refers to the state of the emitter, which can be either in the ground (g) or the excited state (e), while the index i_j, $j \in \{1, \ldots, N\}$, denotes the occupation of the j-th time bin. At the k-th time step, all indices to the left of the emitter index describe past time bins, while the indices to the right of the emitter index can be associated with future time bins and, overall, N time steps are taken into account. The coefficient tensor $\psi \equiv \left(\psi_{i_1,\ldots,i_{k-1},i_\mathrm{S},i_k,\ldots,i_N}\right)$ of the total state now is, in general, $2p^N$-dimensional, where up to $(p-1)$ photons per time bin are considered. Thus, the dimension of the Hilbert space grows exponentially with the number of time bins and handling it numerically becomes quickly infeasible.

5.1.2 Matrix product state decomposition

For the efficient numerical handling of the entangled state of the emitter and the reservoir when calculating the dynamical map in Eq. (5.7), we employ the MPS framework [184]. The key idea of this approach is to express the coefficient tensor ψ in Eq. (5.11) as a product of matrices according to

$$\psi_{i_1,\ldots,i_{k-1},i_\mathrm{S},i_k,\ldots,i_N} = A^{i_1} \cdots A^{i_{k-1}} A^{i_\mathrm{S}} A^{i_k} \cdots A^{i_N}. \tag{5.12}$$

At the heart of the decomposition of a general state into an MPS lies the singular value decomposition (SVD). It allows decomposing an arbitrary matrix M into a product of three matrices according to

$$M = USV^\dagger. \tag{5.13}$$

Here, U is a matrix with orthonormal columns, that is, U is left-normalized. Matrix S is a diagonal matrix, the non-negative entries of which are the singular values. According to convention, these singular values are arranged in descending order, $s_1 \geq s_2 \geq \cdots \geq s_r > 0$. The number of non-zero singular values, r, is called the Schmidt rank of M. Matrix $V^\dagger$ is a right-normalized matrix with orthonormal rows. The SVD can be illustrated as shown in Fig. 5.3 a. The diagrammatic representation is a useful tool for the visualization of tensor networks such as MPS as well as the algorithms performed on it. In this representation, a box denotes a tensor, that is, a generalized matrix. The legs of the tensor correspond to its indices, where the number of indices defines its rank. A tensor of rank zero is a scalar, vectors are tensors of rank one, while matrices are rank two tensors. In the diagrammatic representation, we distinguish two types of indices: Vertical lines, on the one hand, represent physical indices corresponding to actual physical dimensions of the system. They can, for example, refer to a particular time bin or the emitter. Horizontal lines, on the other hand, describe virtual link indices functioning as auxiliary degrees of freedom. They do not correspond to physical quantities but contain information about the entanglement of the tensors they connect. Indices shared by two tensors can be summed over. As the inversion of their decomposition, this results in the contraction of the tensors. The different colors of the tensors in the illustration indicate their orthogonality properties. A green box indicates a left-normalized tensor, while a blue box describes right-normalization. The red diamond corresponds to the diagonal singular value matrix. After the SVD, the singular value matrix can be contracted with one of its neighboring matrices as shown in Fig. 5.3 b. This way, the orthogonality center (OC) is defined, which is marked by a black box in the diagrammatic representation, and the initial matrix is decomposed into a product of two matrices.

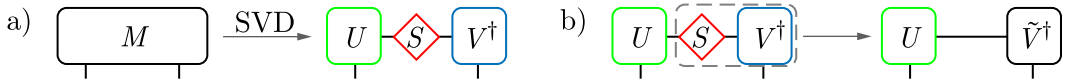

Figure 5.3: Diagrammatic representation of the SVD. (a) The matrix M is decomposed into three matrices via an SVD: the left-normalized matrix U, the diagonal singular value matrix S, and the right-normalized matrix $V^\dagger$. (b) The singular value matrix S can be contracted with one of the other matrices to define the OC, here placed at $\tilde{V}^\dagger$.

In the so-called Schmidt decomposition, the SVD is used to decompose the state of a bipartite quantum system. A general pure state $|\psi\rangle$ in the composite Hilbert space $\mathcal{H}_{\mathrm{AB}} = \mathcal{H}_{\mathrm{A}} \otimes \mathcal{H}_{\mathrm{B}}$ with orthonormal bases $\{|i\rangle_{\mathrm{A}}\}$ and $\{|j\rangle_{\mathrm{B}}\}$ of $\mathcal{H}_{\mathrm{A}}$ and $\mathcal{H}_{\mathrm{B}}$, respectively, can be written as

$$|\psi\rangle = \sum_{i,j} \psi_{i,j} \, |i\rangle_{\mathrm{A}} \otimes |j\rangle_{\mathrm{B}} \,. \tag{5.14}$$

Decomposing the coefficient matrix $\psi \equiv (\psi_{i,j})$ via an SVD, $\psi = USV^\dagger$, this state can be expressed as

$$|\psi\rangle = \sum_{\alpha=1}^{r} s_\alpha \, |\alpha\rangle_{\mathrm{A}} \otimes |\alpha\rangle_{\mathrm{B}} \,. \tag{5.15}$$

Here, $\{s_\alpha\}$ are the singular values of the coefficient tensor ψ with Schmidt rank r, which are also referred to as the Schmidt coefficients. The new basis states can be obtained via

$$|\alpha\rangle_{\mathrm{A}} = \sum_i U_{i,\alpha} \, |i\rangle_{\mathrm{A}} \,, \quad |\alpha\rangle_{\mathrm{B}} = \sum_j V^*_{j,\alpha} \, |j\rangle_{\mathrm{B}} \,. \tag{5.16}$$

If there is only a single non-zero singular value ($r = 1$), the state can be expressed as a product state, that is, the state is separable. The case of multiple non-zero singular values ($r > 1$), in contrast, corresponds to an entangled state, which cannot be written as a product state.

The reduced density matrices of the subsystems can be calculated by taking the partial trace, which yields

$$\rho_{\mathrm{A}} = \sum_{\alpha=1}^{r} s_\alpha^2 \, |\alpha\rangle_{\mathrm{A}} \langle\alpha|_{\mathrm{A}} \,, \quad \rho_{\mathrm{B}} = \sum_{\alpha=1}^{r} s_\alpha^2 \, |\alpha\rangle_{\mathrm{B}} \langle\alpha|_{\mathrm{B}} \,. \tag{5.17}$$

Using the Von-Neumann entropy of the reduced density matrices,

$$S(\rho_{\mathrm{A}}) = S(\rho_{\mathrm{B}}) = -\sum_{\alpha=1}^{r} s_\alpha^2 \log s_\alpha^2, \tag{5.18}$$

the entanglement encoded in the pure state of the composite system can be quantified. If the reduced states are pure ($S(\rho) = 0$), the state of the composite system is separable, while mixed reduced states ($S(\rho) > 0$) imply an entangled state. For a more detailed discussion of the concept of entanglement, see Chap. 4.

By making the entanglement between the subsystems accessible, the SVD allows for a justified truncation of the Hilbert space. To that end, the state of the system $|\psi\rangle$ is approximated by a state $|\psi'\rangle$ with coefficient matrix $\psi' = US'V^\dagger$, where S' is a diagonal

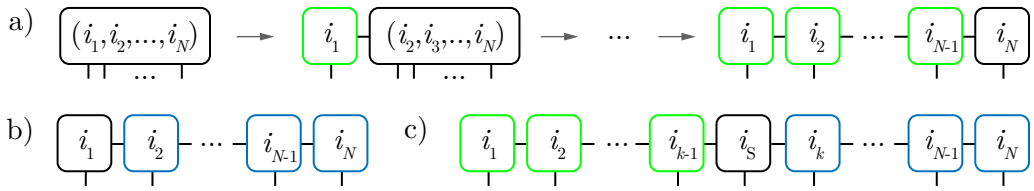

Figure 5.4: Diagrammatic representation of a decomposition of a state into an MPS. (a) The tensor carrying the indices $(i_1, i_2, \ldots, i_N)$ is decomposed into two tensors, one with the index i_1, the other carrying the remaining indices $(i_2, i_3, \ldots, i_N)$. This step is repeated until each tensor carries a single physical index and a left-canonical MPS is created. (b) MPS in right-canonical form. (c) Mixed-canonical MPS where the OC is placed at the TLS bin denoted by the index i_S.

matrix with entries $s_1 \geq s_2 \geq \cdots \geq s_{r'} \geq 0$, $r' < r$. By setting the smallest $(r - r')$ singular values to zero, we neglect only the least important parts of the Hilbert space, and it can be shown that this $|\psi'\rangle$ is the optimal approximation of $|\psi\rangle$ in a state space of dimension r' [184]. This way, we make an approximation of the system state by bringing it formally closer to a product state, which results in a drastic reduction of the numerical complexity of the problem.

To now decompose the state given in Eq. (5.11) into an MPS, a series of SVDs is performed, which is illustrated in Fig. 5.4. Here, the label of each bin refers to its associated physical index or indices. If we start the decomposition on the left, as shown in Fig. 5.4 a, the coefficient tensor is decomposed into a tensor carrying the index i_1 and a tensor carrying the remaining indices $(i_2, i_3, \ldots, i_N)$, which are grouped into a compound index when performing the SVD. To further decompose the tensor with the indices $(i_2, i_3, \ldots, i_N)$, the procedure is repeated for the bipartition into the subsystems defined by the indices i_2 and $(i_3, i_4, \ldots, i_N)$, respectively, and so on until the state has been completely decomposed and each tensor carries a single physical index. Subsequently, all tensors are left-normalized and the OC is positioned at the rightmost tensor. This corresponds to a left-canonical MPS. However, there is gauge freedom with respect to the position of the OC. Another possibility is starting the decomposition from the right, which yields right-normalized tensors and the OC at the leftmost tensor, that is, a right-canonical MPS, see Fig. 5.4 b. Furthermore, we can also start to decompose the state from both sides and place the OC at an arbitrary position, which results in a mixed-canonical MPS containing both left- and right-normalized tensors. In Fig. 5.4 c, an exemplary mixed-canonical MPS is shown where the OC is placed at the TLS bin. In this thesis, in general, we make use of the mixed-canonical form and move around the OC for the inclusion of feedback contributions as well as the application of operators. The position of the OC is particularly important for the efficient evaluation of expectation values as is discussed below in Sec. 5.1.3. It can be shifted via the contraction and the subsequent decomposition of the OC and a neighboring tensor, where the singular value matrix has to be contracted with the tensor we would like the OC to be placed at.

The MPS decomposition yields a state of the form

$$|\psi(t_k)\rangle = \sum_{i_1,\ldots,i_{k-1},i_\mathrm{S},i_k,\ldots,i_N} A^{i_1} \cdots A^{i_{k-1}} A^{i_\mathrm{S}} A^{i_k} \cdots A^{i_N} \, |i_1, \ldots, i_{k-1}, i_\mathrm{S}, i_k, \ldots, i_N\rangle \,, \quad (5.19)$$

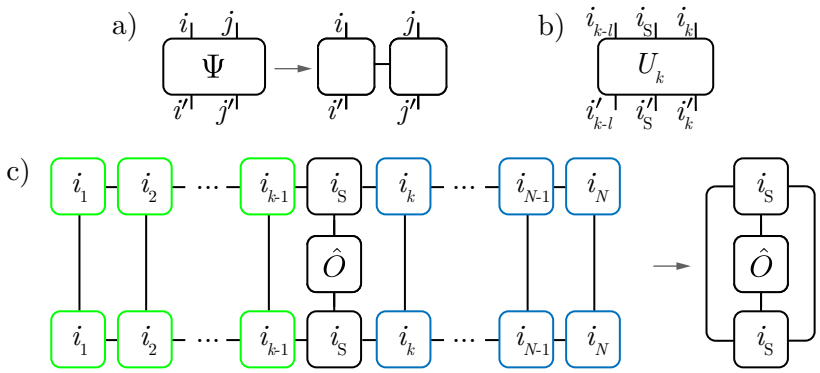

Figure 5.5: Diagrammatic representation of operators in the MPS framework. (a) In analogy to the MPS decomposition, an operator can be decomposed into an MPO where each tensor carries an ingoing and an outgoing index. (b) Diagrammatic representation of the time evolution operator for the TLS inside a semi-infinite waveguide acting on the TLS bin i_S, the current time bin i_k, and on the feedback bin i_{k-l}. (c) Evaluation of the expectation value of the single-site operator $\hat{O}$ acting on the TLS bin, $\langle\psi|\,\hat{O}\,|\psi\rangle$, where due to the construction of the MPS, only the site the operator acts on has to be considered explicitly.

where a time-local description is obtained since each matrix A carries a single physical index and refers either to the emitter or to a particular time bin.

Usually, the coefficient tensor does not have to be decomposed explicitly. If we assume that the emitter and the reservoir are initially separable, we can initialize these subsystems individually. Furthermore, for a reservoir initially in the vacuum state, the time bins are separable among themselves as well so that each time bin can be initialized in the ground state individually. Consequently, there is no entanglement in the system at the beginning of the dynamics. However, the interaction of the light field with the emitter creates entanglement between the emitter and the reservoir as well as between the time bins themselves. This entanglement information between the bins is reflected by their bond dimension, that is, the dimension of their link index, which corresponds to the Schmidt rank of the bipartition. For the separable initial state, all bond dimensions are equal to one at the beginning and grow during the time evolution. Here, the numerical complexity can be reduced by limiting the bond dimension in each SVD performed for the time evolution and setting excess singular values to zero as discussed above, where we, however, have to check for convergence.

5.1.3 Matrix product operators and expectation values

To be able to efficiently evaluate observables as well as to perform the time evolution for an MPS, we need a corresponding formulation for operators. Generalizing the decomposition of an arbitrary state into an MPS, it is possible to decompose an arbitrary operator into a matrix product operator (MPO) by expressing it as a linear combination of projectors and decomposing the associated coefficient tensor. For example, if we consider an operator $\hat{O}$

acting on a bipartite system, it can be written as

$$\hat{O} = \sum_{i',j',i,j} \Psi_{i',j',i,j} \left|i',j'\right\rangle \left\langle i,j\right| = \sum_{i',j',i,j} O^{i',i} O^{j',j} \left|i',j'\right\rangle \left\langle i,j\right|, \tag{5.20}$$

where in the last step, the coefficient tensor $\Psi \equiv \left(\Psi_{i',j',i,j}\right)$ has been decomposed into two matrices via an SVD as illustrated in Fig. 5.5 a. In contrast to the state decomposition, each site now carries two physical indices: an ingoing and an outgoing index. The application of the MPO to an MPS can be realized by performing a bin-wise contraction over their shared indices, where the MPS form is preserved automatically.

At this point, the time-local description of the dynamics in the MPS approach is of great advantage: If we apply an operator that only acts on a limited number of sites, we do not have to calculate its effect on the entire system state but only contract it with the involved bins. This is particularly useful in the case of an operator acting on neighboring sites corresponding to short-range interactions in the condensed matter context. The time evolution operator for our system, consisting of an emitter coupled to a semi-infinite waveguide, as introduced in Eq. (5.8), is illustrated in Fig. 5.5 b. The immediate interaction of the emitter with the light field can be modeled as a short-range interaction. The influence of the feedback signal, however, corresponds to a long-range interaction in time, for the efficient inclusion of which a more complex algorithm is needed that swaps the feedback bin next to the other bins. This swapping algorithm is presented in Sec. 5.1.4.

The MPS approach allows evaluating observables for the emitter as well as for the radiation field efficiently. The expectation value of a single-site operator $\hat{O}$ for a system in the state $\left|\psi\right\rangle$, $\left\langle\psi\right| \hat{O} \left|\psi\right\rangle$, can be calculated as illustrated in Fig. 5.5 c. Note that the complex conjugation of an MPS in the diagrammatic representation corresponds to mirroring the physical indices on the horizontal. If the MPS is in the mixed-canonical gauge with the OC at the site the operator $\hat{O}$ acts on, all tensors to its left are left-normalized so that the contraction with their complex conjugates yields the identity. All tensors to the right of the OC are right-normalized. When contracting them with their complex conjugates, we also obtain the identity by construction of the MPS. Thus, for the evaluation of the expectation value of the operator, it suffices to consider the bin it directly acts on.

5.1.4 Time evolution with matrix product states

Having introduced the basics of the MPS formalism, we now apply it to determine the time evolution for a TLS coupled to a semi-infinite waveguide. As given in Eq. (5.8), the stroboscopic time evolution operator governing the time evolution from time t_k to t_{k+1}, $t_k = k\Delta t$, $k \in \mathbb{N}$, according to $\left|\psi(t_{k+1})\right\rangle = U_k \left|\psi(t_k)\right\rangle$ takes on the form

$$U_k = \exp\left[-\sqrt{\Gamma}\left(\Delta R_k^\dagger \sigma_- - \Delta R_{k-l}^\dagger \sigma_- e^{-i\omega_0 \tau} - \text{H.c.}\right)\right]. \tag{5.21}$$

Here, the operator $\Delta R_k^\dagger$ describes the creation of a photon in the k-th time bin, $\sigma_- = \left|\text{g}\right\rangle \left\langle\text{e}\right|$ is the transition operator of the TLS, which is characterized by the transition frequency ω_0 and the decay rate Γ, and $\tau = l\Delta t$, $l \in \mathbb{N}$, is the feedback delay time. If U_k is applied to the state $\left|\psi(t_k)\right\rangle$ in MPS form, the operator acts on three different bins: The TLS bin (via σ_-), the k-th time bin, that is, the current time bin (via $\Delta R_k^\dagger$), and the $(k-l)$-th time bin, that is, the feedback bin (via $\Delta R_{k-l}^\dagger$).

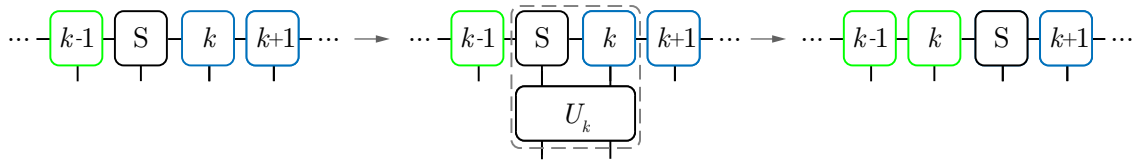

Figure 5.6: Diagrammatic representation of the time evolution in the MPS framework without feedback. The TLS bin S is located to the left of the current time bin k. When performing a time evolution step, the time evolution operator U_k is applied to the TLS bin and the current time bin. The resulting tensor is decomposed and the TLS bin is shifted one step to the right. Thus, after the time evolution step, the former current time bin k is located to the left of the TLS bin and accounts for the emission into the output channel. To the right of the TLS bin, the new current time bin $k+1$ can be found.

If we consider the case of Markovian dynamics inside an infinite waveguide, we can essentially neglect the feedback contribution in Eq. (5.21) so that U_k only acts on the TLS bin and the current time bin. The time evolution algorithm without feedback is illustrated in Fig. 5.6. For the sake of clarity, here, the time bins are labeled with the numbers of the corresponding indices $(1, 2, \ldots, N)$, while the TLS bin is denoted as S. Due to the way we construct the MPS, at the k-th time step, the k-th time bin is located to the right of the TLS bin. Without feedback, we perform the time evolution by simply contracting the TLS bin, the current time bin, and the time evolution operator. Subsequently, we restore the MPS form while shifting the position of the TLS bin one step to the right. The former current time bin, which is positioned to the left of the TLS bin after the time evolution step, accounts for the emission into the output channel. During the time evolution, the OC is kept at the TLS bin. Note that this setup, in principle, corresponds to a chiral waveguide with a unidirectional propagation of light. In the case of a vacuum field in the waveguide, this is equivalent to the case of a bidirectional waveguide with equal coupling strengths to left- and right-propagating modes with an adapted decay rate $\Gamma \to 2\Gamma$. However, if the mirror symmetry about the TLS is broken, either by a quantum pulse encoded in the initial state of the reservoir, see Sec. 5.2, or due to different coupling strengths to left- and right-propagating modes, we have to consider separate channels for left- and right-propagating modes. The implementation in this case works analogously to the case of two TLS coupled to an infinite waveguide as discussed in Chap. 7.

With the feedback mechanism in place, performing the time evolution is a more complex task since long-range interactions in time have to be accounted for. The time evolution algorithm is illustrated in Fig. 5.7. To facilitate the efficient application of the time evolution operator, a swapping algorithm is implemented, which brings the feedback bin to the left of the TLS bin [188]. For this purpose, the feedback bin is contracted with the bin to its right. In the subsequent decomposition, the positions of the two bins are exchanged (Fig. 5.7 a). This procedure is repeated $(l-1)$ times until the feedback bin is situated next to the TLS bin (Fig. 5.7 b). The time evolution operator can then be applied by contracting it with the three bins it acts on (Fig. 5.7 c). The resulting tensor is decomposed via two SVDs. The right bin is the TLS bin, which, as a consequence, is moved one step to the right. The former current time bin is placed to the left of the TLS bin and accounts for the emission into the feedback loop. The former feedback bin represents the emission into the output channel and, after the decomposition, is placed to the left of the former current time bin. It is then swapped back to its original position to restore the correct order of the time

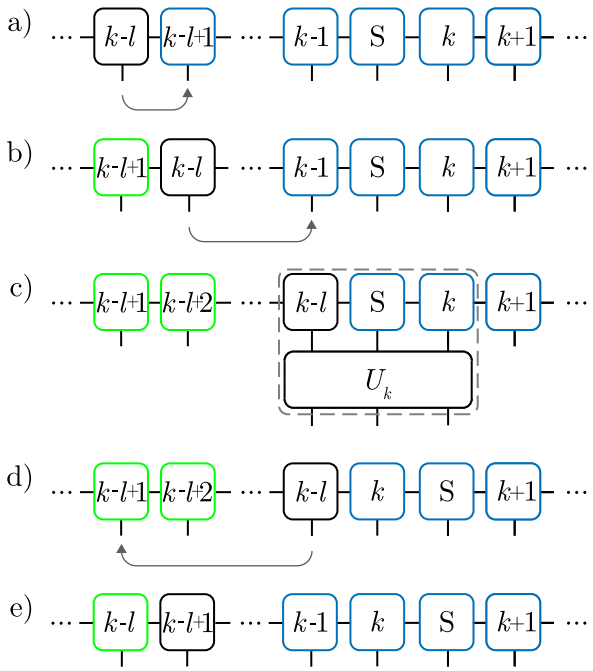

Figure 5.7: Diagrammatic representation of the time evolution in the MPS framework with feedback. (a) The feedback bin $k-l$ is moved one step to the right by swapping the positions of the feedback bin and the bin to its right. (b) The swapping procedure is repeated until the feedback bin is located to the left of the TLS bin S. (c) The time evolution operator U_k is applied to the TLS bin S, the current time bin k, and the feedback bin $k-l$. (d) The resulting tensor is decomposed, and the TLS bin is moved one step to the right. The former current time bin accounting for the emission into the feedback loop is kept to the left of the TLS bin. The former feedback bin is swapped back to its original position to restore the order of the MPS and describes the emission into the output channel. (e) At the end of the time evolution step, the OC is shifted to the new feedback bin $k-l+1$.

bins (Fig. 5.7 d). For the time evolution algorithm with feedback, the OC is kept at the feedback bin unless observables for other bins, for example the TLS bin, are evaluated. In this case, the OC is shifted to the bin under consideration. After one time evolution step is completed, the OC is shifted one step to the right, that is, onto the feedback bin for the next time evolution step (Fig. 5.7 e). Even before the feedback signal itself can influence the dynamics, that is, for $t < \tau$, the interaction of the TLS with the feedback loop has to be accounted for. This is important to ensure a consistent treatment of the dynamics as well as to account for the interaction of the TLS with vacuum noise initially present in the feedback loop. For the numerical implementation, we used the ITensor C++ library [189].

5.2 Modeling quantum pulses

Typically, the TLS (S) and the reservoir (R) are assumed to be initially separable so that the initial state of the entire system can be expressed as

$$|\psi(t_0)\rangle = |i\rangle_{\mathrm{S}} \otimes |\phi_0\rangle_{\mathrm{R}}, \quad i \in \{\mathrm{g}, \mathrm{e}\}. \tag{5.22}$$

Furthermore, it is common to consider a reservoir that, at the beginning, is in the vacuum state, $|\phi_0\rangle_{\mathrm{R}} = |0, \ldots, 0\rangle$. In this case, the bins form a product state and there is no entanglement in the system. As a consequence, each bin can be initialized individually and a numerically expensive decomposition of the initial state into an MPS as discussed in Sec. 5.1.2 is not necessary. Dynamics arise under these circumstances if the TLS is either in the excited state initially ($|i\rangle_{\mathrm{S}} = |\mathrm{e}\rangle_{\mathrm{S}}$) or excited externally, for example by a laser driving the TLS resonantly at frequency $\omega_{\mathrm{L}} = \omega_0$ with amplitude $\Omega(t)$, which can be included by introducing the term

$$H_{\mathrm{L}} = \Omega(t)\,(\sigma_+ + \sigma_-) \tag{5.23}$$

in the interaction picture Hamiltonian given in Eq. (5.1) [53, 55]. If the amplitude can be assumed as constant during one time step, $\Omega(t) \to \Omega_k$, $t \in [t_k, t_{k+1}[$, the time evolution operator given in Eq. (5.8) can be extended to

$$U_k = \exp\left[-i\Omega_k\,(\sigma_+ + \sigma_-)\,\Delta t - \sqrt{\Gamma}\left(\Delta R_k^\dagger \sigma_- - \Delta R_{k-l}^\dagger \sigma_- e^{-i\omega_0 \tau} - \mathrm{H.c.}\right)\right]. \tag{5.24}$$

However, since we pursue a fully quantized and self-consistent description of the light field, we encode the excitation in the initial state of the reservoir so that the TLS is excited by a quantum pulse through the waveguide, as illustrated in Fig. 5.1. For a single-photon pulse, the initial state of the reservoir can be created from the vacuum state according to

$$|\phi_0\rangle_{\mathrm{R}} = a_f^\dagger\,|0, \ldots, 0\rangle, \tag{5.25}$$

where $a_f^\dagger$ is the creation operator of a wave packet with pulse shape $f(t)$ [119]. This pulse shape $f(t)$ has to satisfy the normalization condition

$$\int dt\ |f(t)|^2 = 1. \tag{5.26}$$

The wave packet creation operator $a_f^\dagger$ is a weighted integral over the creation operators $r_t^\dagger$ describing the creation of a photon at time t,

$$a_f^\dagger = \int dt\, f(t) r_t^\dagger. \tag{5.27}$$

An equivalent formulation in frequency space can be obtained using the Fourier transformed coefficients

$$f(\omega) = \frac{1}{\sqrt{2\pi}} \int dt\, f(t) e^{-i(\omega-\omega_0)t}. \tag{5.28}$$

They allow expressing the wave packet creation operator as

$$a_f^\dagger = \int d\omega\, f(w) r_\omega^\dagger. \tag{5.29}$$

The wave packet creation operator satisfies the commutation relation $\left[a_f, a_f^\dagger\right] = 1$ and can be interpreted as the creation operator of a photon in the temporal mode defined by $f(t)$ [190]. Due to the pulse encoded in the reservoir state, the involved time bins, that is, the bins for which there is a finite probability that they contain a photon, are no longer separable but become entangled in the time domain. In the following, we refer to these time bins as pulse bins. For the implementation within the MPS framework, we express the initial state of the reservoir in the time-bin basis assuming the pulse shape to be constant during one time step so that $f(t) = f_k$ for $t \in [\, t_k, t_{k+1}\,[$, $k \in \{1, \ldots, N\}$. This yields the reservoir state

$$|\phi_0\rangle_\mathrm{R} = \sum_{k=1}^{N} f_k \Delta R_k^\dagger \,|0, \ldots, 0\rangle\,. \tag{5.30}$$

As an illustrative example, let us consider a rectangular pulse starting at $t_\mathrm{start} = t_1$ and ending at $t_\mathrm{end} = t_2$. In this case, the reservoir state takes on the form

$$\begin{aligned} |\phi_0\rangle_\mathrm{R} &= \frac{1}{\sqrt{2\Delta t}} \left[\Delta R_1^\dagger + \Delta R_2^\dagger\right] |0, \ldots, 0\rangle \\ &= \frac{1}{\sqrt{2}} \left[|1,0\rangle_{1,2} + |0,1\rangle_{1,2}\right] \otimes |0, \ldots, 0\rangle_{3,\ldots,N}\,, \end{aligned} \tag{5.31}$$

where the subscripts in the second line indicate the associated time bins. From the second line, it is clear that the initial state of the reservoir is no longer a product state. On the contrary, in this example, time bins one and two form a maximally entangled Bell state, see Chap. 4. As a consequence, the pulse bins have to be initialized collectively and subsequently decomposed into the MPS form. For a rectangular single-photon pulse of arbitrary duration, a general formula for the initialization of the pulse bins can be found [191]. To implement a pulse of duration, that is, width $t_\mathrm{D} = M\Delta t$, $M \in \mathbb{N}$, encompassing bins $p_1, p_2, \ldots, p_M$, $p_i \in \mathbb{N}$, $i \in \{1, \ldots, M\}$, the matrices $A[p]^{i_p}$, where p denotes the time step and i_p is the corresponding physical index, are initialized according to

$$A[p_1]^1 = \begin{pmatrix} 1 & 0 \end{pmatrix}, \quad A[p_1]^2 = \begin{pmatrix} 0 & 1 \end{pmatrix}, \tag{5.32}$$

$$A[p_k]^1 = \begin{pmatrix} 1 & 0 \\ 0 & \sqrt{\frac{1}{k}} \end{pmatrix}, \quad A[p_k]^2 = \begin{pmatrix} 0 & \sqrt{\frac{k-1}{k}} \\ 0 & 0 \end{pmatrix}, \tag{5.33}$$

$$A[p_M]^1 = \begin{pmatrix} 0 & \sqrt{\frac{M-1}{M}} \end{pmatrix}^T, \quad A[p_M]^2 = \begin{pmatrix} \sqrt{\frac{1}{M}} & 0 \end{pmatrix}^T \tag{5.34}$$

with $1 < k < M$. Here, we assume time bins of dimension two so that at most one photon per time bin is considered.

After having concentrated on a single photon in the reservoir so far, we now turn to the case of an n-photon pulse. To that end, we generalize the formula for the creation of the reservoir state from the vacuum, Eq. (5.25), to n photons according to

$$|\phi_0\rangle_{\mathrm{R}} = \frac{1}{\sqrt{n!}} \left(a_f^\dagger\right)^n |0,\ldots,0\rangle\,. \tag{5.35}$$

The extension of the example of a rectangular pulse starting at $t_{\mathrm{start}} = t_1$ and ending at $t_{\mathrm{end}} = t_2$ to the case of $n = 2$ photons yields the reservoir state

$$|\phi_0\rangle_{\mathrm{R}} = \frac{1}{\sqrt{4}} \left[|2,0\rangle_{1,2} + |0,2\rangle_{1,2} + \sqrt{2}\,|1,1\rangle_{1,2}\right] \otimes |0,\ldots,0\rangle_{3,\ldots,N}\,. \tag{5.36}$$

For a rectangular two-photon pulse of arbitrary duration, in analogy to the single-photon pulse, an analytical formula can be used to initialize the time bins. In this case, with three-dimensional time bins accounting for up to two photons per bin, the involved matrices take the form

$$A[p_1]^1 = \begin{pmatrix}1 & 0 & 0\end{pmatrix}, \quad A[p_1]^2 = \begin{pmatrix}0 & 1 & 0\end{pmatrix}, \quad A[p_1]^3 = \begin{pmatrix}0 & 0 & 1\end{pmatrix}, \tag{5.37}$$

$$A[p_k]^1 = \begin{pmatrix} 1 & 0 & 0 \\ 0 & \sqrt{\frac{k-1}{k}} & 0 \\ 0 & 0 & \sqrt{\frac{(k-1)^2}{k^2}} \end{pmatrix}, \quad A[p_k]^2 = \begin{pmatrix} 0 & \sqrt{\frac{1}{k}} & 0 \\ 0 & 0 & \sqrt{\frac{2(k-1)}{k^2}} \\ 0 & 0 & 0 \end{pmatrix},$$
$$A[p_k]^3 = \begin{pmatrix} 0 & 0 & \sqrt{\frac{1}{k^2}} \\ 0 & 0 & 0 \\ 0 & 0 & 0 \end{pmatrix}, \tag{5.38}$$

$$A[p_M]^1 = \begin{pmatrix}0 & 0 & \sqrt{\frac{(M-1)^2}{M^2}}\end{pmatrix}^T, \quad A[p_M]^2 = \begin{pmatrix}0 & \sqrt{\frac{2(M-1)}{M^2}} & 0\end{pmatrix}^T,$$
$$A[p_M]^3 = \begin{pmatrix}\sqrt{\frac{1}{M^2}} & 0 & 0\end{pmatrix}^T \tag{5.39}$$

with $1 < k < M$. The extension to three, four, or even more photons is straightforward. The explicit form of the corresponding matrices for three and four photons, as used for the calculations presented in Sec. 5.4, can be found in Appendix A.1. The MPS framework is well suited for the inclusion of a large number of photons due to the efficient handling of the entanglement in the system and, this way, allows surpassing the usual limit of one or two photons. The increase in required computational resources is reflected by an increasing bond dimension as we see below in Sec. 5.4. A possibility to reduce the numerical complexity beyond limiting the bond dimension is limiting the dimension of the time bins, that is, the dimension of the physical indices. In particular, for a pulse encompassing a large number of time bins, that is, for a long pulse duration or in the case of a fine discretization, the probability to find multiple photons per time bin becomes negligibly small.

5.3 Feedback dynamics

Having presented the methodology in the preceding sections, in this section, we look at the resulting dynamics. Here, we concentrate on the TLS and, in particular, evaluate the

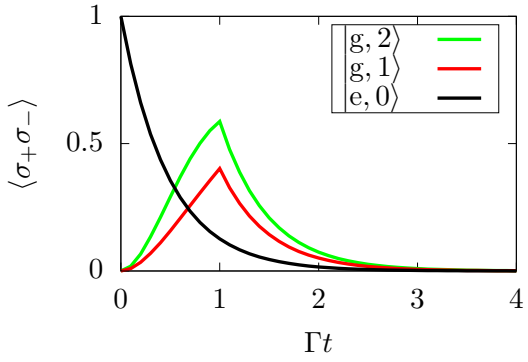

Figure 5.8: Dynamics of the TLS population without feedback for an initially excited emitter decaying in vacuum ($|e,0\rangle$, black line) and for an emitter initially in the ground state subjected to a rectangular pulse of width $\Gamma t_D = 1$ containing a single photon ($|g,1\rangle$, red line) or two photons ($|g,2\rangle$, green line).

expectation value of the occupation operator of its excited state, $\langle\psi(t)|\,\sigma_+\sigma_-\,|\psi(t)\rangle$, also referred to as the TLS population. The MPS framework, moreover, makes the state of the light field directly accessible, which we make use of, for example, in Chap. 8.

Before looking at the non-Markovian dynamics of a TLS coupled to a semi-infinite waveguide, as a reference, we consider the Markovian case of a TLS coupled to an infinite waveguide. The setup is illustrated in Fig. 3.3. Here, however, we treat the light field in a fully quantized manner as indicated by the quantum pulse of shape $f(t)$ in Fig. 5.1. The dynamics we obtain in this case are presented in Fig. 5.8. The initial state of the system is denoted as $|\psi(t_0)\rangle = |i,n\rangle$, where $i \in \{g,e\}$ denotes the state of the emitter and $n \in \{0,1,2\}$ is the number of photons in the reservoir, that is, in the temporal mode defined by the pulse shape $f(t)$. For an initially excited emitter, the population decays exponentially due to the interaction with the vacuum noise in the waveguide (black line). If the emitter is initially in the ground state and excited by a quantum pulse, after the pulse has passed, the emitter decays exponentially to the ground state as well (red line for a single-photon pulse, green line for a two-photon pulse of rectangular shape and width $\Gamma t_D = 1$).

In the case of a semi-infinite waveguide, see Fig. 5.1, the behavior becomes more complex due to the feedback mechanism, which induces memory effects and, thus, renders the dynamics non-Markovian. A signal that is emitted from the TLS toward the mirror returns after the delay time τ. The interference of the emission from the TLS and the feedback signal can strongly modify the dynamics in comparison to the Markovian case. The specific impact of the feedback depends on the phase $\phi \equiv \omega_0\tau$ a resonant photon acquires during one round trip, where ω_0 is the transition frequency of the TLS. An initially excited emitter decays exponentially until, at time $t = \tau$, the feedback mechanism comes into play and either accelerates or slows down the decay, which is illustrated in Fig. 5.9 a. The decay is maximally accelerated for a feedback phase $\phi = (2m+1)\pi$, $m \in \mathbb{N}$ (blue line). The opposite case of a maximally decelerated decay can be observed if $\phi = 2\pi m$ (black line). For this feedback phase, it is even possible to stabilize the TLS at a non-zero steady-state value of the population after a transient time. For all other feedback phases $\phi \neq 2\pi m$, the emitter necessarily decays to the ground state in the long-time limit. In the case of an initially excited emitter, the dynamics are accessible analytically via a solution in the

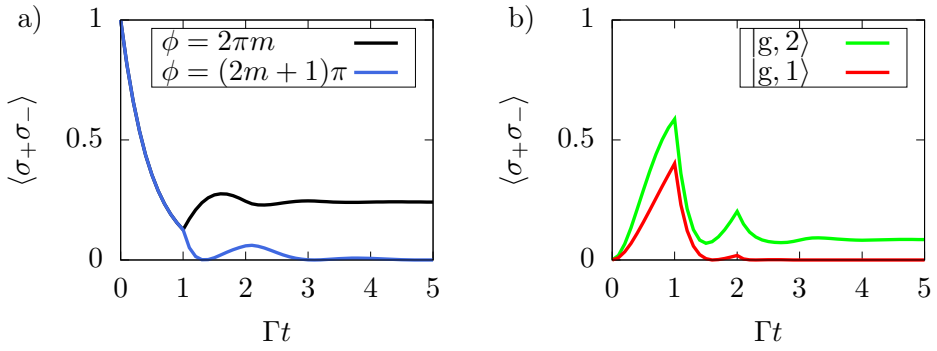

Figure 5.9: Dynamics of the TLS population with feedback at the delay time $\Gamma\tau = 1$. (a) Initially excited emitter subjected to feedback at phase $\phi = (2m+1)\pi$, $m \in \mathbb{N}$, (blue line) and at phase $\phi = 2\pi m$ (black line). (b) Emitter initially in the ground state subjected to feedback at phase $\phi = 2\pi m$. The emitter is excited by a rectangular pulse of width $\Gamma t_\mathrm{D} = 1$ containing a single photon ($|\mathrm{g},1\rangle$, red line) or two photons ($|\mathrm{g},2\rangle$, green line).

Laplace domain, which yields with $|\psi(0)\rangle = |\mathrm{e},0\rangle$ [171, 192]

$$\langle\psi(t)|\,\sigma_+\sigma_-\,|\psi(t)\rangle = |c_\mathrm{e}(t)|^2\,, \quad c_\mathrm{e}(t) = \sum_{k=0}^{\infty} \frac{e^{-\Gamma t}}{k!}\left[\Gamma e^{i\omega_0\tau+\Gamma\tau}\,(t-k\tau)\right]^k \Theta(t-k\tau), \quad (5.40)$$

in accordance with our numerical results. If, instead, the emitter is initially in the ground state and excited by a quantum pulse, the number of photons in the pulse crucially influences the observed behavior. This scenario is illustrated in Fig. 5.9 b, where a feedback phase $\phi = 2\pi m$ is assumed. For a single-photon pulse, the feedback modifies the dynamics (red line). In the long run, however, the TLS decays to the ground state for all values of ϕ. For a pulse containing two or more photons, in contrast, a stabilization of the population is possible (green line).

The stabilization of the TLS population we observe for a feedback phase $\phi = 2\pi m$ can be attributed to the excitation of an atom-photon bound state. In this case, the atom is dressed with a single photon, which is confined to the region between the emitter and the closed end of the waveguide and has a frequency that lies inside the continuum of propagating modes [180]. Bound states are typically observed for frequencies outside the continuum, where the energy cannot be radiated away [193, 194]. Nevertheless, bound states can also be found inside the continuum. Since the imaginary part of the frequency that a state can be associated with corresponds to its leakage rate, these bound states in the continuum can be associated with real frequencies [195].

The atom-photon bound state we observe has the frequency ω_0, which is the same as the transition frequency of the emitter so that the TLS functions as a perfect mirror. The bound state consists of two components: There is an atomic component describing the probability to find the emitter in the excited state and a photonic component associated with the probability to find a photon in the waveguide between TLS and mirror [178]. While, for small separations between the emitter and the mirror, the atomic component dominates, the photonic component becomes more important for increasing separations. Eventually, in the highly non-Markovian regime, where $\Gamma\tau \gg 1$, the photonic component dominates. As we see in Fig. 5.9, there are different excitation schemes for the atom-photon

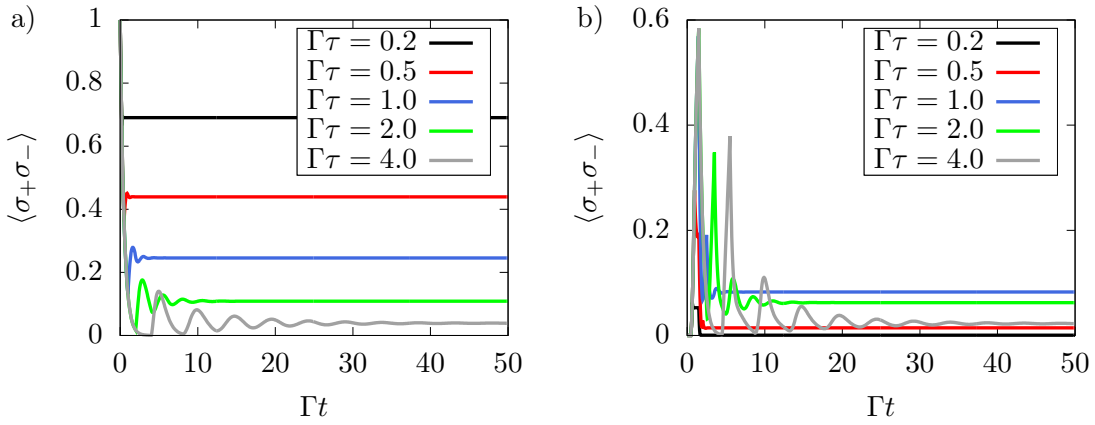

Figure 5.10: Bound-state excitation for different feedback delay times $\Gamma\tau$. (a) Initially excited emitter. (b) Emitter initially in the ground state excited by a rectangular two-photon pulse of width $\Gamma t_\mathrm{D} = 1$.

bound state: The first possibility is letting an initially excited emitter decay in vacuum, while the second possibility is addressing the bound state via multiphoton scattering. In the latter case, it is the intrinsic nonlinearity of the TLS that enables the excitation of the bound state via stimulated emission, which, however, only comes into play if the pulse the emitter is excited by contains at least two photons.

The efficiency of the bound-state excitation depends on the overlap of the initial state of the system with the bound state. Therefore, the specific parameter regime determines which excitation scheme is most efficient. In our investigation, we focus particularly on the steady-state population of the emitter, that is, the atomic component of the bound state, as a measure of the population trapping. Exciting the bound state via the decay of an initially excited emitter is particularly effective in the parameter regime of small separations, $\Gamma\tau < 1$. For this excitation scheme, the steady-state value of the emitter population decreases monotonically with the delay time, see Fig. 5.10 a. The behavior becomes more complex if the bound state is excited by a multiphoton pulse. In this case, the steady-state value of the emitter population depends non-monotonously on the delay time, see Fig. 5.10 b, where a rectangular two-photon pulse of width $\Gamma t_\mathrm{D} = 1$ is considered. A certain minimum separation is crucial for this scheme to work since its efficiency is determined by the overlap of the initial multiphoton state with the photonic component of the bound state. As a consequence, it is interesting to study the impact of the number of photons in a pulse as well as its shape.

5.4 Photon-number dependence of the bound-state excitation

We investigate how the steady-state value at which the emitter population stabilizes when excited by a quantum pulse depends on the number of photons in the pulse. Throughout this section, we assume that a feedback phase $\phi = 2\pi m$, $m \in \mathbb{N}$, is implemented so that the excitation of the atom-photon bound state is possible. Furthermore, we assume a rectangular pulse shape, while the influence of different pulse shapes is the subject of study in Chap. 6.

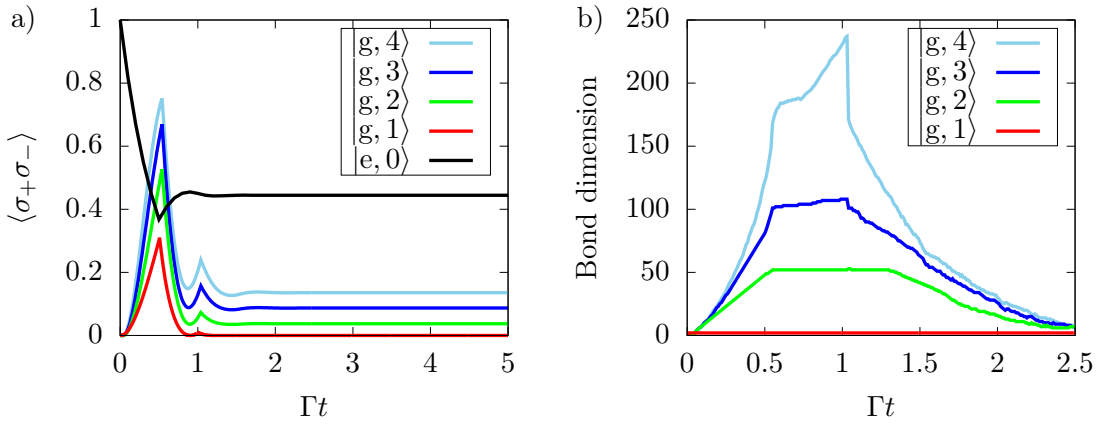

Figure 5.11: TLS subjected to feedback at $\Gamma\tau = 0.5$. (a) Dynamics of the TLS population where the emitter is either initially excited and decays in vacuum ($|e,0\rangle$, black line) or initially in the ground state and excited by a rectangular pulse of width $\Gamma t_D = 0.5$, which contains n photons ($|g,n\rangle$), $n \in \{1,2,3,4\}$. (b) Bond dimension of the time bins in the MPS implementation for an n-photon pulse.

We begin in the regime of medium delay times. For a TLS with $\Gamma\tau = 0.5$ that is excited by rectangular pulses of duration $\Gamma t_D = 0.5$ containing up to four photons, the emitter dynamics that are shown in Fig. 5.11 a can be observed. The behavior for an initially excited emitter decaying spontaneously in vacuum is included for comparison purposes (black line). A single-photon pulse excites the emitter temporarily (red line). Eventually, however, the emitter decays to the ground state. At least two photons in the pulse are essential for the excitation of the atom-photon bound state. In this case, the first photon partially excites the emitter and the scattering of the remaining photons stimulates the population of the atom-photon bound state so that a non-zero steady-state value of the emitter population is possible. For a two-photon pulse, such a non-trivial steady-state value is reached (green line). Increasing the number of photons further to three (dark blue line) and four photons (light blue line), the steady-state value increases, where in the considered parameter regime an approximately linear dependence of the steady-state value on the photon number emerges. When comparing the emitter dynamics for the two excitation schemes, the steady-state population for an initially excited emitter exceeds the value the emitter stabilizes at when excited by the considered multiphoton pulses containing up to four photons. The specific pulse width for the dynamics shown in Fig. 5.11 was chosen since it results in the highest steady-state value possible for the given emitter-mirror separation and a rectangular pulse shape. This observation also holds in general: In the considered parameter range of medium to large separations, the highest steady-state value can be found for pulses satisfying $t_D \lesssim \tau$.

To give an impression of the scaling of the MPS approach with the number of excitations in the pulse, we show the bond dimensions of the time bins for the first five feedback intervals in Fig. 5.11 b. In the MPS framework, the bond dimension functions as a measure of the entanglement between the bins and, this way, quantifies the required computational resources. Here, we did not limit the bond dimension and used $(n+1)$-dimensional time bins for the inclusion of an n-photon pulse to capture the full dynamics. In the case of a single-photon pulse, the maximum value is reached at $t = t_{\text{start}}$ when the pulse begins. For two or three photons in the pulse, the bond dimension is maximum after the first

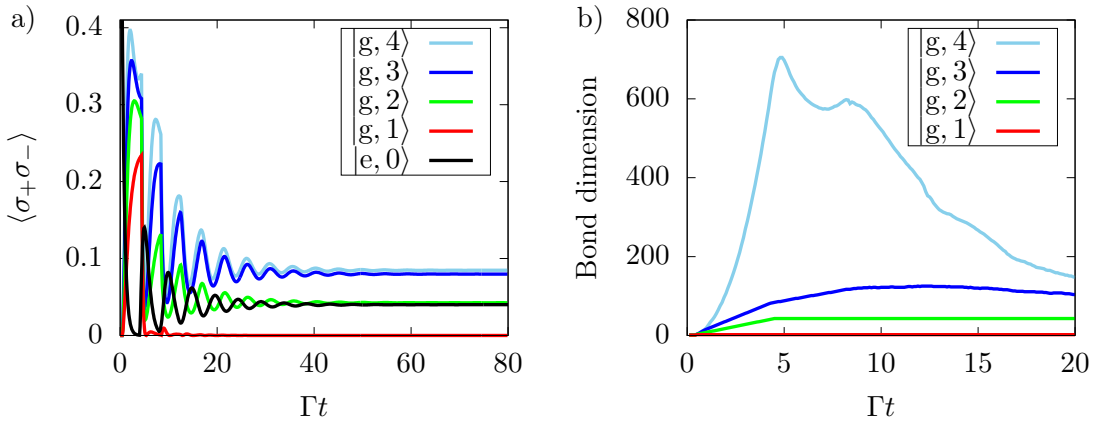

Figure 5.12: TLS subjected to feedback at $\Gamma\tau = 4$. (a) Dynamics of the TLS population where the emitter is either initially excited and decays in vacuum ($|\mathrm{e},0\rangle$, black line) or initially in the ground state and excited by a rectangular pulse of width $\Gamma t_\mathrm{D} = 4$, which contains n photons ($|\mathrm{g},n\rangle$), $n \in \{1,2,3,4\}$. (b) Bond dimension of the time bins in the MPS implementation for an n-photon pulse.

feedback roundtrip time at $t = t_\mathrm{start} + \tau$ before it decreases again later. If a four-photon pulse is considered, the highest bond dimension is found after two feedback intervals at $t = t_\mathrm{start} + 2\tau$.

In the next step, we turn to the highly non-Markovian regime, where $\Gamma\tau \gg 1$. In particular, we consider a system where feedback at the delay time $\Gamma\tau = 4$ is implemented and the emitter is subjected to rectangular pulses of duration $\Gamma t_\mathrm{D} = 4$. This results in the dynamics presented in Fig. 5.12 a. Furthermore, the dynamics for an initially excited emitter are shown. In this parameter regime, the photonic component of the atom-photon bound state dominates, and the excitation via multiphoton scattering is more effective than for small emitter-mirror separations. This opens up a range of possibilities for controlling and specifically maximizing the trapping probability by choosing the number of photons as well as the pulse shape accordingly. For the considered system, a two-photon pulse results in a steady-state population that approximately matches the value an initially excited emitter stabilizes at, $\langle\sigma_+\sigma_-\rangle_\mathrm{st.st.} \equiv \lim_{t\to\infty}\langle\sigma_+(t)\sigma_-(t)\rangle = 0.040$. For an additional photon in the pulse, that is, in the case of a three-photon pulse, we get a result that considerably exceeds this value. A four-photon pulse causes even a slightly higher steady-state population at $\langle\sigma_+\sigma_-\rangle_\mathrm{st.st} = 0.085$, where the dependence of the steady-state value on the photon number is clearly nonlinear. If we compare the two excitation schemes, an increase of about 110 % in the steady-state value of the emitter population is possible if the bound state is excited by multiphoton pulses.

The bond dimensions of the time bins for the calculation of the dynamics in the highly non-Markovian regime are presented in Fig. 5.12 b to allow for an assessment of the required computational resources. Comparing the results to those obtained in the regime of medium delay times shown in Fig. 5.11 b, we see that the scaling of the bond dimensions with the number of photons in the pulse depends critically on the delay time. Thus, in addition to the number of excitations in the system, the emitter-mirror separation has a significant impact on the numerical costs.

5.5 Conclusion

In this chapter, we investigated the non-Markovian feedback dynamics of a two-level emitter coupled to the electromagnetic field in a semi-infinite waveguide focussing, in particular, on the impact of quantum pulses. For the simulation of the time evolution, we employed the MPS framework, which enables the efficient calculation of the feedback dynamics with multiple excitations. We discussed the inclusion of quantum pulses via the initial reservoir state and found an explicit MPS form for them so that no resource-intensive decomposition of the initial state is required.

In the considered system, an atom-photon bound state exists, which can be addressed either via an initially excited emitter decaying in vacuum or via multiphoton scattering. The effectiveness of the schemes depends crucially on the emitter-mirror separation and, thus, on the feedback delay time. For small delay times, the excitation of the bound state via an initially excited emitter is most effective. In the highly non-Markovian regime of large delay times, however, our findings showed that multiphoton pulses allow stabilizing the emitter population at a steady-state value exceeding that of an emitter decaying in vacuum significantly. We considered up to four photons in the pulses and found an increase of 110 % for the system under consideration. The results show that multiphoton pulses are a versatile tool to control the system dynamics and particularly the bound-state excitation, where they induce a stimulated emission process that can enhance the trapping probability in comparison to the spontaneous decay of an initially excited emitter. This way, quantum pulses enable the quantum optical preparation of an excited emitter as well as the realization of tailored trapping scenarios via pulse engineering.

6 Heisenberg treatment of multiphoton pulses in WQED with feedback

Non-Markovian feedback in WQED systems generates strongly entangled system-reservoir states, for which perturbative and master equation methods typically used for Markovian systems fail to capture the essential features of the dynamics, as discussed in Chap. 5. To deal with such systems, over the last years, different approaches have been developed: While it is, in principle, possible to perform a brute-force integration of the full Schrödinger equation [43, 196], this procedure is only feasible for a very limited number of excitations and short times. A more complex approach is based on the evaluation of the Von-Neumann equation, where a series of cascaded quantum systems accounts for the system being driven by a past version of itself [52]. Although this insightful method has been pioneering, it is only applicable to small systems and short-time dynamics because it scales with the exponentially growing dimension of the corresponding Liouvillian. Additionally, the compatibility of the method with factorization schemes is questionable due to the complicated construction of the Liouvillian. Another sophisticated method relies on solving the quantum stochastic Schrödinger equation within the MPS framework [53], as introduced in Chap. 5. The approach allows for long-time simulations and fast convergence times as well as the inclusion of several excitations due to the efficient handling of the entanglement in the system. It is, however, intrinsically limited to unitary evolutions and the exact treatment of additional Hamiltonian-based interactions. Furthermore, the required memory cannot be determined beforehand since the number of necessary Schmidt values is not known without a convergence analysis. Recently, another approach for the study of WQED systems with coherent time-delayed feedback has been proposed that makes use of quantum trajectory simulations in a space-discretized waveguide [55, 197].

Complementing these existing methods and, especially, as a readily accessible alternative to the intricate MPS method employed in Chap. 5, in this chapter, we present a method for the numerically exact simulation of non-Markovian feedback dynamics in WQED systems within a Heisenberg representation. The method gives access to the microscopic dynamics and allows including dissipation channels, where approximation methods can be applied without losing exactness in the coherent quantum feedback dynamics. As an exemplary system, in analogy to Chap. 5, we consider a TLS coupled to a semi-infinite waveguide excited by quantum pulses. To unravel the hierarchy of multi-time correlations arising for the Heisenberg equations due to the non-Markovianity of the system [30], a projection onto a complete set of states in the Hilbert space is performed. The work presented here is based on our publication in Ref. [198]. We start in Sec. 6.1 by introducing the Heisenberg approach, the validity of which is verified by the benchmarks of the dynamics presented in Sec. 6.2. As an illustration of the capabilities of the method, we study the impact of multiphoton pulses of variable shape in Sec. 6.3 and include a phenomenological pure dephasing as an additional dissipation channel in Sec. 6.4.

6.1 Heisenberg-operator approach

We introduce the method that allows calculating the exact feedback dynamics in WQED systems with quantum pulses within a Heisenberg representation using the paradigmatic example of the TLS coupled to a semi-infinite waveguide as considered in Chap. 5 and depicted in Fig. 5.1. The interaction-picture Hamiltonian describing the system, as stated in Eq. (5.1), reads

$$H_{\mathrm{I}} = \int d\omega\, \hbar \left[g(\omega) r_\omega^\dagger \sigma_- e^{i(\omega-\omega_0)t} + \mathrm{H.c.} \right] \tag{6.1}$$

with the bosonic photon annihilation (creation) operator $r_\omega^{(\dagger)}$ and the transition operators of the TLS $\sigma_- = |\mathrm{g}\rangle\langle \mathrm{e}|$ and $\sigma_+ = |\mathrm{e}\rangle\langle \mathrm{g}| = \sigma_-^\dagger$. The TLS is characterized by its transition frequency ω_0 and couples to the photonic reservoir with coupling strength $g(\omega) = g_0 \sin(\omega\tau/2)$ accounting for the implemented feedback mechanism at the delay time τ as introduced in Sec. 5.1.

In order to study the dynamics of the system, we use the Heisenberg equation of motion, see Eq. (2.7), and derive differential equations for the relevant time-dependent system operators $\sigma_-(t)$ and $r_\omega(t)$. This way, we obtain the coupled equations

$$\frac{\mathrm{d}}{\mathrm{d}t}\sigma_-(t) = -i \int d\omega\, g(\omega) e^{-i(\omega-\omega_0)t} \left[\mathbb{1} - 2\sigma_+(t)\sigma_-(t) \right] r_\omega(t), \tag{6.2}$$

$$\frac{\mathrm{d}}{\mathrm{d}t} r_\omega(t) = -i g(\omega) e^{i(\omega-\omega_0)t} \sigma_-(t). \tag{6.3}$$

Since the focus lies on the dynamics of the emitter, it is justified to eliminate the explicit reservoir dynamics. To that end, the reservoir operators can be integrated out, which yields

$$r_\omega(t) = r_\omega(0) - i g(\omega) \int_0^t dt'\, e^{i(\omega-\omega_0)t'} \sigma_-(t'). \tag{6.4}$$

This shows that the occupation of the reservoir modes depends on the interaction with the TLS as well as on the initial occupation of the reservoir. As we saw in Chap. 5, a quantum pulse can be modeled via this initial occupation of the reservoir. To be able to express the quantum pulse in the time domain, a Fourier transform of the initial reservoir operators is performed yielding quantum noise operators as introduced in Chap. 5, see Eq. (5.4),

$$r_t = \frac{1}{\sqrt{2\pi}} \int d\omega\, r_\omega(0) e^{-i(\omega-\omega_0)t}. \tag{6.5}$$

The operator r_t describes the annihilation of a photon at time t and allows an interpretation as an input operator in the context of the input-output theory [115, 199]. Subsequently, with the decay rate $\Gamma = \pi g_0^2/2$, the differential equation for the TLS operator σ_- can be expressed as

$$\begin{aligned} \frac{\mathrm{d}}{\mathrm{d}t}\sigma_-(t) = &-\Gamma\sigma_-(t) - \sqrt{\Gamma}\left[\mathbb{1} - 2\sigma_+(t)\sigma_-(t)\right] r_{t,\tau} \\ &+ \Gamma e^{i\omega_0\tau} \left[\sigma_-(t-\tau) - 2\sigma_+(t)\sigma_-(t)\sigma_-(t-\tau)\right] \Theta(t-\tau), \end{aligned} \tag{6.6}$$

where the delayed input operator

$$r_{t,\tau} \equiv r_{t-\frac{\tau}{2}} e^{i\omega_0\frac{\tau}{2}} - r_{t+\frac{\tau}{2}} e^{-i\omega_0\frac{\tau}{2}} \tag{6.7}$$

has been introduced. The first line on the right-hand side of Eq. (6.6) accounts for the immediate interaction of the emitter with the light field, where the first term describes the decay of the emitter excitation due to spontaneous emission and the second term the interaction of the emitter with potential excitations in the reservoir. The second line, in turn, arises due to the feedback mechanism and only comes into play for times $t \geq \tau$, where the feedback signal interferes with the emission from the TLS, the impact of which is determined by the feedback phase $\phi = \omega_0 \tau$.

In the next step, we evaluate the TLS population, that is, the expectation value of the occupation operator of its excited state, $\langle\psi|\, \sigma_+(t)\sigma_-(t)\, |\psi\rangle$. The initial state $|\psi\rangle$ is the combined state of the TLS and the reservoir. For simplicity, we assume that the TLS and the reservoir are initially separable so that $|\psi\rangle = |j\rangle \otimes |n\rangle \equiv |j,n\rangle$ although the method is not limited to this class of states. It is also applicable in the case of entangled states and can, furthermore, be extended to incorporate mixed states. The state $|j\rangle$ denotes the state of the TLS, that is, either the ground ($|j\rangle = |\mathrm{g}\rangle$) or the excited state ($|j\rangle = |\mathrm{e}\rangle$), while $|n\rangle$ describes n photons in the reservoir, $n \in \mathbb{N}$. To obtain the n-photon state from the vacuum, the wave packet creation operator $a_f^\dagger$ of a photon in the temporal mode defined by the normalized pulse shape $f(t)$ is employed, which, as introduced in Sec. 5.2, satisfies

$$a_f^\dagger = \int dt\, f(t) r_t^\dagger, \quad \int dt\, |f(t)|^2 = 1. \tag{6.8}$$

Its n-fold application yields the n-photon state according to

$$|j,n\rangle = \frac{1}{\sqrt{n!}} \left(a_f^\dagger\right)^n |j,0\rangle\,. \tag{6.9}$$

To calculate the TLS population, as a consequence, the differential equation

$$\begin{aligned}\frac{\mathrm{d}}{\mathrm{d}t} \langle j,n|\, \sigma_+(t)\sigma_-(t)\, |j,n\rangle &= -2\Gamma \langle j,n|\, \sigma_+(t)\sigma_-(t)\, |j,n\rangle \\ &\quad - \sqrt{n\Gamma}\, [f_\tau^*(t) \langle j,n-1|\, \sigma_-(t)\, |j,n\rangle + \mathrm{H.c.}] \\ &\quad + \Gamma \left[e^{-i\omega_0\tau} \langle j,n|\, \sigma_+(t-\tau)\sigma_-(t)\, |j,n\rangle + \mathrm{H.c.}\right] \Theta(t-\tau)\end{aligned} \tag{6.10}$$

has to be solved, where $f_\tau(t)$ denotes the delayed pulse defined as

$$f_\tau(t) \equiv f\left(t - \frac{\tau}{2}\right) e^{i\omega_0 \frac{\tau}{2}} - f\left(t + \frac{\tau}{2}\right) e^{-i\omega_0 \frac{\tau}{2}}. \tag{6.11}$$

The expectation value in Eq. (6.10) couples to the single-time matrix element of the TLS operator $\langle g,n-1|\, \sigma_-(t)\, |g,n\rangle$, which, in turn, obeys the differential equation

$$\begin{aligned}\frac{\mathrm{d}}{\mathrm{d}t} \langle j,n-1|\, \sigma_-(t)\, |j,n\rangle &= -\Gamma \langle j,n-1|\, \sigma_-(t)\, |j,n\rangle \\ &\quad - \sqrt{n\Gamma} f_\tau(t) \left[1 - 2\langle j,n-1|\, \sigma_+(t)\sigma_-(t)\, |j,n-1\rangle\right] \\ &\quad + \Gamma e^{i\omega_0\tau} \left[\langle j,n-1|\, \sigma_-(t-\tau)\, |j,n\rangle - 2\langle j,n-1|\, \sigma_+(t)\sigma_-(t)\sigma_-(t-\tau)\, |j,n\rangle\right] \\ &\quad \times \Theta(t-\tau).\end{aligned} \tag{6.12}$$

Before the feedback mechanism sets in, that is, for times $t < \tau$, we obtain time-local and, therefore, essentially Markovian dynamics since the time-delayed feedback terms do not yet contribute as ensured by $\Theta(t-\tau)$. In this case, the dynamics for n photons in the

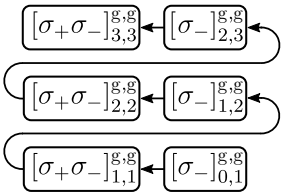

Figure 6.1: Scheme of the contributing matrix elements for the dynamics without feedback for three photons in the reservoir initially. Here, the abbreviation $[A]^{i,j}_{m,n}$ denotes the matrix element $\langle i,m|\, A(t)\, |j,n\rangle$.

reservoir can be calculated recursively using the results for $n-1$ photons [181, 200]. The differential equations that have to be solved in this case are

$$\frac{\mathrm{d}}{\mathrm{d}t}\langle g,n|\,\sigma_+(t)\sigma_-(t)\,|g,n\rangle = -2\Gamma\,\langle g,n|\,\sigma_+(t)\sigma_-(t)\,|g,n\rangle - \sqrt{n\Gamma}\,[f^*_\tau(t)\,\langle g,n-1|\,\sigma_-(t)\,|g,n\rangle + \mathrm{H.c.}]\,, \tag{6.13}$$

$$\frac{\mathrm{d}}{\mathrm{d}t}\langle g,n-1|\,\sigma_-(t)\,|g,n\rangle = -\Gamma\,\langle g,n-1|\,\sigma_-(t)\,|g,n\rangle - \sqrt{n\Gamma}\,f_\tau(t)\,[1-2\,\langle g,n-1|\,\sigma_+(t)\sigma_-(t)\,|g,n-1\rangle]\,. \tag{6.14}$$

The matrix elements relevant for a TLS initially in the ground state and a pulse containing up to three photons are exemplarily sketched in Fig. 6.1. In the figure, the abbreviation $[A]^{i,j}_{m,n}$ denotes the matrix element $\langle i,m|\, A(t)\, |j,n\rangle$. Thus, to determine the TLS population for three photons in the reservoir initially, the results for two photons and for one photon have to be determined.

When feedback effects influence the dynamics, that is, for times $t \geq \tau$, the time-delayed feedback terms in Eqs. (6.10) and (6.12) become relevant and the single-time correlations couple to two-time correlations. In general, these two-time correlations couple to three-time correlations and so on. To deal with this hierarchical structure and obtain a closed set of differential equations, we unravel the multi-time correlations via the insertion of a unity operator between the operators with different time arguments. This unity operator is a projector onto a complete set of states in the Hilbert space of the TLS and the photonic reservoir. With the reservoir in the time domain, it takes the form

$$\mathbb{1} = \{\,|\mathrm{g}\rangle\langle\mathrm{g}| + |\mathrm{e}\rangle\langle\mathrm{e}|\,\} \otimes \left\{\,|0\rangle\langle 0| + \int dt'\,|t'\rangle\langle t'| + \frac{1}{2}\int dt'\int dt''\,|t',t''\rangle\langle t',t''| + \ldots\right\}. \tag{6.15}$$

The variables t' and t'' are, in general, assumed to run from $-\infty$ to $+\infty$. For readability, however, the bounds of integration for the unity operator are omitted here and in the following. The reservoir state $|t'\rangle$ denotes a single photon in the reservoir, created at time t', $|t'\rangle = r^\dagger_{t'}|0\rangle$. The state $|t',t''\rangle$ describes two photons in the reservoir, created at t' and t'', respectively, $|t',t''\rangle = r^\dagger_{t'}r^\dagger_{t''}|0\rangle$, and so on. Since the photons are indistinguishable, the factor $1/2$ ensures normalization. In general, for n photons in the reservoir, the factor $1/(n!)$ is required. With the insertion of the unity operator from Eq. (6.15) between operators at different times when evaluating Eqs. (6.10) and (6.12), the explicit calculation of multi-time correlations with time-ordering can be avoided. Instead, the problem is

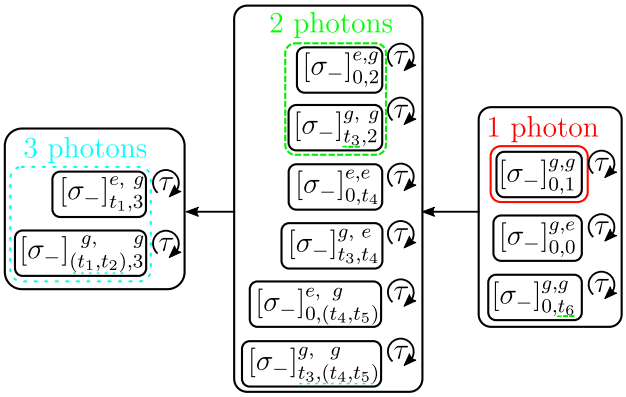

Figure 6.2: Scheme of the contributing matrix elements for the dynamics with feedback. The abbreviation $[A]^{i,j}_{m,n}$ denotes the matrix element $\langle i,m|\,A(t)\,|j,n\rangle$. When decomposing the expectation value of the TLS occupation, the matrix elements in the colored boxes have to be calculated and saved. The elements can be calculated recursively where, however, additionally the matrix elements outside the colored boxes couple to the dynamics. The underlined time variables indicate the scaling of the algorithm for the corresponding number of photons since they have to be integrated over and determine the required computational resources.

shifted to the calculation of matrix elements of single-time Heisenberg operators. If we additionally insert the unity operator between operators at the same time, in particular, in between $\sigma_+(t)\sigma_-(t)$, we only have to deal with matrix elements of the operator σ_- for the calculation of the TLS dynamics.

In principle, an infinite number of matrix elements has to be calculated when inserting the unity operator to account for all possible numbers of photons in the reservoir. It depends, however, on the number of excitations in the system which elements effectively contribute to the dynamics. We study which matrix elements have to be evaluated and, thus, which resources are needed for the calculation depending on the initial state of the system. For simplicity, we focus on the case of a TLS initially in the ground state and all excitations in the reservoir, while the extension to an initially excited TLS is straightforward.

As a first step, we decompose the expectation value of the TLS population according to

$$\langle \mathrm{g},n|\,\sigma_+(t)\sigma_-(t)\,|\mathrm{g},n\rangle = \langle \mathrm{g},n|\,\sigma_+(t)\mathbb{1}\sigma_-(t)\,|\mathrm{g},n\rangle \tag{6.16}$$

to determine the contributing matrix elements as well as to obtain a way to benchmark the decomposition. We find that only matrix elements of the form $\langle\psi_{n-1}|\,\sigma_-(t)\,|g,n\rangle$ contribute to the dynamics, where $|\psi_{n-1}\rangle$ denotes a state comprising $n-1$ excitations. The state $|\psi_{n-1}\rangle$ can describe either the TLS in the excited state and $n-2$ excitations in the reservoir or the TLS in the ground state and $n-1$ excitations in the reservoir. As a consequence, only projectors onto such states $|\psi_{n-1}\rangle$ have to be taken into account in the unity operator. Using this property, we decompose all matrix elements in such a way that we only have to deal with single-time correlations of the operator σ_-.

Analogous to the case without feedback, the results with feedback for n photons in the reservoir can be calculated recursively using the results for $n-1$ photons. Due to the feedback mechanism, however, further matrix elements have to be evaluated as sketched in Fig. 6.2 for up to three photons in the reservoir. Correspondingly, we outline the approach,

starting with a single photon and progressing to two and three photons in the pulse. Higher numbers of photons can then be treated similarly. The explicit differential equations can be found in Appendix A.2.

For a single excitation in the reservoir, we only have to consider the projector onto the state $|g,0\rangle$ describing zero excitations in the system when inserting the unity operator for the evaluation of the TLS population. Therefore, it can be decomposed according to

$$\langle \mathrm{g},1|\,\sigma_+(t)\sigma_-(t)\,|\mathrm{g},1\rangle = \langle \mathrm{g},1|\,\sigma_+(t)\,|\mathrm{g},0\rangle\,\langle \mathrm{g},0|\,\sigma_-(t)\,|\mathrm{g},1\rangle\,. \tag{6.17}$$

This case is represented by the red, solid box in Fig. 6.2. We have to determine a single matrix element and store the past elements up to $t-\tau$ to account for the feedback. The computational resources that are required for the calculation of the dynamics accordingly grow linearly with the number of time steps T, $\mathcal{O}(T)$.

In the case of a two-photon pulse, the elements that describe a single excitation in the system, either in the TLS or in the reservoir, contribute when inserting the unity operator. As a consequence, decomposing the corresponding expectation value yields

$$\begin{aligned}\langle \mathrm{g},2|\,\sigma_+(t)\sigma_-(t)\,|\mathrm{g},2\rangle = {}& \langle \mathrm{g},2|\,\sigma_+(t)\,|\mathrm{e},0\rangle\,\langle \mathrm{e},0|\,\sigma_-(t)\,|\mathrm{g},2\rangle \\ & + \int dt'\,\langle \mathrm{g},2|\,\sigma_+(t)\,|\mathrm{g},t'\rangle\,\langle \mathrm{g},t'|\,\sigma_-(t)\,|\mathrm{g},2\rangle\,. \end{aligned}\tag{6.18}$$

Note that times t' for which $f(t')=0$ cannot be omitted in the integral. Although there is no pulse contribution from these terms, they can still yield a noise contribution. In particular, negative times $t'<0$ have to be considered accounting for the vacuum noise initially in the feedback channel. In Fig. 6.2, this scenario is represented by the green dashed box. For the calculation of the dynamics, as indicated by the green dashed underlined times, two nested integrations have to be performed in each time step. The required computational resources for two excitations in the system, thus, grow with the number of time steps to the power of three, $\mathcal{O}\left(T^3\right)$.

If a three-photon pulse is assumed, all elements describing two excitations in the system contribute when inserting the unity operator. The decomposition of the expectation value of the TLS population, therefore, results in

$$\begin{aligned}\langle \mathrm{g},3|\,\sigma_+(t)\sigma_-(t)\,|\mathrm{g},3\rangle = {}& \int dt'\,\langle \mathrm{g},3|\,\sigma_+(t)\,|\mathrm{e},t'\rangle\,\langle \mathrm{e},t'|\,\sigma_-(t)\,|\mathrm{g},3\rangle \\ & + \frac{1}{2}\int dt' \int dt''\,\langle \mathrm{g},3|\,\sigma_+(t)\,|\mathrm{g},t',t''\rangle\,\langle \mathrm{g},t',t''|\,\sigma_-(t)\,|\mathrm{g},3\rangle\,. \end{aligned}\tag{6.19}$$

Here, the indistinguishability of the photons has to be taken into account. The case is represented by the turquoise dotted box in Fig. 6.2. The turquoise dotted underlined variables indicate the scaling. As five time variables have to be integrated over, the required resources grow with the number of time steps to the power of six, $\mathcal{O}\left(T^6\right)$.

6.2 Benchmark of the dynamics

We perform a benchmark of the dynamics to verify the validity of our Heisenberg approach. To solve the differential equations for the relevant matrix elements, we employ a Runge-Kutta algorithm. First, we consider the case before feedback sets in, that is, for $t<\tau$,

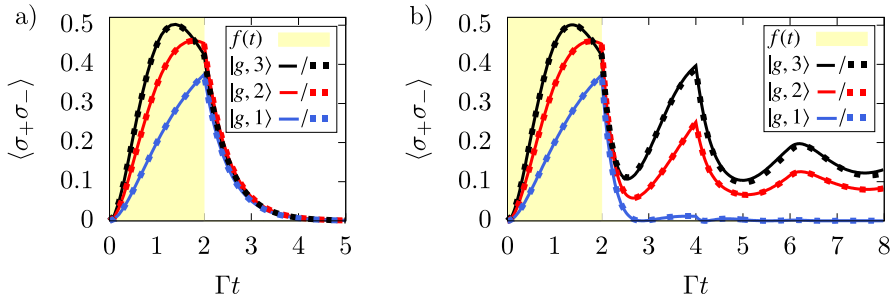

Figure 6.3: Benchmark for the TLS population with the initial state $|g, n\rangle$ as a function of time. The TLS is excited by a rectangular pulse of duration $\Gamma t_D = 2$ (yellow shaded area) containing n photons, $n \in \{1, 2, 3\}$. (a) Benchmark for the decomposition of the expectation value before feedback sets in, where the expectation value is calculated either directly (solid lines) or using the decomposition via the insertion of the unity operator (dashed lines). (b) Benchmark for the feedback dynamics with feedback at the delay time $\Gamma\tau = 2$ and the phase $\phi = 2\pi m$, $m \in \mathbb{N}$, where the results are obtained employing the MPS framework (solid lines) or using the proposed Heisenberg method (dashed lines).

where the dynamics can be calculated recursively, see Eqs. (6.13) and (6.14). In this regime, we compare the results obtained from the direct calculation with those obtained after decomposing the expectation value via the insertion of the unity operator. In Fig. 6.3 a, the dynamics for a TLS excited by a rectangular pulse of duration $\Gamma t_D = 2$ (yellow shaded area) containing up to three photons are shown. The results obtained from the direct calculation (solid lines) and the results for the decomposition of the expectation values (dashed lines) coincide perfectly suggesting the correctness of the decomposition.

Including later times, $t \geq \tau$, where feedback influences the dynamics, the expectation values can no longer be calculated directly. To benchmark the results we obtain with feedback, we employ the MPS framework as discussed in Chap. 5. In Fig. 6.3 b, the dynamics for a TLS excited by a rectangular pulse of duration $\Gamma t_D = 2$ (yellow shaded area) containing up to three photons are shown, where the TLS is subjected to feedback at the delay time $\Gamma\tau = 2$ and the feedback phase $\phi = \omega_0\tau = 2\pi m$, $m \in \mathbb{N}$. The results obtained using the MPS framework (solid lines) and the results of the Heisenberg method (dashed lines) agree perfectly indicating the validity of the latter approach for the calculation of the non-Markovian feedback dynamics.

6.3 Pulse-shape dependence of the bound-state excitation

In Sec. 5.3, we studied the feedback dynamics that can be observed for a TLS coupled to a semi-infinite waveguide. In this system, if a feedback phase $\phi = \omega_0\tau = 2\pi m$, $m \in \mathbb{N}$, is implemented, multiphoton pulses can induce the population of an atom-photon bound state, where the efficiency of the excitation scheme depends on the feedback delay time as well as on the pulse properties. The investigation in Sec. 5.4 using MPS showed that the number of photons in the pulse strongly influences the excitation probability of the bound state. In this section, we explore the pulse shape as an additional way of controlling the system dynamics and, in particular, the bound state excitation. While the MPS method is well suited to account for multiple excitations in the system, the Heisenberg method

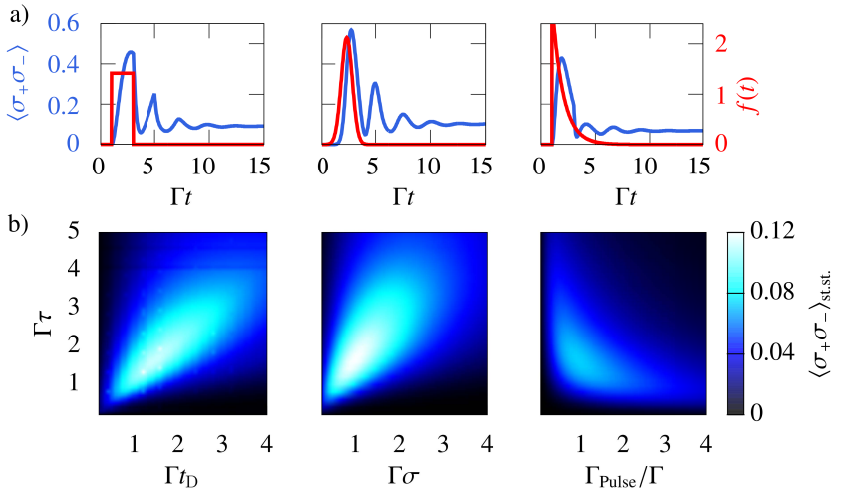

Figure 6.4: Excitation of the atom-photon bound state via two-photon pulses. (a) TLS population as a function of time (blue lines) for a TLS with feedback at $\Gamma\tau = 2$ and $\phi = 2\pi m$, $m \in \mathbb{N}$, excited via a two-photon pulse of shape $f(t)$ (red lines). From left to right: Rectangular pulse with $\Gamma t_\mathrm{D} = 2$, Gaussian pulse with $\Gamma\sigma = 1$, exponentially decaying pulse with $\Gamma_\mathrm{Pulse}/\Gamma = 1$. (b) Steady-state value of the TLS population as a function of the width of the pulse and the feedback delay time, τ. From left to right: Rectangular pulse with duration t_D, Gaussian pulse with width σ, exponentially decaying pulse with decay rate Γ_Pulse.

has the advantage that it makes the inclusion of arbitrary pulse shapes significantly more convenient via the choice of $f(t)$.

In Fig. 6.4, the results for a TLS subjected to feedback at $\phi = 2\pi m$ and excited by two-photon pulses of different shapes are presented. The first considered pulse shape is a rectangular pulse shape characterized by $f(t) = A\Theta(t - t_0)\Theta(t_0 + t_\mathrm{D} - t)$, where A is a constant ensuring that the normalization condition $\int dt\,|f(t)|^2 = 1$ is fulfilled, t_0 is the starting point, and t_D is the duration of the pulse. Furthermore, a Gaussian pulse is applied with $f(t) = A\exp\left[-(t-\mu)^2/(2\sigma^2)\right]$, where A again is a normalization constant, μ is the offset of the pulse, and σ determines its width. Finally, the emitter is subjected to an exponentially decaying pulse, where $f(t) = A\Theta(t - t_0)\exp\left[-\Gamma_\mathrm{Pulse}(t - t_0)\right]$ with normalization constant A, starting point t_0, and decay constant Γ_Pulse. Fig. 6.4 a shows the dynamics of the TLS population (blue lines) for two-photon pulses of different pulse shapes $f(t)$ (red lines) in the case of feedback at the delay time $\Gamma\tau = 2$. The considered pulse shapes are a rectangular pulse with $\Gamma t_\mathrm{D} = 2$, a Gaussian pulse with $\Gamma\sigma = 1$, and an exponentially decaying pulse with $\Gamma_\mathrm{Pulse}/\Gamma = 1$ (from left to right). For all considered pulse shapes, the TLS is excited and, after a transient time, stabilizes at a non-zero steady-state population, which points to the excitation of the atom-photon bound state. The steady-state population $\langle\sigma_+\sigma_-\rangle_\mathrm{st.st.} \equiv \lim_{t\to\infty}\langle \mathrm{g},2|\,\sigma_+(t)\sigma_-(t)\,|\mathrm{g},2\rangle$ for the different pulse shapes as a function of the width of the pulse and the feedback delay time is presented in Fig. 6.4 b. In the results, the non-monotonous dependence of the steady-state population on the delay time can be observed. Furthermore, it can be seen that there is a complex interplay between the feedback delay time and the pulse shape that determines the effectiveness of the bound state excitation.

6.4 Additional dissipation channel

As discussed in Sec. 3.3, a realistic quantum system can never be completely isolated. Instead, the interaction with its larger environment introduces energy dissipation and decoherence in the system dynamics. For example, if WQED setups are realized using a solid-state platform where semiconductor quantum dots function as the emitters, the interaction of the emitters with the surrounding host material plays a crucial, often non-negligible role rendering the dynamics effectively non-unitary [51, 201–206]. For the corresponding theoretical description, the Heisenberg method is ideally suited since it makes the microscopic dynamics accessible and allows for the inclusion of additional exactly or perturbatively treated dissipation channels.

As an exemplary dissipation channel, we include a phenomenological pure dephasing at rate γ and study its impact on the emitter dynamics. Pure dephasing dephases coherences, while it does not directly influence populations. For its inclusion, we, therefore, treat the TLS coherence operator σ_- and the TLS population $E \equiv \sigma_+\sigma_-$ separately and introduce pure dephasing in the equations for the matrix elements of the coherence operator as an additional Markovian, Lindblad-type decay channel. In this model, for example, the matrix element $\langle \mathrm{g}, 0| \sigma_-(t) |\mathrm{g}, 1\rangle$, which has to be calculated to describe a single-photon pulse in the reservoir, obeys the differential equation

$$\frac{\mathrm{d}}{\mathrm{d}t} \langle g, 0| \sigma_-(t) |g, 1\rangle = -(\Gamma + \gamma) \langle g, 0| \sigma_-(t) |g, 1\rangle - \sqrt{\Gamma} f_\tau(t) + \Gamma e^{i\omega_0 \tau} \langle g, 0| \sigma_-(t-\tau) |g, 1\rangle \Theta(t-\tau). \quad (6.20)$$

For more details on the inclusion of pure dephasing see Appendix A.3.

The results for the emitter dynamics in the case of feedback implemented at $\Gamma\tau = 1.2$ are shown in Fig. 6.5, where different scenarios are considered. An initially excited emitter decaying in vacuum is not affected by pure dephasing before the feedback signal returns to the emitter as can be seen in Fig. 6.5 a. Only for $t \geq \tau$, pure dephasing comes into play as it influences the interference between the TLS emission and the feedback signal. In the setup, a feedback phase $\phi = \omega_0\tau = 2\pi m$, $m \in \mathbb{N}$, is implemented, where without pure dephasing the stabilization of the emitter excitation can be observed. For $\gamma > 0$, however, the stabilization becomes impossible and the emitter decays necessarily to the ground state, where it holds that the higher the dephasing rate, the faster the decay.

The stabilization of the excitation can, in principle, also be observed in the case of a multiphoton pulse exciting a TLS initially in the ground state if it holds that $\phi = 2\pi m$. It is, thus, interesting to study the effect of pure dephasing under such circumstances. The results for the case of a rectangular two-photon pulse of duration $\Gamma t_\mathrm{D} = 1$ and different pure dephasing rates γ are illustrated in Fig. 6.5 b. In contrast to the previous case of an initially excited emitter decaying in vacuum, with a quantum pulse in the system, pure dephasing already influences the dynamics for $t < \tau$ and manifests in a reduced excitation efficiency of the emitter. The higher the dephasing rate in relation to the pulse width, the less effective the excitation as pure dephasing counteracts the build-up of coherence. Furthermore, the atom-photon bound state becomes inaccessible with pure dephasing so that the emitter inevitably decays to the ground state in the long-time limit.

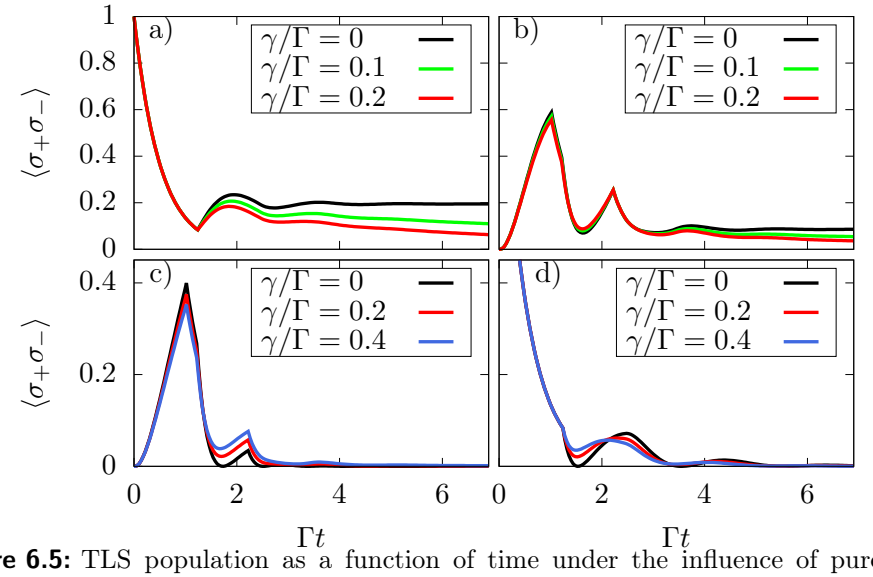

Figure 6.5: TLS population as a function of time under the influence of pure dephasing at different rates γ for feedback at $\Gamma\tau = 1.2$ for a system in the initial state $|\psi\rangle$. (a) Initially excited emitter decaying in vacuum, $|\psi\rangle = |e, 0\rangle$, with feedback phase $\phi = 2\pi m$, $m \in \mathbb{N}$. (b) Emitter initially in the ground state excited by a rectangular two-photon pulse of duration $\Gamma t_\mathrm{D} = 1$, $|\psi\rangle = |g, 2\rangle$, with feedback phase $\phi = 2\pi m$. (c) Emitter initially in the ground state excited by a rectangular single-photon pulse of duration $\Gamma t_\mathrm{D} = 1$, $|\psi\rangle = |g, 1\rangle$, with feedback phase $\phi = 2\pi m$. (d) Initially excited emitter decaying in vacuum, $|\psi\rangle = |e, 0\rangle$, with feedback phase $\phi = (2m + 1)\pi$.

A reduced efficiency of the emitter excitation can also be found in the case of a single-photon pulse. In Fig. 6.5 c, pure dephasing at higher rates than assumed for Figs. 6.5 a and 6.5 b is considered and leads to an even stronger reduction of the excitation efficiency. However, pure dephasing has not necessarily a detrimental effect at all times. As it counteracts constructive as well as destructive interference, dephasing can give rise to a TLS population that is temporarily increased in comparison to the case without dephasing.

Next, we turn away from the premise $\phi = 2\pi m$. Instead, we look at the impact of pure dephasing for an initially excited TLS decaying in vacuum with a feedback phase $\phi = (2m+1)\pi$ as illustrated in Fig. 6.5 d. Without dephasing, the decay is maximally accelerated at this feedback phase. Dephasing, however, reduces the impact of the feedback mechanism and with an increasing dephasing rate, the decay approaches the Wigner-Weißkopf decay that occurs in the absence of feedback.

6.5 Conclusion

In this chapter, we proposed a method for the calculation of the non-Markovian dynamics in WQED setups with feedback within a Heisenberg representation. The arising hierarchical structure of differential equations can be unraveled by introducing a unity operator, that is, a projector onto a complete set of states in the Hilbert space, between the operators with different time arguments so that only single-time correlations have to be calculated. As an alternative to the MPS method introduced in the previous chapter, the Heisenberg approach allows for the efficient calculation of the system dynamics with memory require-

ments known *a priori*. It is, furthermore, a versatile tool for the inclusion of arbitrary pulse shapes as well as additional dissipation channels.

Considering the exemplary system of a TLS coupled to a semi-infinite waveguide excited by quantum pulses, we studied how the number of matrix elements that have to be calculated and with it the required numerical resources depend on the number of excitations in the system. We applied the method to study how the complex interplay of the feedback delay time and the pulse shape affects the excitation efficiency of the atom-photon bound state that exists in the considered system. Furthermore, we included a phenomenological Markovian pure dephasing, which renders the bound state inaccessible.

7 Generating long-lived entanglement of macroscopically separated emitters

Complex quantum networks consist of multiple nodes, which render them quantum many-body systems facilitating cooperative phenomena. In quantum electrodynamics, a well-studied collective effect is Dicke superradiance, where the emission characteristics of an ensemble of emitters differ significantly from those of the individual emitters due to a modification of their common electromagnetic environment [64,207]. In large-scale WQED networks, non-Markovianity arising from non-negligible delay times opens up the possibility to modify the collective emission so that superradiance and subradiance phenomena can be further enhanced or inhibited [208–210]. Moreover, in WQED networks with macroscopically separated nodes, long-range entanglement between the emitters can be generated [211–213]. In this way, entangled natural or artificial atoms in WQED provide an alternative to entangled photons (which are the topic of part III of this thesis) for implementing quantum information processing applications [214].

The most fundamental WQED setup in which feedback effects arise is a single TLS coupled to a semi-infinite waveguide as studied in the previous chapters, Chaps. 5 and 6. On the path toward more complex quantum networks, two TLS coupled to an infinite waveguide provide an ideal toy model for which the onset of collective effects can be observed [215]. Since the emitters act as perfect mirrors on resonance, they form a cavity allowing for the confinement of the electromagnetic field between them and, as a consequence, the existence of a bound state in the continuum of propagating modes [101,216]. In this bound state, the emitters can exhibit a high degree of long-lived entanglement. Its excitation is possible via spontaneous emission, where the emitters can spontaneously relax to an entangled state even in the case of a separable initial state [212, 217, 218]. Furthermore, the bound state can be populated by multiphoton scattering, which allows inducing stable entanglement in the system without the need to drive the emitters continuously [180].

In this chapter, we investigate the dynamics of two two-level emitters coupled to an infinite waveguide at macroscopically separated points. In particular, we focus on the potential of generating stable long-range entanglement with different excitation schemes. Sec. 7.1 serves as an introduction of the setup and the MPS algorithm employed for the efficient numerical simulation of the feedback dynamics. Subsequently, in Sec. 7.2, we study the emergence of emitter entanglement comparing the scenarios of initially excited emitters, emitters excited by an external laser field, and emitters excited by quantum pulses.

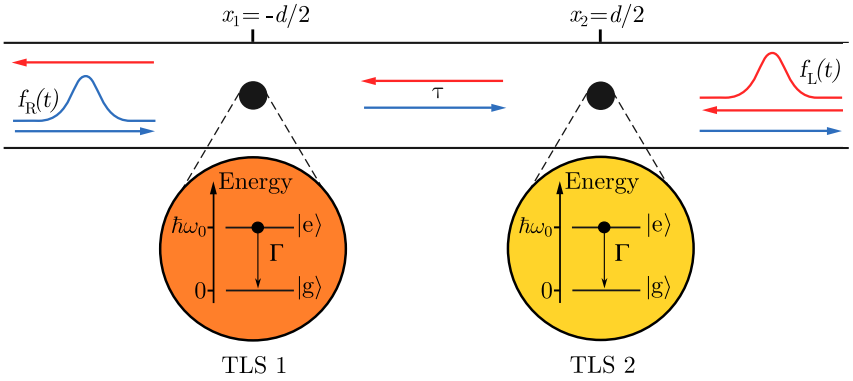

Figure 7.1: Two identical TLS coupling to a waveguide at $x_1 = -d/2$ and $x_2 = d/2$ resulting in the delay time $\tau = d/c$ for the light field between them. The emitters with transition frequency ω_0 between ground state $|\mathrm{g}\rangle$ and excited state $|\mathrm{e}\rangle$ decay with rate Γ. The left (right) emitter can be excited by a right-propagating (left-propagating) pulse with temporal shape $f_R(t)$ ($f_\mathrm{L}(t)$).

7.1 Matrix product state method

The considered system consisting of two TLS coupled to an infinite waveguide at two spatially separated points is depicted in Fig. 7.1. Extending the Hamiltonian from Sec. 3.2 to the case of two emitters, it can be described by

$$\begin{aligned} H = \hbar\omega_0 \sigma_+^{(1)}\sigma_-^{(1)} + \hbar\omega_0 \sigma_+^{(2)}\sigma_-^{(2)} + \int d\omega\, \hbar\omega \left(l_\omega^\dagger l_\omega + r_\omega^\dagger r_\omega \right) \\ + \int d\omega\, \hbar g_0 \Big\{ \left[\left(l_\omega^\dagger e^{-i\omega\tau/2} + r_\omega^\dagger e^{i\omega\tau/2} \right) \sigma_-^{(1)} + \mathrm{H.c.} \right] \\ + \left[\left(l_\omega^\dagger e^{i\omega\tau/2} + r_\omega^\dagger e^{-i\omega\tau/2} \right) \sigma_-^{(2)} + \mathrm{H.c.} \right] \Big\}. \end{aligned} \tag{7.1}$$

The left emitter (TLS 1) and the right emitter (TLS 2) with the transition operators $\sigma_\pm^{(1)}$ and $\sigma_\pm^{(2)}$, respectively, are assumed to be identical with transition frequency ω_0. To account for the two possible directions of propagation for the photons, two separate channels are considered with the bosonic operators $l_\omega^{(\dagger)}$ and $r_\omega^{(\dagger)}$ modeling the annihilation (creation) of left- and right-propagating photons of frequency ω, respectively. The left emitter couples to the waveguide at $x_1 = -d/2$, the right emitter at $x_2 = d/2$. As a consequence, the light field with speed c needs the time $\tau = d/c$ to cover the distance between the emitters resulting in the relative phase factors $e^{\pm i\omega\tau/2}$ in the Hamiltonian. The coupling between the TLS and the reservoir, g_0, is assumed to be constant over the relevant frequency range. Note that here the coupling strength is the same for both directions of propagation, where, however, the extension to a chiral coupling with $g_\mathrm{L} \neq g_\mathrm{R}$ is straightforward. In the next step, the Hamiltonian is transformed into the interaction picture ($H \to H_\mathrm{I}$, see Sec. 2.1) and subjected to a time-independent phase shift $\varphi \to \varphi - \omega\tau/2$ via

$$H' = U^\dagger H_\mathrm{I} U, \quad U = \exp\left[i \int d\omega \left(l_\omega^\dagger l_\omega + r_\omega^\dagger r_\omega \right) \omega\tau/2 \right], \tag{7.2}$$

so that the left emitter interacts with the right-moving field without delay and the right emitter interacts with the left-moving field without delay. This results in

$$H' = \int d\omega\, \hbar g_0 \Big\{ \left[\left(l_\omega^\dagger e^{-i\omega\tau} + r_\omega^\dagger \right) \sigma_-^{(1)} e^{i(\omega-\omega_0)t} + \text{H.c.} \right] + \left[\left(l_\omega^\dagger + r_\omega^\dagger e^{-i\omega\tau} \right) \sigma_-^{(2)} e^{i(\omega-\omega_0)t} + \text{H.c.} \right] \Big\}. \tag{7.3}$$

Proceeding analogously to Sec. 5.1, the quantum noise operators for the left- and the right-propagating photon channels are introduced according to

$$l_t^\dagger = \frac{1}{\sqrt{2\pi}} \int d\omega\, l_\omega^\dagger e^{i(\omega-\omega_0)t}, \quad r_t^\dagger = \frac{1}{\sqrt{2\pi}} \int d\omega\, r_\omega^\dagger e^{i(\omega-\omega_0)t}. \tag{7.4}$$

This way, we cast the Hamiltonian from Eq. (7.3) into the form

$$H' = \hbar\sqrt{\Gamma} \Big\{ \left[\left(l_{t-\tau}^\dagger e^{-i\omega_0\tau} + r_t^\dagger \right) \sigma_-^{(1)} + \text{H.c.} \right] + \left[\left(l_t^\dagger + r_{t-\tau}^\dagger e^{-i\omega_0\tau} \right) \sigma_-^{(2)} + \text{H.c.} \right] \Big\} \tag{7.5}$$

with $\Gamma \equiv 2\pi g_0^2$. The corresponding stroboscopic time evolution operator describing the time evolution from time t_k to t_{k+1}, $t_k = k\Delta t$, $k \in \mathbb{N}$, according to

$$|\psi(t_{k+1})\rangle = U_k |\psi(t_k)\rangle, \quad U_k = \exp\left[-\frac{i}{\hbar} \int_{t_k}^{t_{k+1}} dt'\, H'(t') \right], \tag{7.6}$$

can be expressed by introducing the noise increments for the left- and right-propagating photons

$$\Delta L_k^\dagger = \int_{t_k}^{t_{k+1}} dt\, l_t^\dagger, \quad \Delta R_k^\dagger = \int_{t_k}^{t_{k+1}} dt\, r_t^\dagger, \tag{7.7}$$

which satisfy $\left[\Delta L_k, \Delta L_{k'}^\dagger \right] = \Delta t\, \delta_{kk'}$ and $\left[\Delta R_k, \Delta R_{k'}^\dagger \right] = \Delta t\, \delta_{kk'}$. Under the assumption of a delay time τ that is a multiple of the step size, $\tau = l\Delta t$, $l \in \mathbb{N}$, this yields

$$U_k = \exp\Big\{ -i\sqrt{\Gamma} \left[\left(\Delta L_{k-l}^\dagger e^{-i\omega_0\tau} + \Delta R_k^\dagger \right) \sigma_-^{(1)} + \text{H.c.} \right] - i\sqrt{\Gamma} \left[\left(\Delta L_k^\dagger + \Delta R_{k-l}^\dagger e^{-i\omega_0\tau} \right) \sigma_-^{(2)} + \text{H.c.} \right] \Big\}. \tag{7.8}$$

A scheme of the time evolution is presented in Fig. 7.2. The noise increments introduced in Eq. (7.7) define discrete time-bin bases for the left- and the right-propagating photons. Both emitters have an immediate interaction with one of the channels and a time-delayed interaction with the other channel. For each time evolution step, the two "conveyor belts" of time bins are shifted one step in the corresponding direction of propagation. The emitters are modeled as a collective four-level system, with the possible states $|\mathrm{g}_1, \mathrm{g}_2\rangle$, $|\mathrm{e}_1, \mathrm{g}_2\rangle$, $|\mathrm{g}_1, \mathrm{e}_2\rangle$, and $|\mathrm{e}_1, \mathrm{e}_2\rangle$, where the first entry denotes the state of the left emitter (TLS 1), while the second entry indicates the state of the right emitter (TLS 2). Thus, the interaction of the collective emitter system with four time bins has to be accounted for in each time step.

The time evolution in the MPS framework is performed in analogy to Sec. 5.1.4, where, however, there are now two time bins for each time step, one right- and one left-propagating

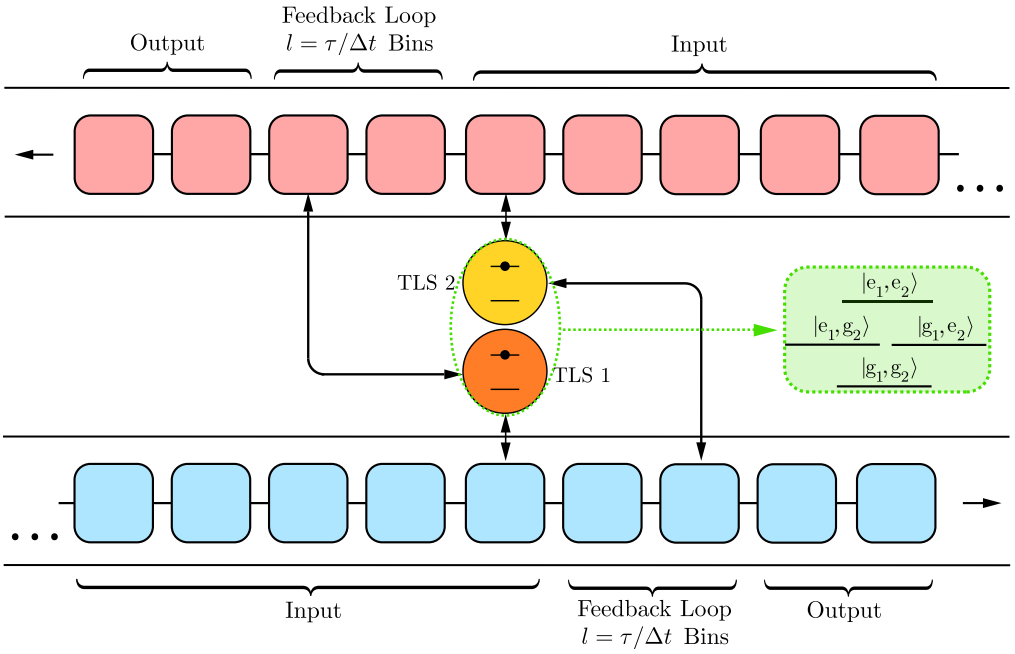

Figure 7.2: Schematic representation of the discretization of the reservoir dynamics into two separate conveyor belts of time bins for the left-propagating (red) and the right-propagating photons (blue) interacting with the emitters successively. The two emitters TLS 1 (orange) and TLS 2 (yellow) are treated as a collective four-level system (green). The time-delayed interaction between the emitters is accounted for by an additional feedback loop for each direction of propagation containing $l = \tau/\Delta t$ time bins (here $l = 2$) so that the collective emitter system interacts with two time bins per direction of propagation.

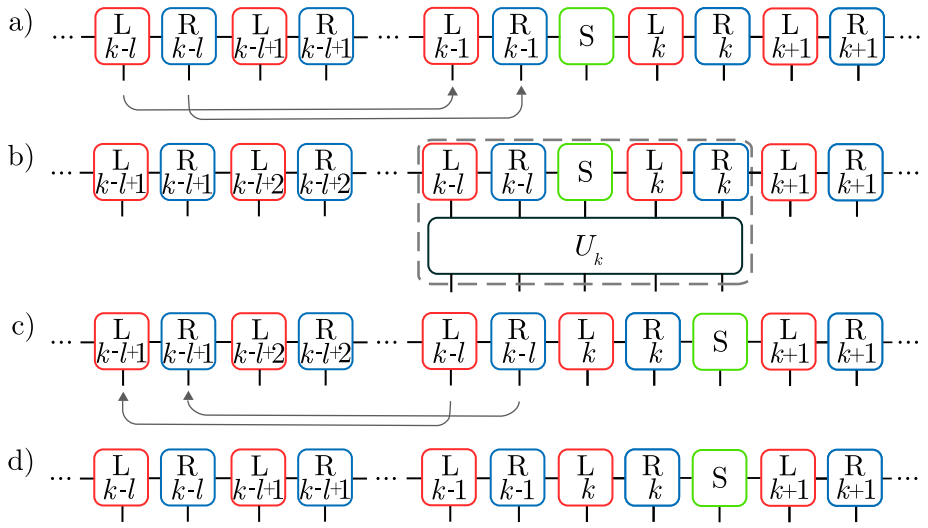

Figure 7.3: Diagrammatic representation of the time evolution for the two TLS in the MPS framework. For each time step, two time bins are accounting for the propagation to the left (L, red boxes) and the right (R, blue boxes). (a) The feedback bins at time step $k-l$ are brought next to the emitter bin S. (b) The time evolution operator U_k is applied to the feedback bins, the emitter bin, and the current time bins at time step k. (c) When decomposing the contracted tensor, the emitter bin is moved two steps to the right. The former current time bins account for the emission into the feedback loops and are kept to the left of the emitter bin. The former feedback bins are returned to their original position and contain the output signal. (d) After the correct order of the MPS has been reestablished, the next time evolution step can be performed.

time bin. In the diagrammatic representation, the time evolution can be visualized as is shown in Fig. 7.3. Here, the colors of the time bins, in contrast to Sec. 5.1, do not denote their orthogonality properties but encode their direction of propagation (red boxes, L: propagation to the left; blue boxes, R: propagation to the right). During the time evolution, the OC is kept at one of the feedback bins except when evaluating operators acting on other bins. At the beginning of each time evolution step, the left- and the right-moving feedback bin are swapped to the right and placed to the left of the emitter bin (Fig. 7.3 a). This way, it is possible to apply the time evolution operator efficiently by contracting it with the feedback bins, the emitter bin, and the current time bins (Fig. 7.3 b). Subsequently, the resulting tensor is decomposed in such a way that the emitter bin is moved two steps to the right and the former feedback bins are swapped back to restore the original order of the MPS (Fig. 7.3 c). After that, the procedure can be repeated for the following time step (Fig. 7.3 d).

If the excitation in the system is stored in the emitters at the starting point of our investigation, the emitter state and the reservoir state are initially separable. Since the reservoir is in the vacuum state at the beginning of the dynamics, in addition to that, all time bins are separable and can be initialized in the ground state individually. The same assumptions are valid if the emitters are excited externally by a laser field. This external excitation, in analogy to the case of a driven single TLS discussed in Sec. 5.2, can be modeled semiclassically by introducing the term

$$H_{\mathrm{L}} = \Omega^{(j)}(t)\left(\sigma_{+}^{(j)} + \sigma_{-}^{(j)}\right), \quad j \in \{1,2\}, \tag{7.9}$$

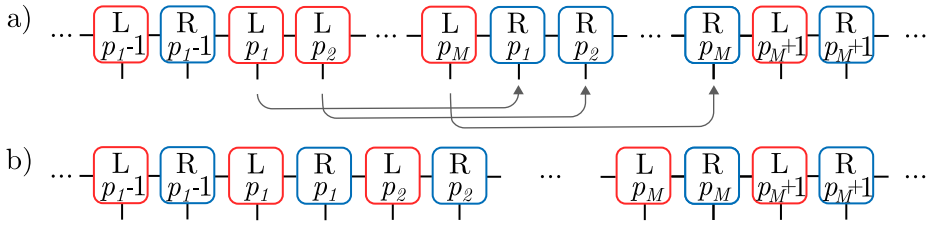

Figure 7.4: Diagrammatic representation of the initialization of the reservoir time bins in the case of quantum pulses involving the time steps $p_1, \ldots, p_M$. (a) For the time bins involved in the pulse, first all left-moving time bins, then all right-moving time bins are initialized. Depending on the specific pulse configuration, the bins are set to the ground state or describe a quantum pulse. The left-moving bins are swapped to the right to establish the correct order of the MPS. (b) After the pulse bins have been rearranged, the time evolution of the MPS can be performed.

into the interaction picture Hamiltonian, Eq. (7.3), for a laser with amplitude $\Omega^{(j)}(t)$ driving the TLS j resonantly at frequency $\omega_\mathrm{L} = \omega_0$. Assuming the laser amplitudes to be constant during one time step, $\Omega^{(j)}(t) \to \Omega_k^{(j)}$, $t \in [t_k, t_{k+1}[$, the time evolution operator from Eq. (7.8) can be extended to

$$U_k = \exp\Bigg\{ -i \sum_{j=1,2} \Omega_k^{(j)} \left(\sigma_+^{(j)} + \sigma_-^{(j)}\right) \Delta t - i\sqrt{\Gamma} \left[\left(\Delta L_{k-l}^\dagger e^{-i\omega_0 \tau} + \Delta R_k^\dagger\right) \sigma_-^{(1)} + \mathrm{H.c.}\right] \\ - i\sqrt{\Gamma} \left[\left(\Delta L_k^\dagger + \Delta R_{k-l}^\dagger e^{-i\omega_0 \tau}\right) \sigma_-^{(2)} + \mathrm{H.c.}\right] \Bigg\}. \quad (7.10)$$

Quantum pulses, in contrast, are included in the initial state of the reservoir. As a consequence, the reservoir time bins involved in the pulses are not separable anymore but are in an entangled initial state as discussed in Sec. 5.2. In contrast to the case of a single emitter in front of a mirror, in the setup considered in this chapter, the two possible directions of propagation have to be accounted for. To initialize the reservoir accordingly, we proceed as illustrated in Fig. 7.4. For a pulse of duration $t_\mathrm{D} = M\Delta t$, $M \in \mathbb{N}$, encompassing the time steps $p_1, \ldots, p_M$, $p_i \in \mathbb{N}$, $i \in \{1, \ldots, M\}$, first, all left-moving bins are initialized followed by the right-moving bins. Depending on whether there is a pulse propagating to the left with temporal shape $f_\mathrm{L}(t)$, a pulse propagating to the right with temporal shape $f_\mathrm{R}(t)$, or pulses in both directions, these bins are either initialized in the ground state or the pulse state as given explicitly for a rectangular pulse containing up to two photons in Sec. 5.2 and up to four photons in Appendix A.1. Subsequently, the left-moving pulse bins are swapped to the right to bring the bins in the correct order for the time evolution of the state.

7.2 Bound state excitation and stable entanglement

After having introduced the considered setup of two TLS coupled to an infinite waveguide as well as the MPS algorithm for its simulation, in this section, we study the resulting dynamics. In particular, we explore the possibilities to generate emitter entanglement with different excitation schemes, namely, initially excited emitters, emitters excited by an external laser field, and emitters subjected to quantum pulses.

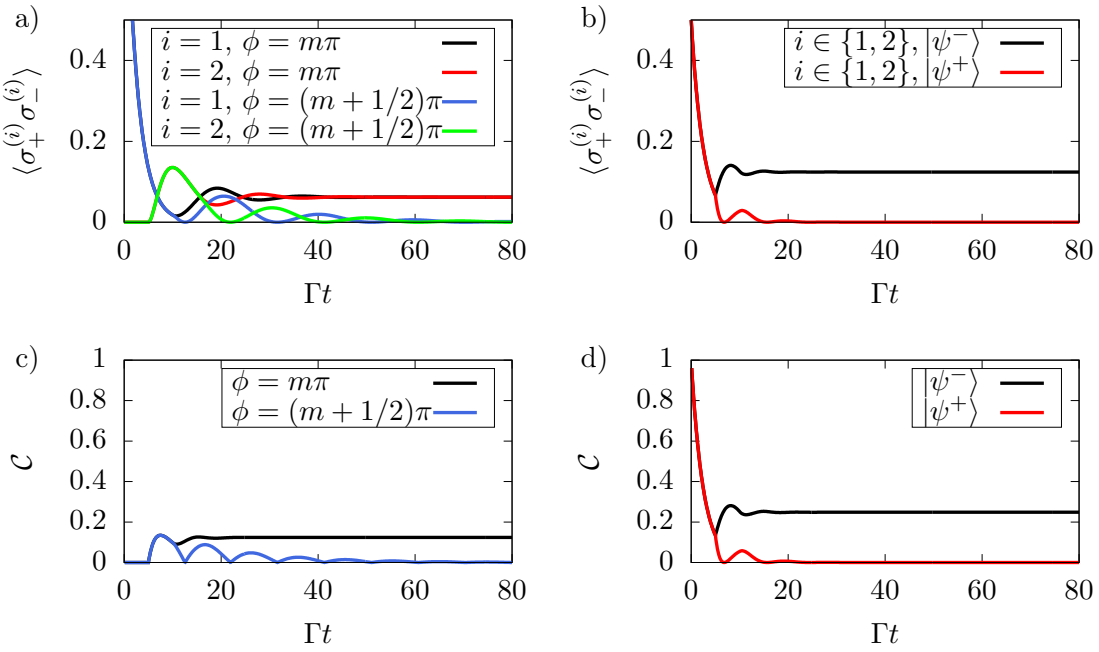

Figure 7.5: Dynamics of the TLS populations and the concurrence with feedback at $\Gamma\tau = 5$. (a) Population of emitter i, $i \in \{1, 2\}$, for the initial state $|e_1, g_2\rangle$ with different feedback phases ϕ, where $m \in \mathbb{N}$. (b) Population of the emitters for the subradiant initial state ($|\psi^-\rangle$, black line) and the superradiant initial state ($|\psi^+\rangle$, red line) with feedback phase $\phi = m\pi$. (c) Concurrence of the emitters for the initial state $|e_1, g_2\rangle$ with different feedback phases ϕ. (d) Concurrence of the emitters for the subradiant initial state ($|\psi^-\rangle$, black line) and the superradiant initial state ($|\psi^+\rangle$, red line) with $\phi = m\pi$.

7.2.1 Initially excited emitters

Let us first consider the case where the emitters initially carry all excitation in the system and the reservoir is prepared in the vacuum state. For an emitter system with a single excitation in the initial state $|e_1, g_2\rangle$, that is, the left TLS in the excited state and the right TLS in the ground state, the population dynamics presented in Fig. 7.5 a can be observed, where $\Gamma\tau = 5$. The population of the left TLS starts at $\langle\psi(0)|\, \sigma_+^{(1)} \sigma_-^{(1)}\, |\psi(0)\rangle = 1$ and decays exponentially due to the interaction of the emitter with the vacuum field in the waveguide (black/blue line). At $t = \tau$, the right emitter becomes excited by the right-moving signal emitted from the left emitter (red/green line). After another delay interval, at $t = 2\tau$, the left emitter receives a feedback signal from the right emitter, where the feedback phase $\phi \equiv \omega_0\tau$ determines the impact of the feedback signal. For $\phi = m\pi$, $m \in \mathbb{N}$, the populations of both emitters stabilize at a non-zero steady-state value (black/red line). In this case, it is possible to measure a photon in the region between the two TLS in the long-time limit due to the existence of a bound state in the continuum of propagating modes. For phases $\phi \neq m\pi$, no stabilization can be observed and the fastest decay occurs if $\phi = (m + 1/2)\,\pi$ (blue/green line). This is in analogy to the case of a single emitter in front of a mirror with $\phi \to 2\phi$, see Sec. 5.3, since, in the two-emitter setup, a signal emitted from one of the TLS returns to the same TLS only after two delay intervals 2τ.

Collective effects are particularly pronounced if the emitters are initially prepared in the subradiant state $|\psi^-\rangle = (|e_1, g_2\rangle - |g_1, e_2\rangle)/\sqrt{2}$ or the superradiant state $|\psi^+\rangle = (|e_1, g_2\rangle + |g_1, e_2\rangle)/\sqrt{2}$. In the subradiant state, the emitter populations do not decay completely due to the possibility of exciting the bound state. In the superradiant state, in contrast, the interaction of the emitters results in a decay rate exceeding that of emitters decaying individually in vacuum. While these effects were originally described employing the Markov approximation, taking the time-delayed feedback of the emitters into account gives rise to non-Markovian dynamics beyond the usual Dicke sub- and superradiance [209]. The dynamics for both initial states are shown in Fig. 7.5 b for a system characterized by $\Gamma\tau = 5$ and $\phi = m\pi$, where the results for the left and the right emitter coincide.

While the emitters exchange excitation through the waveguide, their entanglement evolves. Here, the entanglement is evaluated in terms of the concurrence $\mathcal{C}$ of the collective density matrix of the emitters as introduced in Sec. 4.2. The concurrence as a function of time for the systems assumed for Figs. 7.5 a and b are presented in Figs. 7.5 c and d. As can be seen in Fig. 7.5 c, in the case of an initial emitter state $|e_1, g_2\rangle$, there is a "sudden birth of entanglement" at $t = \tau$, where the emitters begin to influence each other [219]. Thus, even though their initial state is separable, the emitters become entangled as a consequence of their spontaneous emission into the waveguide. After another delay interval, the emission signals start to interfere and, for a phase $\phi = m\pi$, stable entanglement can be generated as there is a finite probability of finding the emitters in the excited state in the long-time limit (black line). For a phase $\phi \neq m\pi$, where the emitters eventually decay to the separable ground state $|g_1, g_2\rangle$, after a transient time, the concurrence decays to zero (blue line). In Fig. 7.5 d, the maximally entangled sub- and superradiant initial states $|\psi^-\rangle$ (black line) and $|\psi^+\rangle$ (red line) are considered with $\phi = m\pi$, where it is noteworthy that the dynamics of the population and the concurrence coincide except for a factor of two.

The steady-state value that the population stabilizes at strongly depends on the emitter separation. In Fig. 7.6 a, the steady-state population $\langle \sigma_+^{(i)} \sigma_-^{(i)} \rangle_{\text{st.st.}} \equiv \lim_{t\to\infty} \langle \psi(t)| \sigma_+^{(i)} \sigma_-^{(i)} |\psi(t)\rangle$ as a function of the delay time for different initial states is presented. Here, we assume that a phase $\phi = m\pi$ is implemented, where a non-zero steady-state population is, in principle, possible. The steady-state value decays monotonically in the considered cases with a single excitation in the system, that is, for $|e_1, g_2\rangle$ (black line) and $|\psi^-\rangle$ (blue line), while the doubly excited initial state $|e_1, e_1\rangle$ evokes a more complex and non-monotonic behavior (red line). The corresponding steady-state concurrence $\mathcal{C}_{\text{st.st}} \equiv \lim_{t\to\infty} \mathcal{C}(t)$ shows an analogous behavior, see Fig. 7.6 b.

7.2.2 Semiclassical excitation

If the emitters are excited by an external laser field, the number of excitations in the system is no longer conserved. In the case of a resonant continuous-wave laser field at Rabi frequency Ω, Rabi oscillations of the emitter populations are induced as can be seen in Fig. 7.7 a. Here, only the left emitter is driven with $\Omega = 0.1\Gamma$ and the delay time between the emitters is $\Gamma\tau = 1$. The interplay of driving and decay results in an equilibrium state, where the populations of the two emitters stabilize at, in general, different non-zero steady-state values. Note that this steady state differs fundamentally from the bound state that can be excited by an initially excited emitter decaying in vacuum, as considered

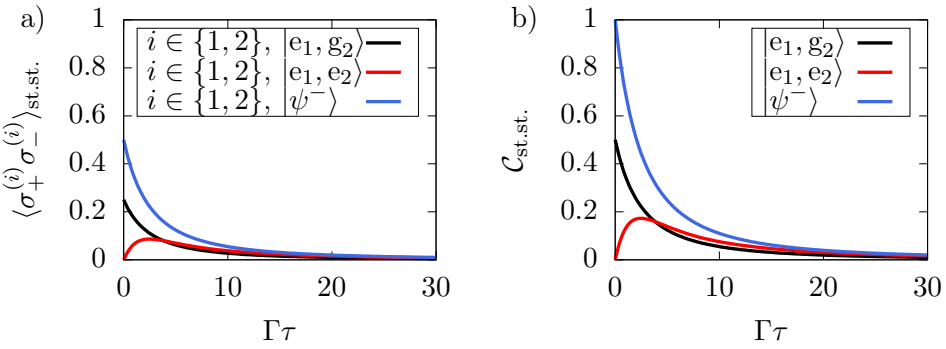

Figure 7.6: Steady-state values of the TLS population and the concurrence as a function of the delay time between the emitters with feedback phase $\phi = m\pi$, $m \in \mathbb{N}$, for different initial states of the emitters. (a) Steady-state population. (b) Steady-state concurrence.

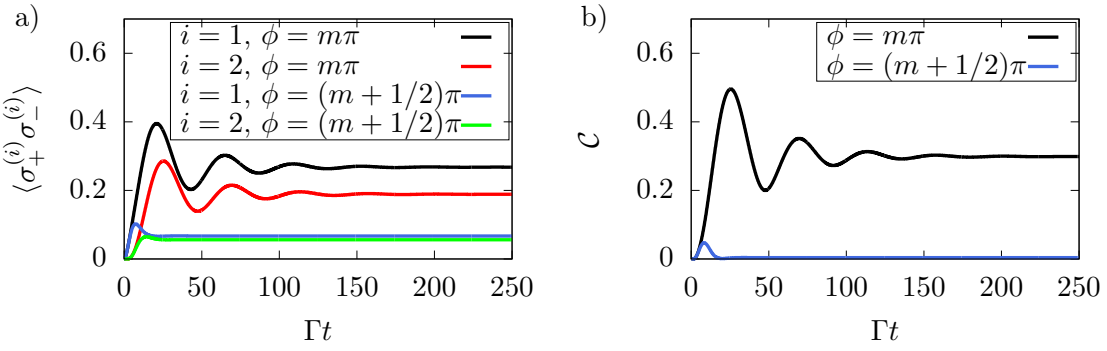

Figure 7.7: Dynamics of the TLS populations and the concurrence with feedback at $\Gamma\tau = 1$ and different phases ϕ with $m \in \mathbb{N}$ for emitters initially in the ground state $|g_1, g_2\rangle$. The left TLS is excited by a continuous-wave laser field with Rabi frequency $\Omega = 0.1\Gamma$. (a) Population of emitter i, $i \in \{1, 2\}$. (b) Concurrence of the emitters.

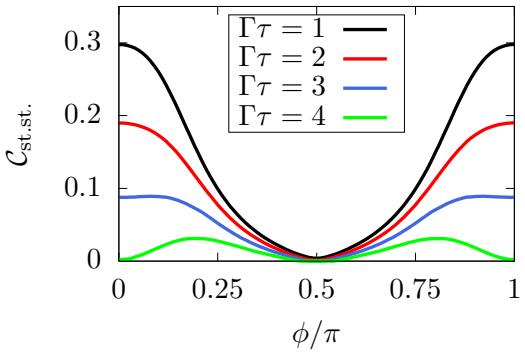

Figure 7.8: Steady-state value of the concurrence as a function of the feedback phase ϕ (mod π) for different delay times τ between the emitters. The left TLS is excited by a continuous-wave laser field with Rabi frequency $\Omega = 0.1\Gamma$.

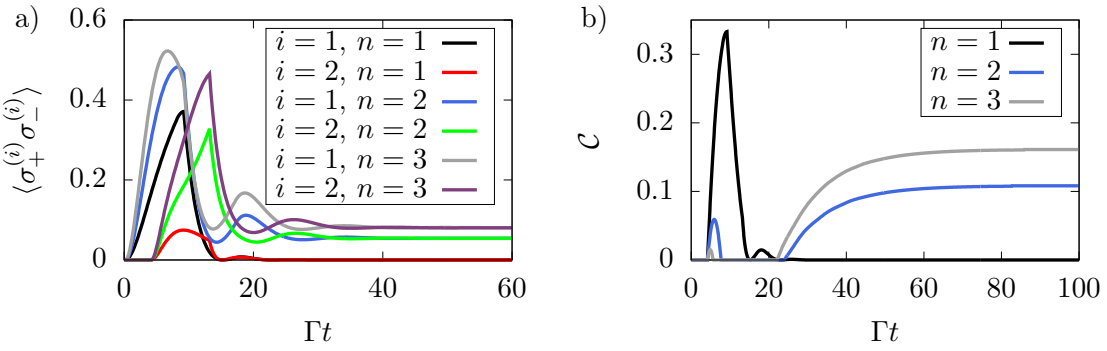

Figure 7.9: Dynamics of the TLS populations and the concurrence with feedback at $\Gamma\tau = 4$ and phase $\phi = m\pi$, $m \in \mathbb{N}$, between emitters initially in the ground state $|g_1, g_2\rangle$, where a rectangular pulse of width $\Gamma t_D = 9$ containing n photons, $n \in \{1, 2, 3\}$, is incident from the left. (a) Population of emitter i, $i \in \{1, 2\}$. (b) Concurrence of the emitters.

in Sec. 7.2.1, or by multiphoton scattering, as discussed in Sec. 7.2.3 below, since energy must be continuously supplied to the system. The feedback mechanism crucially influences the steady state of the system. In the system assumed for Fig. 7.7, the highest steady-state populations can be obtained with a phase $\phi = m\pi$ (black/red line), while a phase $\phi = (m + 1/2)\pi$ results in the lowest steady-state values (blue/green line). In contrast to the bound state, however, a non-zero steady-state population can still be found even for $\phi \neq m\pi$. Like the emitter populations, the concurrence also stabilizes after a transient, where the particular steady-state value strongly depends on the feedback phase as can be seen in Fig. 7.7 b.

The impact of the phase on the steady-state concurrence depends on the degree of non-Markovianity in the system. This can be concluded from Fig. 7.8, where the steady-state concurrence as a function of the feedback phase ϕ is shown for different delay times τ. The attainable concurrence decreases with the separation of the emitters. For large separations, $\Gamma\tau > 3$, the behavior even changes qualitatively exhibiting the highest steady-state concurrence for phases other than $\phi = m\pi$.

7.2.3 Quantum pulses

Accounting for the excitation of the emitters through the waveguide by implementing quantum pulses, we observe a significantly different behavior than in the case of the excitation by an external laser field. In Fig. 7.9 a, the population dynamics for a system consisting of two emitters initially in the ground state $|g_1, g_2\rangle$ with the delay time $\Gamma\tau = 4$ and the phase $\phi = m\pi$ are presented. A pulse is incident from the left and propagates to the right until reaching and exciting the left emitter. Here, the pulse is assumed to have a rectangular temporal shape of width $\Gamma t_D = 9$. The behavior that can be observed depends crucially on the number of photons in the pulse. A single-photon pulse evokes oscillations of the emitter populations, where the excitation is exchanged between the two TLS (black/red line). In the long run, however, the emitters return to the ground state. Multiphoton pulses, in contrast, allow for the excitation of a bound state similar to the case of a single TLS in front of a mirror, see Sec. 5.3 and Ref. [180]. Thus, there is a finite probability

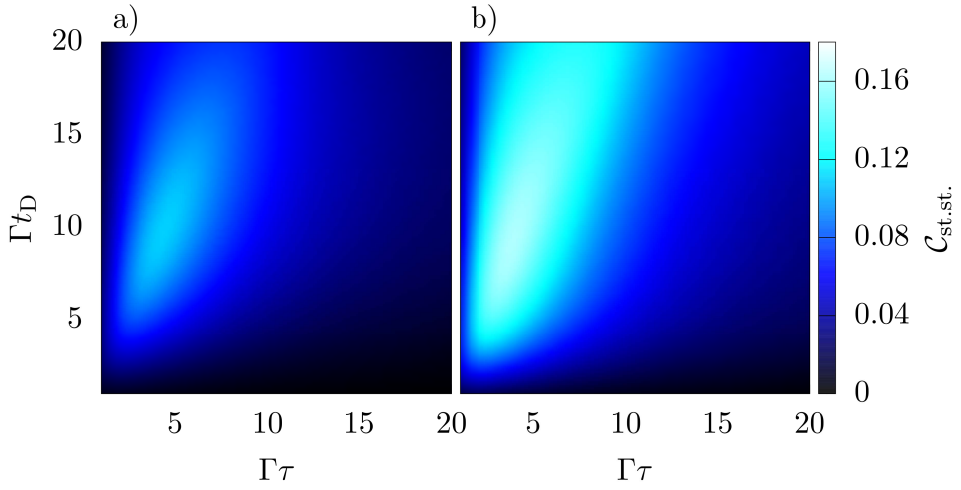

Figure 7.10: Steady-state value of the concurrence for emitters subjected to a rectangular multiphoton pulse as a function of the delay time and the width of the pulse. (a) Two-photon pulse. (b) Three-photon pulse.

to find the emitters in the excited state in the long-time limit as well as the possibility to measure a photon confined to the region between them. Comparing the results for two (blue/green line) and three photons in the pulse (grey/purple line), we observe that an increased number of photons leads to an enhanced excitation probability of the bound state.

The concurrence of the setup considered in Fig. 7.9 a as a function of time is shown in Fig. 7.9 b and indicates that the incident pulse induces entanglement in the system. If the emitters decay to the separable ground state, as they do for a single-photon pulse, their concurrence vanishes in the long-time limit (black line). In the case of multiphoton pulses allowing for the excitation of a bound state, in contrast, the concurrence stabilizes which points to the generation of stable long-range entanglement between the emitters. As the steady-state population increases when adding a photon to the pulse, the same can be observed for the steady-state concurrence (blue line for two, grey line for three photons in the pulse).

To explore ways to maximize the entanglement, it is interesting to study how it depends on the spatial separation of the emitters as well as on the pulse properties. In Fig. 7.10, the steady-state concurrence as a function of the emitter delay time and the pulse width is shown for the case of a rectangular pulse containing two (Fig. 7.10 a) or three photons (Fig. 7.10 b). It becomes apparent that the concurrence depends non-monotonically on the distance of the emitters as well as on the pulse width. The highest value for a given separation can be found for a pulse width that corresponds to approximately twice the delay time, $t_\mathrm{D} \approx 2\tau$. Thus, the highest amount of entanglement is generated if the pulse ends at the point in time at which the left TLS starts to receive the feedback signal from the right TLS. Since we find the steady-state concurrence to be proportional to the steady-state population of the emitters, the observed behavior matches our findings for a single emitter in front of a mirror, where we found the highest steady-state excitation for $t_\mathrm{D} \approx \tau$, see Chaps. 5 and 6. Proceeding from two to three photons in the pulses, we find that a higher steady-state concurrence is obtained for the whole parameter regime under consideration,

which can be attributed to the fact that an increased number of photons renders the bound state excitation by stimulated emission more efficient.

7.3 Conclusion

In this chapter, we explored possibilities to generate entanglement between two macroscopically separated emitters in a WQED setup using different excitation schemes. Under the assumption of initially excited emitters, entanglement develops even in the case of initial separability with a non-negligible delay time giving rise to a "sudden birth of entanglement". For certain emitter separations, a bound state in the continuum can be populated allowing for long-lived entanglement, where the achievable degree of entanglement depends on the emitter separation as well as on the initial state of the emitters. To account for an influx of energy, we included an external continuous-wave laser field. The resulting equilibrium state of the emitters and their entanglement appeared to depend sensitively on the feedback mechanism, the impact of which changes with the degree of non-Markovianity in the system. To generate long-lived entanglement with this excitation scheme, however, a continuous supply of energy is necessary to maintain the steady state. If the emitters are driven with quantum pulses through the waveguide instead, the bound state in the continuum can be populated by multiphoton scattering. This opens up the possibility to induce stable long-range entanglement between the emitters, which can be controlled by tuning the emitter separation as well as the pulse shape.

Part III

Controlling photon entanglement

8 Boosting energy-time entanglement using coherent time-delayed feedback

Many quantum information processing protocols with entangled photon pairs involve polarization-entangled photons, which are, however, sensitive to the dispersion of the polarization mode when transported in optical fibers [220–222]. Another degree of freedom in which photons can be entangled is with respect to their energies and their times of emission, as proposed by Franson in 1989 [128]. This energy-time entanglement and its discretized version, time-bin entanglement [223], are robust when transported in optical fibers over long distances, as has been demonstrated experimentally [224]. It can be used for various applications such as quantum key distribution [225, 226] or quantum-enhanced positioning and clock synchronization [227].

Franson suggested a setup to visualize the energy-time entanglement of a pair of photons emitted from a three-level system (3LS) in ladder configuration via an interference in the second-order correlation function. The visibility of the interference fringes depends strongly on the decay rates of the 3LS. If the upper state decays slowly in comparison to the middle state, a high visibility can be observed. In this case, the photons are highly correlated with respect to their times of emission, which, following Heisenberg's uncertainty principle, is accompanied by a high correlation in the energies of the emitted photons, see Fig. 8.1 a. In the opposite case of an upper state decaying fast in relation to the middle state, the visibility is low since the emitted photons are little correlated in their times of emission and, correspondingly, their energies, see Fig. 8.1 b.

The Franson interferometer has been realized in a variety of experiments [228–233], where the entangled photon pairs have been created via spontaneous parametric down-conversion, spontaneous four-wave mixing, or sampling from the Mollow triplet. Another typical source of entangled photons is given by semiconductor quantum dots [234], see also Chap. 9. In such systems, a biexciton cascade can be used for the creation of energy-time entangled photon pairs, where, however, the expected visibility of the interference fringes in the Franson interferometer is low since the biexciton state generally has a shorter lifetime than the exciton state [222, 235–237]. As a consequence, possibilities to control the emission dynamics in such a way that the visibility is enhanced are of interest. One option to achieve this goal is using resonator-based schemes, where, however, the device geometry limits the accessible scenarios [238–241]. Complementarily, coherent time-delayed feedback provides the opportunity to steer the emission dynamics. Since it inherently preserves coherence, this type of feedback is particularly well-suited for the control of entanglement [43].

In this chapter, we explore the potential of coherent time-delayed feedback to increase the visibility of the interference in the second-order correlation function that can be detected using the Franson interferometer. The chapter is based on our work presented in Ref. [242]. For reference, we first consider the conventional Franson setup without feedback in Sec. 8.1,

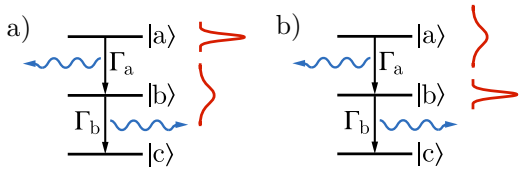

Figure 8.1: Schematic representation of the radiative broadening of the energy levels in a ladder-type 3LS. (a) Slowly decaying upper state $|a\rangle$ in comparison to the middle state $|b\rangle$, that is, $\Gamma_a \ll \Gamma_b$. (b) Fast decaying upper state $|a\rangle$ in comparison to the middle state $|b\rangle$, that is, $\Gamma_a \gg \Gamma_b$.

where the second-order correlation function can be calculated analytically. Subsequently, in Sec. 8.2, we study the influence of feedback simulating the system dynamics within the MPS framework.

8.1 Two-photon interference in the Franson interferometer

The Franson interferometer allows for the analysis of two-photon correlations. To start with, we look at the setup of the interferometer without feedback and evaluate the second-order correlation function analytically. This serves as a benchmark for the numerical simulation in the MPS framework and provides a basis on which we can study the effect of feedback.

8.1.1 Setup of the interferometer

The setup of the conventional Franson interferometer is depicted in Fig. 8.2. We model the source of the photons as a ladder-type 3LS initially in the upper state $|a\rangle$. Under the emission of a photon, the 3LS decays with rate Γ_a to the middle state $|b\rangle$. From the state $|b\rangle$, the emitter, in turn, decays with rate Γ_b to the ground state $|c\rangle$ and emits a second photon. After their emission, the photons impinge on a 50:50 beam splitter and enter one of two arms constituting the Franson interferometer. Each of these arms forms an unbalanced Mach-Zehnder interferometer, where the photons can take either a short path (S) of length l_S or a long path (L) of length l_L, defined by beam splitters and mirrors, to the corresponding detector D_1 or D_2. Here, we assume a symmetric setup with identical arms.

Only those events in which either both photons take the short or both photons take the long paths to the corresponding detector contribute to the interference effect as we will see below. As a consequence, postselection is inherent in the Franson setup as already touched upon in Chap. 4. Even in the ideal case without any losses, 50 % of all possible events are discarded so that a loophole is opened up. This loophole allows constructing a local hidden-variable model even if a Bell-type inequality is apparently violated [152, 243]. It is, however, possible to adapt the Franson setup to show the violation of a chained Bell inequality and proof the presence of genuine energy-time entanglement [153, 244–246].

For the later inclusion of a feedback mechanism that enables the individual control of

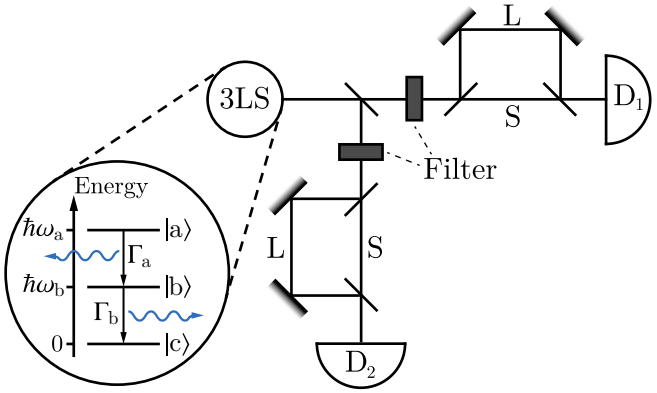

Figure 8.2: Setup of the Franson interferometer, which enables the measurement of the second-order correlation function of two photons emitted from a 3LS in ladder configuration. The interferometer consists of two arms separated by a beamsplitter. Frequency filters can be installed to ensure that the first photon is detected by the detector D_1 and the second photon is registered by the detector D_2. The photons take either a short (S) or a long path (L) defined by beamsplitters and mirrors to the respective detector.

the photons, we assume that the first photon enters the first arm and is detected by the detector D_1, while the second photon enters the second arm and is registered by the detector D_2. Experimentally, this can be realized by placing frequency filters in the optical paths. In general, it is possible to omit this assumption and implement a feedback mechanism affecting both photons collectively. For the sake of simplicity and numerical convenience, however, we make the distinction. In this case, the effects that occur are more pronounced and serve as a proof of principle.

Two-photon interference in the Franson interferometer manifests as an oscillation of the central peak in the second-order correlation function with the relative phase between the short and the long paths to the detectors. This interference is visible even in the parameter regime of a time delay between the short and the long paths, $T = (l_\mathrm{L} - l_\mathrm{S})/c$, where c is the speed of light, that exceeds the first-order coherence time of the photons, $\Gamma_{\mathrm{a/b}} T \gg 1$. In this case, single-photon interference in the individual arms of the interferometer can be ruled out and the oscillation can be attributed solely to the interference of the two-photon probability amplitudes of the photons taking the different paths to the detectors. The visibility of this interference can be used as an indicator of the energy-time entanglement of the photons.

Proceeding analogously to Sec. 3.2, we obtain the Hamiltonian governing the dynamics in the case of a three-level emitter in ladder configuration and two separate photon reservoirs in the dipole and the rotating wave approximation,

$$H = \hbar\omega_\mathrm{a}\sigma_\mathrm{aa} + \hbar\omega_\mathrm{b}\omega_\mathrm{bb} + \int d\omega\, \hbar\omega \left(r_\omega^{\dagger(1)} r_\omega^{(1)} + r_\omega^{\dagger(2)} r_\omega^{(2)} \right) + \int d\omega\, \hbar g_\mathrm{a}(\omega) \left(r_\omega^{\dagger(1)} \sigma_-^{(1)} + \mathrm{H.c.} \right) + \int d\omega\, \hbar g_\mathrm{b}(\omega) \left(r_\omega^{\dagger(2)} \sigma_-^{(2)} + \mathrm{H.c.} \right). \quad (8.1)$$

The operator σ_aa (σ_bb) describes the occupation of the upper (middle) level of the 3LS with the energy $\hbar\omega_\mathrm{a}$ ($\hbar\omega_\mathrm{b}$), while the energy of the ground state $|\mathrm{c}\rangle$ is set to zero. A photon of energy $\hbar\omega$ can be annihilated (created) via the bosonic operator $r_\omega^{(\dagger)(i)}$, $i \in \{1, 2\}$, where

i refers either to the first or to the second arm of the interferometer. These two separate reservoirs are considered since we distinguish between the first and the second photon using frequency filters as discussed above. The second line of Eq. (8.1) arises due to the coupling between the 3LS and the reservoirs. We assume that the $|\mathrm{a}\rangle \leftrightarrow |\mathrm{b}\rangle$ ($|\mathrm{b}\rangle \leftrightarrow |\mathrm{c}\rangle$) transition, which is encoded in the transition operator $\sigma_-^{(1)} \equiv |\mathrm{b}\rangle\langle\mathrm{a}|$ ($\sigma_-^{(2)} \equiv |\mathrm{c}\rangle\langle\mathrm{b}|$), couples to the first (second) reservoir with coupling strength $g_\mathrm{a}(\omega)$ [$g_\mathrm{b}(\omega)$]. In general, the coupling strengths are frequency dependent. Under the assumption of Markovian dynamics, where there is no backflow of information from the photonic reservoirs into the emitter, we can, however, set the coupling to a constant value, $g_\mathrm{a}(\omega) \to g_\mathrm{a}$, [$g_\mathrm{b}(\omega) \to g_\mathrm{b}$]. If we transform the Hamiltonian from Eq. (8.1) into the rotating frame defined by its non-interacting part, that is, its first line, it takes the form

$$H_\mathrm{I} = \int d\omega\, \hbar g_\mathrm{a} \left(r_\omega^{\dagger(1)} \sigma_-^{(1)} e^{-i(\omega_\mathrm{ab}-\omega)t} + \mathrm{H.c.} \right) + \int d\omega\, \hbar g_\mathrm{b} \left(r_\omega^{\dagger(2)} \sigma_-^{(2)} e^{-i(\omega_\mathrm{b}-\omega)t} + \mathrm{H.c.} \right), \quad (8.2)$$

where $\omega_\mathrm{ab} \equiv \omega_\mathrm{a} - \omega_\mathrm{b}$ is the transition frequency of the $|\mathrm{a}\rangle \leftrightarrow |\mathrm{b}\rangle$ transition.

8.1.2 Second-order correlation function

The second-order correlation function as a function of the delay time between the detection events of the two photons, τ_D, is given as

$$G^{(2)}(\tau_\mathrm{D}) = \int_0^\infty dt_1\, G^{(2)}(t_1, t_2)\Big|_{t_2 \to t_1 + \tau_\mathrm{D}}, \quad (8.3)$$

$$G^{(2)}(t_1, t_2) = \langle\Psi|\, E_1^{(-)}(t_1) E_2^{(-)}(t_2) E_2^{(+)}(t_2) E_1^{(+)}(t_1)\, |\Psi\rangle\,. \quad (8.4)$$

Here, the state $|\Psi\rangle$ represents the two-photon state that is emitted from the 3LS. The operators $E_i^{(+)}$ and $E_i^{(-)}$, $i \in \{1, 2\}$, are the positive and negative frequency parts of the electric field operator at the detector D_i, E_i, respectively, see Sec. 2.3, with

$$E_i(t) = E_i^{(+)}(t) + E_i^{(-)}(t). \quad (8.5)$$

The operator $E_i^{(+)}$ comprises the photon annihilation operators in Eq. (2.31), while its complex conjugate $E_i^{(-)}$ describes the photon creation. Since the photons can reach the detectors via two equiprobable paths, we split up the operators according to

$$E_i^{(+)}(t) = \frac{1}{2}\left[E_{i,\mathrm{S}}^{(+)}(t) + E_{i,\mathrm{L}}^{(+)}(t) \right]. \quad (8.6)$$

This way, we account for the photon i taking either the short (first term on the right-hand side) or the long path (second term on the right-hand side) to the detector D_i.

For the evaluation of the second-order correlation function, the two-photon state that is emitted from the 3LS has to be determined. As shown in Appendix A.4, it takes the form

$$|\Psi\rangle = \int d\omega \int d\omega' \frac{-g_\mathrm{a} g_\mathrm{b}}{\left[i\left(\omega + \omega' - \omega_\mathrm{a}\right) - \frac{\Gamma_\mathrm{a}}{2} \right] \left[i\left(\omega' - \omega_\mathrm{b}\right) - \frac{\Gamma_\mathrm{b}}{2} \right]} |1_\omega, 1_{\omega'}\rangle\,, \quad (8.7)$$

where Γ_a and Γ_b are the decay rates of the upper and middle state of the 3LS, respectively, and the state $|1_\omega, 1_{\omega'}\rangle$ denotes one photon of frequency ω and a second photon of frequency ω'. From the two-photon state $|\Psi\rangle$, we can evaluate the second-order correlation function. To that end, we rewrite the two-time second-order correlation function $G^{(2)}(t_1, t_2)$ as

$$G^{(2)}(t_1, t_2) = |\Psi(t_1, t_2)|^2, \tag{8.8}$$

where we introduce the two-photon probability amplitude $\Psi(t_1, t_2)$. Inserting a unity operator between the positive and the negative frequency parts in Eq. (8.4), only the projector onto the vacuum state ($|0\rangle\langle 0|$) survives and the probability amplitude can be expressed as

$$\begin{aligned}\Psi(t_1, t_2) &= \frac{1}{4}\langle 0| \left[E^{(+)}_{2,\mathrm{S}}(t_2) + E^{(+)}_{2,\mathrm{L}}(t_2)\right]\left[E^{(+)}_{1,\mathrm{S}}(t_1) + E^{(+)}_{1,\mathrm{L}}(t_1)\right]|\Psi\rangle \\ &= \Psi_{\mathrm{S,S}}(t_1, t_2) + \Psi_{\mathrm{S,L}}(t_1, t_2) + \Psi_{\mathrm{L,S}}(t_1, t_2) + \Psi_{\mathrm{L,L}}(t_1, t_2).\end{aligned} \tag{8.9}$$

In the second line, the quantity

$$\Psi_{r_1,r_2}(t_1, t_2) = \langle 0| E^{(+)}_{2,r_2}(t_2) E^{(+)}_{1,r_1}(t_1) |\Psi\rangle, \quad r_1, r_2 \in \{\mathrm{S}, \mathrm{L}\}, \tag{8.10}$$

arises, which can be interpreted as the two-photon probability amplitude of the first photon taking the path r_1 to the detector D_1 and the second photon reaching the detector D_2 via the path r_2. As shown in Appendix A.5, it takes the form

$$\begin{aligned}\Psi_{r_1,r_2}(t_1, t_2) = \eta e^{-\left(i\omega_\mathrm{a} + \frac{\Gamma_\mathrm{a}}{2}\right)\left(t_1 - \frac{r_1}{c}\right)} \Theta\left(t_1 - \frac{r_1}{c}\right) \\ \times e^{-\left(i\omega_\mathrm{b} + \frac{\Gamma_\mathrm{b}}{2}\right)\left[\left(t_2 - \frac{r_2}{c}\right) - \left(t_1 - \frac{r_1}{c}\right)\right]} \Theta\left[\left(t_2 - \frac{r_2}{c}\right) - \left(t_1 - \frac{r_1}{c}\right)\right]\end{aligned} \tag{8.11}$$

with the constant η defined in the appendix. Subsequently, we can evaluate the two-time second-order correlation function $G^{(2)}(t_1, t_2)$ and integrate it to obtain the second-order correlation function as a function of the delay time of the detection events, τ_D, according to Eq. (8.3). For simplicity, we assume a variable but equivalent relative phase ϕ_T between the short and the long path for both photons,

$$\phi_T \equiv \omega_\mathrm{ab} T = \omega_\mathrm{b} T + 2\pi z, \quad z \in \mathbb{Z}. \tag{8.12}$$

Alternatively, it would also be possible to consider non-equivalent phases or adjust the phases via an asymmetric interferometer with different delay times T_a and T_b in the two arms. Evaluating the second-order correlation function defined piecewise, we obtain

$$G^{(2)}(\tau_\mathrm{D}) = \begin{cases} 0, & -T > \tau_\mathrm{D} \\ \frac{\eta^2}{4\Gamma_\mathrm{a}} e^{-\Gamma_\mathrm{b}(\tau_\mathrm{D} + T)}, & -T \leq \tau_\mathrm{D} < 0 \\ \frac{\eta^2}{2\Gamma_\mathrm{a}} e^{-\Gamma_\mathrm{b}\tau_\mathrm{D}} \Big[1 + \frac{1}{2} e^{-\Gamma_\mathrm{b} T} + e^{-\Gamma_\mathrm{a}\frac{T}{2}} \cos(2\phi_T) & \\ \qquad + \left(e^{-\Gamma_\mathrm{b}\frac{T}{2}} + e^{-(\Gamma_\mathrm{a} + \Gamma_\mathrm{b})\frac{T}{2}}\right) \cos(\phi_T)\Big], & 0 \leq \tau_\mathrm{D} < T \\ \frac{\eta^2}{2\Gamma_\mathrm{a}} e^{-\Gamma_\mathrm{b}\tau_\mathrm{D}} \Big[1 + \frac{1}{2}\left(e^{-\Gamma_\mathrm{b} T} + e^{\Gamma_\mathrm{b} T}\right) + e^{-\Gamma_\mathrm{a}\frac{T}{2}} + e^{-\Gamma_\mathrm{a}\frac{T}{2}} \cos(2\phi_T) & \\ \qquad + \left(1 + e^{-\Gamma_\mathrm{a}\frac{T}{2}}\right)\left(e^{-\Gamma_\mathrm{b}\frac{T}{2}} + e^{\Gamma_\mathrm{b}\frac{T}{2}}\right) \cos(\phi_T)\Big], & T \leq \tau_\mathrm{D}. \end{cases} \tag{8.13}$$

The analytical results for the second-order correlation function are presented in Fig. 8.3 for different phases ϕ_T between the short and the long paths to the detectors. Fig. 8.3 a shows

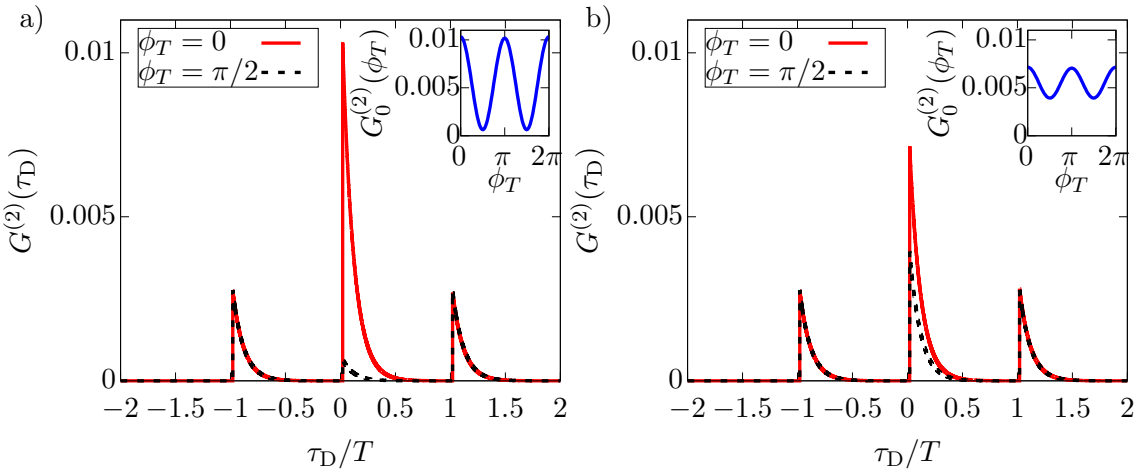

Figure 8.3: Second-order correlation function as a function of the delay time between the registration of the first and the second photon for different phases ϕ_T (mod 2π) between the short and the long paths to the detectors. Inset: Height of the central peak at $\tau_D = 0$ as a function of ϕ_T (mod 2π). (a) $\Gamma_a T = 0.25$, $\Gamma_b T = 10$. (b) $\Gamma_a T = 2.5$, $\Gamma_b T = 10$.

the results for $\Gamma_a T = 0.25$, $\Gamma_b T = 10$ and Fig. 8.3 b for $\Gamma_a T = 2.5$, $\Gamma_b T = 10$. In this limit of $\Gamma_a T \ll \Gamma_b T$, three separate peaks arise. While the two side peaks at $\tau_D = -T$ and $\tau_D = T$ are independent of ϕ_T, the height of the central peak at $\tau_D = 0$ changes when ϕ_T is varied. This is due to the fact, that the left peak at $\tau_D = -T$ can be uniquely associated with the scenario of the first photon taking the long path and the second photon taking the short path to the respective detector. The right peak can be clearly attributed to the first photon taking the short and the second photon taking the long path. The central peak, in contrast, originates from either both photons taking the short or both photons taking the long paths to the detectors. The ignorance of the actual paths the photons take gives rise to interference manifesting as an oscillation of the height of the central peak with the phase ϕ_T. This oscillation is shown in the insets of Fig. 8.3. The asymmetric shape of the peaks in Fig. 8.3 can be attributed to the fact that we frequency-filter the photons and, therefore, know which photon is detected by which detector. Without this assumption, additional terms arise in Eq. (8.11) where the roles of the photons are interchanged. This leads to symmetric peaks in the second-order correlation function $G^{(2)}(\tau_D)$ as discussed in more detail in Appendix A.6.

8.1.3 Visibility of the interference

When comparing Figs. 8.3 a and b, we see that the amplitude with which the height of the central peak oscillates depends strongly on the system parameters. The height of the central peak as a function of the relative phase between the short and the long paths to the detectors, $G_0^{(2)}(\phi_T)$, for $\Gamma_a T \ll \Gamma_b T$, obeys

$$G_0^{(2)}(\phi_T) = \frac{\eta^2}{2\Gamma_a}\left[1 + e^{-\Gamma_a \frac{T}{2}} \cos(2\phi_T)\right], \tag{8.14}$$

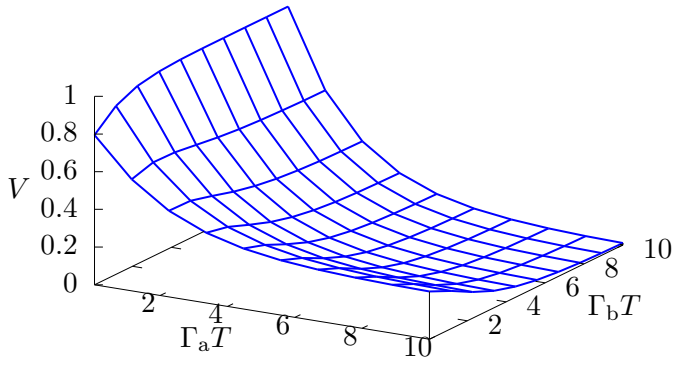

Figure 8.4: Visibility of the $G^{(2)}$ interference in the Franson interferometer as a function of the system parameters $\Gamma_a T$ and $\Gamma_b T$.

which takes on its minimal value at $\phi_T = \left(n + \frac{1}{2}\right)\pi$, $n \in \mathbb{N}$, and its maximal value at $\phi_T = n\pi$. We can quantify how pronounced the oscillation with the phase ϕ_T is by introducing the visibility of the interference, V, according to

$$V \equiv \frac{G_0^{(2)}(0) - G_0^{(2)}\left(\frac{\pi}{2}\right)}{G_0^{(2)}(0) + G_0^{(2)}\left(\frac{\pi}{2}\right)}. \tag{8.15}$$

For the system considered in Fig. 8.3 a, the visibility we find is $V = 0.88$, while the parameters used for Fig. 8.3 b result in $V = 0.29$. The visibility as a function of the decay rates of the 3LS scaled with the delay time T between the long and the short paths to the detectors, that is, $\Gamma_a T$ and $\Gamma_b T$, is shown in Fig. 8.4. A high visibility can be found for systems in which it holds that $\Gamma_a T \ll 1$ and $\Gamma_b T \gg 1$, while systems in which the decay rates are comparable, and especially if $\Gamma_a T \gtrapprox \Gamma_b T > 1$, a relatively low visibility is to be expected.

8.2 Controlling the visibility of the two-photon interference

After studying how the visibility of the $G^{(2)}$ interference in the Franson setup depends on the system parameters, we include a feedback mechanism to control the emitter dynamics and, hence, the second-order correlation function. We simulate the system within the MPS framework, as introduced in Sec. 5.1, which allows for an efficient and numerically exact treatment of the non-Markovian system dynamics.

8.2.1 Setup of the Franson interferometer with feedback

We subject the 3LS to coherent time-delayed feedback at the delay time τ_{FB} by implementing an additional feedback loop as shown in Fig. 8.5. We consider separate channels to be able to subject the transitions of the 3LS to feedback individually. As a proof of

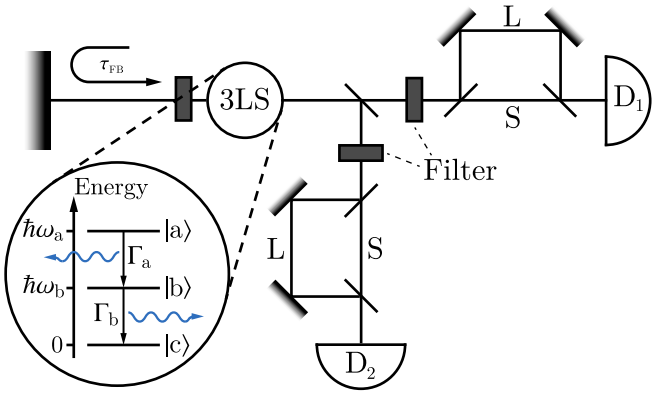

Figure 8.5: Setup of the Franson interferometer with feedback. To the conventional Franson setup, shown in Fig. 8.2, a feedback loop is added, which allows subjecting the $|\mathrm{a}\rangle \leftrightarrow |\mathrm{b}\rangle$ transition of the 3LS to feedback at the delay time τ_{FB}.

principle, we implement feedback solely on the $|\mathrm{a}\rangle \leftrightarrow |\mathrm{b}\rangle$ transition of the 3LS, which is realizable experimentally by frequency-filtering the photons. In the Hamiltonian of the system, given in Eq. (8.1), the feedback mechanism can be encoded via the coupling strength between the 3LS transition and the corresponding reservoir, see Sec. 5.1.1. With feedback, the coupling of the $|\mathrm{a}\rangle \leftrightarrow |\mathrm{b}\rangle$ transition to the first channel takes on a sinusoidal form, $g_{\mathrm{a}}(\omega) = g_a \sin(\omega\tau_{\mathrm{FB}}/2)$, while the coupling of the $|\mathrm{b}\rangle \leftrightarrow |\mathrm{c}\rangle$ transition to the second channel without feedback can be assumed as constant, $g_{\mathrm{b}}(\omega) = g_b$. The Hamiltonian describing the system with feedback in the rotating frame of its non-interacting part, thus, reads

$$H_{\mathrm{I}} = \int d\omega\, \hbar g_{\mathrm{a}} \sin(\omega\tau_{\mathrm{FB}}/2) \left(r_\omega^{\dagger(1)} \sigma_-^{(1)} e^{-i(\omega_{\mathrm{ab}}-\omega)t} + \mathrm{H.c.} \right) + \int d\omega\, \hbar g_{\mathrm{b}} \left(r_\omega^{\dagger(2)} \sigma_-^{(2)} e^{-i(\omega_{\mathrm{b}}-\omega)t} + \mathrm{H.c.} \right). \quad (8.16)$$

In the next step, this Hamiltonian is used for the simulation of the system dynamics.

8.2.2 Simulation within the matrix product state framework

For the simulation of the time evolution in the Franson interferometric setup, the MPS framework is employed. In analogy to Sec. 5.1.1, we derive the stroboscopic time evolution operator U_k describing the time evolution from time t_k to t_{k+1}, $t_k = k\Delta t$, $k \in \mathbb{N}$, according to

$$|\psi(t_{k+1})\rangle = U_k |\psi(t_k)\rangle, \quad U_k = \mathcal{T} \exp\left[-\frac{i}{\hbar} \int_{t_k}^{t_{k+1}} dt'\, H'(t) \right]. \quad (8.17)$$

The Hamiltonian H' is obtained from H_{I}, Eq. (8.16), by performing the time-independent phase shift

$$H' = U^\dagger H_{\mathrm{I}} U, \quad U = \exp\left[i \int d\omega\, r_\omega^{\dagger(1)} r_\omega^{(1)} \omega\tau_{\mathrm{FB}}/2 \right], \quad (8.18)$$

and transforming the Hamiltonian into the time domain via the quantum noise operators

$$r_t^{\dagger(i)} = \frac{1}{\sqrt{2\pi}} \int d\omega\, r_\omega^{\dagger(i)} e^{i(\omega-\omega_i)t}, \quad i \in \{1, 2\}, \quad (8.19)$$

where $\omega_1 = \omega_{\mathrm{ab}}$ and $\omega_2 = \omega_{\mathrm{b}}$. In contrast to Sec. 5.1.1, where we looked at a two-level emitter interacting with a single photonic reservoir, here, a three-level emitter coupling to two separate reservoirs is considered. The photon creation in the different reservoirs is reflected by two types of noise operators describing the photon creation in the first ($i = 1$) or the second reservoir ($i = 2$). The noise operators satisfy $\left[r_t^{(i)}, r_{t'}^{\dagger(j)}\right] = \delta_{ij}\delta(t - t')$ and lead to the expression

$$H' = i\hbar\sqrt{\Gamma_{\mathrm{a}}}\left[\left(r_t^{\dagger(1)} - r_{t-\tau_{\mathrm{FB}}}^{\dagger(1)} e^{i\omega_{\mathrm{ab}}\tau_{\mathrm{FB}}}\right)\sigma_-^{(1)} - \mathrm{H.c.}\right] + \hbar\sqrt{\Gamma_{\mathrm{b}}}\left[r_t^{\dagger(2)}\sigma_-^{(2)} + \mathrm{H.c.}\right] \tag{8.20}$$

with the decay rates $\Gamma_{\mathrm{a}} = \pi g_{\mathrm{a}}^2/2$ and $\Gamma_{\mathrm{b}} = 2\pi g_{\mathrm{b}}^2$. Note that the definitions of the decay rates differ by a factor four, which allows treating the non-Markovian feedback channel and the Markovian channel without feedback on an equal footing without having to take additional time bins for the Markovian channel into consideration, see Sec. 5.1.4. We evaluate the stroboscopic time evolution operator and introduce the noise increments for the two channels,

$$\Delta R_k^{\dagger(i)} = \int_{t_k}^{t_{k+1}} dt\, r_t^{\dagger(i)} \tag{8.21}$$

with the commutation relation $\left[\Delta R_k^{(i)}, \Delta R_{k'}^{\dagger(j)}\right] = \Delta t\delta_{ij}\delta_{kk'}$. Assuming $\tau_{\mathrm{FB}} = l\Delta t$, $l \in \mathbb{N}$, we obtain

$$U_k = \exp\left\{\sqrt{\Gamma_{\mathrm{a}}}\left[\sigma_+^{(1)}\left(\Delta R_k^{(1)} - \Delta R_{k-l}^{(1)} e^{i\omega_{\mathrm{ab}}\tau_{\mathrm{FB}}}\right) - \mathrm{H.c.}\right] - i\sqrt{\Gamma_{\mathrm{b}}}\left[\sigma_+^{(2)}\Delta R_k^{(2)} + \mathrm{H.c.}\right]\right\}. \tag{8.22}$$

When setting up the MPS, the two channels are accounted for by two time bins per time step, one for each channel. Furthermore, in analogy to Eq. (8.6), the noise increments are split up to account for the two equiprobable paths to the detectors according to

$$\Delta R_k^{\dagger(i)} = \frac{1}{2}\left(\Delta R_{k,\mathrm{S}}^{\dagger(i)} + \Delta R_{k,\mathrm{L}}^{\dagger(i)}\right), \tag{8.23}$$

where the delay time between the short and the long paths to the detectors is assumed to be a multiple of the step size $T = N_T\Delta t$, $N_T \in \mathbb{N}$. Thus, in total, there are four time bins per time step. The time evolution algorithm is illustrated in Fig. 8.6. The four types of time bins are denoted as S-1 (short path to detector D_1, red box), S-2 (short path to D_2, orange box), L-1 (long path to D_1, green box), and L-2 (long path to D_2, black box). At the beginning of each time step, the bins containing the feedback signal (S-1 and L-1) are swapped $2(l-1)$ steps to the right so that they are placed next to the 3LS bin (blue box) (Fig. 8.6 a). This way the time evolution can be performed efficiently by contracting the 3LS bin, the feedback bins, and the current time bins with the stroboscopic time evolution operator (purple box) (Fig. 8.6 b). Afterward, the resulting tensor is decomposed. The four output bins are swapped to the left of the feedback loop, while the two time bins that are kept next to the 3LS bin account for the emission into this feedback loop (Fig. 8.6 c). Subsequently, the next time evolution step can be performed (Fig. 8.6 d). After N time steps, the time evolution is completed and we rearrange the bins to include the different path lengths and the relative phase between the short and the long paths. To that end, all bins describing the photons taking the short paths to the detectors are swapped $2N_T$ steps to the left and subjected to a phase shift (Fig. 8.6 e). The $2N_T$ vacuum bins placed at the beginning of the MPS describe the vacuum signal reaching the detectors via the

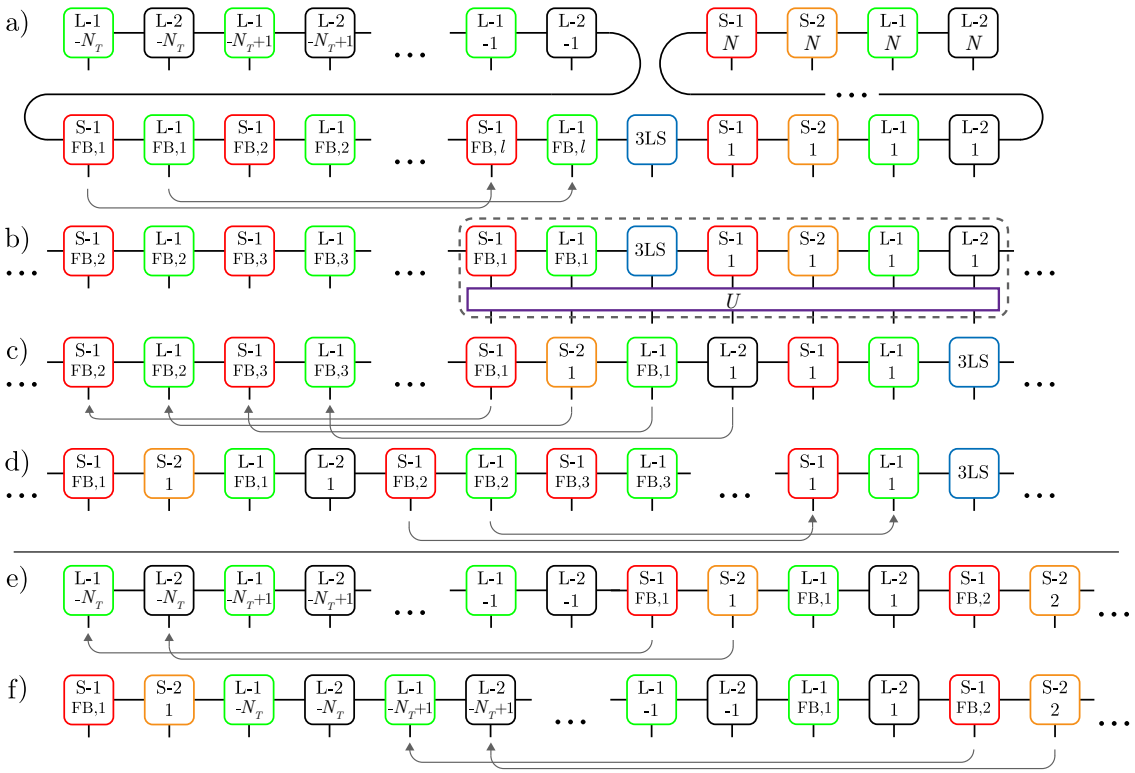

Figure 8.6: Diagrammatic representation of the time evolution algorithm for the Franson setup with feedback within the MPS framework. There are four types of time bins describing the short path to the detector D_1 (S-1, red box), the short path to D_2 (S-2, orange box), the long path to D_1 (L-1, green box), and the long path to D_2 (L-2, black box) as well as a bin representing the three-level system (3LS, blue box). (a) The time bins containing the feedback signal are swapped next to the 3LS bin. (b) The feedback bins, the 3LS bin, and the current time bins are contracted with the stroboscopic time evolution operator (U, purple box). (c) The output bins are placed to the left of the bins in the feedback loop. (d) The procedure is repeated N times. (e) After the time evolution is completed, the bins referring to the short paths are swapped $2N_T$ steps to the left and subjected to a phase shift to account for the delay time and the relative phase between the short and the long paths. (f) The procedure is repeated N times.

long paths initially. The step is repeated until all bins accounting for the short paths have been moved (Fig. 8.6 f). Note that the colors used in the diagrams in this section do not describe the orthogonality properties of the bins as in Sec. 5.1. Instead, we use them to distinguish the different types of bins. During the time evolution, the OC is kept at one of the feedback bins. Subsequently, when rearranging the bins, the OC is moved to the short bins that are shifted to the left in each step.

After the time evolution has been completed and the time and phase shifts between short and long paths to the detectors have been included, we can evaluate the second-order correlation function of the photons. To that end, we calculate the two-time second-order correlation function $G^{(2)}(t_1, t_2)$ as introduced in Eq. (8.4) via the MPS algorihm illustrated in Fig. 8.7. The output bins describe the signal that reaches the detectors at the time step u_i, $i \in \{1, \ldots, N\}$. We start at the left end of the MPS by calculating $G^{(2)}(u_1, u_1)$ (Fig. 8.7 a). Subsequently, the time bins describing the signal at the detector D_1 for time step u_1 are swapped with the corresponding bins for the next time step u_2 (Fig. 8.7 b) so that it is possible to evaluate $G^{(2)}(u_1, u_2)$ efficiently (Fig. 8.7 c). This is repeated until we have evaluated $G^{(2)}(u_1, u_k)$ for all $k \in \{1, \ldots, N\}$. We then start again at the beginning and calculate $G^{(2)}(u_2, u_1)$ and so on, until $G^{(2)}(t_1, t_2)$ has been determined for all possible combinations of t_1 and t_2, where t_1, $t_2 \in \{u_1, \ldots, u_N\}$. Integrating the two-time second-order correlation function according to Eq. (8.3), we finally obtain the second-order correlation function as a function of the delay time of the photon detection events, $G^{(2)}(\tau_\mathrm{D})$.

To ensure the validity of the MPS approach, the results are benchmarked in the case without feedback using the analytical results presented in Sec. 8.1, see Appendix A.7 for more details.

8.2.3 Enhancing the visibility of the interference

The implementation of a coherent time-delayed feedback mechanism opens up the possibility to modify the decay of the excitation in the 3LS and, thus, allows controlling the times of emission of the photons. Here, we study the effect of feedback on the dynamics as well as on the second-order correlation function focussing on the case where only the first channel coupled to the $|\mathrm{a}\rangle \leftrightarrow |\mathrm{b}\rangle$ transition of the 3LS with transition frequency ω_ab is subjected to feedback.

If a photon is emitted into the feedback loop, it is reflected on the mirror and fed back to the 3LS after the delay time τ_FB. During one round trip, a resonant photon acquires a feedback phase $\phi_\mathrm{FB} = \omega_\mathrm{ab}\tau_\mathrm{FB}$, which determines the impact of the feedback signal on the system dynamics in analogy to Sec. 5.3. On the one hand, the interference of the emission from the 3LS and the feedback signal can result in an accelerated decay of the excitation in the 3LS compared to the usual Markovian behavior. The strongest effect occurs for a phase $\phi_\mathrm{FB} = (2m + 1)\pi$, $m \in \mathbb{N}$. On the other hand, the decay can be slowed down, where the impact is highest for $\phi_\mathrm{FB} = 2\pi m$. In comparison to the two-level emitter we considered in Sec. 5.3, however, it is not possible to stabilize the emitter excitation at a non-zero value in the long-time limit. Eventually, the emitter decays to the ground state and two photons are emitted.

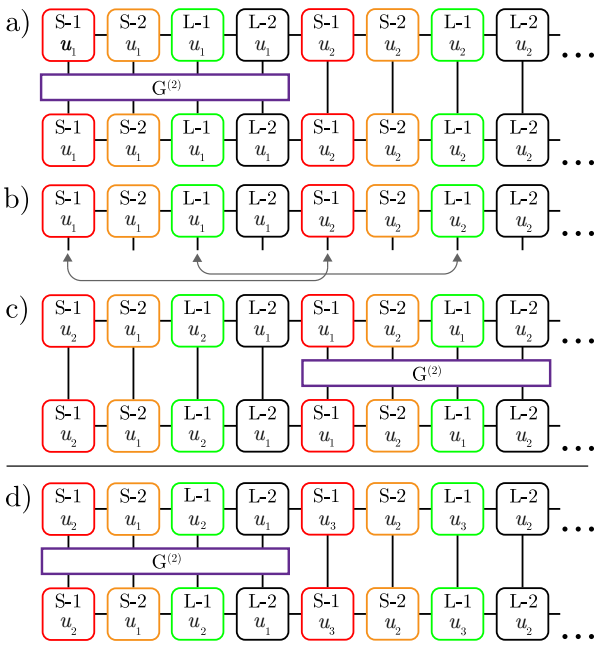

Figure 8.7: Diagrammatic representation of the algorithm for the evaluation of the two-time second-order correlation function $G^{(2)}(t_1, t_2)$, t_1, $t_2 \in \{u_1, \ldots, u_N\}$. Two nested loops are necessary to account for all possible combinations of t_1 and t_2. (a) Evaluation of $G^{(2)}(u_1, u_1)$. (b) The time bins describing the signal registered at the detector D_1, S-1 and L-1, are exchanged with the corresponding time bins for the next time step u_2. (c) $G^{(2)}(u_1, u_2)$ is calculated. The procedure is repeated until $G^{(2)}(u_1, u_k)$ has been determined for all $k \in \{1, \ldots, N\}$. (d) Afterward, we start the second loop through the MPS by calculating $G^{(2)}(u_2, u_1)$ until we have completely determined $G^{(2)}(t_1, t_2)$.

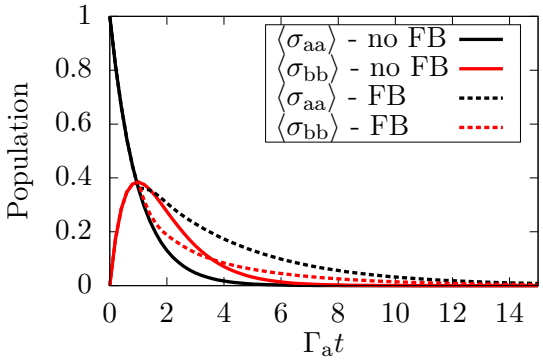

Figure 8.8: Dynamics of the population of the upper state, $\langle\sigma_{aa}\rangle$, and of the middle state, $\langle\sigma_{bb}\rangle$, of a 3LS characterized by $\Gamma_a = \Gamma_b$ in the case without feedback (no FB, solid lines) and with feedback at $\Gamma_a\tau_{FB} = 1$ (FB, dashed lines).

In Sec. 8.1, we saw that the visibility of the $G^{(2)}$ interference for the conventional Franson interferometer depends strongly on the decay rates of the 3LS. A high visibility can be found if the upper state of the 3LS decays slowly in comparison to the middle state. Therefore, it is interesting to implement a feedback mechanism that slows down the decay of the upper state and study the possibility to enhance the visibility of the $G^{(2)}$ interference in this way. Since the decay is slowed down maximally for a feedback phase $\phi_{FB} = 2\pi m$, in the following, we assume that this condition is fulfilled in the considered systems.

As an exemplary system, we look at a 3LS with $\Gamma_a = \Gamma_b$ and compare the emitter dynamics without feedback and with feedback at $\Gamma_a\tau_{FB} = 1$ on the $|a\rangle \leftrightarrow |b\rangle$ transition as shown in Fig. 8.8. With feedback, the decay from the upper state is slowed down (dashed black line) in comparison to the case without feedback (solid black line). The modified decay of the emitter from the upper to the middle state also modifies the population dynamics of the middle state itself (dashed red line) compared to the dynamics without feedback (solid red line). Overall, the feedback mechanism results in an accelerated decay of the upper state in relation to the decay of the middle state.

In the next step, we study the impact the feedback mechanism has on the second-order correlation function for the system considered above. Evaluating $G^{(2)}(\tau_D)$ without and with feedback for the 3LS with $\Gamma_a = \Gamma_b$, here $\Gamma_a T = \Gamma_b T = 4$, we observe the behavior shown in Fig. 8.9. To obtain the depicted results, we simulated the dynamics up to $\Gamma_a t_{max} = 20$ to ensure that two photons have been emitted from the 3LS. In the considered parameter regime, a relatively low visibility of the $G^{(2)}$ interference is to be expected, see Fig. 8.4. More precisely, without feedback (solid black and red lines) we find a visibility of the $G^{(2)}$ interference of $V = 0.19$. If feedback is implemented, the peaks are split and shifted on the x-axis by $-\tau_{FB}$ due to the additional time a photon needs in the feedback loop. The height of the central peak at $\tau_D = -\tau_{FB}$ is increased for a relative phase between the short and the long paths to the detectors of $\phi_T = 2\pi n$, $n \in \mathbb{N}$, (dashed black line). For a relative phase $\phi_T = 2(n + 1/2)\pi$, the height is reduced (dashed red line). The visibility that can be observed in the case with feedback is $V = 0.51$. Thus, there is a 168 % increase in the visibility in comparison to the case without feedback. With feedback, the visibility is raised above the classical threshold of $V = 0.5$ [228, 230, 247]. A visibility surpassing this limit does not imply a violation of a Bell-type inequality, which would require a different setup and a higher visibility, as discussed in Sec. 8.1.1, but points toward the non-classical

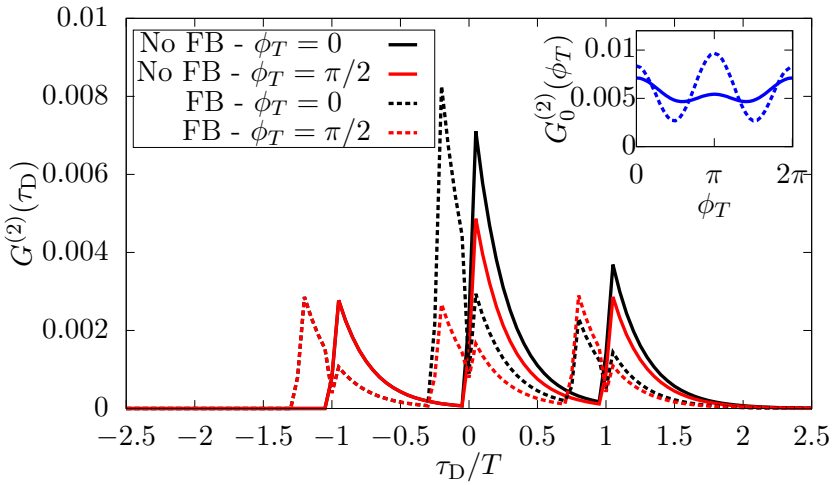

Figure 8.9: Second-order correlation function for $\Gamma_a T = \Gamma_b T = 4$ without feedback (no FB, solid lines) and with feedback at $\Gamma_a \tau_{FB} = 1$ (FB, dashed lines) for different relative phases between the short and the long paths to the detectors, ϕ_T (mod 2π). Inset: Height of the central peak as a function of ϕ_T (mod 2π) without feedback (solid line) and with feedback (dashed line).

nature of the light. The inset of Fig. 8.9 illustrates that the oscillation of the height of the central peak with ϕ_T is significantly more pronounced with feedback (dashed blue line) than without feedback (solid blue line).

The potential to increase the visibility of the $G^{(2)}$ interference depends strongly on the system parameters. In Fig. 8.10, the visibility as a function of $\Gamma_a T$ and $\Gamma_b T$ is presented for the case of feedback at $\tau_{FB} = T/4$ (green plane) and compared to the visibility without feedback (blue plane). The classical limit of $V = 0.5$ is indicated by the grey plane. To ensure that two photons have been emitted from the 3LS, we have adjusted the simulation time t_{max} according to the decay rates Γ_a and Γ_b and checked for the complete decay of the 3LS from the upper to the ground state. We focus on the parameter regime of relatively large $\Gamma_a T$ and $\Gamma_b T$, where without feedback a visibility well below the classical threshold of $V = 0.5$ is found. With feedback, the visibility is raised above this limit in much of the considered parameter area. In the considered regime, the feedback mechanism has a larger impact than in the regime of small decay rates. In Fig. 8.11, the visibility with feedback in relation to the visibility without feedback, $V_{FB}/V_{no\ FB}$, as a function of $\Gamma_a T$ and $\Gamma_b T$ is shown and we can conclude that the effectiveness of the feedback control scheme depends particularly on the decay rate of the upper state, while the decay rate of the middle state plays a minor role.

8.3 Conclusion

In this chapter, we studied the potential of coherent time-delayed feedback to enhance the visibility of the interference in the second-order correlation function that can be observed using the Franson interferometer. In the conventional setup of the interferometer, that is, without feedback, the visibility depends strongly on the system parameters. For two photons emitted from a 3LS in ladder configuration, a high visibility can only be observed

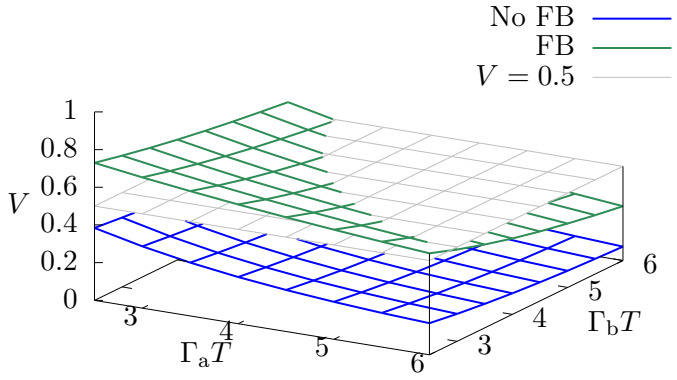

Figure 8.10: Comparison of the visibility of the $G^{(2)}$ interference in the Franson interferometer as a function of the system parameters $\Gamma_a T$ and $\Gamma_b T$ without feedback (no FB, blue plane) and with feedback at $\tau_{FB} = T/4$ (FB, green plane). The classical threshold of $V = 0.5$ is indicated by the grey plane.

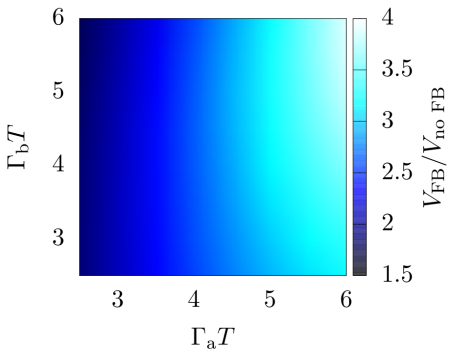

Figure 8.11: Enhancement of the visibility of the $G^{(2)}$ interference with feedback at $\tau_{FB} = T/4$, V_{FB}, in relation to the visibility without feedback, $V_{no\ FB}$, as a function of $\Gamma_a T$ and $\Gamma_b T$.

if the upper state decays slowly in comparison to the middle state. In common two-photon sources, such as the biexciton-exciton cascade in a semiconductor quantum dot, however, this requirement is typically not met. To nevertheless obtain a high visibility, we suggested implementing coherent time-delayed feedback to decelerate the decay of the excitation from the upper state of the 3LS. Simulating the non-Markovian dynamics within the MPS framework, we studied the impact of feedback on the second-order correlation function and found that the approach can increase the visibility significantly. The effect of the feedback mechanism is particularly strong in the case of a fast decaying upper state. Since the visibility of the two-photon interference in the Franson interferometer indicates the energy-time entanglement of the photons, we conclude that coherent feedback opens up the possibility to control and, in particular, enhance the energy-time entanglement of the photons.

9 Entanglement robustness to excitonic spin precession in a biexciton cascade

As a promising source of polarization-entangled photon pairs, the radiative biexciton cascade in a semiconductor quantum dot has attracted considerable attention [248–250]. It is of interest due to its integrability and scalability and, furthermore, allows for the on-demand creation of entangled photon pairs via two-photon excitation [222, 251]. For the realization of quantum information processing protocols it, therefore, has an advantage over probabilistic ways of generating polarization-entangled photon pairs such as spontaneous parametric down-conversion [252].

A biexciton is a zero-spin bound complex of two electrons and two holes. If the electron-hole pairs recombine, two photons are emitted successively. These photons are of opposite circular polarization since angular momentum has to be conserved. As a consequence, there are two equally probable decay paths from the biexcitonic state to the ground state via two possible intermediate excitonic states. If the excitonic states are degenerate, a maximally polarization-entangled photon pair is emitted, which, in the rectilinear $\{|\mathrm{H}\rangle, |\mathrm{V}\rangle\}$ polarization basis of horizontally (H) or vertically (V) polarized photons, is described by the state

$$|\Psi\rangle = \frac{1}{\sqrt{2}} \left(|\mathrm{HH}\rangle + |\mathrm{VV}\rangle\right). \tag{9.1}$$

Typically, however, the excitonic states are nondegenerate and exhibit a fine-structure splitting $\hbar\Delta_{\mathrm{FSS}}$ due to an anisotropic electron-hole exchange interaction [253, 254]. In the emitted two-photon state, the fine structure manifests as a relative phase that precesses with time so that

$$|\Psi(t)\rangle = \frac{1}{\sqrt{2}} \left(|\mathrm{HH}\rangle + e^{-i\Delta_{\mathrm{FSS}}t} |\mathrm{VV}\rangle\right), \tag{9.2}$$

where t is the time between the emission of the biexciton photon and the emission of the exciton photon. The fine-structure splitting makes it, in principle, possible to spectrally distinguish the decay paths and, therefore, is detrimental to maximal entanglement in a time-integrated measurement setup [255]. To deal with this problem, various techniques have been developed that aim at reducing the fine-structure splitting below the radiative linewidth [256–259] or at reducing the influence of the nondegeneracy [249, 250]. In a time-resolved polarization measurement, a highly entangled two-photon state is possible despite a finite fine-structure splitting [260]. A perfect temporal resolution, according to Heisenberg's uncertainty principle, results in ignorance with respect to the energy of the photons so that the which-path information is erased and a maximally entangled two-photon state can be obtained. A finite temporal resolution limits the attainable degree of entanglement but still allows for highly entangled photon pairs.

Another obstacle for the generation of maximal entanglement from the biexciton cascade are spin-flip dephasing processes in the excitonic states, which are thought to result from

the interaction of the exciton with nuclear spins or the scattering with excess charges [261]. In this context, an excitonic spin precession leading to transitions between the excitonic states and enabling the emission of crosslinearly polarized photons (one horizontally and one vertically polarized photon) has usually been viewed as a disqualifier for the respective quantum dot as a source of highly entangled photon pairs. However, as we show here, in a time-resolved measurement setup such an undifferentiated preselection is not justified.

In this chapter, which is based on our work presented in Ref. [262], we study the impact of an excitonic spin precession on the polarization entanglement of a photon pair emitted from a biexciton cascade. We show that, when it can be modeled as a coherent process, this spin precession does not necessarily have a detrimental impact and for a sufficiently high temporal resolution, a highly entangled photon pair can be obtained. To that end, in Sec. 9.1, we construct a theoretical model including transitions between the excitonic states in the unitary time evolution of the system, which we validate by comparison with experimental data from a polarization tomography. Subsequently, in Sec. 9.2, we evaluate the impact of the excitonic transitions on the entanglement of the emitted photons in a time-resolved measurement setup.

9.1 Modeling the biexciton cascade with excitonic transitions

The biexciton cascade with a fine-structure splitting $\hbar\Delta_{\mathrm{FSS}}$ and excitonic transitions at rate f is illustrated in Fig 9.1. The Hamiltonian governing the dynamics of the quantum dot interacting with the electromagnetic field in the dipole and rotating-wave approximation, see Sec. 3.2, reads

$$\begin{aligned} H = {} & \hbar\omega_{\mathrm{B}}\sigma_{\mathrm{BB}} + \hbar\left(\omega_{\mathrm{XG}} - \frac{\Delta_{\mathrm{FSS}}}{2}\right)\sigma_{\mathrm{HH}} + \hbar\left(\omega_{\mathrm{XG}} + \frac{\Delta_{\mathrm{FSS}}}{2}\right)\sigma_{\mathrm{VV}} + \hbar f\left(\sigma_{\mathrm{HV}} + \sigma_{\mathrm{VH}}\right) \\ & + \int d\omega\, \hbar\omega \left(a^{\dagger}_{\omega,\mathrm{BH}}a_{\omega,\mathrm{BH}} + a^{\dagger}_{\omega,\mathrm{BV}}a_{\omega,\mathrm{BV}} + a^{\dagger}_{\omega,\mathrm{XH}}a_{\omega,\mathrm{XH}} + a^{\dagger}_{\omega,\mathrm{XV}}a_{\omega,\mathrm{XV}}\right) \\ & + \int d\omega\, \hbar g_0 \left(a^{\dagger}_{\omega,\mathrm{BH}}\sigma_{\mathrm{HB}} + a^{\dagger}_{\omega,\mathrm{BV}}\sigma_{\mathrm{VB}} + a^{\dagger}_{\omega,\mathrm{XH}}\sigma_{\mathrm{GH}} + a^{\dagger}_{\omega,\mathrm{XV}}\sigma_{\mathrm{GV}} + \mathrm{H.c.}\right). \end{aligned} \tag{9.3}$$

Here, the operators $\sigma_{ij} = |i\rangle\langle j|$ describe transitions between the electronic states, $|i\rangle, |j\rangle \in \{|\mathrm{B}\rangle, |\mathrm{X_H}\rangle, |\mathrm{X_V}\rangle, |\mathrm{G}\rangle\}$. These states denote the biexciton, the exciton about to emit a horizontally polarized photon, the exciton about to emit a vertically polarized photon, and the ground state, respectively. As a subscript, the excitonic label is replaced by the corresponding direction of polarization for readibility, $\mathrm{X_H} \to \mathrm{H}$, $\mathrm{X_V} \to \mathrm{V}$. The two excitonic states are separated by the energy $\hbar\Delta_{\mathrm{FSS}}$ and centered around the energy $\hbar\omega_{\mathrm{XG}}$ so that the $|\mathrm{X_H}\rangle$ exciton has the energy $\hbar\omega_{\mathrm{H}} = \hbar\left(\omega_{\mathrm{XG}} - \frac{\Delta_{\mathrm{FSS}}}{2}\right)$ while the energy of the $|\mathrm{X_V}\rangle$ exciton is $\hbar\omega_{\mathrm{V}} = \hbar\left(\omega_{\mathrm{XG}} + \frac{\Delta_{\mathrm{FSS}}}{2}\right)$. The energy of the biexciton is $\hbar\omega_{\mathrm{B}} = \hbar\left(\omega_{\mathrm{XG}} + \omega_{\mathrm{BX}}\right)$ with the biexciton-exciton transition energy $\hbar\omega_{\mathrm{BX}} = \hbar\left(\omega_{\mathrm{XG}} - \omega_{\mathrm{bind}}\right)$, where $\hbar\omega_{\mathrm{bind}}$ describes the biexciton binding energy. With respect to the photonic reservoir, we distinguish between the biexciton photon (B) and the exciton photon (X) as well as between the horizontal (H) and the vertical polarization direction (V). The annihilation (creation) of a photon with frequency ω is described by the operator $a^{(\dagger)}_{\omega,im}$ satisfying the bosonic commutation relation $\left[a_{\omega,im}, a^{\dagger}_{\omega',jn}\right] = \delta(\omega-\omega')\delta_{ij}\delta_{mn}$, $i,j \in \{\mathrm{B},\mathrm{X}\}$, $m,n \in \{\mathrm{H},\mathrm{V}\}$. The

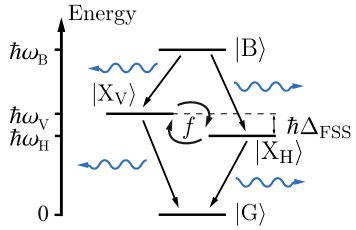

Figure 9.1: Biexciton cascade in a semiconductor quantum dot functioning as a source of polarization-entangled photon pairs. From the biexcitonic state $|\mathrm{B}\rangle$, the quantum dot decays to one of the intermediate excitonic states $|\mathrm{X_H}\rangle$ and $|\mathrm{X_V}\rangle$ emitting either a horizontally or a vertically polarized biexciton photon. Transitions between these excitonic states, which exhibit a fine-structure splitting of $\hbar\Delta_{\mathrm{FSS}}$, occur at rate f. From the excitonic states, the quantum dot decays to the ground state emitting a second photon of either horizontal or vertical polarization.

coupling strength between the emitter and the photonic reservoirs, g_0, is considered to be constant since we assume Markovian dynamics, while it would be also interesting to study the impact of feedback on the considered system in future research. The coupling strength is related to the radiative decay rate Γ according to $g_0 = \sqrt{\Gamma}/\pi$.

In the interaction picture, this Hamiltonian can be expressed as

$$\begin{aligned} H_{\mathrm{I}} = \hbar\frac{\Delta_{\mathrm{FSS}}}{2}\left(\sigma_{\mathrm{VV}} - \sigma_{\mathrm{HH}}\right) + \hbar f\left(\sigma_{\mathrm{HV}} + \sigma_{\mathrm{VH}}\right) \\ + \int d\omega\, \hbar g_0 \Big(a^\dagger_{\omega,\mathrm{BH}}\sigma_{\mathrm{HB}} e^{i(\omega-\omega_{\mathrm{BX}})t} + a^\dagger_{\omega,\mathrm{BV}}\sigma_{\mathrm{VB}} e^{i(\omega-\omega_{\mathrm{BX}})t} \\ + a^\dagger_{\omega,\mathrm{XH}}\sigma_{\mathrm{GH}} e^{i(\omega-\omega_{\mathrm{XG}})t} + a^\dagger_{\omega,\mathrm{XV}}\sigma_{\mathrm{GV}} e^{i(\omega-\omega_{\mathrm{XG}})t} + \mathrm{H.c.}\Big). \end{aligned} \tag{9.4}$$

We show that the excitonic transitions do not change the system qualitatively but like the excitonic fine-structure splitting lead to a phase precession at a generalized frequency Ω in an adapted excitonic basis. To that end, we diagonalize the Hamiltonian in Eq. (9.4) with respect to the emitter contribution by transforming the excitonic states according to

$$|X_-\rangle = \alpha\,|X_{\mathrm{H}}\rangle - \beta\,|X_{\mathrm{V}}\rangle\,, \quad |X_+\rangle = \beta\,|X_{\mathrm{H}}\rangle + \alpha\,|X_{\mathrm{V}}\rangle\,, \tag{9.5}$$

where $\alpha^2 = \left[1 + \Delta_{\mathrm{FSS}}/\left(2\Omega\right)\right]/2$, $\beta^2 = \left[1 - \Delta_{\mathrm{FSS}}/\left(2\Omega\right)\right]/2$, and $\Omega^2 = f^2 + \left(\Delta_{\mathrm{FSS}}/2\right)^2$. Analogously, the photonic states are transformed as

$$|-\rangle = \alpha\,|\mathrm{H}\rangle - \beta\,|\mathrm{V}\rangle\,, \quad |+\rangle = \beta\,|\mathrm{H}\rangle + \alpha\,|\mathrm{V}\rangle \tag{9.6}$$

with the corresponding photon annihilation (creation) operators $a^{(\dagger)}_{\omega,im}$ satisfying the bosonic commutation relation $\left[a_{\omega,im}, a^\dagger_{\omega',jn}\right] = \delta(\omega-\omega')\delta_{ij}\delta_{mn}$, $i,j \in \{\mathrm{B},\mathrm{X}\}$, $m,n \in \{-,+\}$. In this basis, the Hamiltonian reads

$$\begin{aligned} H_{\mathrm{I}} = \hbar\Omega\left(\sigma_{++} - \sigma_{--}\right) + \int d\omega\, \hbar g_0 \Big(a^\dagger_{\omega,\mathrm{B}\text{-}}\sigma_{\text{-B}} e^{i(\omega-\omega_{\mathrm{BX}})t} + a^\dagger_{\omega,\mathrm{B}+}\sigma_{+\mathrm{B}} e^{i(\omega-\omega_{\mathrm{BX}})t} \\ + a^\dagger_{\omega,\mathrm{X}\text{-}}\sigma_{\mathrm{G}\text{-}} e^{i(\omega-\omega_{\mathrm{XG}})t} + a^\dagger_{\omega,\mathrm{X}+}\sigma_{\mathrm{G}+} e^{i(\omega-\omega_{\mathrm{XG}})t} + \mathrm{H.c.}\Big). \end{aligned} \tag{9.7}$$

By comparison with Eq. (9.4), it becomes clear that the excitonic transitions do not change the physics of the system qualitatively since the Hamiltonian describing its dynamics can

be mapped isomorphically to a Hamiltonian without excitonic transitions, $f \to 0$, but with a renormalized fine-structure splitting, $\Delta_{\mathrm{FSS}} \to 2\Omega$.

What we are interested in is the two-photon state that is emitted during the decay of the biexciton cascade. As shown in Appendix A.8, it takes the form

$$|\Psi\rangle = \int_0^\infty dt' \int_0^{t'} dt'' \left[P_{\mathrm{col}}(t'',t')\,|\mathrm{H}(t''),\mathrm{H}(t')\rangle + P^*_{\mathrm{col}}(t'',t')\,|\mathrm{V}(t''),\mathrm{V}(t')\rangle \right. \\ \left. + P_{\mathrm{xl}}(t'',t')\,|\mathrm{H}(t''),\mathrm{V}(t')\rangle - P^*_{\mathrm{xl}}(t'',t')\,|\mathrm{V}(t''),\mathrm{H}(t')\rangle\right] \quad (9.8)$$

with the coefficients for the collinear (col) and crosslinear (xl) components

$$P_{\mathrm{col}}(t'',t') = -2\Gamma e^{-\Gamma(t'+t'')}\left\{\cos\left[\Omega\left(t'-t''\right)\right] + i\frac{\Delta_{\mathrm{FSS}}}{2\Omega}\sin\left[\Omega\left(t'-t''\right)\right]\right\}, \quad (9.9)$$

$$P_{\mathrm{xl}}(t'',t') = i2\Gamma\frac{f}{\Omega}e^{-\Gamma(t'+t'')}\sin\left[\Omega\left(t'-t''\right)\right]. \quad (9.10)$$

In Eq. (9.8), the state

$$|m(t''),n(t')\rangle = a^\dagger_{\mathrm{X}n}(t')a^\dagger_{\mathrm{B}m}(t'')\,|\mathrm{vac}\rangle \quad (9.11)$$

with

$$a^\dagger_{\mathrm{B}m}\left(t''\right) = \frac{1}{\sqrt{2\pi}}\int d\omega\, e^{i(\omega-\omega_{\mathrm{BX}})t''}a^\dagger_{\omega,\mathrm{B}m}, \quad (9.12)$$

$$a^\dagger_{\mathrm{X}n}\left(t'\right) = \frac{1}{\sqrt{2\pi}}\int d\omega\, e^{i(\omega-\omega_{\mathrm{XG}})t'}a^\dagger_{\omega,\mathrm{X}n}, \quad (9.13)$$

$m,n \in \{\mathrm{H},\mathrm{V}\}$, describes the biexciton photon of polarization m emitted at time t'' and the exciton photon of polarization n emitted at time t'. Correspondingly, the detection of the biexciton photon with polarization m emitted at time t'' and the detection of the exciton photon with polarization n emitted at t' can be described by the operators $a_{\mathrm{B}m}(t'')$ and $a_{\mathrm{X}n}(t')$, respectively. As a consequence, the detection of the biexciton photon emitted at time t'' and the exciton photon emitted at t' in the different polarization states can be expressed via the state

$$|\Psi\left(t'',t'\right)\rangle = P_{\mathrm{col}}\left(t'',t'\right)|\mathrm{H}(t''),\mathrm{H}(t')\rangle + P^*_{\mathrm{col}}\left(t'',t'\right)|\mathrm{V}(t''),\mathrm{V}(t')\rangle \\ + P_{\mathrm{xl}}\left(t'',t'\right)|\mathrm{H}(t''),\mathrm{V}(t')\rangle - P^*_{\mathrm{xl}}\left(t'',t'\right)|\mathrm{V}(t''),\mathrm{H}(t')\rangle \quad (9.14)$$

with the corresponding measurement matrix elements

$$\rho_{kl,mn}\left(t'',t'\right) = \langle k(t''),l(t')|\Psi(t'',t')\rangle\,\langle\Psi(t'',t')|m(t''),n(t')\rangle\,, \quad (9.15)$$

$k,l,m,n \in \{\mathrm{H},\mathrm{V}\}$. Note that the state $|\Psi(t'',t')\rangle$ itself is not normalized but the state $|\Psi\rangle = \int_0^\infty dt' \int_0^{t'} dt''\,|\Psi(t'',t')\rangle$ is. If we normalize the state $|\Psi(t'',t')\rangle$, this gives us the probability amplitudes to measure the photons with certain polarizations under the condition that they are emitted at t'' and t'.

With the measurement matrix ρ, the elements of which are given in Eq. (9.15), we can model the polarization tomography that is performed experimentally to reconstruct the density matrix of the two photons emitted from the biexciton cascade and, this way, verify the validity of our approach. The key idea of a quantum state tomography is that a series of measurements on identically prepared copies of the system is performed so that it is

possible to reconstruct its density matrix using linear transformations of the measured quantities. To reconstruct the polarization state of the two photons, we have to perform sixteen independent correlation measurements, where the two photons are each projected onto a set of states from the three orthogonal polarization bases $\{|\mathrm{H}\rangle, |\mathrm{V}\rangle\}$, $\{|\mathrm{D}\rangle, |\mathrm{A}\rangle\}$ with

$$|\mathrm{D}\rangle = \frac{1}{\sqrt{2}}\left(|\mathrm{H}\rangle + |\mathrm{V}\rangle\right), \quad |\mathrm{A}\rangle = \frac{1}{\sqrt{2}}\left(|\mathrm{H}\rangle - |\mathrm{V}\rangle\right), \tag{9.16}$$

and $\{|\mathrm{R}\rangle, |\mathrm{L}\rangle\}$ with

$$|\mathrm{R}\rangle = \frac{1}{\sqrt{2}}\left(|\mathrm{H}\rangle + i\,|\mathrm{V}\rangle\right), \quad |\mathrm{L}\rangle = \frac{1}{\sqrt{2}}\left(|\mathrm{H}\rangle - i\,|\mathrm{V}\rangle\right). \tag{9.17}$$

From these measurements, it is possible to calculate the two-photon Stokes parameters, which fully characterize the polarization state of the photons [263].

In Fig. 9.2, the correlation measurements that are necessary for the full tomography of the two-photon polarization state are shown. The black lines represent experimental data obtained by Dr. S. Bounouar and co-workers in the group of Prof. Dr. S. Reitzenstein using an InGaAs/GaAs quantum dot. Details on the experimental realization can be found in Ref. [262]. The red lines are obtained from our theoretical model. The joint detection probability to measure the biexciton photon with polarization m and the exciton photon with polarization n, $m, n \in \{\mathrm{H}, \mathrm{V}, \mathrm{D}, \mathrm{R}\}$, as a function of the delay time t between the detection of the biexciton photon emitted at t'' and the detection of the exciton photon emitted at t' is given by

$$P_{mn}(t) = \int_0^\infty dt''\, \rho_{mn,mn}(t'', t')\Big|_{t' \to t''+t}. \tag{9.18}$$

To account for the finite temporal resolution of the detectors, we convolve the theoretical results with the system response function, which we assume to be a Gaussian $G(t)$ with a full width at half maximum of 100 ps, so that

$$P_{mn}^{\mathrm{conv}}(t) = \int_{-\infty}^{\infty} d\tau\, P_{mn}(t) G(t-\tau). \tag{9.19}$$

To fit the experimental data, we used the parameters $\Gamma = 2.4\,\mathrm{ns}^{-1}$ and $\hbar\Delta_{\mathrm{FSS}} = 12.7\,\mu\mathrm{eV}$. From the measurements, we estimated the excitonic transition rate to be $f = 9.5\,\mathrm{ns}^{-1}$.

If no excitonic transitions were taking place, we would find an exponential decay for the HH and the VV measurements and no signal for the HV and the VH measurements [260, 262]. The oscillations nevertheless observable in the measurements in Fig. 9.2 provide evidence for the occurrence of excitonic transitions, as included in our model as a manifestation of an excitonic spin precession. The frequency of the oscillations in our model is determined by the transition rate f. The oscillations that arise for the measurements in the $\{|\mathrm{D}\rangle, |\mathrm{A}\rangle\}$ and the $\{|\mathrm{R}\rangle, |\mathrm{L}\rangle\}$ bases, in contrast, can be attributed to an excitonic phase precession due to a fine-structure splitting. Since they can be observed in different bases, it is possible to study the two processes independently.

The experimental data and the theoretical model agree well for most polarization directions. However, some discrepancies arise, for example, in the RV and VR measurements, where the theoretical model underestimates the coincidences observed in the experiment. Among other points related to the specific experimental realization, a reason for this could

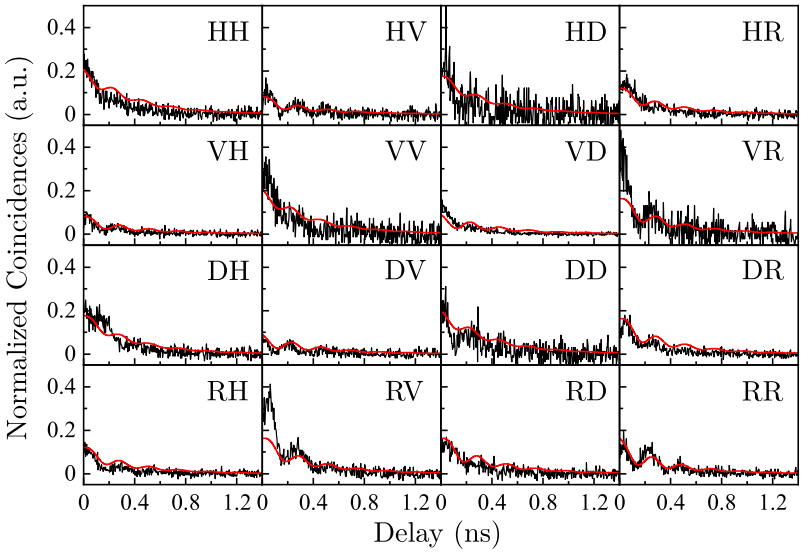

Figure 9.2: Sixteen correlation measurements that are needed for the full tomography of the two-photon polarization state (black lines) and theoretical model (red lines), where the normalized coincidences are shown as a function of the delay between the detection of the biexciton and the exciton photon. The label in each subgraph indicates the directions of polarization onto which the biexciton and the exciton photon have been projected for the respective measurement. Adapted from Ref. [262].

be that the model assumes a deterministic preparation of the biexciton while, experimentally, the situation is more complex due to the preparation of the biexciton by a continuous-wave laser. Another possible explanation for the slight deviations between experiment and theory is that, theoretically, we assume a unitary time evolution while dissipation and decoherence processes may have an influence in the experiment. While it has been shown that pure dephasing does not affect the entanglement in the case of degenerate excitonic states without transitions [264], for the general case, a more detailed model taking into account pure dephasing as well as other incoherent processes could provide further insights [265].

9.2 Polarization entanglement of the photons

After developing and validating our model, we study the impact of the excitonic transitions on the entanglement of the two photons emitted from the quantum dot. As we saw in Sec. 9.1, the considered system can be mapped isomorphically to the biexciton cascade without excitonic transitions, which allows for the creation of a maximally entangled photon pair in the case of a perfect temporal resolution [260]. Since unitary transformations do not affect the entanglement of a composite system, we can infer that two maximally entangled photons are produced in the case of a perfect temporal resolution despite the excitonic transitions. To confirm this, we use the negativity of the normalized two-photon density matrix $\rho_{\mathrm{N}}(t'',t') = \rho(t'',t')/\mathrm{tr}\left[\rho(t'',t')\right]$, describing the emission of the biexciton photon at t'' and the emission of the exciton photon at t', as a measure of the entanglement, see Sec. 4.2. Indeed, we find for the density matrix of the system, the elements of which are given in Eq. (9.15),

$$N\left[\rho_{\mathrm{N}}\left(t'',t'\right)\right] = \frac{1}{2} \tag{9.20}$$

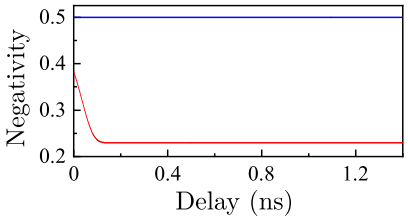

Figure 9.3: Negativity that can be extracted from the polarization tomography as a function of the delay between the detection of the biexciton and the exciton photon for a temporal resolution of 100 ps (red line) compared to the negativity that we find theoretically in the case of a perfect temporal resolution (blue line) corresponding to maximal entanglement. Adapted from Ref. [262].

corresponding to maximal entanglement for all times t'', t' with $t'' < t'$.

In realistic experiments, however, the temporal resolution is limited. The density matrix reconstructed from the polarization tomography shown in Fig. 9.2 results in the negativity presented in Fig. 9.3 (red line), where it is compared to the negativity we obtain theoretically in the case of a perfect temporal resolution (blue line). The theoretical model we developed in Sec. 9.1 allows for an estimation of the degree of entanglement of a pair of photons emitted from the quantum dot for a finite temporal resolution. Assuming, for simplicity, a rectangular system response function of width δ_{res}, we obtain the averaged density matrix

$$\rho_{\mathrm{av}}\left(t, \delta_{\mathrm{res}}\right) = \frac{1}{\delta_{\mathrm{res}}} \int_{t}^{t+\delta_{\mathrm{res}}} dt' \, \rho_{\mathrm{N}}(0, t'), \tag{9.21}$$

where, without loss of generality, we set the time of the emission of the biexciton photon to zero. The negativity that can be calculated for the averaged density matrix is

$$N\left[\rho_{\mathrm{av}}(t, \delta_{\mathrm{res}})\right] = \frac{1}{2} \left|\mathrm{sinc}(\Omega \delta_{\mathrm{res}})\right| . \tag{9.22}$$

Thus, the negativity oscillates as a function of the renormalized frequency $\Omega = \sqrt{f^2 + \left(\Delta_{\mathrm{FSS}}/2\right)^2}$ and of the temporal resolution δ_{res}. The negativity as a function of the excitonic transition rate f and the fine-structure splitting frequency Δ_{FSS} for different temporal resolutions is shown in Fig. 9.4. We see that, depending on the temporal resolution, the entanglement of the two photons is more or less robust to a fine-structure splitting and excitonic transitions. For a sufficiently high resolution, that is, a sufficiently small δ_{res}, highly entangled photon pairs can be generated from the biexciton cascade despite the phase and spin precession. The limit of the time-integrated measurement arises naturally from our model, where the presence of even a small fine-structure splitting or excitonic transition rate is detrimental to the entanglement of the photons.

9.3 Conclusion

We studied the radiative biexciton cascade in a semiconductor quantum dot focussing on the impact of excitonic spin precession processes on the polarization entanglement of the emitted photons. Such processes manifest experimentally as anomalous oscillations in the rectilinear $\{|\mathrm{H}\rangle, |\mathrm{V}\rangle\}$ basis correlations and are commonly thought to prohibit the generation of highly entangled photon pairs. Including the spin precession in the form of excitonic

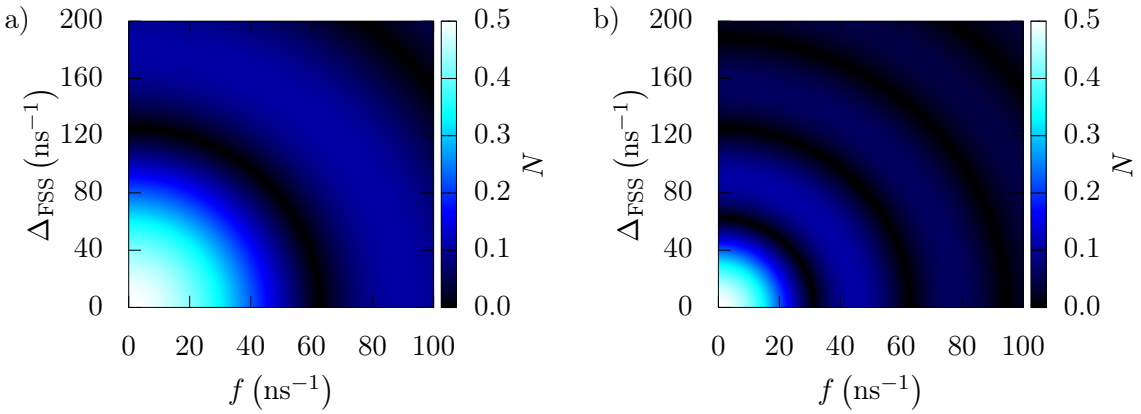

Figure 9.4: Negativity N of the density matrix describing the state of the photon pair emitted from the biexciton cascade with the fine-structure splitting frequency Δ_{FSS} and the excitonic transition rate f for a finite temporal resolution δ_{res} of the measurement obtained from our theoretical model. (a) $\delta_{\mathrm{res}} = 0.05\,\mathrm{ns}$. (b) $\delta_{\mathrm{res}} = 0.1\,\mathrm{ns}$.

transitions, we showed that the data obtained in a polarization tomography can be modelled adequately without taking decoherence processes into account, which can, thus, be considered as slow in comparison to the excitonic lifetime. The estimation of the entanglement of the photons emitted from the cascade showed that excitonic transitions have the same influence as a fine-structure splitting of the excitonic states. While a perfect temporal resolution allows for maximally entangled photons due to the erasure of which-path information, in a time-integrated measurement setup, excitonic transitions are detrimental to the entanglement of the photons. For a finite detector resolution, the negativity as a measure of the entanglement was found to be oscillating with the excitonic transition rate as well as with the fine-structure splitting, so that a high degree of entanglement is possible despite excitonic transitions during the decay of the biexciton cascade.

10 Conclusion and outlook

The aim of this thesis was to explore the emergence of entanglement in non-Markovian WQED systems. After an introduction of the basic concepts in part I, we presented our results in parts II and III of the thesis.

In part II, we considered the fundamental setup of WQED with feedback, a TLS with self-feedback realized by coupling the emitter to a semi-infinite waveguide. The simulation of the non-Markovian dynamics within the MPS framework allows accounting for multiple excitations due to the efficient handling of the entanglement in the system. The modeling of quantum pulses enables a self-consistent description of the transmission of quantum information. They can be included via an entangled initial state of the reservoir, for which a decomposition into the MPS form has to be performed. To avoid this numerically expensive procedure, we calculated the explicit decomposition for rectangular pulses of arbitrary duration. This way, we were able to study the feedback dynamics for pulses containing up to four photons. A striking feature in the considered system is the existence of a bound state in the continuum, which can be excited either via the decay of an initially excited emitter in vacuum or via multiphoton scattering. We studied the excitation probability of the bound state for pulses containing different numbers of photons and compared it to that of an initially excited emitter. In the regime of short delay times, the excitation via an initially excited emitter is most effective. We showed that in the highly non-Markovian regime of long delay times, in contrast, multiphoton pulses can result in a strikingly higher excitation probability depending nonlinearly on the number of photons in the pulse.

As an alternative approach for simulating the feedback dynamics of the considered system, we proposed a method based on a Heisenberg representation. To unravel the arising hierarchical structure of differential equations for multi-time correlations, we performed a projection onto a complete set of states in the Hilbert space. The method makes the microscopic dynamics accessible and allows for efficient calculations, where the required numerical resources are known in advance. This way, we were able to explore the complex interplay of the feedback delay time and the pulse shape with respect to the excitation efficiency of the atom-photon bound state. Furthermore, the introduced approach enables the inclusion of additional dissipation channels. The phenomenological pure dephasing we considered exemplarily resulted in a reduced excitation efficiency of the emitter and the inaccessibility of the bound state. In future work, it would be interesting to include dissipation channels perturbatively. Of particular interest is the study of the effects of non-Markovian dephasing, which can have a stabilizing effect under certain conditions as has been shown in Refs. [51, 266].

To proceed in the direction of more complex WQED setups exhibiting collective dynamics, we considered two macroscopically separated TLS and studied their dynamics for different excitation schemes using MPS. The results in the case of initially excited emitters showed that entanglement can be generated by spontaneous emission. In the system, similar to

the single TLS with self-feedback, a bound state in the continuum exists. Letting the emitters decay, the bound state can be populated, which is accompanied by the emergence of long-lived entanglement between the emitters. An influx of energy can be modeled, on the one hand, by introducing an external laser field that drives the emitters. In this case, we only obtain stable entanglement when driving the emitters continuously. Alternatively, the emitters can be excited by quantum pulses through the waveguide. In this scenario, the population of the bound state by multiphoton scattering facilitates the generation of long-lived entanglement, where the degree of entanglement can be controlled by adjusting the emitter separation and tuning the pulse properties.

In part III, we considered a pair of photons correlated in their energies and times of emission. A sufficiently high visibility of the two-photon interference that is observable in the Franson interferometer indicates the nonclassical energy-time entanglement of the photons. As our analytical calculations showed, the visibility depends strongly on the system parameters. To enhance it, we proposed the implementation of an additional feedback channel. Studying the resulting second-order correlation function numerically within the MPS framework, we found that feedback has the potential to increase the visibility of the interference significantly, for example, by delaying the emission of the first photon. The results, thus, point to the fact that the energy-time entanglement of a pair of photons can be controlled using coherent time-delayed feedback. In further research, an adaptation of the model to a concrete experimental situation, for example, the description of the photon generation by resonance fluorescence, could provide further insights.

Turning to another type of photon entanglement, we studied the polarization entanglement of a pair of photons emitted from a biexciton cascade in a semiconductor quantum dot. In particular, we focused on the impact of an excitonic spin precession resulting in anomalous oscillations in cross-correlation measurements due to the possibility of transitions between the excitonic states. We found a good agreement with experimental data accounting for the transitions as a coherent process. In this model, the entanglement is affected by the transitions in the same way as by a fine-structure splitting, which, in a time-integrated measurement setup, has a detrimental effect. In a time-resolved measurement setup, in contrast, a highly entangled photon pair is possible, where the attainable degree of entanglement depends on the detector resolution as well as on the excitonic transition rate and the fine-structure splitting. While decoherence processes are typically slow in comparison to the excitonic lifetime, including them in the model in subsequent investigations is of interest to complete the picture.

In summary, from a methodical point of view, we extended the toolbox for the treatment of non-Markovian WQED by extending and proposing state-of-the-art numerical methods. We applied them to study characteristic features of feedback systems with strongly entangled emitter-reservoir states as well as to explore ways to control the entanglement of pairs of emitters and photons. In this way, the work contributes to a better understanding of the theoretical basis of implementations for quantum information processing.

A Appendix

A.1 Initialization of the matrix product state pulse bins

If the TLS we consider in Chap. 5 is subjected to a quantized pulse, we have to decompose the tensor describing the entangled state of the involved time bins to allow the initialization of the reservoir state in MPS form. For a rectangular pulse starting at $t_{\text{start}} = p_1 \Delta t$ and ending at $t_{\text{end}} = p_M \Delta t$ containing three photons, the matrices have to be initialized according to

$$\begin{aligned} A[p_1]^1 &= \begin{pmatrix} 1 & 0 & 0 & 0 \end{pmatrix}, \quad A[p_1]^2 = \begin{pmatrix} 0 & 1 & 0 & 0 \end{pmatrix}, \\ A[p_1]^3 &= \begin{pmatrix} 0 & 0 & 1 & 0 \end{pmatrix}, \quad A[p_1]^4 = \begin{pmatrix} 0 & 0 & 0 & 1 \end{pmatrix}, \end{aligned} \tag{A.1}$$

$$\begin{aligned} A[p_k]^1 &= \begin{pmatrix} 1 & 0 & 0 & 0 \\ 0 & \sqrt{\frac{k-1}{k}} & 0 & 0 \\ 0 & 0 & \sqrt{\frac{(k-1)^2}{k^2}} & 0 \\ 0 & 0 & 0 & \sqrt{\frac{(k-1)^3}{k^3}} \end{pmatrix}, \quad A[p_k]^2 = \begin{pmatrix} 0 & \sqrt{\frac{1}{k}} & 0 & 0 \\ 0 & 0 & \sqrt{\frac{2(k-1)}{k^2}} & 0 \\ 0 & 0 & 0 & \sqrt{\frac{3(k-1)^2}{k^3}} \\ 0 & 0 & 0 & 0 \end{pmatrix}, \\ A[p_k]^3 &= \begin{pmatrix} 0 & 0 & \sqrt{\frac{1}{k^2}} & 0 \\ 0 & 0 & 0 & \sqrt{\frac{3(k-1)}{k^3}} \\ 0 & 0 & 0 & 0 \\ 0 & 0 & 0 & 0 \end{pmatrix}, \quad A[p_k]^4 = \begin{pmatrix} 0 & 0 & 0 & \sqrt{\frac{1}{k^3}} \\ 0 & 0 & 0 & 0 \\ 0 & 0 & 0 & 0 \\ 0 & 0 & 0 & 0 \end{pmatrix}, \end{aligned} \tag{A.2}$$

$$\begin{aligned} A[p_M]^1 &= \begin{pmatrix} 0 & 0 & 0 & \sqrt{\frac{(M-1)^3}{N^3}} \end{pmatrix}^T, \quad A[p_M]^2 = \begin{pmatrix} 0 & 0 & \sqrt{\frac{3(M-1)^2}{M^3}} & 0 \end{pmatrix}^T, \\ A[p_M]^3 &= \begin{pmatrix} 0 & \sqrt{\frac{3(M-1)}{M^3}} & 0 & 0 \end{pmatrix}^T, \quad A[p_M]^4 = \begin{pmatrix} \sqrt{\frac{1}{M^3}} & 0 & 0 & 0 \end{pmatrix}^T \end{aligned} \tag{A.3}$$

with $1 < k < M$. Here, the time bins are of dimension four to be able to account for up to three photons per time bin. If the same pulse but with a photon number of four is considered, we have to use five-dimensional time bins if we want to capture the full dynamics. The involved matrices, in this case, have to be initialized as

$$\begin{aligned} A[p_1]^1 &= \begin{pmatrix} 1 & 0 & 0 & 0 & 0 \end{pmatrix}, \quad A[p_1]^2 = \begin{pmatrix} 0 & 1 & 0 & 0 & 0 \end{pmatrix}, \\ A[p_1]^3 &= \begin{pmatrix} 0 & 0 & 1 & 0 & 0 \end{pmatrix}, \quad A[p_1]^4 = \begin{pmatrix} 0 & 0 & 0 & 1 & 0 \end{pmatrix}, \\ A[p_1]^5 &= \begin{pmatrix} 0 & 0 & 0 & 0 & 1 \end{pmatrix}, \end{aligned} \tag{A.4}$$

$$
A[p_k]^1 = \begin{pmatrix} 1 & 0 & 0 & 0 & 0 \\ 0 & \sqrt{\frac{k-1}{k}} & 0 & 0 & 0 \\ 0 & 0 & \sqrt{\frac{(k-1)^2}{k^2}} & 0 & 0 \\ 0 & 0 & 0 & \sqrt{\frac{(k-1)^3}{k^3}} & 0 \\ 0 & 0 & 0 & 0 & \sqrt{\frac{(k-1)^4}{k^4}} \end{pmatrix},
$$

$$
A[p_k]^2 = \begin{pmatrix} 0 & \sqrt{\frac{1}{k}} & 0 & 0 & 0 \\ 0 & 0 & \sqrt{\frac{2(k-1)}{k^2}} & 0 & 0 \\ 0 & 0 & 0 & \sqrt{\frac{3(k-1)^2}{k^3}} & 0 \\ 0 & 0 & 0 & 0 & \sqrt{\frac{4(k-1)^3}{k^4}} \\ 0 & 0 & 0 & 0 & 0 \end{pmatrix},
$$

$$
A[p_k]^3 = \begin{pmatrix} 0 & 0 & \sqrt{\frac{1}{k^2}} & 0 & 0 \\ 0 & 0 & 0 & \sqrt{\frac{3(k-1)}{k^3}} & 0 \\ 0 & 0 & 0 & 0 & \sqrt{\frac{6(k-1)^2}{k^4}} \\ 0 & 0 & 0 & 0 & 0 \end{pmatrix},
$$

$$
A[p_k]^4 = \begin{pmatrix} 0 & 0 & 0 & \sqrt{\frac{1}{k^3}} & 0 \\ 0 & 0 & 0 & 0 & \sqrt{\frac{4(k-1)}{k^4}} \\ 0 & 0 & 0 & 0 & 0 \\ 0 & 0 & 0 & 0 & 0 \\ 0 & 0 & 0 & 0 & 0 \end{pmatrix},
$$

$$
A[p_k]^5 = \begin{pmatrix} 0 & 0 & 0 & 0 & \sqrt{\frac{1}{k^4}} \\ 0 & 0 & 0 & 0 & 0 \\ 0 & 0 & 0 & 0 & 0 \\ 0 & 0 & 0 & 0 & 0 \\ 0 & 0 & 0 & 0 & 0 \end{pmatrix}, \tag{A.5}
$$

$$
A[p_M]^1 = \begin{pmatrix} 0 & 0 & 0 & 0 & \sqrt{\frac{(M-1)^4}{M^4}} \end{pmatrix}^T, \quad A[p_M]^2 = \begin{pmatrix} 0 & 0 & 0 & \sqrt{\frac{4(M-1)^3}{M^4}} & 0 \end{pmatrix}^T,
$$

$$
A[p_M]^3 = \begin{pmatrix} 0 & 0 & \sqrt{\frac{6(M-1)^2}{M^4}} & 0 & 0 \end{pmatrix}^T, \quad A[p_M]^4 = \begin{pmatrix} 0 & \sqrt{\frac{4(M-1)}{M^4}} & 0 & 0 & 0 \end{pmatrix}^T,
$$

$$
A[p_M]^5 = \begin{pmatrix} \sqrt{\frac{1}{M^4}} & 0 & 0 & 0 & 0 \end{pmatrix}^T. \tag{A.6}
$$

A.2 Heisenberg equations of motion

For the calculation of the dynamics employing the Heisenberg approach as proposed in Chap. 6, when the feedback mechanism influences the dynamics, we insert the unity oper-

ator

$$\mathbb{1} = \{ |\mathrm{g}\rangle\langle\mathrm{g}| + |\mathrm{e}\rangle\langle\mathrm{e}| \} \otimes \left\{ |0\rangle\langle 0| + \int dt' \, |t'\rangle\langle t'| + \frac{1}{2}\int dt' \int dt'' \, |t', t''\rangle\langle t', t''| + \dots \right\} \quad \text{(A.7)}$$

between the operators with different time arguments to unravel the arising multi-time correlations. Additionally, we can insert the unity operator between the operators $\sigma_+(t)$ and $\sigma_-(t)$ so that we only have to deal with single-time matrix elements of the TLS operator σ_-. The operator obeys the differential equation

$$\frac{\mathrm{d}}{\mathrm{d}t}\sigma_-(t) = -\Gamma\sigma_-(t) - \sqrt{\Gamma}\left[\mathbb{1} - 2\sigma_+(t)\sigma_-(t)\right] r_{t,\tau} + \Gamma e^{i\omega_0\tau}\left[\sigma_-(t-\tau) - 2\sigma_+(t)\sigma_-(t)\sigma_-(t-\tau)\right]\Theta(t-\tau). \quad \text{(A.8)}$$

Here, the explicit calculations for the matrix elements of σ_- for up to three photons are presented.

Single-photon pulse

For the initial state $|\mathrm{g}, 1\rangle$, only the projector onto the state $|\mathrm{g}, 0\rangle$ describing the TLS in the ground state and no photons in the reservoir contributes when decomposing the expectation value of the TLS occupation into matrix elements of the TLS operator σ_- and it holds that

$$\langle \mathrm{g}, 1| \sigma_+(t)\sigma_-(t) |\mathrm{g}, 1\rangle = \langle \mathrm{g}, 1| \sigma_+(t) |\mathrm{g}, 0\rangle \langle \mathrm{g}, 0| \sigma_-(t) |\mathrm{g}, 1\rangle . \quad \text{(A.9)}$$

Thus, the only relevant matrix element is $\langle \mathrm{g}, 0| \sigma_-(t) |\mathrm{g}, 1\rangle$, which can be determined via the differential equation

$$\frac{\mathrm{d}}{\mathrm{d}t}\langle \mathrm{g}, 0| \sigma_-(t) |\mathrm{g}, 1\rangle = -\Gamma \langle \mathrm{g}, 0| \sigma_-(t) |\mathrm{g}, 1\rangle - \sqrt{\Gamma} f_\tau(t) + \Gamma e^{i\omega_0\tau} \langle \mathrm{g}, 0| \sigma_-(t-\tau) |\mathrm{g}, 1\rangle \Theta(t-\tau). \quad \text{(A.10)}$$

Two-photon pulse

In the case of an initial state $|\mathrm{g}, 2\rangle$, the projector onto states describing one excitation in the system, either in the TLS or in the reservoir, contributes to the dynamics and we can decompose the expectation value of the TLS occupation according to

$$\langle \mathrm{g}, 2| \sigma_+(t)\sigma_-(t) |\mathrm{g}, 2\rangle = \langle \mathrm{g}, 2| \sigma_+(t) |\mathrm{e}, 0\rangle \langle \mathrm{e}, 0| \sigma_-(t) |\mathrm{g}, 2\rangle + \int dt' \, \langle \mathrm{g}, 2| \sigma_+(t) |\mathrm{g}, t'\rangle \langle \mathrm{g}, t'| \sigma_-(t) |\mathrm{g}, 2\rangle . \quad \text{(A.11)}$$

A Appendix

The matrix elements of the TLS operator σ_- describing the transition from two to one excitation in the system that have to be evaluated evolve as

$$\begin{aligned}\frac{\mathrm{d}}{\mathrm{d}t}\langle \mathrm{e},0|\,\sigma_-(t)\,|\mathrm{g},2\rangle &= -\Gamma\langle \mathrm{e},0|\,\sigma_-(t)\,|\mathrm{g},2\rangle + 2\sqrt{2\Gamma}f_\tau(t)\langle \mathrm{e},0|\,\sigma_+(t)\,|\mathrm{g},0\rangle\langle \mathrm{g},0|\,\sigma_-(t)\,|\mathrm{g},1\rangle \\ &+\Gamma e^{i\omega_0\tau}\Bigg\{\langle \mathrm{e},0|\,\sigma_-(t-\tau)\,|\mathrm{g},2\rangle - 2\Bigg[\langle \mathrm{e},0|\,\sigma_+(t)\,|\mathrm{g},0\rangle\langle \mathrm{g},0|\,\sigma_-(t)\,|\mathrm{e},0\rangle\langle \mathrm{e},0|\,\sigma_-(t-\tau)\,|\mathrm{g},2\rangle \\ &+\int dt_1\,\langle \mathrm{e},0|\,\sigma_+(t)\,|\mathrm{g},0\rangle\langle \mathrm{g},0|\,\sigma_-(t)\,|\mathrm{g},t_1\rangle\langle \mathrm{g},t_1|\,\sigma_-(t-\tau)\,|\mathrm{g},2\rangle\Bigg]\Bigg\}\Theta(t-\tau) \quad \text{(A.12)}\end{aligned}$$

and

$$\begin{aligned}\frac{\mathrm{d}}{\mathrm{d}t}\langle \mathrm{g},t'|\,\sigma_-(t)\,|\mathrm{g},2\rangle &= -\Gamma\langle \mathrm{g},t'|\,\sigma_-(t)\,|\mathrm{g},2\rangle \\ &\quad -\sqrt{2\Gamma}f_\tau(t)\left[\langle g,t'|g,1\rangle - 2\langle \mathrm{g},t'|\,\sigma_+(t)\,|\mathrm{g},0\rangle\langle \mathrm{g},0|\,\sigma_-(t)\,|\mathrm{g},1\rangle\right] \\ &+\Gamma e^{i\omega_0\tau}\Bigg\{\langle \mathrm{g},t'|\,\sigma_-(t-\tau)\,|\mathrm{g},2\rangle - 2\Bigg[\langle \mathrm{g},t'|\,\sigma_+(t)\,|\mathrm{g},0\rangle\langle \mathrm{g},0|\,\sigma_-(t)\,|\mathrm{e},0\rangle\langle \mathrm{e},0|\,\sigma_-(t-\tau)\,|\mathrm{g},2\rangle \\ &+\int dt_1\,\langle \mathrm{g},t'|\,\sigma_+(t)\,|\mathrm{g},0\rangle\langle \mathrm{g},0|\,\sigma_-(t)\,|\mathrm{g},t_1\rangle\langle \mathrm{g},t_1|\,\sigma_-(t-\tau)\,|\mathrm{g},2\rangle\Bigg]\Bigg\}\Theta(t-\tau) \quad \text{(A.13)}\end{aligned}$$

with $\langle \mathrm{g},t'|\mathrm{g},1\rangle = f(t')$. These equations, in turn, couple to matrix elements of σ_- that refer to the transition from one to zero excitations. The matrix elements that contribute in addition to the element $\langle \mathrm{g},0|\,\sigma_-(t)\,|\mathrm{g},1\rangle$, which has already been introduced in the single-excitation case above, obey

$$\frac{\mathrm{d}}{\mathrm{d}t}\langle \mathrm{g},0|\,\sigma_-(t)\,|\mathrm{e},0\rangle = -\Gamma\langle \mathrm{g},0|\,\sigma_-(t)\,|\mathrm{e},0\rangle + \Gamma e^{i\omega_0\tau}\langle \mathrm{g},0|\,\sigma_-(t-\tau)\,|\mathrm{e},0\rangle\,\Theta(t-\tau) \quad \text{(A.14)}$$

and

$$\begin{aligned}\frac{\mathrm{d}}{\mathrm{d}t}\langle \mathrm{g},0|\,\sigma_-(t)\,|\mathrm{g},t'\rangle &= -\Gamma\langle \mathrm{g},0|\,\sigma_-(t)\,|\mathrm{g},t'\rangle - \sqrt{\Gamma}\langle \mathrm{g},0|\,r_{t,\tau}\,|\mathrm{g},t'\rangle \\ &\quad +\Gamma e^{i\omega_0\tau}\langle \mathrm{g},0|\,\sigma_-(t-\tau)\,|\mathrm{g},t'\rangle\,\Theta(t-\tau) \quad \text{(A.15)}\end{aligned}$$

with

$$r_{t,\tau}\,|\mathrm{g},t'\rangle = \left[\delta\left(t'-t+\frac{\tau}{2}\right)e^{i\omega_0\frac{\tau}{2}} - \delta\left(t'-t-\frac{\tau}{2}\right)e^{-i\omega_0\frac{\tau}{2}}\right]|\mathrm{g},0\rangle\,. \quad \text{(A.16)}$$

Three-photon pulse

If the system is in the state $|\mathrm{g},3\rangle$ initially, the projector onto states describing two excitations in the system contributes and we obtain

$$\begin{aligned}\langle \mathrm{g},3|\,\sigma_+(t)\sigma_-(t)\,|\mathrm{g},3\rangle &= \int dt'\,\langle \mathrm{g},3|\,\sigma_+(t)\,|\mathrm{e},t'\rangle\langle \mathrm{e},t'|\,\sigma_-(t)\,|\mathrm{g},3\rangle \\ &\quad +\frac{1}{2}\int dt'\int dt''\,\langle \mathrm{g},3|\,\sigma_+(t)\,|\mathrm{g},t',t''\rangle\langle \mathrm{g},t',t''|\,\sigma_-(t)\,|\mathrm{g},3\rangle\,. \quad \text{(A.17)}\end{aligned}$$

The arising matrix elements of σ_- referring to the transition from three to two excitations in the system can be determined via

$$\begin{aligned}
&\frac{\mathrm{d}}{\mathrm{d}t}\langle \mathrm{e}, t'|\,\sigma_-(t)\,|\mathrm{g},3\rangle = -\Gamma\,\langle \mathrm{e}, t'|\,\sigma_-(t)\,|\mathrm{g},3\rangle \\
&+2\sqrt{3\Gamma}f_\tau(t)\left[\langle \mathrm{e}, t'|\,\sigma_+(t)\,|\mathrm{e},0\rangle\,\langle \mathrm{e},0|\,\sigma_-(t)\,|\mathrm{g},2\rangle + \int dt_1\,\langle \mathrm{e}, t'|\,\sigma_+(t)\,|\mathrm{g},t_1\rangle\,\langle \mathrm{g},t_1|\,\sigma_-(t)\,|\mathrm{g},2\rangle\right] \\
&+\Gamma e^{i\omega_0\tau}\Bigg\{\langle \mathrm{e}, t'|\,\sigma_-(t-\tau)\,|\mathrm{g},3\rangle \\
&\qquad -2\left[\int dt_2\,\langle \mathrm{e}, t'|\,\sigma_+(t)\,|\mathrm{e},0\rangle\,\langle \mathrm{e},0|\,\sigma_-(t)\,|\mathrm{e},t_2\rangle\,\langle \mathrm{e},t_2|\,\sigma_-(t-\tau)\,|\mathrm{g},3\rangle\right. \\
&\qquad +\int dt_1\int dt_2\,\langle \mathrm{e}, t'|\,\sigma_+(t)\,|\mathrm{g},t_1\rangle\,\langle \mathrm{g},t_1|\,\sigma_-(t)\,|\mathrm{e},t_2\rangle\,\langle \mathrm{e},t_2|\,\sigma_-(t-\tau)\,|\mathrm{g},3\rangle \\
&\qquad +\frac{1}{2}\int dt_2\int dt_3\,\langle \mathrm{e}, t'|\,\sigma_+(t)\,|\mathrm{e},0\rangle\,\langle \mathrm{e},0|\,\sigma_-(t)\,|\mathrm{g},t_2,t_3\rangle\,\langle \mathrm{g},t_2,t_3|\,\sigma_-(t-\tau)\,|\mathrm{g},3\rangle \\
&\qquad \left.+\frac{1}{2}\int dt_1\int dt_2\int dt_3\,\langle \mathrm{e}, t'|\,\sigma_+(t)\,|\mathrm{g},t_1\rangle\,\langle \mathrm{g},t_1|\,\sigma_-(t)\,|\mathrm{g},t_2,t_3\rangle\,\langle \mathrm{g},t_2,t_3|\,\sigma_-(t-\tau)\,|\mathrm{g},3\rangle\right]\Bigg\} \\
&\qquad\qquad \times\Theta(t-\tau) \quad \text{(A.18)}
\end{aligned}$$

and

$$\begin{aligned}
&\frac{\mathrm{d}}{\mathrm{d}t}\langle \mathrm{g}, t', t''|\,\sigma_-(t)\,|\mathrm{g},3\rangle = -\Gamma\,\langle \mathrm{g}, t', t''|\,\sigma_-(t)\,|\mathrm{g},3\rangle - \sqrt{3\Gamma}f_\tau(t)\Bigg\{\langle g, t', t''|g,2\rangle \\
&-2\left[\langle \mathrm{g}, t', t''|\,\sigma_+(t)\,|\mathrm{e},0\rangle\,\langle \mathrm{e},0|\,\sigma_-(t)\,|\mathrm{g},2\rangle + \int dt_1\,\langle \mathrm{g}, t', t''|\,\sigma_+(t)\,|\mathrm{g},t_1\rangle\,\langle \mathrm{g},t_1|\,\sigma_-(t)\,|\mathrm{g},2\rangle\right]\Bigg\} \\
&+\Gamma e^{i\omega_0\tau}\Bigg\{\langle \mathrm{g}, t', t''|\,\sigma_-(t-\tau)\,|\mathrm{g},3\rangle \\
&\qquad -2\left[\int dt_2\,\langle \mathrm{g}, t', t''|\,\sigma_+(t)\,|\mathrm{e},0\rangle\,\langle \mathrm{e},0|\,\sigma_-(t)\,|\mathrm{e},t_2\rangle\,\langle \mathrm{e},t_2|\,\sigma_-(t-\tau)\,|\mathrm{g},3\rangle\right. \\
&\qquad +\int dt_1\int dt_2\,\langle \mathrm{g}, t', t''|\,\sigma_+(t)\,|\mathrm{g},t_1\rangle\,\langle \mathrm{g},t_1|\,\sigma_-(t)\,|\mathrm{e},t_2\rangle\,\langle \mathrm{e},t_2|\,\sigma_-(t-\tau)\,|\mathrm{g},3\rangle \\
&\qquad +\frac{1}{2}\int dt_2\int dt_3\,\langle \mathrm{g}, t', t''|\,\sigma_+(t)\,|\mathrm{e},0\rangle\,\langle \mathrm{e},0|\,\sigma_-(t)\,|\mathrm{g},t_2,t_3\rangle\,\langle \mathrm{g},t_2,t_3|\,\sigma_-(t-\tau)\,|\mathrm{g},3\rangle \\
&\qquad \left.+\frac{1}{2}\int dt_1\int dt_2\int dt_3\,\langle \mathrm{g}, t', t''|\,\sigma_+(t)\,|\mathrm{g},t_1\rangle\,\langle \mathrm{g},t_1|\,\sigma_-(t)\,|\mathrm{g},t_2,t_3\rangle\,\langle \mathrm{g},t_2,t_3|\,\sigma_-(t-\tau)\,|\mathrm{g},3\rangle\right]\Bigg\} \\
&\qquad\qquad \times\Theta(t-\tau), \quad \text{(A.19)}
\end{aligned}$$

where $\langle \mathrm{g}, t', t''|\mathrm{g},2\rangle = \sqrt{2}f(t')f(t'')$.

For the relevant matrix elements that describe the transition from two to one excitation,

beyond the equations already considered in the two-excitation case, we have to evaluate

$$\begin{aligned}\frac{\mathrm{d}}{\mathrm{d}t}\langle \mathrm{e},0|\,\sigma_-(t)\,|\mathrm{e},t'\rangle &= -\Gamma\,\langle \mathrm{e},0|\,\sigma_-(t)\,|\mathrm{e},t'\rangle \\ &\quad -\sqrt{\Gamma}\left[\langle \mathrm{e},0|\,r_{t,\tau}\,|\mathrm{e},t'\rangle - 2\,\langle \mathrm{e},0|\,\sigma_+(t)\,|\mathrm{g},0\rangle\,\langle \mathrm{g},0|\,\sigma_-(t) r_{t,\tau}\,|\mathrm{e},t'\rangle\right] \\ +\Gamma e^{i\omega_0\tau}\Bigg\{ &\langle \mathrm{e},0|\,\sigma_-(t-\tau)\,|\mathrm{e},t'\rangle - 2\Bigg[\langle \mathrm{e},0|\,\sigma_+(t)\,|\mathrm{g},0\rangle\,\langle \mathrm{g},0|\,\sigma_-(t)\,|\mathrm{e},0\rangle\,\langle \mathrm{e},0|\,\sigma_-(t-\tau)\,|\mathrm{e},t'\rangle \\ &+\int dt_1\,\langle \mathrm{e},0|\,\sigma_+(t)\,|\mathrm{g},0\rangle\,\langle \mathrm{g},0|\,\sigma_-(t)\,|\mathrm{g},t_1\rangle\,\langle \mathrm{g},t_1|\,\sigma_-(t-\tau)\,|\mathrm{e},t'\rangle\Bigg]\Bigg\}\Theta(t-\tau), \quad \text{(A.20)}\end{aligned}$$

$$\begin{aligned}\frac{\mathrm{d}}{\mathrm{d}t}\langle \mathrm{g},t'|\,\sigma_-(t)\,|\mathrm{e},t''\rangle &= -\Gamma\,\langle \mathrm{g},t'|\,\sigma_-(t)\,|\mathrm{e},t''\rangle + 2\sqrt{\Gamma}\,\langle \mathrm{g},t'|\,\sigma_+(t)\,|\mathrm{g},0\rangle\,\langle \mathrm{g},0|\,\sigma_-(t) r_{t,\tau}\,|\mathrm{e},t''\rangle \\ +\Gamma e^{i\omega_0\tau}\Bigg\{ &\langle \mathrm{g},t'|\,\sigma_-(t-\tau)\,|\mathrm{e},t''\rangle - 2\Bigg[\langle \mathrm{g},t'|\,\sigma_+(t)\,|\mathrm{g},0\rangle\,\langle \mathrm{g},0|\,\sigma_-(t)\,|\mathrm{e},0\rangle\,\langle \mathrm{e},0|\,\sigma_-(t-\tau)\,|\mathrm{e},t''\rangle \\ &+\int dt_1\,\langle \mathrm{g},t'|\,\sigma_+(t)\,|\mathrm{g},0\rangle\,\langle \mathrm{g},0|\,\sigma_-(t)\,|\mathrm{g},t_1\rangle\,\langle \mathrm{g},t_1|\,\sigma_-(t-\tau)\,|\mathrm{e},t''\rangle\Bigg]\Bigg\}\Theta(t-\tau), \quad \text{(A.21)}\end{aligned}$$

$$\begin{aligned}\frac{\mathrm{d}}{\mathrm{d}t}\langle \mathrm{e},0|\,\sigma_-(t)\,|\mathrm{g},t',t''\rangle &= -\Gamma\,\langle \mathrm{e},0|\,\sigma_-(t)\,|\mathrm{g},t',t''\rangle + 2\sqrt{\Gamma}\,\langle \mathrm{e},0|\,\sigma_+(t)\,|\mathrm{g},0\rangle\,\langle \mathrm{g},0|\,\sigma_-(t) r_{t,\tau}\,|\mathrm{g},t',t''\rangle \\ +\Gamma e^{i\omega_0\tau}\Bigg\{ &\langle \mathrm{e},0|\,\sigma_-(t-\tau)\,|\mathrm{g},t',t''\rangle - 2\Bigg[\langle \mathrm{e},0|\,\sigma_+(t)\,|\mathrm{g},0\rangle\,\langle \mathrm{g},0|\,\sigma_-(t)\,|\mathrm{e},0\rangle\,\langle \mathrm{e},0|\,\sigma_-(t-\tau)\,|\mathrm{g},t',t''\rangle \\ &+\int dt_1\,\langle \mathrm{e},0|\,\sigma_+(t)\,|\mathrm{g},0\rangle\,\langle \mathrm{g},0|\,\sigma_-(t)\,|\mathrm{g},t_1\rangle\,\langle \mathrm{g},t_1|\,\sigma_-(t-\tau)\,|\mathrm{g},t',t''\rangle\Bigg]\Bigg\}\Theta(t-\tau), \quad \text{(A.22)}\end{aligned}$$

and

$$\begin{aligned}\frac{\mathrm{d}}{\mathrm{d}t}\langle \mathrm{g},t'|\,\sigma_-(t)\,|\mathrm{g},t'',t'''\rangle &= -\Gamma\,\langle \mathrm{g},t'|\,\sigma_-(t)\,|\mathrm{g},t'',t'''\rangle \\ &\quad -\sqrt{\Gamma}\left[\langle \mathrm{g},t'|\,r_{t,\tau}\,|\mathrm{g},t'',t'''\rangle - 2\,\langle \mathrm{g},t'|\,\sigma_+(t)\,|\mathrm{g},0\rangle\,\langle \mathrm{g},0|\,\sigma_-(t) r_{t,\tau}\,|\mathrm{g},t'',t'''\rangle\right] \\ &\quad +\Gamma e^{i\omega_0\tau}\Bigg\{\langle \mathrm{g},t'|\,\sigma_-(t-\tau)\,|\mathrm{g},t'',t'''\rangle \\ &\quad -2\Bigg[\langle \mathrm{g},t'|\,\sigma_+(t)\,|\mathrm{g},0\rangle\,\langle \mathrm{g},0|\,\sigma_-(t)\,|\mathrm{e},0\rangle\,\langle \mathrm{e},0|\,\sigma_-(t-\tau)\,|\mathrm{g},t'',t'''\rangle \\ &+\int dt_1\,\langle \mathrm{g},t'|\,\sigma_+(t)\,|\mathrm{g},0\rangle\,\langle \mathrm{g},0|\,\sigma_-(t)\,|\mathrm{g},t_1\rangle\,\langle \mathrm{g},t_1|\,\sigma_-(t-\tau)\,|\mathrm{g},t'',t'''\rangle\Bigg]\Bigg\}\Theta(t-\tau). \quad \text{(A.23)}\end{aligned}$$

The elements $\langle \mathrm{e},0|\,r_{t,\tau}\,|\mathrm{e},t'\rangle$ and $\langle \mathrm{g},0|\,\sigma_-(t) r_{t,\tau}\,|\mathrm{e},t'\rangle$ can be evaluated in analogy to Eq. (A.16), while, for the elements $\langle \mathrm{g},0|\,\sigma_-(t) r_{t,\tau}\,|\mathrm{g},t',t''\rangle$ and $\langle \mathrm{g},t'|\,r_{t,\tau}\,|\mathrm{g},t'',t'''\rangle$, the effect of the operator $r_{t,\tau}$ on the two-photon state $|\mathrm{g},t',t''\rangle$ has to be taken into account, which yields

$$\begin{aligned}r_{t,\tau}\,|\mathrm{g},t',t''\rangle &= \left[\delta(t'-t+\frac{\tau}{2})e^{i\omega_0\frac{\tau}{2}} - \delta(t'-t-\frac{\tau}{2})e^{-i\omega_0\frac{\tau}{2}}\right]|\mathrm{g},t''\rangle \\ &\quad +\left[\delta(t''-t+\frac{\tau}{2})e^{i\omega_0\frac{\tau}{2}} - \delta(t''-t-\frac{\tau}{2})e^{-i\omega_0\frac{\tau}{2}}\right]|\mathrm{g},t'\rangle\,. \quad \text{(A.24)}\end{aligned}$$

A.3 Phenomenological pure dephasing within the Heisenberg representation

Pure dephasing dephases coherences, while populations are not directly affected. To be able to account for this fact when including a phenomenological pure dephasing in Chap. 6, not all matrix elements are decomposed into single-time matrix elements of the operator σ_- but are distinguished into matrix elements of the coherence operator σ_- and the TLS occupation operator $E \equiv \sigma_+\sigma_-$. This way, for the calculation of the dynamics for a TLS initially in the ground state and a single-photon pulse in the reservoir, we have to solve

$$\frac{\mathrm{d}}{\mathrm{d}t}\langle \mathrm{g},1|\, E(t)\,|\mathrm{g},1\rangle = -2\Gamma\,\langle \mathrm{g},1|\, E(t)\,|\mathrm{g},1\rangle - \sqrt{\Gamma}\,[f_\tau^*(t)\,\langle \mathrm{g},0|\,\sigma_-(t)\,|\mathrm{g},1\rangle + \mathrm{H.c.}] \\ + \Gamma\left[e^{-i\omega_0\tau}\,\langle \mathrm{g},1|\,\sigma_+(t-\tau)\sigma_-(t)\,|\mathrm{g},1\rangle + \mathrm{H.c.}\right]\Theta(t-\tau). \quad \text{(A.25)}$$

The insertion of the unity operator between the operators with different time arguments yields

$$\frac{\mathrm{d}}{\mathrm{d}t}\langle \mathrm{g},1|\, E(t)\,|\mathrm{g},1\rangle = -2\Gamma\,\langle \mathrm{g},1|\, E(t)\,|\mathrm{g},1\rangle - \sqrt{\Gamma}\,[f_\tau^*(t)\,\langle \mathrm{g},0|\,\sigma_-(t)\,|\mathrm{g},1\rangle + \mathrm{H.c.}] \\ + \Gamma\left[e^{-i\omega_0\tau}\,\langle \mathrm{g},1|\,\sigma_+(t-\tau)\,|\mathrm{g},0\rangle\,\langle \mathrm{g},0|\,\sigma_-(t)\,|\mathrm{g},1\rangle + \mathrm{H.c.}\right]\Theta(t-\tau). \quad \text{(A.26)}$$

The expectation value couples to the matrix element $\langle \mathrm{g},0|\,\sigma_-(t)\,|\mathrm{g},1\rangle$, for which we add a phenomenological pure dephasing at rate γ so that it obeys

$$\frac{\mathrm{d}}{\mathrm{d}t}\langle \mathrm{g},0|\,\sigma_-(t)\,|\mathrm{g},1\rangle = -(\Gamma+\gamma)\,\langle \mathrm{g},0|\,\sigma_-(t)\,|\mathrm{g},1\rangle - \sqrt{\Gamma}f_\tau(t) \\ + \Gamma e^{i\omega_0\tau}\,\langle \mathrm{g},0|\,\sigma_-(t-\tau)\,|\mathrm{g},1\rangle\,\Theta(t-\tau). \quad \text{(A.27)}$$

Analogously, for a two-photon pulse in the reservoir, we have to evaluate the expectation value

$$\frac{\mathrm{d}}{\mathrm{d}t}\langle \mathrm{g},2|\, E(t)\,|\mathrm{g},2\rangle = -2\Gamma\,\langle \mathrm{g},2|\, E(t)\,|\mathrm{g},2\rangle - \sqrt{2\Gamma}\,[f_\tau^*(t)\,\langle \mathrm{g},1|\,\sigma_-(t)\,|\mathrm{g},2\rangle + \mathrm{H.c.}] \\ + \Gamma\Bigg\{e^{-i\omega_0\tau}\Bigg[\langle \mathrm{g},2|\,\sigma_+(t-\tau)\,|\mathrm{e},0\rangle\,\langle \mathrm{e},0|\,\sigma_-(t)\,|\mathrm{g},2\rangle \\ + \int dt'\,\langle \mathrm{g},2|\,\sigma_+(t-\tau)\,|\mathrm{g},t'\rangle\,\langle \mathrm{g},t'|\,\sigma_-(t)\,|\mathrm{g},2\rangle\Bigg] + \mathrm{H.c.}\Bigg\}\Theta(t-\tau). \quad \text{(A.28)}$$

After the introduction of a phenomenological pure dephasing at rate γ, the matrix element $\langle \mathrm{g},1|\,\sigma_-(t)\,|\mathrm{g},2\rangle$ coupling to the dynamics obeys the differential equation

$$\frac{\mathrm{d}}{\mathrm{d}t}\langle \mathrm{g},1|\,\sigma_-(t)\,|\mathrm{g},2\rangle = -(\Gamma+\gamma)\,\langle \mathrm{g},1|\,\sigma_-(t)\,|\mathrm{g},2\rangle - \sqrt{2\Gamma}f_\tau(t)\,[1-2\,\langle \mathrm{g},1|\, E(t)\,|\mathrm{g},1\rangle] \\ + \Gamma e^{i\omega_0\tau}\Bigg[\langle \mathrm{g},1|\,\sigma_-(t-\tau)\,|\mathrm{g},2\rangle - 2\,\langle \mathrm{g},1|\, E(t)\,|\mathrm{e},0\rangle\,\langle \mathrm{e},0|\,\sigma_-(t)\,|\mathrm{g},2\rangle \\ -2\int dt'\,\langle \mathrm{g},1|\, E(t)\,|\mathrm{g},t'\rangle\,\langle \mathrm{g},t'|\,\sigma_-(t-\tau)\,|\mathrm{g},2\rangle\Bigg]\Theta(t-\tau). \quad \text{(A.29)}$$

The remaining elements that contribute to the dynamics can be treated analogously until, eventually, the system of differential equations closes.

The calculation of the dynamics for other initial states, such as $|\mathrm{e},0\rangle$ describing the TLS initially in the excited state and the reservoir in the vacuum state, works analogously. For the differentiation into matrix elements of the operators σ_- and E, the number of matrix elements that have to be determined and saved increases. The asymptotic runtime, however, remains unchanged.

A.4 Two-photon state emitted from the ladder-type three-level system

To evaluate the second-order correlation function for the Franson interferometer introduced in Chap. 8 without feedback analytically, we need to determine the two-photon state $|\Psi\rangle$ that is emitted from the 3LS. We do this following Ref. [102]. The state of the combined system of the 3LS and the photonic reservoirs, in the two-excitation limit, takes on the general form

$$|\psi(t)\rangle = c_{\mathrm{a}}(t)\,|\mathrm{a},0\rangle + \int d\omega\, c_{\mathrm{b},\omega}(t)\,|\mathrm{b},1_\omega\rangle + \int d\omega \int d\omega'\, c_{\mathrm{c},\omega,\omega'}(t)\,|\mathrm{c},1_\omega,1_{\omega'}\rangle\,. \tag{A.30}$$

The first term on the right-hand side of Eq. (A.30) describes the 3LS in the upper state $|\mathrm{a}\rangle$ and no photons in the reservoir. The second term refers the 3LS in the middle state $|\mathrm{b}\rangle$ and a single photon with frequency ω in the reservoir. The third term eventually represents the emitter in the ground state $|\mathrm{c}\rangle$ and two photons in the reservoir, the first one with frequency ω, the second one with frequency ω'. From the Schrödinger equation, Eq. (2.6), we determine the dynamics of the coefficients using the Hamiltonian given in Eq. (8.2),

$$\begin{aligned} H_{\mathrm{I}} = \int d\omega\, \hbar g_{\mathrm{a}} \left(r_\omega^{\dagger(1)} \sigma_-^{(1)} e^{-i(\omega_{\mathrm{ab}}-\omega)t} + \mathrm{H.c.} \right) \\ + \int d\omega\, \hbar g_{\mathrm{b}} \left(r_\omega^{\dagger(2)} \sigma_-^{(2)} e^{-i(\omega_{\mathrm{b}}-\omega)t} + \mathrm{H.c.} \right), \end{aligned} \tag{A.31}$$

and find

$$\dot{c}_{\mathrm{a}}(t) = -ig_{\mathrm{a}} \int d\omega\, e^{i(\omega_{\mathrm{ab}}-\omega)t} c_{\mathrm{b},\omega}(t), \tag{A.32}$$

$$\dot{c}_{\mathrm{b},\omega}(t) = -ig_{\mathrm{a}} e^{-i(\omega_{\mathrm{ab}}-\omega)t} c_{\mathrm{a}}(t) - i \int d\omega'\, g_{\mathrm{b}} e^{i(\omega_{\mathrm{b}}-\omega')t} c_{\mathrm{c},\omega,\omega'}(t), \tag{A.33}$$

$$\dot{c}_{\mathrm{c},\omega,\omega'}(t) = -ig_{\mathrm{b}} e^{-i(\omega_{\mathrm{b}}-\omega')t} c_{\mathrm{b},\omega}(t). \tag{A.34}$$

In the Weisskopf-Wigner theory of spontaneous emission, the decay of an atomic state in a continuum of photon modes can be approximated using the decay rates Γ_{a} and Γ_{b} of the upper state $|\mathrm{a}\rangle$ and the middle state $|\mathrm{b}\rangle$, respectively, according to

$$-ig_{\mathrm{a}} \int d\omega\, e^{i(\omega_{\mathrm{ab}}-\omega)t} c_{\mathrm{b},\omega}(t) = -\frac{\Gamma_{\mathrm{a}}}{2} c_{\mathrm{a}}(t), \tag{A.35}$$

$$-ig_{\mathrm{b}} \int d\omega'\, e^{i(\omega_{\mathrm{b}}-\omega')t} c_{\mathrm{c},\omega,\omega'}(t) = -\frac{\Gamma_{\mathrm{b}}}{2} c_{\mathrm{b},\omega}(t). \tag{A.36}$$

If the 3LS is initially in the upper state, that is, with $c_{\mathrm{a}}(0) = 1$ and $c_{\mathrm{b},\omega}(0) = c_{\mathrm{c},\omega,\omega'}(0) = 0$ for all values of ω, ω', the integration of Eqs. (A.32) – (A.34) yields

$$c_{\mathrm{a}}(t) = e^{-\frac{\Gamma_{\mathrm{a}}}{2}t}, \tag{A.37}$$

$$c_{\mathrm{b},\omega}(t) = \frac{-ig_{\mathrm{a}}}{i\left(\omega-\omega_{\mathrm{ab}}\right)-\left(\frac{\Gamma_{\mathrm{a}}}{2}-\frac{\Gamma_{\mathrm{b}}}{2}\right)}\left(e^{-i(\omega_{\mathrm{ab}}-\omega)t-\frac{\Gamma_{\mathrm{a}}}{2}t}-e^{-\frac{\Gamma_{\mathrm{b}}}{2}t}\right), \tag{A.38}$$

$$\begin{aligned} c_{\mathrm{c},\omega,\omega'}(t) = {} & \frac{-ig_{\mathrm{a}}g_{\mathrm{b}}}{i\left(\omega-\omega_{\mathrm{ab}}\right)-\left(\frac{\Gamma_{\mathrm{a}}}{2}-\frac{\Gamma_{\mathrm{b}}}{2}\right)} \\ & \times\int_0^t dt'\left(e^{-i(\omega_{\mathrm{a}}-\omega-\omega')t'-\frac{\Gamma_{\mathrm{a}}}{2}t'}-e^{-i(\omega_{\mathrm{b}}-\omega')t'-\frac{\Gamma_{\mathrm{b}}}{2}t'}\right). \end{aligned} \tag{A.39}$$

In the long-time limit, for $t\to\infty$, the coefficients $c_{\mathrm{a}}(t)$ and $c_{\mathrm{b},\omega}(t)$ go to zero since the 3LS decays to the ground state and two photons are emitted into the reservoir. In this limit, the state is completely determined by $\lim_{t\to\infty} c_{\mathrm{c},\omega,\omega'}(t)$. Omitting the 3LS contribution, we, thus, arrive at the two-photon state emitted from the 3LS in the long-time limit

$$|\Psi\rangle = \int d\omega \int d\omega' \frac{-g_{\mathrm{a}}g_{\mathrm{b}}}{\left[i\left(\omega+\omega'-\omega_{\mathrm{a}}\right)-\frac{\Gamma_{\mathrm{a}}}{2}\right]\left[i\left(\omega'-\omega_{\mathrm{b}}\right)-\frac{\Gamma_{\mathrm{b}}}{2}\right]}\,|1_\omega,1_{\omega'}\rangle\,. \tag{A.40}$$

A.5 Two-photon probability amplitudes in the Franson interferometer

In this section, we derive an explicit expression for the two-photon probability amplitude in the Franson interferometer as discussed in Chap. 8,

$$\Psi_{r_1,r_2}(t_1,t_2) = \langle 0|\, E^{(+)}_{2,r_2}(t_2)E^{(+)}_{1,r_1}(t_1)\,|\Psi\rangle\,, \tag{A.41}$$

describing the first photon reaching the detector D_1 via the path r_1 and the second photon taking the path r_2 to the detector D_2, $r_1, r_2 \in \{\mathrm{S},\mathrm{L}\}$. The two-photon state $|\Psi\rangle$ that is emitted from the 3LS is given in Eq. (A.40). In Eq. (A.41), the operator $E^{(+)}_{i,r_i}$, $i\in\{1,2\}$, contains the positive frequency part of the electric field operator at the detector D_i for photons that have taken the path r_i,

$$E_{i,r_i}(t) = E^{(+)}_{i,r_i}(t) + E^{(-)}_{i,r_i}(t), \quad E^{(-)}_{i,r_i}(t) = \left[E^{(+)}_{i,r_i}(t)\right]^\dagger. \tag{A.42}$$

The operator $E^{(+)}_{i,r_i}$ comprises the photon annihilation operators $r^{(i)}_k$ according to

$$E^{(+)}_{i,r}(t) = i\sum_k \mathcal{E}(\omega_k) r^{(i)}_k e^{-i\omega_k\left(t-\frac{r}{c}\right)}, \quad \mathcal{E}(\omega_k) = \sqrt{\frac{\hbar\omega_k}{2\epsilon_0 V}}, \tag{A.43}$$

with vacuum permittivity ϵ_0 and quantization volume V as derived in Sec. 2.3. Since we consider a continuum of photon modes in a one-dimensional geometry, it is justified to switch from a sum over the multi-index $k=(\lambda,\mathbf{k})$ to an integral over the photon frequency $\omega = c\,|\mathbf{k}|$ so that

$$E^{(+)}_{i,r}(t) = i\int d\omega\, \sigma(\omega)\mathcal{E}(\omega) r^{(i)}_\omega e^{-i\omega\left(t-\frac{r}{c}\right)}, \tag{A.44}$$

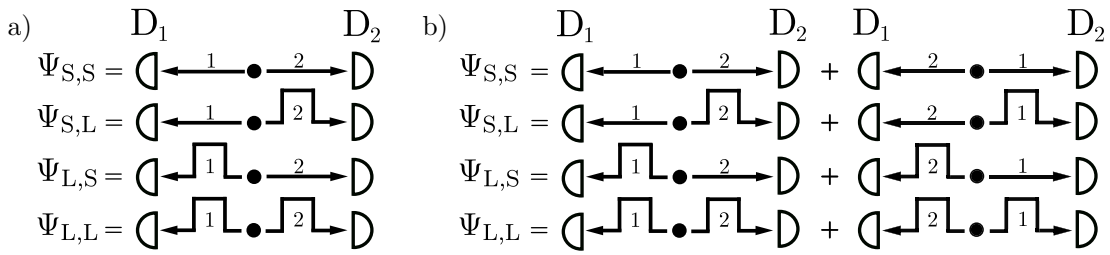

Figure A.1: Illustration of the possible paths the two photons can take in the arms of the Franson interferometer as described by the two-photon probability amplitudes Ψ_{r_1,r_2}, $r_1, r_2 \in \{\mathrm{S}, \mathrm{L}\}$. (a) With frequency filters, we can ensure that photon 1 is registered by detector D_1 and photon 2 is registered by D_2. As a consequence, there are four different possibilities for the two photons to reach the detectors. (b) Without frequency filters, we do not know which photon is registered by which detector, so additional terms have to be included where the roles of the photons are swapped.

where $\sigma(\omega)$ is the density of states. We approximate $\sigma(\omega)$ and $\mathcal{E}(\omega)$ with their values at the atomic resonances, that is, at $\omega = \omega_{\mathrm{ab}}$ and $\omega = \omega_{\mathrm{b}}$, and, this way, obtain

$$\Psi_{r_1,r_2}(t_1,t_2) = g_{\mathrm{a}} g_{\mathrm{b}} \sigma\left(\omega_{\mathrm{ab}}\right) \sigma\left(\omega_{\mathrm{b}}\right) \mathcal{E}\left(\omega_{\mathrm{ab}}\right) \mathcal{E}\left(\omega_{\mathrm{b}}\right) \times \int d\omega \int d\omega' \frac{e^{-i\omega\left(t_1 - \frac{r_1}{c}\right)} e^{-i\omega'\left(t_2 - \frac{r_2}{c}\right)}}{\left[i\left(\omega + \omega' - \omega_a\right) - \frac{\Gamma_{\mathrm{a}}}{2}\right]\left[i\left(\omega' - \omega_b\right) - \frac{\Gamma_{\mathrm{b}}}{2}\right]}. \quad \text{(A.45)}$$

For the evaluation of the double integral, we use the residue theorem, which finally results in the expression

$$\Psi_{r_1,r_2}(t_1,t_2) = \eta e^{-\left(i\omega_{\mathrm{a}} + \frac{\Gamma_{\mathrm{a}}}{2}\right)\left(t_1 - \frac{r_1}{c}\right)} \Theta\left(t_1 - \frac{r_1}{c}\right) \times e^{-\left(i\omega_{\mathrm{b}} + \frac{\Gamma_{\mathrm{b}}}{2}\right)\left[\left(t_2 - \frac{r_2}{c}\right) - \left(t_1 - \frac{r_1}{c}\right)\right]} \Theta\left[\left(t_2 - \frac{r_2}{c}\right) - \left(t_1 - \frac{r_1}{c}\right)\right], \quad \text{(A.46)}$$

where $\eta \equiv -4\pi^2 g_{\mathrm{a}} g_{\mathrm{b}} \sigma\left(\omega_{\mathrm{ab}}\right) \sigma\left(\omega_{\mathrm{b}}\right) \mathcal{E}\left(\omega_{\mathrm{ab}}\right) \mathcal{E}\left(\omega_{\mathrm{b}}\right)$.

A.6 Franson interferometer without frequency filters

If we omit the frequency filters in the Franson setup, Chap. 8, we admit the possibility that the first photon is registered by detector D_2 and the second photon is registered by D_1. This leads to additional terms when evaluating $\Psi_{r_1,r_2}(t_1,t_2)$, see Eq. (8.11), where the roles of the two photons are interchanged according to

$$\Psi_{r_1,r_2}(t_1,t_2) = \eta e^{-\left(i\omega_{\mathrm{a}} + \frac{\Gamma_{\mathrm{a}}}{2}\right)\left(t_1 - \frac{r_1}{c}\right)} \Theta\left(t_1 - \frac{r_1}{c}\right) \times e^{-\left(i\omega_{\mathrm{b}} + \frac{\Gamma_{\mathrm{b}}}{2}\right)\left[\left(t_2 - \frac{r_2}{c}\right) - \left(t_1 - \frac{r_1}{c}\right)\right]} \Theta\left[\left(t_2 - \frac{r_2}{c}\right) - \left(t_1 - \frac{r_1}{c}\right)\right] + (1 \leftrightarrow 2). \quad \text{(A.47)}$$

The possible scenarios for both cases, with and without frequency filters, are illustrated in Fig. A.1. Due to the ignorance which photon is registered by which detector, additional

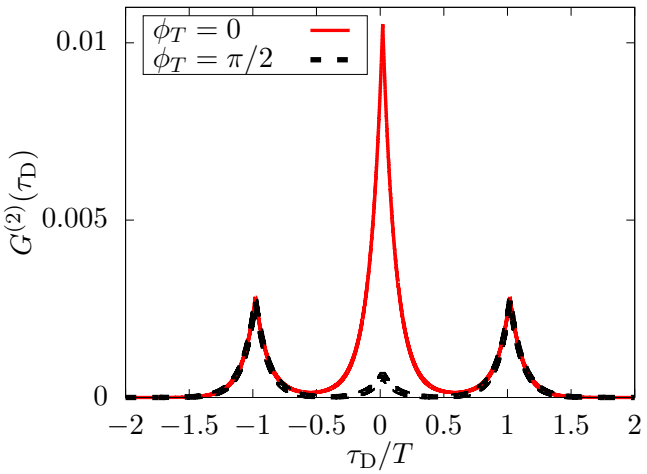

Figure A.2: Second-order correlation function for a system without frequency filters, $\Gamma_a T = 0.25$, $\Gamma_b T = 10$, and different phases ϕ_T (mod 2π).

interference terms arise. The resulting second-order correlation function is

$$G^{(2)}(\tau_D) =$$
$$\begin{cases} \frac{\eta^2}{2\Gamma_a}\Big\{e^{-\Gamma_b|\tau_D|}\Big[1+\frac{1}{2}\left(e^{-\Gamma_b T}+e^{\Gamma_b T}\right)+e^{-\Gamma_a\frac{T}{2}}\cos\left(2\phi_T\right) \\ \qquad\qquad +\left(e^{-\Gamma_b\frac{T}{2}}+e^{\Gamma_b\frac{T}{2}}\right)\left(1+e^{-\Gamma_a\frac{T}{2}}\right)\cos\left(\phi_T\right)\Big]\Big\}, & |\tau_D|\leq T \\ \frac{\eta^2}{2\Gamma_a}\Big\{e^{-\Gamma_b|\tau_D|}\left(1+\frac{1}{2}e^{-\Gamma_b T}\right)+\frac{1}{2}e^{\Gamma_b|\tau|-\Gamma_b T}+e^{-\Gamma_b|\tau_D|-\Gamma_a\frac{T}{2}}\cos(2\phi_T) \\ \quad +\left[e^{-\Gamma_b|\tau_D|}\left(e^{-(\Gamma_a+\Gamma_b)\frac{T}{2}}+e^{-\Gamma_b\frac{T}{2}}\right)+e^{-\Gamma_a\frac{|\tau|}{2}-\Gamma_b\frac{T}{2}}+e^{-(\Gamma_a+\Gamma_b)\frac{T}{2}}\right]\cos(\phi_T)\Big\}, & |\tau_D|>T \end{cases} \tag{A.48}$$

In Fig. A.2, the results for a system with $\Gamma_a T = 0.25$, $\Gamma_b T = 10$ are shown. In contrast to the case with filters as shown in Fig. 8.3, the three peaks are symmetric since it is equally likely for both detectors to register the first or the second photon.

A.7 Benchmark of the matrix product state results for the second-order correlation function in the Franson interferometer

To verify the validity of our MPS approach for the calculation of the dynamics in the Franson interferometer, Chap. 8, we benchmark the results in the case without feedback. To that end, we compare the second-order correlation function we obtain using MPS with the one calculated analytically. In the MPS framework, this can be realized by omitting the feedback channel when deriving the stroboscopic time evolution operator, that is, by setting $g_a(\omega) = g_a$ and $g_b(\omega) = g_b$ in Eq. (8.16). In this case, instead of U_k given in

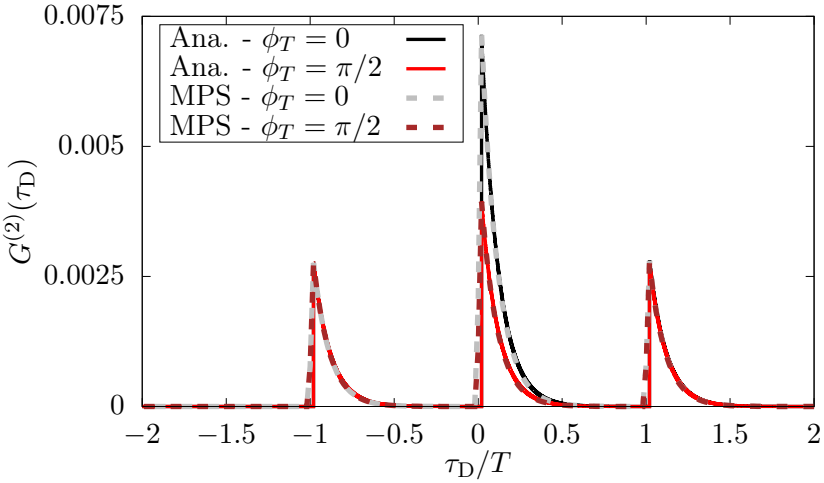

Figure A.3: Benchmark of the MPS results for the second-order correlation function without feedback. The MPS solution (dashed lines) is compared to the analytical solution (Ana., solid lines) for different values of the relative phase ϕ_T between the short and the long paths to the detectors. Here $\Gamma_a T = 2.5$, $\Gamma_b T = 10$, $\Gamma_a \Delta t = 0.05$, $\Gamma_a t_{max} = 10$.

Eq. (8.22), we obtain

$$U_k^{\text{no FB}} = \exp\left\{ -i\sqrt{\Gamma_a}\left[\sigma_+^{(1)}\Delta R_k^{(1)} + \text{H.c.}\right] - i\sqrt{\Gamma_b}\left[\sigma_+^{(2)}\Delta R_k^{(2)} + \text{H.c.}\right] \right\}, \tag{A.49}$$

where $\Gamma_a = 2\pi g_a^2$, $\Gamma_b = 2\pi g_b^2$. We can perform the Markovian time evolution in the MPS framework straightforwardly, see Sec. 5.1.4, without having to perform a swapping algorithm to include the feedback contributions. The subsequent evaluation of $G^{(2)}(\tau)$ as described in Sec. 8.2.2 then yields the results shown in Fig. A.3, where we reproduced the results of Fig. 8.3 a using MPS for a system characterized by $\Gamma_a T = 2.5$, $\Gamma_b T = 10$. For the numerical simulation, we used a step size of $\Gamma_a \Delta t = 0.05$ and simulated the dynamics up to $\Gamma_a t_{max} = 10$. The agreement of the MPS (dashed lines) and the analytical results (solid lines) indicates the validity of our MPS approach.

A.8 Two-photon state emitted from the biexciton cascade

We use the Hamiltonian H_I given in Eq. (9.7),

$$H_I = \hbar\Omega\left(\sigma_{++} - \sigma_{--}\right) + \hbar g_0 \int d\omega \left(a^\dagger_{\omega,\text{B-}}\sigma_{\text{-B}} e^{i(\omega-\omega_{BX})t} + a^\dagger_{\omega,\text{B+}}\sigma_{\text{+B}} e^{i(\omega-\omega_{BX})t} \right.$$
$$\left. + a^\dagger_{\omega,\text{X-}}\sigma_{\text{G-}} e^{i(\omega-\omega_{XG})t} + a^\dagger_{\omega,\text{X+}}\sigma_{\text{G+}} e^{i(\omega-\omega_{XG})t} + \text{H.c.} \right), \tag{A.50}$$

to determine the two-photon state $|\Psi(t)\rangle$ emitted from the biexciton cascade discussed in Chap. 9 via the Schrödinger equation, see Eq. (2.6). Initially, the system is in the state $|\Psi(0)\rangle = |\text{B}, \text{vac}\rangle$, that is, the quantum dot is in the biexciton state and there are no photons in the reservoir. The transformation of the photon creation operators from the

frequency into the time domain according to

$$a^\dagger_{\mathrm{B}\pm}(t) = \frac{1}{\sqrt{2\pi}} \int d\omega\, e^{i(\omega-\omega_{\mathrm{BX}})t} a^\dagger_{\omega,\mathrm{B}\pm}, \tag{A.51}$$

$$a^\dagger_{\mathrm{X}\pm}(t) = \frac{1}{\sqrt{2\pi}} \int d\omega\, e^{i(\omega-\omega_{\mathrm{XG}})t} a^\dagger_{\omega,\mathrm{X}\pm} \tag{A.52}$$

describing the creation of a biexciton photon and an exciton photon in $\pm$ polarization at time t, respectively, allows writing the state as

$$\begin{aligned}|\Psi(t)\rangle = e^{-2\Gamma t}\,&|\mathrm{B},\mathrm{vac}\rangle \\ &- i\sqrt{2\Gamma}e^{-\Gamma t}\int_0^t dt'\, e^{-\Gamma t'}\left[e^{-i\Omega(t-t')}\,|\mathrm{X}_-,-(t')\rangle + e^{i\Omega(t-t')}\,|\mathrm{X}_+,+(t')\rangle\right] \\ -2\Gamma\int_0^t dt'\int_0^{t'} dt''\, e^{-\Gamma(t'+t'')}&\left[e^{-i\Omega(t'-t'')}\,|+(t''),+(t')\rangle + e^{i\Omega(t'-t'')}\,|-(t''),-(t')\rangle\right].\end{aligned} \tag{A.53}$$

The state $|\mathrm{X}_\pm,\pm(t')\rangle$ denotes the quantum dot in the exciton state after the emission of a $\pm$ polarized photon at time t'. The state $|\pm(t''),\pm(t')\rangle$ describes two $\pm$ polarized photons emitted at t'' and t'. In this case, the quantum dot is found in the ground state, which has been neglected in the notation. Since we are interested in the two-photon state emitted from the quantum dot, we focus on the limit $t \to \infty$, where the decay is completed. In this limit, transformed back into the $\{\mathrm{H},\mathrm{V}\}$ basis, the state takes the form

$$\begin{aligned}|\Psi(\infty)\rangle = -2\Gamma\int_0^\infty dt'\int_0^{t'} dt''\, e^{-\Gamma(t'+t'')}& \\ \times\Bigg(\left\{\cos\left[\Omega(t'-t'')\right] + i\frac{\Delta_{\mathrm{FSS}}}{2\Omega}\sin\left[\Omega(t'-t'')\right]\right\}&|\mathrm{H}(t''),\mathrm{H}(t')\rangle \\ +\left\{\cos\left[\Omega(t'-t'')\right] - i\frac{\Delta_{\mathrm{FSS}}}{2\Omega}\sin\left[\Omega(t'-t'')\right]\right\}&|\mathrm{V}(t''),\mathrm{V}(t')\rangle \\ -i\frac{f}{\Omega}\sin\left[\Omega(t'-t'')\right]&\left[|\mathrm{H}(t''),\mathrm{V}(t')\rangle + |\mathrm{V}(t''),\mathrm{H}(t')\rangle\right]\Bigg).\end{aligned} \tag{A.54}$$

Bibliography

[1] P. W. Shor, "Polynomial-Time Algorithms for Prime Factorization and Discrete Logarithms on a Quantum Computer", SIAM J. Comput. **26**, 1484 (1997).

[2] L. K. Grover, "A fast quantum mechanical algorithm for database search", in *Proceedings of the twenty-eighth annual ACM symposium on Theory of Computing*, 212, (ACM Press, New York, 1996).

[3] A. K. Ekert, "Quantum cryptography based on Bell's theorem", Phys. Rev. Lett. **67**, 661 (1991).

[4] C. H. Bennett and G. Brassard, "Quantum cryptography: Public key distribution and coin tossing", Theor. Comput. Sci. **560**, 7 (2014).

[5] S. Lloyd, "Universal Quantum Simulators", Science **273**, 1073 (1996).

[6] H. J. Kimble, "The quantum internet", Nature **453**, 1023 (2008).

[7] S. Wehner, D. Elkouss, and R. Hanson, "Quantum internet: A vision for the road ahead", Science **362**, eaam9288 (2018).

[8] E. Schrödinger, "Discussion of Probability Relations between Separated Systems", Math. Proc. Camb. Philos. Soc. **31**, 555 (1935).

[9] A. Einstein, B. Podolsky, and N. Rosen, "Can Quantum-Mechanical Description of Physical Reality Be Considered Complete?", Phys. Rev. **47**, 777 (1935).

[10] J. S. Bell, "On the Einstein Podolsky Rosen paradox", Phys. Phys. Fiz. **1**, 195 (1964).

[11] J. F. Clauser, M. A. Horne, A. Shimony, and R. A. Holt, "Proposed Experiment to Test Local Hidden-Variable Theories", Phys. Rev. Lett. **23**, 880 (1969).

[12] C. H. Bennett, "Quantum Information", Phys. Scr. **T76**, 210 (1998).

[13] R. Jozsa, D. S. Abrams, J. P. Dowling, and C. P. Williams, "Quantum Clock Synchronization Based on Shared Prior Entanglement", Phys. Rev. Lett. **85**, 2010 (2000).

[14] H. Buhrman, R. Cleve, and W. van Dam, "Quantum Entanglement and Communication Complexity", SIAM J. Comput. **30**, 1829 (2001).

[15] Č. Brukner, M. Żukowski, J.-W. Pan, and A. Zeilinger, "Bell's Inequalities and Quantum Communication Complexity", Phys. Rev. Lett. **92**, 127901 (2004).

[16] V. Giovannetti, S. Lloyd, and L. Maccone, "Quantum-enhanced measurements: Beating the standard quantum limit", Science **306**, 1330 (2004).

[17] Č. Brukner, N. Paunković, T. Rudolph, and V. Vedral, "Entanglement-Assisted Orientation in Space", Int. J. Quantum Inf. **04**, 365 (2006).

[18] R. Horodecki, P. Horodecki, M. Horodecki, and K. Horodecki, "Quantum entanglement", Rev. Mod. Phys. **81**, 865 (2009).

[19] E. Chitambar and G. Gour, "Quantum resource theories", Rev. Mod. Phys. **91**, 025001 (2019).

[20] J. L. O'Brien, A. Furusawa, and J. Vučković, "Photonic quantum technologies", Nat. Photonics **3**, 687 (2009).

[21] D. Roy, C. M. Wilson, and O. Firstenberg, "Colloquium: Strongly interacting photons in one-dimensional continuum", Rev. Mod. Phys. **89**, 021001 (2017).

[22] F. Flamini, N. Spagnolo, and F. Sciarrino, "Photonic quantum information processing: a review", Rep. Prog. Phys. **82**, 016001 (2019).

[23] M. K. Tey, Z. Chen, S. A. Aljunid, B. Chng, F. Huber, G. Maslennikov, and C. Kurtsiefer, "Strong interaction between light and a single trapped atom without the need for a cavity", Nat. Phys. **4**, 924 (2008).

[24] D. E. Chang, A. S. Sørensen, E. A. Demler, and M. D. Lukin, "A single-photon transistor using nanoscale surface plasmons", Nat. Phys. **3**, 807 (2007).

[25] J. Hwang, M. Pototschnig, R. Lettow, G. Zumofen, A. Renn, S. Götzinger, and V. Sandoghdar, "A single-molecule optical transistor", Nature **460**, 76 (2009).

[26] H.-P. Breuer and F. Petruccione, *The Theory of Open Quantum Systems*, (Oxford University Press, Oxford, 2007).

[27] V. Gorini, "Completely positive dynamical semigroups of N-level systems", J. Math. Phys. **17**, 821 (1976).

[28] G. Lindblad, "On the generators of quantum dynamical semigroups", Commun. Math. Phys. **48**, 119 (1976).

[29] H.-P. Breuer, E.-M. Laine, J. Piilo, and B. Vacchini, "Colloquium: Non-Markovian dynamics in open quantum systems", Rev. Mod. Phys. **88**, 021002 (2016).

[30] I. de Vega and D. Alonso, "Dynamics of non-Markovian open quantum systems", Rev. Mod. Phys. **89**, 015001 (2017).

[31] K. Pyragas, "Continuous control of chaos by self-controlling feedback", Phys. Lett. A **170**, 421 (1992).

[32] K. J. Åström and P. Kumar, "Control: A perspective", Automatica (Oxf) **50**, 3 (2014).

[33] E. Schöll, S. H. L. Klapp, and P. Hövel (eds.), *Control of Self-Organizing Nonlinear Systems*, (Springer International Publishing, Basel, 2016).

[34] J. Kabuss, F. Katsch, A. Knorr, and A. Carmele, "Unraveling coherent quantum feedback for Pyragas control", J. Opt. Soc. Am. B **33**, C10 (2016).

[35] N. Német and S. Parkins, "Enhanced optical squeezing from a degenerate parametric amplifier via time-delayed coherent feedback", Phys. Rev. A **94**, 023809 (2016).

[36] J. Zhang, Y.-X. Liu, R.-B. Wu, K. Jacobs, and F. Nori, "Quantum feedback: Theory, experiments, and applications", Phys. Rep. **679**, 1 (2017).

[37] L. Droenner, N. L. Naumann, E. Schöll, A. Knorr, and A. Carmele, "Quantum Pyragas control: Selective control of individual photon probabilities", Phys. Rev. A **99**, 023840 (2019).

[38] F. Katsch and A. Knorr, "Optical Preparation and Coherent Control of Ultrafast Nonlinear Quantum Superpositions in Exciton Gases: A Case Study for Atomically Thin Semiconductors", Phys. Rev. X **10**, 041039 (2020).

[39] H. M. Wiseman and G. J. Milburn, "All-optical versus electro-optical quantum-limited feedback", Phys. Rev. A **49**, 4110 (1994).

[40] C. Sayrin, I. Dotsenko, X. Zhou, B. Peaudecerf, T. Rybarczyk, S. Gleyzes, P. Rouchon, M. Mirrahimi, H. Amini, M. Brune, J.-M. Raimond, and S. Haroche, "Real-time quantum feedback prepares and stabilizes photon number states", Nature **477**, 73 (2011).

[41] M. Rossi, D. Mason, J. Chen, Y. Tsaturyan, and A. Schliesser, "Measurement-based quantum control of mechanical motion", Nature **563**, 53 (2018).

[42] S. Lloyd, "Coherent quantum feedback", Phys. Rev. A **62**, 022108 (2000).

[43] S. M. Hein, F. Schulze, A. Carmele, and A. Knorr, "Optical Feedback-Enhanced Photon Entanglement from a Biexciton Cascade", Phys. Rev. Lett. **113**, 027401 (2014).

[44] S. M. Hein, F. Schulze, A. Carmele, and A. Knorr, "Entanglement control in quantum networks by quantum-coherent time-delayed feedback", Phys. Rev. A **91**, 052321 (2015).

[45] Y. Zhou, X. Jia, F. Li, J. Yu, C. Xie, and K. Peng, "Quantum Coherent Feedback Control for Generation System of Optical Entangled State", Sci. Rep. **5**, 11132 (2015).

[46] B. Zhang, S. You, and M. Lu, "Enhancement of spontaneous entanglement generation via coherent quantum feedback", Phys. Rev. A **101**, 032335 (2020).

[47] H. Pichler, S. Choi, P. Zoller, and M. D. Lukin, "Universal photonic quantum computation via time-delayed feedback", Proc. Natl. Acad. Sci. U.S.A. **114**, 11362 (2017).

[48] A. J. Leggett, S. Chakravarty, A. T. Dorsey, M. P. A. Fisher, A. Garg, and W. Zwerger, "Dynamics of the dissipative two-state system", Rev. Mod. Phys. **59**, 1 (1987).

[49] L. Diósi, N. Gisin, and W. T. Strunz, "Non-Markovian quantum state diffusion", Phys. Rev. A **58**, 1699 (1998).

[50] W. T. Strunz, L. Diósi, and N. Gisin, "Open System Dynamics with Non-Markovian Quantum Trajectories", Phys. Rev. Lett. **82**, 1801 (1999).

[51] A. Carmele and S. Reitzenstein, "Non-Markovian features in semiconductor quantum optics: quantifying the role of phonons in experiment and theory", Nanophotonics **8**, 655 (2019).

[52] A. L. Grimsmo, "Time-Delayed Quantum Feedback Control", Phys. Rev. Lett. **115**, 060402 (2015).

[53] H. Pichler and P. Zoller, "Photonic Circuits with Time Delays and Quantum Feedback", Phys. Rev. Lett. **116**, 093601 (2016).

[54] G. Crowder, H. Carmichael, and S. Hughes, "Quantum trajectory theory of few-photon cavity-QED systems with a time-delayed coherent feedback", Phys. Rev. A **101**, 023807 (2020).

[55] S. Arranz Regidor, G. Crowder, H. Carmichael, and S. Hughes, "Modeling quantum light-matter interactions in waveguide QED with retardation, nonlinear interactions, and a time-delayed feedback: Matrix product states versus a space-discretized waveguide model", Phys. Rev. Research **3**, 023030 (2021).

[56] M. Planck, "Ueber das Gesetz der Energieverteilung im Normalspectrum", Ann. Phys. **309**, 553 (1901).

[57] A. Einstein, "Über einen die Erzeugung und Verwandlung des Lichtes betreffenden heuristischen Gesichtspunkt", Ann. Phys. **322**, 132 (1905).

[58] P. A. M. Dirac, "The quantum theory of the emission and absorption of radiation", Proc. R. Soc. Lond. A **114**, 243 (1927).

[59] C. Cohen-Tannoudji, J. Dupont-Roc, and G. Grynberg, *Photons and Atoms*, (Wiley-VCH, Weinheim, 1997).

[60] F. Scheck, *Theoretische Physik 4*, (Springer, Berlin, 2001).

[61] D. F. Walls and G. J. Milburn, *Quantum Optics*, (Springer, Berlin, 2008).

[62] W. P. Schleich, *Quantum Optics in Phase Space*, (Wiley-VCH, Weinheim, 2001).

[63] W. E. Lamb and R. C. Retherford, "Fine Structure of the Hydrogen Atom by a Microwave Method", Phys. Rev. **72**, 241 (1947).

[64] R. H. Dicke, "Coherence in Spontaneous Radiation Processes", Phys. Rev. **93**, 99 (1954).

[65] M. O. Scully and W. E. Lamb, "Quantum Theory of an Optical Maser. I. General Theory", Phys. Rev. **159**, 208 (1967).

[66] H. J. Kimble, "Strong Interactions of Single Atoms and Photons in Cavity QED", Phys. Scr. **T76**, 127 (1998).

[67] S. Haroche and J.-M. Raimond, *Exploring the Quantum*, (Oxford University Press, Oxford, 2006).

[68] S. Ritter, C. Nölleke, C. Hahn, A. Reiserer, A. Neuzner, M. Uphoff, M. Mücke, E. Figueroa, J. Bochmann, and G. Rempe, "An elementary quantum network of single atoms in optical cavities", Nature **484**, 195 (2012).

[69] A. Reiserer and G. Rempe, "Cavity-based quantum networks with single atoms and optical photons", Rev. Mod. Phys. **87**, 1379 (2015).

[70] E. M. Purcell, H. C. Torrey, and R. V. Pound, "Resonance Absorption by Nuclear Magnetic Moments in a Solid", Phys. Rev. **69**, 37 (1946).

[71] H. B. G. Casimir and D. Polder, "The Influence of Retardation on the London-van der Waals Forces", Phys. Rev. **73**, 360 (1948).

[72] E. Jaynes and F. Cummings, "Comparison of quantum and semiclassical radiation theories with application to the beam maser", Proc. IEEE **51**, 89 (1963).

[73] M. Brune, F. Schmidt-Kaler, A. Maali, J. Dreyer, E. Hagley, J. M. Raimond, and S. Haroche, "Quantum Rabi Oscillation: A Direct Test of Field Quantization in a Cavity", Phys. Rev. Lett. **76**, 1800 (1996).

[74] Z. Liao, X. Zeng, H. Nha, and M. S. Zubairy, "Photon transport in a one-dimensional nanophotonic waveguide QED system", Phys. Scr. **91**, 063004 (2016).

[75] P. Lodahl, S. Mahmoodian, S. Stobbe, A. Rauschenbeutel, P. Schneeweiss, J. Volz, H. Pichler, and P. Zoller, "Chiral quantum optics", Nature **541**, 473 (2017).

[76] D. E. Chang, J. S. Douglas, A. González-Tudela, C.-L. Hung, and H. J. Kimble, "Colloquium: Quantum matter built from nanoscopic lattices of atoms and photons", Rev. Mod. Phys. **90**, 031002 (2018).

[77] D. P. DiVincenzo, "The Physical Implementation of Quantum Computation", Fortschritte der Phys. **48**, 771 (2000).

[78] A. S. Sheremet, M. I. Petrov, I. V. Iorsh, A. V. Poshakinskiy, and A. N. Poddubny,

"Waveguide quantum electrodynamics: collective radiance and photon-photon correlations", arXiv:2103.06824 (2021).

[79] I. Bloch, "Quantum coherence and entanglement with ultracold atoms in optical lattices", Nature **453**, 1016 (2008).

[80] R. Blatt and D. Wineland, "Entangled states of trapped atomic ions", Nature **453**, 1008 (2008).

[81] N. V. Corzo, J. Raskop, A. Chandra, A. S. Sheremet, B. Gouraud, and J. Laurat, "Waveguide-coupled single collective excitation of atomic arrays", Nature **566**, 359 (2019).

[82] A. Goban, C.-L. Hung, J. D. Hood, S.-P. Yu, J. A. Muniz, O. Painter, and H. J. Kimble, "Superradiance for Atoms Trapped along a Photonic Crystal Waveguide", Phys. Rev. Lett. **115**, 063601 (2015).

[83] A. Blais, R.-S. Huang, A. Wallraff, S. M. Girvin, and R. J. Schoelkopf, "Cavity quantum electrodynamics for superconducting electrical circuits: An architecture for quantum computation", Phys. Rev. A **69**, 062320 (2004).

[84] N. V. Corzo, B. Gouraud, A. Chandra, A. Goban, A. S. Sheremet, D. V. Kupriyanov, and J. Laurat, "Large Bragg Reflection from One-Dimensional Chains of Trapped Atoms Near a Nanoscale Waveguide", Phys. Rev. Lett. **117**, 133603 (2016).

[85] P. Solano, P. Barberis-Blostein, F. K. Fatemi, L. A. Orozco, and S. L. Rolston, "Super-radiance reveals infinite-range dipole interactions through a nanofiber", Nat. Commun. **8**, 1857 (2017).

[86] T. Nieddu, V. Gokhroo, and S. N. Chormaic, "Optical nanofibres and neutral atoms", J. Opt. **18**, 053001 (2016).

[87] P. Solano, J. A. Grover, J. E. Hoffman, S. Ravets, F. K. Fatemi, L. A. Orozco, and S. L. Rolston, "Optical Nanofibers", in *Advances in Atomic, Molecular, and Optical Physics*, vol. 66, 439, (Academic Press, Cambridge, 2017).

[88] T. Baba, "Slow light in photonic crystals", Nat. Photonics **2**, 465 (2008).

[89] P. Lodahl, S. Mahmoodian, and S. Stobbe, "Interfacing single photons and single quantum dots with photonic nanostructures", Rev. Mod. Phys. **87**, 347 (2015).

[90] A. Goban, C.-L. Hung, S.-P. Yu, J. Hood, J. Muniz, J. Lee, M. Martin, A. McClung, K. Choi, D. Chang, O. Painter, and H. Kimble, "Atom–light interactions in photonic crystals", Nat. Commun. **5**, 3808 (2014).

[91] R. Hanson, L. P. Kouwenhoven, J. R. Petta, S. Tarucha, and L. M. K. Vandersypen, "Spins in few-electron quantum dots", Rev. Mod. Phys. **79**, 1217 (2007).

[92] R. Hanson and D. D. Awschalom, "Coherent manipulation of single spins in semiconductors", Nature **453**, 1043 (2008).

[93] L. Scarpelli, B. Lang, F. Masia, D. M. Beggs, E. A. Muljarov, A. B. Young, R. Oulton, M. Kamp, S. Höfling, C. Schneider, and W. Langbein, "99% beta factor and directional coupling of quantum dots to fast light in photonic crystal waveguides determined by spectral imaging", Phys. Rev. B **100**, 035311 (2019).

[94] M. V. G. Dutt, L. Childress, L. Jiang, E. Togan, J. Maze, F. Jelezko, A. S. Zibrov, P. R. Hemmer, and M. D. Lukin, "Quantum Register Based on Individual Electronic and Nuclear Spin Qubits in Diamond", Science **316**, 1312 (2007).

[95] J. Clarke and F. K. Wilhelm, "Superconducting quantum bits", Nature **453**, 1031 (2008).

[96] F. Arute, K. Arya, R. Babbush, D. Bacon, J. C. Bardin, R. Barends, R. Biswas, S. Boixo, F. G. S. L. Brandao, D. A. Buell, B. Burkett, Y. Chen, Z. Chen, B. Chiaro, R. Collins, W. Courtney, A. Dunsworth, E. Farhi, B. Foxen, A. Fowler, C. Gidney, M. Giustina, R. Graff, K. Guerin, S. Habegger, M. P. Harrigan, M. J. Hartmann, A. Ho, M. Hoffmann, T. Huang, T. S. Humble, S. V. Isakov, E. Jeffrey, Z. Jiang, D. Kafri, K. Kechedzhi, J. Kelly, P. V. Klimov, S. Knysh, A. Korotkov, F. Kostritsa, D. Landhuis, M. Lindmark, E. Lucero, D. Lyakh, S. Mandrà, J. R. McClean, M. McEwen, A. Megrant, X. Mi, K. Michielsen, M. Mohseni, J. Mutus, O. Naaman, M. Neeley, C. Neill, M. Y. Niu, E. Ostby, A. Petukhov, J. C. Platt, C. Quintana, E. G. Rieffel, P. Roushan, N. C. Rubin, D. Sank, K. J. Satzinger, V. Smelyanskiy, K. J. Sung, M. D. Trevithick, A. Vainsencher, B. Villalonga, T. White, Z. J. Yao, P. Yeh, A. Zalcman, H. Neven, and J. M. Martinis, "Quantum supremacy using a programmable superconducting processor", Nature **574**, 505 (2019).

[97] C. Palacios-Berraquero, L. Mueck, and D. M. Persaud, "Instead of 'supremacy' use 'quantum advantage'", Nature **576**, 213 (2019).

[98] X. Gu, A. F. Kockum, A. Miranowicz, Y.-X. Liu, and F. Nori, "Microwave photonics with superconducting quantum circuits", Phys. Rep. **718-719**, 1 (2017).

[99] A. Wallraff, D. I. Schuster, A. Blais, L. Frunzio, R. S. Huang, J. Majer, S. Kumar, S. M. Girvin, and R. J. Schoelkopf, "Strong coupling of a single photon to a superconducting qubit using circuit quantum electrodynamics", Nature **431**, 162 (2004).

[100] A. Blais, A. L. Grimsmo, S. M. Girvin, and A. Wallraff, "Circuit quantum electrodynamics", Rev. Mod. Phys. **93**, 025005 (2021).

[101] M. Mirhosseini, E. Kim, X. Zhang, A. Sipahigil, P. B. Dieterle, A. J. Keller, A. Asenjo-Garcia, D. E. Chang, and O. Painter, "Cavity quantum electrodynamics with atom-like mirrors", Nature **569**, 692 (2019).

[102] M. O. Scully and M. S. Zubairy, *Quantum Optics*, (Cambridge University Press, Cambridge, 1997).

[103] M. Pletyukhov and V. Gritsev, "Scattering of massless particles in one-dimensional chiral channel", New J. Phys. **14**, 095028 (2012).

[104] M. P. Schneider, T. Sproll, C. Stawiarski, P. Schmitteckert, and K. Busch, "Green's-function formalism for waveguide QED applications", Phys. Rev. A **93**, 013828 (2016).

[105] Á. Rivas, S. F. Huelga, and M. B. Plenio, "Quantum non-Markovianity: characterization, quantification and detection", Rep. Prog. Phys. **77**, 094001 (2014).

[106] Á. Rivas, S. F. Huelga, and M. B. Plenio, "Entanglement and Non-Markovianity of Quantum Evolutions", Phys. Rev. Lett. **105**, 050403 (2010).

[107] H.-P. Breuer, E.-M. Laine, and J. Piilo, "Measure for the Degree of Non-Markovian Behavior of Quantum Processes in Open Systems", Phys. Rev. Lett. **103**, 210401 (2009).

[108] H.-P. Breuer, "Genuine quantum trajectories for non-Markovian processes", Phys. Rev. A **70**, 012106 (2004).

[109] M. J. W. Hall, J. D. Cresser, L. Li, and E. Andersson, "Canonical form of master equations and characterization of non-Markovianity", Phys. Rev. A **89**, 042120 (2014).

[110] R. Feynman and F. Vernon, "The theory of a general quantum system interacting with a linear dissipative system", Ann. Phys. **24**, 118 (1963).

[111] U. Weiss, *Quantum Dissipative Systems*, (World Scientific, Singapore, 2008).

[112] L. Diósi and W. T. Strunz, "The non-Markovian stochastic Schrödinger equation for open systems", Phys. Rev. A **235**, 569 (1997).

[113] P. Gaspard and M. Nagaoka, "Non-Markovian stochastic Schrödinger equation", J. Chem. Phys. **111**, 5676 (1999).

[114] M. W. Jack and M. J. Collett, "Continuous measurement and non-Markovian quantum trajectories", Phys. Rev. A **61**, 062106 (2000).

[115] C. W. Gardiner and M. J. Collett, "Input and output in damped quantum systems: Quantum stochastic differential equations and the master equation", Phys. Rev. A **31**, 3761 (1985).

[116] L. Diósi, "Non-Markovian open quantum systems: Input-output fields, memory, and monitoring", Phys. Rev. A **85**, 034101 (2012).

[117] W.-M. Zhang, P.-Y. Lo, H.-N. Xiong, M. W.-Y. Tu, and F. Nori, "General Non-Markovian Dynamics of Open Quantum Systems", Phys. Rev. Lett. **109**, 170402 (2012).

[118] C. Gardiner and P. Zoller, *The Quantum World of Ultra-Cold Atoms and Light Book I: Foundations of Quantum Optics*, (Imperial College Press, London, 2014).

[119] R. Loudon, *The Quantum Theory of Light*, (Oxford University Press, Oxford, 1974).

[120] A. Steane, "Quantum computing", Rep. Prog. Phys. **61**, 117 (1998).

[121] N. Gisin and R. Thew, "Quantum communication", Nat. Photonics **1**, 165 (2007).

[122] Z.-S. Yuan, X.-H. Bao, C.-Y. Lu, J. Zhang, C.-Z. Peng, and J.-W. Pan, "Entangled photons and quantum communication", Phys. Rep. **497**, 1 (2010).

[123] M. W. Mitchell, J. S. Lundeen, and A. M. Steinberg, "Super-resolving phase measurements with a multiphoton entangled state", Nature **429**, 161 (2004).

[124] V. Giovannetti, S. Lloyd, and L. MacCone, "Advances in quantum metrology", Nat. Photonics **5**, 222 (2011).

[125] S. Slussarenko, M. M. Weston, H. M. Chrzanowski, L. K. Shalm, V. B. Verma, S. W. Nam, and G. J. Pryde, "Unconditional violation of the shot-noise limit in photonic quantum metrology", Nat. Photonics **11**, 700 (2017).

[126] D. Bohm and Y. Aharonov, "Discussion of Experimental Proof for the Paradox of Einstein, Rosen, and Podolsky", Phys. Rev. **108**, 1070 (1957).

[127] A. Mair, A. Vaziri, G. Weihs, and A. Zeilinger, "Entanglement of the orbital angular momentum states of photons", Nature **412**, 313 (2001).

[128] J. D. Franson, "Bell inequality for position and time", Phys. Rev. Lett. **62**, 2205 (1989).

[129] J. A. Formaggio, D. I. Kaiser, M. M. Murskyj, and T. E. Weiss, "Violation of the Leggett-Garg Inequality in Neutrino Oscillations", Phys. Rev. Lett. **117**, 050402 (2016).

[130] B. Hensen, H. Bernien, A. E. Dréau, A. Reiserer, N. Kalb, M. S. Blok, J. Ruitenberg, R. F. L. Vermeulen, R. N. Schouten, C. Abellán, W. Amaya, V. Pruneri, M. W. Mitchell, M. Markham, D. J. Twitchen, D. Elkouss, S. Wehner, T. H. Taminiau, and R. Hanson, "Loophole-free Bell inequality violation using electron spins separated by 1.3 kilometres", Nature **526**, 682 (2015).

[131] K. C. Lee, M. R. Sprague, B. J. Sussman, J. Nunn, N. K. Langford, X.-M. Jin, T. Champion, P. Michelberger, K. F. Reim, D. England, D. Jaksch, and I. A. Walmsley, "Entangling Macroscopic Diamonds at Room Temperature", Science **334**, 1253 (2011).

[132] R. A. Thomas, M. Parniak, C. Østfeldt, C. B. Møller, C. Bærentsen, Y. Tsaturyan, A. Schliesser, J. Appel, E. Zeuthen, and E. S. Polzik, "Entanglement between distant macroscopic mechanical and spin systems", Nat. Phys. **17**, 228 (2021).

[133] V. Coffman, J. Kundu, and W. K. Wootters, "Distributed entanglement", Phys. Rev. A **61**, 052306 (2000).

[134] F. Verstraete, J. Dehaene, and B. De Moor, "Normal forms and entanglement measures for multipartite quantum states", Phys. Rev. A **68**, 012103 (2003).

[135] M. Hein, J. Eisert, and H. J. Briegel, "Multiparty entanglement in graph states", Phys. Rev. A **69**, 062311 (2004).

[136] M. B. Plenio and S. Virmani, "An introduction to entanglement measures", Quant. Inf. Comput. **7**, 1 (2007).

[137] S. Nezami and M. Walter, "Multipartite Entanglement in Stabilizer Tensor Networks", Phys. Rev. Lett. **125**, 241602 (2020).

[138] B. M. Terhal, "Bell inequalities and the separability criterion", Phys. Lett. A **271**, 319 (2000).

[139] V. Vedral, M. B. Plenio, M. A. Rippin, and P. L. Knight, "Quantifying Entanglement", Phys. Rev. Lett. **78**, 2275 (1997).

[140] G. Vidal, "Entanglement monotones", J. Mod. Opt. **47**, 355 (2000).

[141] B. S. Cirel'son, "Quantum generalizations of Bell's inequality", Lett. Math. Phys. **4**, 93 (1980).

[142] A. Aspect, P. Grangier, and G. Roger, "Experimental Tests of Realistic Local Theories via Bell's Theorem", Phys. Rev. Lett. **47**, 460 (1981).

[143] G. Lima, G. Vallone, A. Chiuri, A. Cabello, and P. Mataloni, "Experimental Bell-inequality violation without the postselection loophole", Phys. Rev. A **81**, 040101 (2010).

[144] S. J. Freedman and J. F. Clauser, "Experimental Test of Local Hidden-Variable Theories", Phys. Rev. Lett. **28**, 938 (1972).

[145] A. Aspect, P. Grangier, and G. Roger, "Experimental Realization of Einstein-Podolsky-Rosen-Bohm Gedankenexperiment: A New Violation of Bell's Inequalities", Phys. Rev. Lett. **49**, 91 (1982).

[146] W. Tittel, J. Brendel, H. Zbinden, and N. Gisin, "Violation of Bell Inequalities by Photons More Than 10 km Apart", Phys. Rev. Lett. **81**, 3563 (1998).

[147] G. Weihs, T. Jennewein, C. Simon, H. Weinfurter, and A. Zeilinger, "Violation of Bell's Inequality under Strict Einstein Locality Conditions", Phys. Rev. Lett. **81**, 5039 (1998).

[148] M. Giustina, A. Mech, S. Ramelow, B. Wittmann, J. Kofler, J. Beyer, A. Lita,

B. Calkins, T. Gerrits, S. W. Nam, R. Ursin, and A. Zeilinger, "Bell violation using entangled photons without the fair-sampling assumption", Nature **497**, 227 (2013).

[149] B. G. Christensen, K. T. McCusker, J. B. Altepeter, B. Calkins, T. Gerrits, A. E. Lita, A. Miller, L. K. Shalm, Y. Zhang, S. W. Nam, N. Brunner, C. C. W. Lim, N. Gisin, and P. G. Kwiat, "Detection-Loophole-Free Test of Quantum Nonlocality, and Applications", Phys. Rev. Lett. **111**, 130406 (2013).

[150] M. Giustina, M. A. M. Versteegh, S. Wengerowsky, J. Handsteiner, A. Hochrainer, K. Phelan, F. Steinlechner, J. Kofler, J.-Å. Larsson, C. Abellán, W. Amaya, V. Pruneri, M. W. Mitchell, J. Beyer, T. Gerrits, A. E. Lita, L. K. Shalm, S. W. Nam, T. Scheidl, R. Ursin, B. Wittmann, and A. Zeilinger, "Significant-Loophole-Free Test of Bell's Theorem with Entangled Photons", Phys. Rev. Lett. **115**, 250401 (2015).

[151] L. K. Shalm, E. Meyer-Scott, B. G. Christensen, P. Bierhorst, M. A. Wayne, M. J. Stevens, T. Gerrits, S. Glancy, D. R. Hamel, M. S. Allman, K. J. Coakley, S. D. Dyer, C. Hodge, A. E. Lita, V. B. Verma, C. Lambrocco, E. Tortorici, A. L. Migdall, Y. Zhang, D. R. Kumor, W. H. Farr, F. Marsili, M. D. Shaw, J. A. Stern, C. Abellán, W. Amaya, V. Pruneri, T. Jennewein, M. W. Mitchell, P. G. Kwiat, J. C. Bienfang, R. P. Mirin, E. Knill, and S. W. Nam, "Strong Loophole-Free Test of Local Realism", Phys. Rev. Lett. **115**, 250402 (2015).

[152] S. Aerts, P. Kwiat, J.-Å. Larsson, and M. Żukowski, "Two-Photon Franson-Type Experiments and Local Realism", Phys. Rev. Lett. **83**, 2872 (1999).

[153] A. Cabello, A. Rossi, G. Vallone, F. De Martini, and P. Mataloni, "Proposed Bell Experiment with Genuine Energy-Time Entanglement", Phys. Rev. Lett. **102**, 040401 (2009).

[154] F. Vedovato, C. Agnesi, M. Tomasin, M. Avesani, J.-Å. Larsson, G. Vallone, and P. Villoresi, "Postselection-Loophole-Free Bell Violation with Genuine Time-Bin Entanglement", Phys. Rev. Lett. **121**, 190401 (2018).

[155] M. A. Nielsen and I. L. Chuang, *Quantum Computation and Quantum Information*, (Cambridge University Press, Cambridge, 2010).

[156] R. Horodecki and P. Horodecki, "Quantum redundancies and local realism", Phys. Lett. A **194**, 147 (1994).

[157] R. Horodecki and M. Horodecki, "Information-theoretic aspects of inseparability of mixed states", Phys. Rev. A **54**, 1838 (1996).

[158] M. A. Nielsen and J. Kempe, "Separable States Are More Disordered Globally than Locally", Phys. Rev. Lett. **86**, 5184 (2001).

[159] V. Vedral and M. B. Plenio, "Entanglement measures and purification procedures", Phys. Rev. A **57**, 1619 (1998).

[160] S. Hill and W. K. Wootters, "Entanglement of a Pair of Quantum Bits", Phys. Rev. Lett. **78**, 5022 (1997).

[161] W. K. Wootters, "Entanglement of Formation of an Arbitrary State of Two Qubits", Phys. Rev. Lett. **80**, 2245 (1998).

[162] A. Peres, "Separability Criterion for Density Matrices", Phys. Rev. Lett. **77**, 1413 (1996).

[163] K. Życzkowski, P. Horodecki, A. Sanpera, and M. Lewenstein, "Volume of the set of separable states", Phys. Rev. A **58**, 883 (1998).

[164] J. I. Cirac, P. Zoller, H. J. Kimble, and H. Mabuchi, "Quantum State Transfer and Entanglement Distribution among Distant Nodes in a Quantum Network", Phys. Rev. Lett. **78**, 3221 (1997).

[165] J.-T. Shen and S. Fan, "Coherent Single Photon Transport in a One-Dimensional Waveguide Coupled with Superconducting Quantum Bits", Phys. Rev. Lett. **95**, 213001 (2005).

[166] T. E. Northup and R. Blatt, "Quantum information transfer using photons", Nat. Photonics **8**, 356 (2014).

[167] B. Vermersch, P.-O. Guimond, H. Pichler, and P. Zoller, "Quantum State Transfer via Noisy Photonic and Phononic Waveguides", Phys. Rev. Lett. **118**, 133601 (2017).

[168] A. H. Kiilerich and K. Mølmer, "Input-Output Theory with Quantum Pulses", Phys. Rev. Lett. **123**, 123604 (2019).

[169] A. H. Kiilerich and K. Mølmer, "Quantum interactions with pulses of radiation", Phys. Rev. A **102**, 023717 (2020).

[170] R. J. Cook and P. W. Milonni, "Quantum theory of an atom near partially reflecting walls", Phys. Rev. A **35**, 5081 (1987).

[171] U. Dorner and P. Zoller, "Laser-driven atoms in half-cavities", Phys. Rev. A **66**, 023816 (2002).

[172] J. Eschner, C. Raab, F. Schmidt-Kaler, and R. Blatt, "Light interference from single atoms and their mirror images", Nature **413**, 495 (2001).

[173] M. A. Wilson, P. Bushev, J. Eschner, F. Schmidt-Kaler, C. Becher, R. Blatt, and U. Dorner, "Vacuum-Field Level Shifts in a Single Trapped Ion Mediated by a Single Distant Mirror", Phys. Rev. Lett. **91**, 213602 (2003).

[174] F. Dubin, D. Rotter, M. Mukherjee, C. Russo, J. Eschner, and R. Blatt, "Photon Correlation versus Interference of Single-Atom Fluorescence in a Half-Cavity", Phys. Rev. Lett. **98**, 183003 (2007).

[175] I.-C. Hoi, A. F. Kockum, L. Tornberg, A. Pourkabirian, G. Johansson, P. Delsing, and C. M. Wilson, "Probing the quantum vacuum with an artificial atom in front of a mirror", Nat. Phys. **11**, 1045 (2015).

[176] P. Y. Wen, A. F. Kockum, H. Ian, J. C. Chen, F. Nori, and I.-C. Hoi, "Reflective Amplification without Population Inversion from a Strongly Driven Superconducting Qubit", Phys. Rev. Lett. **120**, 063603 (2018).

[177] P. Y. Wen, K.-T. Lin, A. F. Kockum, B. Suri, H. Ian, J. C. Chen, S. Y. Mao, C. C. Chiu, P. Delsing, F. Nori, G.-D. Lin, and I.-C. Hoi, "Large Collective Lamb Shift of Two Distant Superconducting Artificial Atoms", Phys. Rev. Lett. **123**, 233602 (2019).

[178] T. Tufarelli, F. Ciccarello, and M. S. Kim, "Dynamics of spontaneous emission in a single-end photonic waveguide", Phys. Rev. A **87**, 013820 (2013).

[179] A. I. Lvovsky, B. C. Sanders, and W. Tittel, "Optical quantum memory", Nat. Photonics **3**, 706 (2009).

[180] G. Calajó, Y.-L. L. Fang, H. U. Baranger, and F. Ciccarello, "Exciting a Bound State in the Continuum through Multiphoton Scattering Plus Delayed Quantum Feedback", Phys. Rev. Lett. **122**, 073601 (2019).

[181] K. Barkemeyer, A. Knorr, and A. Carmele, "Strongly entangled system-reservoir dynamics with multiphoton pulses beyond the two-excitation limit: Exciting the atom-photon bound state", Phys. Rev. A **103**, 033704 (2021).

[182] S. R. White, "Density matrix formulation for quantum renormalization groups", Phys. Rev. Lett. **69**, 2863 (1992).

[183] A. J. Daley, C. Kollath, U. Schollwöck, and G. Vidal, "Time-dependent density-matrix renormalization-group using adaptive effective Hilbert spaces", J. Stat. Mech.: Theory Exp. **2004.04**, P04005 (2004).

[184] U. Schollwöck, "The density-matrix renormalization group in the age of matrix product states", Ann. Phys. (N. Y.) **326**, 96 (2011).

[185] J. C. Bridgeman and C. T. Chubb, "Hand-waving and interpretive dance: an introductory course on tensor networks", J. Phys. A **50**, 223001 (2017).

[186] J. I. Cirac, D. Pérez-García, N. Schuch, and F. Verstraete, "Matrix product states and projected entangled pair states: Concepts, symmetries, theorems", Rev. Mod. Phys. **93**, 045003 (2021).

[187] A. Carmele, J. Kabuss, F. Schulze, S. Reitzenstein, and A. Knorr, "Single Photon Delayed Feedback: A Way to Stabilize Intrinsic Quantum Cavity Electrodynamics", Phys. Rev. Lett. **110**, 013601 (2013).

[188] J. Schachenmayer, I. Lesanovsky, A. Micheli, and A. J. Daley, "Dynamical crystal

creation with polar molecules or Rydberg atoms in optical lattices", New J. Phys. **12**, 103044 (2010).

[189] M. Fishman, S. R. White, and E. M. Stoudenmire, "The ITensor Software Library for Tensor Network Calculations", arXiv:2007.14822 (2020).

[190] M. G. Raymer and I. A. Walmsley, "Temporal modes in quantum optics: then and now", Phys. Scr. **95**, 064002 (2020).

[191] P.-O. Guimond, M. Pletyukhov, H. Pichler, and P. Zoller, "Delayed coherent quantum feedback from a scattering theory and a matrix product state perspective", Quantum Sci. Technol. **2**, 044012 (2017).

[192] J. Kabuss, D. O. Krimer, S. Rotter, K. Stannigel, A. Knorr, and A. Carmele, "Analytical study of quantum-feedback-enhanced Rabi oscillations", Phys. Rev. A **92**, 053801 (2015).

[193] P. Longo, P. Schmitteckert, and K. Busch, "Few-Photon Transport in Low-Dimensional Systems: Interaction-Induced Radiation Trapping", Phys. Rev. Lett. **104**, 023602 (2010).

[194] G. Calajó, F. Ciccarello, D. Chang, and P. Rabl, "Atom-field dressed states in slow-light waveguide QED", Phys. Rev. A **93**, 033833 (2016).

[195] C. W. Hsu, B. Zhen, A. D. Stone, J. D. Joannopoulos, and M. Soljačić, "Bound states in the continuum", Nat. Rev. Mater. **1**, 16048 (2016).

[196] Y. Lu, N. L. Naumann, J. Cerrillo, Q. Zhao, A. Knorr, and A. Carmele, "Intensified antibunching via feedback-induced quantum interference", Phys. Rev. A **95**, 063840 (2017).

[197] G. Crowder, L. Ramunno, and S. Hughes, "Quantum Trajectory Theory and Simulations of Nonlinear Spectra and Multi-Photon Effects in Waveguide-QED Systems with a Time-Delayed Coherent Feedback", arXiv:2110.09362 (2021).

[198] K. Barkemeyer, A. Knorr, and A. Carmele, "Heisenberg treatment of multiphoton pulses in non-Markovian waveguide-QED", arXiv:2111.02816 (2021).

[199] C. W. Gardiner and P. Zoller, *Quantum noise*, (Springer, Berlin, 2004).

[200] Y. Wang, J. Minář, G. Hétet, and V. Scarani, "Quantum memory with a single two-level atom in a half cavity", Phys. Rev. A **85**, 013823 (2012).

[201] B. Krummheuer, V. M. Axt, and T. Kuhn, "Theory of pure dephasing and the resulting absorption line shape in semiconductor quantum dots", Phys. Rev. B **65**, 195313 (2002).

[202] A. J. Ramsay, A. V. Gopal, E. M. Gauger, A. Nazir, B. W. Lovett, A. M. Fox, and

M. S. Skolnick, "Damping of Exciton Rabi Rotations by Acoustic Phonons in Optically Excited InGaAs/GaAs Quantum Dots", Phys. Rev. Lett. **104**, 017402 (2010).

[203] A. V. Kuhlmann, J. Houel, A. Ludwig, L. Greuter, D. Reuter, A. D. Wieck, M. Poggio, and R. J. Warburton, "Charge noise and spin noise in a semiconductor quantum device", Nat. Phys. **9**, 570 (2013).

[204] K. Roy-Choudhury and S. Hughes, "Quantum theory of the emission spectrum from quantum dots coupled to structured photonic reservoirs and acoustic phonons", Phys. Rev. B **92**, 205406 (2015).

[205] A. Nazir and D. P. S. McCutcheon, "Modelling exciton–phonon interactions in optically driven quantum dots", J. Phys. Condens. Matter **28**, 103002 (2016).

[206] J. Iles-Smith, D. P. S. McCutcheon, A. Nazir, and J. Mørk, "Phonon scattering inhibits simultaneous near-unity efficiency and indistinguishability in semiconductor single-photon sources", Nat. Photonics **11**, 521 (2017).

[207] M. Gross and S. Haroche, "Superradiance: An essay on the theory of collective spontaneous emission", Phys. Rep. **93**, 301 (1982).

[208] F. Dinc, I. Ercan, and A. M. Branczyk, "Exact Markovian and non-Markovian time dynamics in waveguide QED: Collective interactions, bound states in continuum, superradiance and subradiance", Quantum **3**, 213 (2019).

[209] K. Sinha, P. Meystre, E. A. Goldschmidt, F. K. Fatemi, S. L. Rolston, and P. Solano, "Non-Markovian Collective Emission from Macroscopically Separated Emitters", Phys. Rev. Lett. **124**, 043603 (2020).

[210] A. Carmele, N. Nemet, V. Canela, and S. Parkins, "Pronounced non-Markovian features in multiply excited, multiple emitter waveguide QED: Retardation induced anomalous population trapping", Phys. Rev. Research **2**, 013238 (2020).

[211] H. Zheng and H. U. Baranger, "Persistent Quantum Beats and Long-Distance Entanglement from Waveguide-Mediated Interactions", Phys. Rev. Lett. **110**, 113601 (2013).

[212] P. Facchi, M. S. Kim, S. Pascazio, F. V. Pepe, D. Pomarico, and T. Tufarelli, "Bound states and entanglement generation in waveguide quantum electrodynamics", Phys. Rev. A **94**, 043839 (2016).

[213] C. Gonzalez-Ballestero, F. J. García-Vidal, and E. Moreno, "Non-Markovian effects in waveguide-mediated entanglement", New J. Phys. **15**, 073015 (2013).

[214] V. Paulisch, H. J. Kimble, and A. González-Tudela, "Universal quantum computation in waveguide QED using decoherence free subspaces", New J. Phys. **18**, 043041 (2016).

[215] Z. Ficek and R. Tanaś, "Entangled states and collective nonclassical effects in two-atom systems", Phys. Rep. **372**, 369 (2002).

[216] G. Ordonez, K. Na, and S. Kim, "Bound states in the continuum in quantum-dot pairs", Phys. Rev. A **73**, 022113 (2006).

[217] A. Gonzalez-Tudela, D. Martin-Cano, E. Moreno, L. Martin-Moreno, C. Tejedor, and F. J. Garcia-Vidal, "Entanglement of Two Qubits Mediated by One-Dimensional Plasmonic Waveguides", Phys. Rev. Lett. **106**, 020501 (2011).

[218] E. S. Redchenko and V. I. Yudson, "Decay of metastable excited states of two qubits in a waveguide", Phys. Rev. A **90**, 063829 (2014).

[219] Z. Ficek and R. Tanaś, "Delayed sudden birth of entanglement", Phys. Rev. A **77**, 054301 (2008).

[220] P. G. Kwiat, K. Mattle, H. Weinfurter, A. Zeilinger, A. V. Sergienko, and Y. Shih, "New High-Intensity Source of Polarization-Entangled Photon Pairs", Phys. Rev. Lett. **75**, 4337 (1995).

[221] T. Jennewein, C. Simon, G. Weihs, H. Weinfurter, and A. Zeilinger, "Quantum Cryptography with Entangled Photons", Phys. Rev. Lett. **84**, 4729 (2000).

[222] M. Müller, S. Bounouar, K. D. Jöns, M. Glässl, and P. Michler, "On-demand generation of indistinguishable polarization-entangled photon pairs", Nat. Photonics **8**, 224 (2014).

[223] J. Brendel, N. Gisin, W. Tittel, and H. Zbinden, "Pulsed Energy-Time Entangled Twin-Photon Source for Quantum Communication", Phys. Rev. Lett. **82**, 2594 (1999).

[224] Q. Zhang, H. Takesue, S. W. Nam, C. Langrock, X. Xie, B. Baek, M. M. Fejer, and Y. Yamamoto, "Distribution of time-energy entanglement over 100 km fiber using superconducting singlephoton detectors", Opt. Express **16**, 5776 (2008).

[225] J. Nunn, L. J. Wright, C. Söller, L. Zhang, I. A. Walmsley, and B. J. Smith, "Large-alphabet time-frequency entangled quantum key distribution by means of time-to-frequency conversion", Opt. Express **21**, 15959 (2013).

[226] J. M. Lukens, A. Dezfooliyan, C. Langrock, M. M. Fejer, D. E. Leaird, and A. M. Weiner, "Orthogonal Spectral Coding of Entangled Photons", Phys. Rev. Lett. **112**, 133602 (2014).

[227] V. Giovannetti, S. Lloyd, and L. Maccone, "Quantum-enhanced positioning and clock synchronization", Nature **412**, 417 (2001).

[228] Z. Y. Ou, X. Y. Zou, L. J. Wang, and L. Mandel, "Observation of nonlocal interference in separated photon channels", Phys. Rev. Lett. **65**, 321 (1990).

[229] J. Brendel, E. Mohler, and W. Martienssen, "Time-resolved dual-beam two-photon interferences with high visibility", Phys. Rev. Lett. **66**, 1142 (1991).

[230] P. G. Kwiat, A. M. Steinberg, and R. Y. Chiao, "High-visibility interference in a Bell-inequality experiment for energy and time", Phys. Rev. A **47**, R2472 (1993).

[231] D. Grassani, S. Azzini, M. Liscidini, M. Galli, M. J. Strain, M. Sorel, J. E. Sipe, and D. Bajoni, "Micrometer-scale integrated silicon source of time-energy entangled photons", Optica **2**, 88 (2015).

[232] M. Peiris, K. Konthasinghe, and A. Muller, "Franson Interference Generated by a Two-Level System", Phys. Rev. Lett. **118**, 030501 (2017).

[233] J. Park, T. Jeong, H. Kim, and H. S. Moon, "Time-Energy Entangled Photon Pairs from Doppler-Broadened Atomic Ensemble via Collective Two-Photon Coherence", Phys. Rev. Lett. **121**, 263601 (2018).

[234] A. J. Shields, "Semiconductor quantum light sources", Nat. Photonics **1**, 215 (2007).

[235] P. K. Pathak and S. Hughes, "Coherent generation of time-bin entangled photon pairs using the biexciton cascade and cavity-assisted piecewise adiabatic passage", Phys. Rev. B **83**, 245301 (2011).

[236] H. Jayakumar, A. Predojević, T. Kauten, T. Huber, G. S. Solomon, and G. Weihs, "Time-bin entangled photons from a quantum dot", Nat. Commun. **5**, 4251 (2014).

[237] T. Heindel, A. Thoma, M. von Helversen, M. Schmidt, A. Schlehahn, M. Gschrey, P. Schnauber, J. H. Schulze, A. Strittmatter, J. Beyer, S. Rodt, A. Carmele, A. Knorr, and S. Reitzenstein, "A bright triggered twin-photon source in the solid state", Nat. Commun. **8**, 14870 (2017).

[238] M. Bayer, T. L. Reinecke, F. Weidner, A. Larionov, A. McDonald, and A. Forchel, "Inhibition and Enhancement of the Spontaneous Emission of Quantum Dots in Structured Microresonators", Phys. Rev. Lett. **86**, 3168 (2001).

[239] D. G. Gevaux, A. J. Bennett, R. M. Stevenson, A. J. Shields, P. Atkinson, J. Griffiths, D. Anderson, G. A. C. Jones, and D. A. Ritchie, "Enhancement and suppression of spontaneous emission by temperature tuning InAs quantum dots to photonic crystal cavities", Appl. Phys. Lett. **88**, 131101 (2006).

[240] T. Jakubczyk, H. Franke, T. Smoleński, M. Ściesiek, W. Pacuski, A. Golnik, R. Schmidt-Grund, M. Grundmann, C. Kruse, D. Hommel, and P. Kossacki, "Inhibition and Enhancement of the Spontaneous Emission of Quantum Dots in Micropillar Cavities with Radial-Distributed Bragg Reflectors", ACS Nano **8**, 9970 (2014).

[241] E. Schöll, L. Schweickert, L. Hanschke, K. D. Zeuner, F. Sbresny, T. Lettner, R. Trivedi, M. Reindl, S. F. Covre da Silva, R. Trotta, J. J. Finley, J. Vučković, K. Müller, A. Rastelli, V. Zwiller, and K. D. Jöns, "Crux of Using the Cascaded

Emission of a Three-Level Quantum Ladder System to Generate Indistinguishable Photons", Phys. Rev. Lett. **125**, 233605 (2020).

[242] K. Barkemeyer, M. Hohn, S. Reitzenstein, and A. Carmele, "Boosting energy-time entanglement using coherent time-delayed feedback", Phys. Rev. A **103**, 062423 (2021).

[243] J. Jogenfors and J.-Å. Larsson, "Energy-time entanglement, elements of reality, and local realism", J. Phys. A **47**, 424032 (2014).

[244] A. Cuevas, G. Carvacho, G. Saavedra, J. Cariñe, W. Nogueira, M. Figueroa, A. Cabello, P. Mataloni, G. Lima, and G. Xavier, "Long-distance distribution of genuine energy-time entanglement", Nat. Commun. **4**, 2871 (2013).

[245] J. Jogenfors, A. M. Elhassan, J. Ahrens, M. Bourennane, and J.-Å. Larsson, "Hacking the Bell test using classical light in energy-time entanglement–based quantum key distribution", Sci. Adv. **1**, e1500793 (2015).

[246] M. Tomasin, E. Mantoan, J. Jogenfors, G. Vallone, J.-Å. Larsson, and P. Villoresi, "High-visibility time-bin entanglement for testing chained Bell inequalities", Phys. Rev. A **95**, 032107 (2017).

[247] J. D. Franson, "Two-photon interferometry over large distances", Phys. Rev. A **44**, 4552 (1991).

[248] O. Benson, C. Santori, M. Pelton, and Y. Yamamoto, "Regulated and Entangled Photons from a Single Quantum Dot", Phys. Rev. Lett. **84**, 2513 (2000).

[249] N. Akopian, N. H. Lindner, E. Poem, Y. Berlatzky, J. Avron, D. Gershoni, B. D. Gerardot, and P. M. Petroff, "Entangled Photon Pairs from Semiconductor Quantum Dots", Phys. Rev. Lett. **96**, 130501 (2006).

[250] A. Dousse, J. Suffczyński, A. Beveratos, O. Krebs, A. Lemaître, I. Sagnes, J. Bloch, P. Voisin, and P. Senellart, "Ultrabright source of entangled photon pairs", Nature **466**, 217 (2010).

[251] S. Bounouar, M. Müller, A. M. Barth, M. Glässl, V. M. Axt, and P. Michler, "Phonon-assisted robust and deterministic two-photon biexciton preparation in a quantum dot", Phys. Rev. B **91**, 161302 (2015).

[252] P. G. Kwiat, E. Waks, A. G. White, I. Appelbaum, and P. H. Eberhard, "Ultrabright source of polarization-entangled photons", Phys. Rev. A **60**, R773 (1999).

[253] D. Gammon, E. S. Snow, B. V. Shanabrook, D. S. Katzer, and D. Park, "Fine Structure Splitting in the Optical Spectra of Single GaAs Quantum Dots", Phys. Rev. Lett. **76**, 3005 (1996).

[254] M. Bayer, G. Ortner, O. Stern, A. Kuther, A. A. Gorbunov, A. Forchel, P. Hawrylak, S. Fafard, K. Hinzer, T. L. Reinecke, S. N. Walck, J. P. Reithmaier, F. Klopf,

and F. Schäfer, "Fine structure of neutral and charged excitons in self-assembled In(Ga)As/(Al)GaAs quantum dots", Phys. Rev. B **65**, 195315 (2002).

[255] T. M. Stace, G. J. Milburn, and C. H. W. Barnes, "Entangled two-photon source using biexciton emission of an asymmetric quantum dot in a cavity", Phys. Rev. B **67**, 085317 (2003).

[256] R. J. Young, R. M. Stevenson, P. Atkinson, K. Cooper, D. A. Ritchie, and A. J. Shields, "Improved fidelity of triggered entangled photons from single quantum dots", New J. Phys. **8**, 29 (2006).

[257] A. J. Bennett, M. A. Pooley, R. M. Stevenson, M. B. Ward, R. B. Patel, A. B. de la Giroday, N. Sköld, I. Farrer, C. A. Nicoll, D. A. Ritchie, and A. J. Shields, "Electric-field-induced coherent coupling of the exciton states in a single quantum dot", Nat. Phys. **6**, 947 (2010).

[258] M. A. M. Versteegh, M. E. Reimer, K. D. Jöns, D. Dalacu, P. J. Poole, A. Gulinatti, A. Giudice, and V. Zwiller, "Observation of strongly entangled photon pairs from a nanowire quantum dot", Nat. Commun. **5**, 5298 (2014).

[259] J. Zhang, J. S. Wildmann, F. Ding, R. Trotta, Y. Huo, E. Zallo, D. Huber, A. Rastelli, and O. G. Schmidt, "High yield and ultrafast sources of electrically triggered entangled-photon pairs based on strain-tunable quantum dots", Nat. Commun. **6**, 10067 (2015).

[260] R. Winik, D. Cogan, Y. Don, I. Schwartz, L. Gantz, E. R. Schmidgall, N. Livneh, R. Rapaport, E. Buks, and D. Gershoni, "On-demand source of maximally entangled photon pairs using the biexciton-exciton radiative cascade", Phys. Rev. B **95**, 235435 (2017).

[261] D. Huber, M. Reindl, S. F. Covre da Silva, C. Schimpf, J. Martín-Sánchez, H. Huang, G. Piredda, J. Edlinger, A. Rastelli, and R. Trotta, "Strain-Tunable GaAs Quantum Dot: A Nearly Dephasing-Free Source of Entangled Photon Pairs on Demand", Phys. Rev. Lett. **121**, 033902 (2018).

[262] S. Bounouar, G. Rein, K. Barkemeyer, J. Schleibner, P. Schnauber, M. Gschrey, J.-H. Schulze, A. Strittmatter, S. Rodt, A. Knorr, A. Carmele, and S. Reitzenstein, "Entanglement robustness to excitonic spin precession in a quantum dot", Phys. Rev. B **102**, 045304 (2020).

[263] D. F. V. James, P. G. Kwiat, W. J. Munro, and A. G. White, "Measurement of qubits", Phys. Rev. A **64**, 052312 (2001).

[264] A. Carmele and A. Knorr, "Analytical solution of the quantum-state tomography of the biexciton cascade in semiconductor quantum dots: Pure dephasing does not affect entanglement", Phys. Rev. B **84**, 075328 (2011).

[265] D. E. Reiter, T. Kuhn, and V. M. Axt, "Distinctive characteristics of carrier-phonon

interactions in optically driven semiconductor quantum dots", Adv. Phys.: X **4**, 1655478 (2019).

[266] O. Kaestle, R. Finsterhoelzl, A. Knorr, and A. Carmele, "Continuous and time-discrete non-Markovian system-reservoir interactions: Dissipative coherent quantum feedback in Liouville space", Phys. Rev. Research **3**, 023168 (2021).

Acknowledgements

First of all, I thank Prof. Dr. Andreas Knorr for making it possible for me to work on the topics presented in this thesis. As a part of his group, I had the opportunity to follow my scientific curiosity and explore the quantum world of light and matter. I am grateful for the support and guidance he has given me, which have always been an anchor during the ups and downs of my doctoral studies. I would like to express my gratitude to Prof. Dr. Scott Parkins for being interested in my research and agreeing to assess this thesis. Furthermore, I would like to acknowledge Prof. Dr. Janik Wolters for chairing the dissertation committee.

My special thanks go to Dr. Alexander Carmele for his support and faith in me, which were of great importance for the success of my dissertation project. I am particularly grateful for his infectious excitement for physics. Working with him was a great inspiration, and every conversation we had has opened up new perspectives. Moreover, I would like to thank all current and former members of the AG Knorr for stimulating scientific discussions, eventful conferences, as well as enjoyable breaks. It was valuable to have colleagues with whom to share the experiences of the past years. In particular, I would like to mention my office mates Dr. Dr. Regina Finsterhölzl, Jasmin Justen, Manuel Katzer, and Manuel Kraft, who always had an open ear for me, as well as Vanessa Dehn, who worked on the two-emitter WQED setup with me.

The fruitful collaboration with Prof. Dr. Stephan Reitzenstein and his group made it possible to compare theory with experiment. I thank him, Dr. Samir Bounouar, and Marcel Hohn for this. The CRC 910 of the DFG has provided financial support for my work. For this, I would like to express my gratitude. For inviting me to conduct research with them at the NTT Basic Research Laboratories in Atsugi, Japan, I would, furthermore, like to thank Dr. William Munro and Dr. Victor Bastidas.

I owe it to my mother that I have made it to this point. I am indebted to her and the rest of my family for their constant support. Moreover, it would not have been possible to complete this work without diversion, which is why I am very grateful to my friends inside and outside the university. Last but not least, I thank Robert for accompanying me in life and being there for me.